

# **Optical diagnostics for spray, ignition, and combustion in a light-duty Diesel engine**

Von der Fakultät für Ingenieurwissenschaften, Abteilung Maschinenbau und Verfahrenstechnik

der

Universität Duisburg-Essen

zur Erlangung des akademischen Grades

eines

Doktors der Ingenieurwissenschaften

Dr.-Ing.

genehmigte Dissertation

von

Ming Zhao

aus

Liaoning, China

Gutachter: Prof. Dr. Sebastian A. Kaiser

Prof. Dr. Christof Schulz

Tag der mündlichen Prüfung: 19.05.2020



---

## Acknowledgment

---

First, I would like to thank for the opportunity, which Prof. Christof Schulz and Prof. Sebastian Kaiser gave me five years ago, of accepting me for doing a PhD in this wonderful institute, IVG. This experience in a foreign country, in the sense of both working and living, is an invaluable treasure in my life. From my advisor, Sebastian, I learnt a lot about science and more importantly, having opinions, being open-minded and kind, and finally becoming a person of integrity. I acquired working and professional skills as well thanks to my colleagues. I am grateful for the help from Philipp Barth, Sebastian Wiemann, Martin Schild, Syahar Shawal, Martin Goschütz, and Daniel Fuhrmann of integrating me into the research group as well as into the German culture in the beginning. I thank Philipp Barth especially for teaching me how to run the complex engine test bench. I am thankful to our technicians, Jörg Albrecht, Erdal Akyildiz, Natascha Schlösser, Beate Endres, Ludger Jerig, Sebastian Rosendahl, and Birgit Nelius, for their help on the experiment. On this point, the help from our student assistants, Jörg Wende, Pascal Prüß, Joel Albrecht, and Arnold Litterscheid is also valuable. Particularly, for me Jörg Wende is both a reliable helper and an advisor on mechanics. Also, my students, namely Jan Bühnen, Irfan Tahir, Simon Lohwasser, Guanyu Wang, and Kee Tian Tee, supported me on the other sub-projects, such that I can focus on my research. In addition, I appreciate the work of our secretary, Barbara Nota, for the ordering and all the emails she sent to me. The colleagues in the other groups in IVG, such as Ralf Starke, Thomas Dreier, Bo Shu, Rongchao Pan, Lisong Xiao, Lin Shi, Florian Schneider, Philipp Niegemann, Matthias Beuting, Torsten Endres, Simon Görs, and Siavash Zabeti, gave me aid on different aspects on working or living. Ulrich Visser and Michael Eisenhut from the mechanical workshop in our university offered suggestions on the mechanical designs. I am grateful for that. Last but not least, I really appreciate working with my groupmates, especially Patrick Kranz, Niklas Jüngst, and Muhammad Ali Shahbaz, for their warm hearts and the fun we had together.

I would like to thank our ECN colleagues, too. Lyle Pickett, Louis-Marie Malbec, Scott Skeen, Paul Miles, Gilles Bruneaux, Jose Garcia-Oliver, Andrés López, Valerie von Koerber, Mark Musculus, and other ECN colleagues gave suggestions on the experiment and shared information and data with us. I am really honored to have worked in this community.

In addition, I thank my friends I made here, including Lei Yang, Wei Deng, Chen Jin, Fangfei Li, Aswin Vijai, Yang Yuan, Xiaoyi Ma, Xiaowei Hu, Dong He, Guoxin Tian, Xiaotong Mi, Guannan Liu, and so on, for their company and help during these years in my private life. I thank Andrea Lax-Küten for teaching me German for three semesters, although I did not keep improving it thereafter, unfortunately.

I sincerely thank the China Scholarship Council (CSC) for funding my study. It provided me with the access to a higher platform.

Finally, I thank my favorite rock music, soccer teams, and movies, which accompanied me in the dark days and offered me the mental power to move on. I appreciate much the concern and encouragement from my families, relatives, and friends in China during these years. Especially, I truly thank my parents for their unconditional support and love all the time.

---

*If you don't walk out, you will think that this is the whole world.*

Cinema Paradiso

---

---

## Abstract

---

A series of optical diagnostics was used in a light-duty optically accessible Diesel engine to investigate the in-cylinder thermofluidic conditions, the spray and combustion characteristics, and compression-ignition (CI) knock. Most of the experiments were performed with Spray B from the Engine Combustion Network's (ECN) series of standardized injectors and experimental conditions.

To determine the in-cylinder flow field, particle image velocimetry (PIV) was performed for both low-swirl and high-swirl conditions. From the resulting flow fields, the time evolutions of the turbulent kinetic energy and the swirl ratio were calculated. The in-cylinder temperature field at compression top-dead center was obtained from laser-induced fluorescence (LIF) of toluene evaporated into the intake charge. At low swirl, the ensemble-average temperature field was found to be almost uniform throughout the piston bowl. At high swirl, temperatures in the bowl are lower and radially inhomogeneous with a thicker boundary layer.

The ECN Spray B (three jets, injector 211201) was investigated by "fire-deck retro-reflection" with illumination by a pulsed light-emitting diode (LED). The liquid and the gas phase of the fuel spray were captured simultaneously with high temporal resolution (about 50 000 frames/second) and identified in the images in post-processing. The effects of ambient temperature and density, injection pressure, swirl level, and hole-to-hole variation on liquid length, vapor penetration, spray dispersion angle, ignition delay, ignition location, flame luminosity, and heat release rate were investigated. The effects of swirl and hole-to-hole variation were found to be complex and are likely to be related to thermofluidic conditions and spray/flow interactions that are beyond the scope of this work. The quasi-steady liquid length and the ignition delay measured in this work were compared to data from the literature on Spray B in high-pressure vessels and engines. The effect of facilities (in the sense of chamber size and flow field) was found to be less significant than the effect of the different diagnostics used in the various investigations.

To clarify the effect of diagnostics on the detection of ignition delay, multi-spectral high-speed imaging was performed. Chemiluminescence (CL) in the UV (from OH\* and other species) and in the visible spectral range was recorded simultaneously by an intensified camera and a color camera, respectively. The area-averaged flame luminosity in the flame contours, obtained with by segmentation via dynamic thresholding, was compared with pressure-based metrics close to ignition. The results show that the OH\*-CL and visible-CL signals roughly match but have different sensitivities to the low- and high-temperature reaction. The low-temperature reactions also make traditional heat-release analysis unreliable for detecting the ignition delay. The net pressure rise (the fired pressure minus the motored one) was a better metric.

Finally, knocking combustion after compression ignition was investigated. High-speed image sequences of combustion luminosity were processed based on the concept of optical-flow. The resulting flow fields show a "sloshing" movement of the flame that is due to acoustic resonance. The corresponding oscillation frequencies were obtained from the velocity-vector time-series. They match those from pressure-trace analysis and theoretical calculations. Here, knock originated from auto-ignition of the end gas, resembling knock in spark-ignition engines. In one very severe cycle, a shock wave was seen.

---

---

## Kurzfassung

---

In dieser Arbeit wurden verschiedene bildgebende Messtechniken in einem optisch zugänglichen Dieselmotor eingesetzt, um die innermotorische Strömung und Temperatur, die Sprayausbreitung und -zündung sowie Klopfphänomene zu untersuchen. Für die meisten Versuche wurde „Spray B“ aus der vom Engine Combustion Network (ECN) standardisierten Reihe an Injektoren und Versuchsbedingungen eingesetzt.

Die Strömung im Zylinder wurde während Einlass- und Verdichtungstakt durch Particle Image Velocimetry (PIV) zweidimensional für niedrigen und hohen Drall erfasst. Daraus wurde die zeitliche Entwicklung von turbulenter kinetischer Energie und Drallzahl berechnet. Das Temperaturfeld in der Zylindermulde wurde am oberen Totpunkt der Verdichtung durch laserinduzierte Fluoreszenz (LIF) von Toluol gemessen. Bei niedrigem Drall ist im Mehrzyklen-Mittel die Temperatur über weite Bereiche der Mulde fast einheitlich. Bei hohem Drall hingegen ist sie in der Mulde insgesamt höher, aber radial inhomogen mit einer deutlich dickeren Wandgrenzschicht.

Das ECN Spray B (drei Düsenlöcher, Injektor Nummer 211201) wurde durch die hier entwickelte „Zylinderkopf-Retroreflektion“ untersucht. Die Beleuchtung erfolgte durch eine gepulste Leuchtdiode (LED). Dabei wurden die flüssige und die gasförmige Phase des Kraftstoffjets simultan erfasst und in den zeitlich hochaufgelösten Bildserien durch geeignete Bildverarbeitung identifiziert. Die Einflüsse von Ladungstemperatur und -dichte, Einspritzdruck, Drallzahl sowie der Geometrie der (drei) einzelnen Düsenlöcher auf Flüssigstrahllänge, Eindringtiefe und Dispersionswinkel des Gasjets, Zündverzug und Zündort, Flammeneigenleuchten und Wärmefreisetzungsrates wurden untersucht. Insbesondere der Einfluss von Drall und Düsengeometrie stellte sich als komplex heraus und steht wahrscheinlich in einem weiteren, hier noch nicht geklärten Zusammenhang mit dem thermofluidischen Zustand der Ladung und der Spray/Strömungs-Interaktion. Die hier gemessene quasistationäre Flüssigstrahllänge und der Zündverzug wurden mit Literaturdaten zu Spray B in Hochdruck-Messkammern und Motoren verglichen. Der Einfluss der verschiedenen Versuchsträger tritt dabei hinter den zurück, der den Unterschieden zwischen den eingesetzten Messtechniken zuzuordnen ist.

Um den Einfluss der Messtechnik auf die Bestimmung der Zündverzugszeit zu klären, wurden multispektrale, zeitlich hochaufgelöste Bildserien aufgenommen. Sie erfassten zeitgleich Chemilumineszenz (CL) im UV (von OH\*) und im sichtbaren Spektralbereich mit einer bildverstärkten monochromen bzw. einer Farbkamera. Die Bilder wurden morphologisch segmentiert, und das Flammeneigenleuchten im entsprechenden Vordergrund räumlich gemittelt. Dieses zeitaufgelöste Signal in den verschiedenen Spektralbändern wurde mit druckbasierten Messgrößen im Zeitraum nahe der Zündung verglichen. Die Ergebnisse zeigen, dass OH\*-CL und sichtbare CL einander in ihrem zeitlichen Verlauf grob entsprechen, aber unterschiedlich sensitiv die Niedertemperatur-Verbrennungsreaktionen anzeigen. Diese Reaktionen führen auch zu Unsicherheiten in dem Zündverzug, der über der traditionell aus dem Druck hergeleiteten Größe der Wärmefreisetzung bestimmt wird. Der Netto-Druckanstieg, d.h., der Druck nach Abzug des Schleppdruckverlaufs, ist geeigneter.

Schließlich wurde die klopfende Verbrennung nach Kompressionszündung untersucht. Dazu wurden zeitlich hochaufgelöste Bildserien des Flammeneigenleuchtens mit einer Variante der Methode *Optical Flow* verarbeitet. Die resultierenden Geschwindigkeitsfelder zeigen eine „hin-und-herschwappende“ Bewegung der Zylinderladung, die auf akustischer Resonanz beruht. Deren Eigenfrequenzen wurden aus den Vektorzeitserien bestimmt und entsprechen in guter Übereinstimmung den Werten aus der Druckverlaufsanalyse und theoretischen Berechnungen. Im betrachteten Fall ist der Ursprung des Klopfens in der Selbstzündung des Endgases, wie es auch in im klassischen ottomotorischen Klopfen der Fall ist. In einem extremen Zyklus wurde eine Stoßwelle beobachtet.

---

---

## Table of contents

---

<b>Acknowledgment .....</b>	<b>I</b>
<b>Abstract .....</b>	<b>III</b>
<b>Kurzfassung .....</b>	<b>IV</b>
<b>Table of contents .....</b>	<b>V</b>
<b>Table of symbols and indices .....</b>	<b>IX</b>
<b>List of abbreviations .....</b>	<b>XII</b>
<b>Definitions and conventions .....</b>	<b>XV</b>
<b>Chapter 1 Introduction.....</b>	<b>1</b>
1.1 Challenges of internal combustion engines .....	1
1.2 Objective and outline .....	2
<b>Chapter 2 Scientific background.....</b>	<b>4</b>
2.1 Modern Diesel engines .....	4
2.1.1 Working principle .....	4
2.1.2 Intake and charge motion .....	5
2.1.3 Fuel injection and combustion systems.....	8
2.1.4 Diesel spray, ignition, and flame.....	10
2.1.5 Conventional diagnostics for engine performance.....	14
2.1.6 Modelling flow and combustion in engines .....	16
2.2 Optically accessible engines .....	17
2.2.1 Bowditch-type optical engines .....	17
2.2.2 Difference between optically-accessible engines and metal engines .....	18
2.3 Selected optical diagnostics for IC engines .....	19
2.3.1 Overview .....	19
2.3.2 Particle imaging velocimetry.....	23
2.3.3 Single-color tracer LIF thermometry .....	24
2.3.4 Mie scattering.....	26
2.3.5 Schlieren.....	28
2.3.6 Diffuse back-illumination.....	29
2.3.7 Natural flame luminosity.....	31
2.3.8 Multi-spectral imaging .....	33
2.3.9 Optical flow.....	34
2.4 Illumination and detection in optical diagnostics .....	36

---

---

2.4.1	Overview .....	36
2.4.2	Laser .....	36
2.4.3	Light-emitting diode (LED).....	37
2.4.4	CCD and CMOS sensor.....	38
2.5	Engine Combustion Network.....	40
2.5.1	Concept and structure of the ECN.....	40
2.5.2	Target conditions and nozzles .....	41
2.5.3	Facilities .....	43
2.5.4	Spray and combustion metrics.....	43
<b>Chapter 3 PIV and LIF for measurements of the in-cylinder flow and temperature fields .....</b>		<b>45</b>
3.1	Introduction.....	45
3.2	In-cylinder flow field .....	47
3.2.1	Experiment .....	47
3.2.2	Data post-processing.....	50
3.2.3	Results and discussion .....	51
3.2.4	Swirl ratio .....	54
3.3	In-cylinder temperature field.....	56
3.3.1	Experiment .....	56
3.3.2	Data post-processing.....	59
3.3.3	Results and discussion .....	65
3.4	Summary and conclusions.....	68
<b>Chapter 4 Fire-deck retro-reflection with skip-illumination applied to Spray B</b>		<b>70</b>
4.1	Introduction.....	70
4.2	Experiment.....	72
4.3	Data post-processing .....	74
4.3.1	Pressure-trace processing .....	74
4.3.2	Image processing .....	76
4.4	Results and discussion .....	84
4.4.1	Temporal evolution of spray.....	84
4.4.2	Effect of operating conditions .....	86
4.4.3	Hole-to-hole variation.....	94
4.4.4	Comparison with the ECN database .....	97
4.5	Summary and conclusions.....	103
4.5.1	Current results.....	103
4.5.2	Future work .....	104

---

---

<b>Chapter 5</b>	<b>Multi-spectral high-speed imaging of Spray B .....</b>	<b>105</b>
5.1	Introduction.....	105
5.2	Experimental apparatus and conditions .....	105
5.3	Data post-processing.....	109
5.3.1	Pressure-trace processing .....	109
5.3.2	Image processing.....	109
5.4	Results and discussion .....	110
5.4.1	Temporal evolution of combustion .....	110
5.4.2	Effect of the sensitivity of the imaging system .....	115
5.4.3	Monochrome system .....	118
5.4.4	Discussion .....	118
5.4.5	Comparison with the ECN database.....	119
5.4.6	Ignition location .....	120
5.4.7	Effect of swirl ratio on ignition delay .....	121
5.4.8	Hole-to-hole variation of ignition delay .....	122
5.5	Summary and conclusions .....	122
<b>Chapter 6</b>	<b>Optical-flow analysis of knock in CI engines .....</b>	<b>124</b>
6.1	Introduction.....	124
6.2	Experimental apparatus and conditions .....	125
6.3	Results, analysis, and discussion .....	126
6.3.1	Temporal evolution of knock .....	126
6.3.2	Knocking frequency analysis .....	131
6.3.3	Spatial origin of knock .....	139
6.3.4	Knock intensity .....	140
6.4	Summary and conclusions .....	142
<b>Chapter 7</b>	<b>Summary, conclusions, and future work.....</b>	<b>143</b>
7.1	Summary and conclusions .....	143
7.2	Future work.....	144
<b>Chapter 8</b>	<b>Bibliography .....</b>	<b>146</b>
8.1	Posters, presentations, and publications.....	146
8.1.1	Peer-reviewed journal papers .....	146
8.1.2	Conferences.....	146
8.1.3	ECN workshops.....	146
8.2	Supervised student theses .....	147
8.3	References.....	147
<b>Chapter 9</b>	<b>Appendices.....</b>	<b>172</b>

---

9.1	Comparison of retro-reflection with Mie scattering and schlieren.....	172
9.1.1	Introduction .....	172
9.1.2	Liquid spray measurement by Mie scattering.....	172
9.1.3	Gaseous spray measurement by schlieren imaging .....	176
9.1.4	Conclusions .....	179

---

## Table of symbols and indices

Symbol / Index	Unit	Meaning
$\mathcal{L}$	-	Spray axis
$\alpha_{mn}$	-	Root of the first-order derivative of the Bessel function
$\varepsilon_{abs}$	$L \cdot mol^{-1} \cdot cm^{-1}$	Molar attenuation coefficient of the tracer
$\eta$	-	Detection efficiency of the optical recording system
$\theta$	°	Spray dispersion angle
$\lambda_{op}$	-	Weighting coefficient for $E_{Prior}$
$\rho_a$	$kg/m^3$	Ambient gas density
$\rho_b$	$kg/m^3$	In-cylinder bulk-gas density
$\rho_c$	$kg/m^3$	In-cylinder gas density in the core region
$\rho_f$	$kg/m^3$	Liquid-fuel density
$\tau$	-	Optical thickness
$\gamma$	-	Specific heat ratio
$\phi$	-	Fuel/air equivalence ratio
$\phi_{qv}$	-	Fluorescence quantum yield
$\omega$	-	Angular velocity
$A_{ID1}$	-	Pre-exponential constant for ignition-delay in Equation (2.9)
$A_{ID2}$	-	Pre-exponential constant for ignition-delay in Equation (4.5)
$A_p$	$mm^2$	Projected area of the spray
$A_{p,s/2}$	$mm^2$	Projected area of the upstream half of the spray
$B$	mm	Diameter of a cylindrical cavity
$c_s$	m/s	Speed of sound
$c_{tra}$	mol/L	Molar concentration of the tracer
$C$	-	Correlation coefficient in PIV vector calculation
$C_a$	-	Orifice area-contraction coefficient
$C_d$	-	Orifice discharge coefficient
$C_{ext}^*$	$mm^2$	Extinction cross-section from Mie-theory
$C_v$	-	Orifice velocity coefficient
$d_d$	$\mu m$	Droplet diameter
$d_i$	$\mu m$	Orifice inlet diameter of the nozzle
$d_o$	$\mu m$	Orifice outlet diameter of the nozzle
$E$	J	Energy

$E_a$	J	Activation energy in an Arrhenius expression
$E_{data}$	J	Data-term of the global energy optimization for optical flow
$E_{Global}$	J	Global energy of the differential method for optical flow
$E_{laser}$	mJ	Laser energy
$E_{Prior}$	J	Prior-term of the global energy optimization for optical flow
$f$	mm	Focal length
$f_r$	kHz	Resonant frequency in a cavity
$I$	counts	Image intensity or optical signal
$I_l$	counts	Transmitted-light intensity
$I_0$	counts	Incident-light intensity
$I_{BG}$	counts	Image intensity of the BG image
$I_{dark}$	counts	Image intensity of the dark image
$I_{FF}$	counts	Image intensity of the flat-field image
$I_{ratio}$	-	Local signal ratio
$L_{abs}$	mm	Optical path length of absorption
$L$	mm	Length of a cylindrical cavity
$M_{v1}$	m <sup>2</sup> /s	Angular momentum in the measured ensemble-average vector field (specific)
$M_{v2}$	m <sup>2</sup> /s	Angular momentum of the assumed rotating solid body for swirl-ratio calculation (specific)
$n$	pixel	Size of the interrogation window for cross-correlation
$N$	min <sup>-1</sup> or “rpm”	Engine speed
$r$	mm	Radial distance
$R$	J/(mol·K)	Universal gas constant
$R_s$	J/(kg·K)	Specific gas constant
$p$	bar	Pressure
$p_{cyl}$	bar	In-cylinder pressure
$\tilde{p}_{cyl}$	bar	Filtered in-cylinder pressure
$p_{mi}$	bar	Indicated mean effective pressure
$\Delta p$	bar	Fuel pressure drop at the nozzle
$s$	mm	Spray penetration
$t$	ms	Time after start of (fuel) injection
$\Delta t$	μs	Time interval between the two laser pulses in PIV
$T$	K	Temperature
$T_a$	K	Ambient gas temperature surrounding the spray

$T_b$	K	In-cylinder bulk temperature
$T_c$	K	In-cylinder core temperature
$W_t$	°CA	Time window of knock
$W_i$	J	Theoretical work in an engine work cycle
$v$	m/s	Velocity
$v_\theta$	m/s	Circumferential component of velocity vectors
$v_r$	m/s	Radial component of velocity vectors
$v_{std\_x}$	m/s	Standard deviation of the local vectors in the $x$ direction
$v_{std\_y}$	m/s	Standard deviation of the local vectors in the $y$ direction
$V$	L	Volume
$V_{cyl}$	L	In-cylinder volume
$V_d$	L	Engine displacement volume
$Z_{st}$	-	Stoichiometric mixture fraction for ignition-delay
$K$ factor	-	An indicator for nozzle cavitation level $K = (d_i - d_o) / 10 \mu\text{m}$
$KL$ factor	-	An indicator proportional to the line-of-sight integral of soot volume fraction.
$AHRR$	J/°CA, W	Apparent heat release rate
$CA$	°	Crank angle
$HRR$	J/°CA, W	Heat release rate
$ID$	$\mu\text{s}$ , ms	Ignition delay
$IMPO$	bar·°CA	Integral of modulus of pressure oscillations
$KI_{opt}$	m/s	Knock intensity from the optical-flow vectors
$LL$	mm	Liquid length of the spray
$LVF$	-	Liquid volume fraction in the spray
$MAPO$	bar	Maximum amplitude of pressure oscillations
$QE$	-	Quantum efficiency
$SC$	-	Scaling factor in the dynamic thresholding method
$SNR$	-	Signal-to-noise ratio
$SR$	-	Swirl ratio
$TKE$	$\text{m}^2/\text{s}^2$	Turbulent kinetic energy

## List of abbreviations

Abbreviation	Meaning
°CA	Degree(s) crank angle
(A)HRR	(Apparent) heat-release rate
ANL	Argonne National Laboratory
APS	Advanced Photon Source
ASOI	After start of injection
BDC	Bottom dead center (piston position)
BG	Background (for images, if not optical filters)
CAI	Controlled auto-ignition
CARS	Coherent anti-Stokes Raman spectroscopy
CCD	Charge-coupled device
CFD	Computational fluid dynamics
CI	Compression ignition
CL	Chemiluminescence
CMOS	Complementary metal-oxide-semiconductor
CMT	CMT-Motores Térmicos
CPF	Constant-pressure flow
CVP	Constant-volume preburn
DBI	Diffuse back-illumination
DFCD	Digital flame color discrimination
DI	Direct injection
DNS	Direct numerical simulation
DPF	Diesel particulate filter
ECN	Engine Combustion Network
EGR	Exhaust gas recirculation
EOC	End of combustion
EOI	End of injection
EV	Electric vehicles
FF	Flat-field
FIR	Finite impulse response
FOV	Field-of-view
FPN	Fixed pattern noise
GVWR	Gross vehicle weight rating

---

HC	Hydrocarbon
HCCI	Homogeneous charge compression ignition
HR	High-reflective
HSDI	High-speed direct-injection
HSV	Hue-saturation-value
HTR	High-temperature reaction
ICCD	Intensified charge-coupled device
ICE	Internal combustion engine
IDI	Indirect injection
IFPEN	French Institute of Petroleum
IFTS	Imaging Fourier-transform spectrometer
IR	Infrared
IRO	Intensified relay optics
IVC	Intake valve closing
IVG	Institute for Combustion and Gas Dynamics
IVO	Intake valve opening
LES	Large eddy simulation
LDA	Laser Doppler anemometry
LED	Light-emitting diode
LIBS	Laser-induced breakdown spectroscopy
LIEF	Laser-induced exciplex fluorescence
LIF	Laser-induced fluorescence
LIGS	Laser induced grating spectroscopy
LII	Laser-induced incandescence
LTR	low-temperature reaction
MCP	Micro-channel plate
MSI	Mie scattering interferometry
ND	Neutral-density (for filters)
PAH	Poly-aromatic hydrocarbon
PCCI	Premixed-charge compression-ignition
PDPA	Phase Doppler particle analyzer
PFI	Port fuel injection
PIV	Particle image velocimetry
PLIF	Planar laser-induced fluorescence
PPC	Partially premixed combustion

---

---

PRNU	Photon response non-uniformity
PSD	Power spectral density
PTV	Particle tracking velocimetry
RCCI	Reactivity-controlled compression ignition
RCEM	Rapid compression-expansion machine
RMS	Root mean square
ROI	Region of interest
SI	Spark ignition
SNL	Sandia National Laboratories
SOC	Start of combustion
SOI	Start of injection
TDC	Top dead center (piston position)
TDLAS	Tunable diode laser absorption spectroscopy
TNF	International workshop on measurement and computation of turbulent non-premixed flames
TPA	Three Pressure Analysis
UHC	Unburned hydrocarbon
UV	Ultraviolet
VCO	Valve-covered orifice

---

---

## Definitions and conventions

---

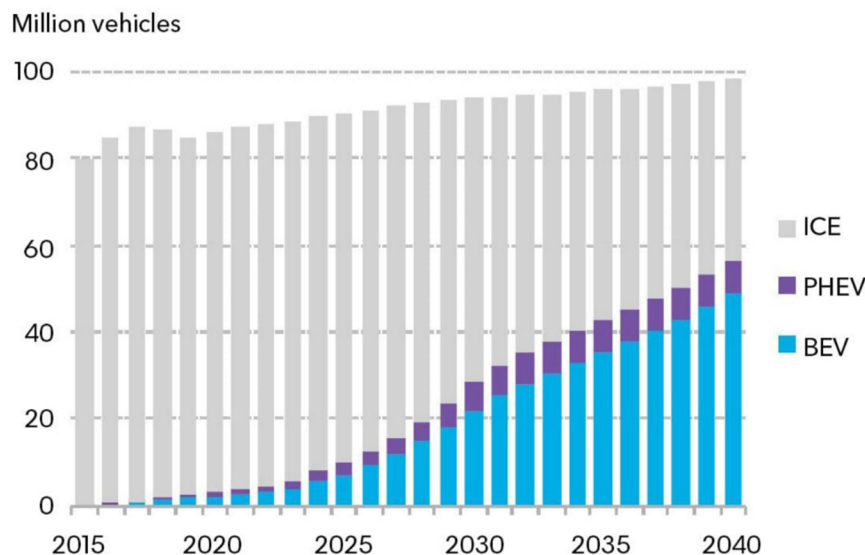
- The crank angle convention assigns  $0^\circ\text{CA}$  to combustion TDC, i.e., crank angles during compression are negative.
  - If not specially stated, “ignition” refers to high-temperature ignition, and “SOC” targets high-temperature reaction.
-



## Chapter 1 Introduction

### 1.1 Challenges of internal combustion engines

In the last ten years, the internal combustion engine (ICE) has been encountering the greatest challenge since it was invented in 1876 by Nikolaus Otto. The main question lies in the future of the powertrain of automobiles, although the ICEs have been dominant so far. Apart from the non-sustainability of fossil fuel and increasingly stricter emission regulations, a recent important factor for the ICE “panic” is the electric-car revolution in most countries. First, the governments favor the electric vehicles (EV) and make incentives for EV sales and purchase. Most of the countries set targets and timeline for phase-outs of Diesel and then gasoline engines for vehicles at least in the city between 2025 and 2050. For example, the German Bundesrat, or the Federal Council, passed a resolution in early 2019 to approve only emission-free cars for use on the roads by 2030 [1]. China is developing a long-term plan to phase out combustion engines [2] and will entirely eliminate ICEs in Hainan Province by 2030 [3]. Nearly ten federal states in the US have announced that they will reduce national vehicle emissions to zero by 2050 [2]. Second, relevant technology has been developing very fast, laying a good foundation for the EV revolution. The EV is expected to run averagely 300 miles at a single charge within 10 years, compared to 200 miles currently [4]. The cost for battery manufacturing is also decreasing, from \$176/kWh to \$87/kWh by 2025 and \$62/kWh in 2030 [5]. The infrastructure is improving as well. The chargers will be able to fill a car's battery pack to 80% in under 10 minutes [4]. The number of public charging outlets keeps increasing, with 630 000 public charging points installed globally in 2019 [5]. In addition to the EV newcomer Tesla, traditional automobile brands are already rolling out battery-powered vehicles, such as the Nissan Leaf in 2010, BMW i3 in 2013, Audi R8 E-tron in 2015, VW ID in 2016, and Porsche Taycan in 2019. These facts indicate a transition from ICE vehicles to EVs in the near future. As can be seen in Figure 1.1, analysts at Bloomberg New Energy Finance predict that 20 years from now, more than half of new passenger cars sold will be electric [5].



Source: BloombergNEF

Figure 1.1 Global long-term passenger-vehicle sales by drivetrain [5]. PHEV: plug-in hybrid electric vehicle. BEV: battery electric vehicle.

However, the transition to an all-EV fleet will not happen immediately. A series of technical questions need to be solved for EVs to take over from ICE vehicles. Before that, the ICE is still more competitive than batteries, especially for long-distance commercial vehicles, which are mostly powered

by Diesel. The maximum energy density of lithium-ion battery in 2012 is about 792 kJ/kg [6], while that of Diesel is about 44.8 MJ/kg [7]. Therefore, an EV is much heavier than an ICE vehicle with the same propulsion energy (if neglecting the weight difference between the ICE and the electric motor). In addition, the weight of the battery does not decrease with energy consumption as that of fuel does. The heavier vehicle body will need more energy for acceleration and deceleration and cause a shorter tire life [8]. With the up-to-date charging technique (charging current limited by the battery), recharging a car battery will take much longer time than refueling a fuel tank. For example, considering a truck with a range of 800 km and an average energy use of 140 kWh/100 km, the energy amount that a truck should carry after recharging or refueling is 1120 kWh. With the energy density mentioned above, a lithium-ion battery will weigh around five tons, approximately the same weight of a full-loaded class 3 light-duty truck according to gross vehicle weight rating (GVWR) [9]. Using an average charge power of 100 kW (the peak charge power of the latest Tesla V3 Supercharger is 250 kW [10]), more than 10 hours are needed to recharge the electric truck. Therefore, it is hardly possible for EVs to take over from long-distance commercial vehicles in the near future. The demand of Diesel fuel for transport is expected to still increase until 2050 [11]. Apart from transport, stationary Diesel engines also play an important role in power plants, especially in the near future when the demand of electricity extremely increases due to the EV revolution.

There will be one billion new ICEs produced between now and 2040 [12]. It is reasonable to make them cleaner, more efficient, and lower-cost. To achieve this target, in-cylinder processes, including charge flows, spray, ignition, and combustion, have to be understood and predictable, with the aid of computational fluid dynamics (CFD). To better understand the in-cylinder processes as well as provide database for CFD validation, optical diagnostics have become a powerful tool. Some optical diagnostics are mature and robust, like Mie scattering and soot visualization. Others, however, need to be developed and adapted to the unique challenges and questions in a specific scenario. Optically accessible engines are commonly used for directly studying the engine combustion with non-intrusive access. Because of the very high temperature and pressure, strong turbulence, and short time-scales in the combustion chamber, optical diagnostics in engines still need further development for higher accuracy and less complexity. Interestingly, development in optical diagnostics for engines sometimes can be re-used for electric motors, e.g. oil-flow visualization [13].

## 1.2 Objective and outline

The main objective of this work is to develop or improve optical diagnostics needed to investigate the spray combustion characteristics. A main target is the Engine Combustion Network (ECN) Spray B in a small-bore light-duty engine. First, the scientific background, including an introduction to both the metal and optical Diesel engine, theory and literature review for the optical diagnostics used in this work, and an overview of the ECN, will be given in Chapter 2. Second, in order to characterize the ambient conditions of the spray, the first half of Chapter 3 will show the measurement of in-cylinder flow field by particle image velocimetry (PIV). Thereby, the swirl ratios in the optical Diesel engine at the Institute for Combustion and Gas Dynamics (IVG) are determined. Single-color laser-induced fluorescence (LIF) thermometry was performed to determine the in-cylinder temperature field, where a method for flat-field correction with a standing engine was developed. This investigation will be shown in the second half of Chapter 3. Third, to obtain fundamental spray and combustion metrics, a simple but effective method based on the fire-deck retro-reflection with illumination by pulsed light-emitting diode (LED) was developed. Chapter 4 will show this method and the corresponding quasi-simultaneously imaging of both liquid and gas phase of the fuel spray as well as combustion. An overview of the evolution of fuel injection, ignition, and combustion of Spray B in a small-bore engine will be also given in Chapter 4. Finally, to examine the effect of diagnostics on the measurement of ignition-delay, including both

---

optical and pressure-based methods, multi-spectral high-speed imaging was performed and the results will be shown in Chapter 5. The temporal relation between the OH\*, visible-chemiluminescence, and pressure-rise signal at ignition will be clarified. Chapter 5 will focus on the metrics in detail, giving guidelines on ignition-delay measurements for conventional compression-ignition (CI) combustion. Using similar diagnostics and post-processing tools, the optical-flow concept was applied to the flame oscillation during knocking combustion, to be shown in Chapter 6. A series of post-processing tools was developed to obtain temporal and spatial origin of knock, knock frequency information, and knock intensity from the flow fields calculated based on cross-correlation. This investigation used a 7-hole injector. In the end, a short summary with the main conclusions as well as outlook of this work will be given in Chapter 7.

---

## Chapter 2 Scientific background

### 2.1 Modern Diesel engines

#### 2.1.1 Working principle

In a gasoline engine, the premixed fuel/air mixture is ignited by a spark plug. In contrast, in a Diesel engine fresh air is aspirated into the cylinder in the intake stroke, together with some exhaust gas (known as exhaust gas recirculation, EGR). After compression, liquid Diesel fuel is injected into the high-pressure and high-temperature gas and auto-ignited, achieving a short premixed phase followed by a long mixing-controlled phase of combustion. With temperature, the gas pressure increases, producing work by pushing the piston downward. Thereafter, the piston expels the exhaust gas out of the cylinder, followed by intake stroke of the next work cycle. A  $p$ - $V$  diagram of a real engine run with direct fuel injection near TDC is shown in Figure 2.1, left. During intake, the pressure is higher than that during exhaust because of supercharging. After combustion, the pressure during expansion is higher than that during compression, indicating work output. By neglecting the gas exchange process, the  $p$ - $V$  diagram is simplified to an ideal model with isentropic processes, as shown in Figure 2.1, right. This is designated as a “Seiliger” cycle with a pressure limit. The heat addition is composed of an isochoric process (b to c) and an isobaric process (c to c’), while usually only an isochoric process is used to represent a gasoline engine cycle. This is because in a typical Diesel combustion, the premixed part is much less compared to the mixing-controlled part, resulting slower combustion than in premixed spark-ignition (SI) combustion. Another difference from the gasoline engine lies in the compression process (a to b). For Diesel engines, the slope is greater, since fuel does not exist in the intake charge and correspondingly the specific heat ratio is higher. In the ideal model, the gas exchange process is simplified as an isochoric heat rejection from d to a. The overall indicated work  $W_i$  in a work cycle can be expressed as

$$W_i = \oint p_{cyl} \cdot dV_{cyl} \quad (2.1)$$

where  $p_{cyl}$  is the in-cylinder pressure and  $V_{cyl}$  is the in-cylinder volume.

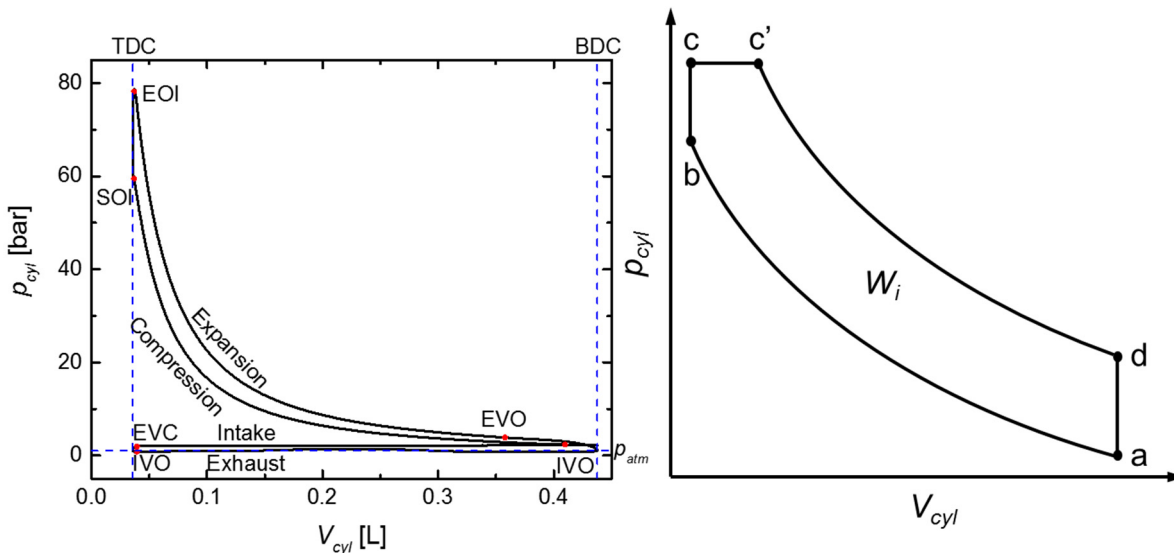


Figure 2.1  $p$ - $V$  diagrams of (left) a real engine run with supercharging and (right) an ideal model for the work cycle of conventional Diesel engines.  $a \rightarrow b$ : isentropic compression,  $b \rightarrow c$ : isochoric heat addition,  $c \rightarrow c'$ : isobaric heat addition,  $c' \rightarrow d$ : isentropic expansion,  $d \rightarrow a$ : isochoric heat rejection.

The indicated mean effective pressure  $p_{mi}$  is a very important indicator to evaluate an engine's capacity to do work independently of the displacement. It can be regarded as the average pressure acting on the piston.  $p_{mi}$  is calculated as

$$p_{mi} = \frac{W_i}{V_d} \quad (2.2)$$

where  $V_d$  is the engine displacement volume.

The first prototype Diesel engine was built in 1893 by Rudolf Diesel [14]. Through the development of over one hundred years, modern Diesel engines have become highly efficient and clean (in terms of emissions), with the aid of various new systems and concepts, such as intake swirl, downsizing, supercharging and exhaust gas turbocharging, intercooler, EGR, four valves, variable valve timing, electronic fuel injection system, high-pressure direct-injection, common rail system, Diesel particulate filter (DPF), selective catalytic reduction, etc. In this work, the experiments are performed in an optically accessible engine representing light-duty high-speed Diesel engines. Correspondingly, the following sections will focus on modern high-speed Diesel engines. Here only the important systems and concepts relating to this work are introduced. The exhaust-gas aftertreatment system, for example, is left out.

### 2.1.2 Intake and charge motion

The concept "engine downsizing" was proposed by the car manufacturers at the beginning of the century to increase the engine efficiency, to reduce the emissions, as well as to follow the regulation (e.g. road tax in the UK), by matching the power of smaller engines with that of larger engines. Turbocharging is the main approach to downsizing. It is one type of supercharging, which is to increase the air density before the intake port higher than the ambient air density. Thereby, more fuel can be injected and burnt, increasing the power of the engine with the displacement unchanged. The schematic of a typical turbocharging system is shown in Figure 2.2. The turbine (1) is driven by the engine exhaust gas, and drives the compressor (2). The exhaust gas then passes to the exhaust pipe. On the other side, air enters the centrifugal compressor (2) where it is accelerated to high velocity. Then, the air passes through a diffuser and the volute casing where the kinetic energy is converted to pressure energy. After compression, the temperature of the intake air is elevated. This will lead to lower intake-charge density and more harmful engine emissions, e.g.  $\text{NO}_x$ . Therefore, a charge air cooler (3) is used after the compressor to cool the intake air before entering the intake manifold. The intake pressure of a modern turbocharged high-speed Diesel engine can go up to 3 bar [15].

The EGR system is used to reduce engine-out  $\text{NO}_x$  emissions. It recirculates a portion of an engine's exhaust gas back to the engine intake port. This dilutes the oxygen in the intake charge and provides inert gases for combustion, slowing down the ignition and combustion as well as reducing the peak in-cylinder temperature. Exhaust gas is mainly composed of nitrogen, carbon dioxide, and water vapor, having a higher specific heat than air, which also contributes to lower combustion temperatures. Thereby,  $\text{NO}_x$  formation is suppressed. In Diesel engines, the fuel/air equivalence ratio is always lower than one. The EGR rate (the ratio of the recirculated gas mass to the whole intake gas mass) can be as high as 50% (25% in gasoline engines with port fuel injection (PFI) [16]). For the same reason for which the charge air cooler is used in the case of turbocharging, a heat exchanger is usually used to cool the EGR.

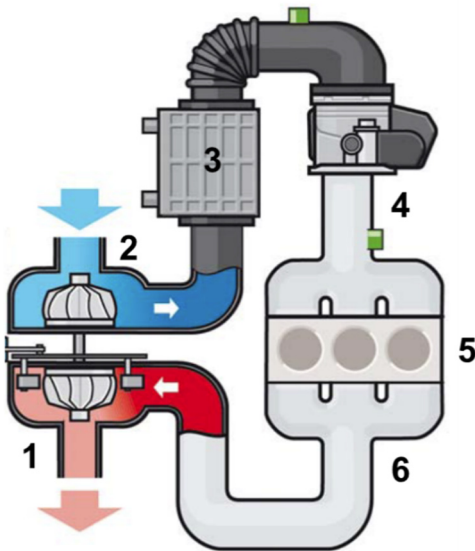


Figure 2.2 Schematic of a typical turbocharging system. (1) Turbine, (2) compressor, (3) charge air cooler, (4) intake manifold, (5) engine cylinders, (6) exhaust manifold [17].

Intake swirl is essentially a rotary flow around the cylinder axis. It is usually used in high-speed direct-injection (HSDI) Diesel engines to improve fuel/air mixing. As illustrated in Figure 2.3, a simplified picture of the process is that the swirl breaks up the compact fuel spray to mix the air sectors located between the fuel sprays with the fuel [18]. The intensity of swirl usually increases with engine speed due to the rise of piston speed. A common way to achieve swirl flow in the cylinder is beveling one side of the annular valve seat, which facilitates the discharge of the air in the direction of swirl and increases swirl in the lower valve lift range. For example, on the cylinder head of the optical Diesel engine at the IVG at the University of Duisburg-Essen, one intake valve seat is beveled at the side that the swirl is designed to flow to, as shown in Figure 2.4. In addition, the intake port can be designed to achieve a tangential flow of the intake air or a helical flow, where the air already spirals in the port. The helical port is better in terms of volumetric efficiency, producing a linear increase of swirl level as a function of engine speed [18]. Nowadays, HSDI engines usually have two intake ports. The swirl level can be varied by designing the ports with different swirl properties and throttling one of them. As shown in Figure 2.5, at low engine speed or low-load operation, the fill port is blocked (or throttled) and the air is mainly flowing through the swirl port to achieve a high swirl level, while at high engine speed, high-load, or idle operation, both ports are fully open for less charge loss and more intake charge in the cylinder.

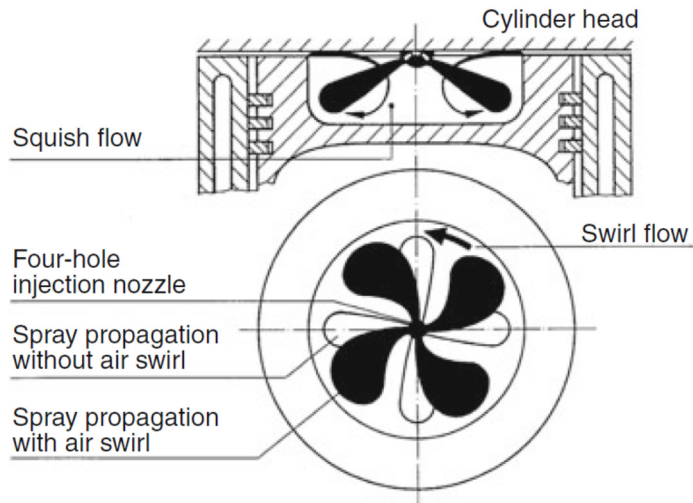


Figure 2.3 Schematic for the effect of swirl on spray propagation and mixture formation [18].

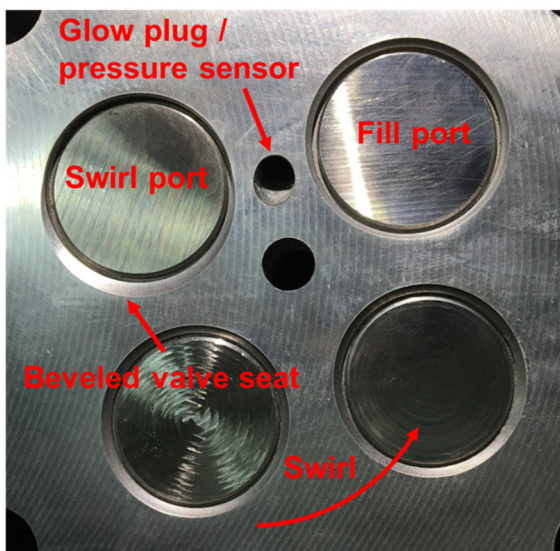


Figure 2.4 Beveled intake valve seat on the light-duty optical Diesel engine at the IVG (photo taken from below the cylinder head).

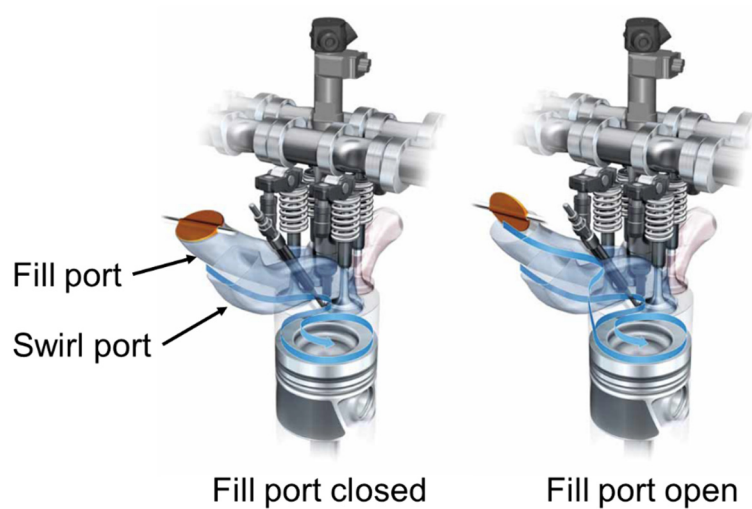


Figure 2.5 Variation of swirl level by throttling the fill port in an HSDI Diesel engine [17].

The swirl ratio,  $SR$ , is often used as a metric of the level of swirl motion in the engine. It is defined as the angular velocity of a solid-body rotating flow  $\omega$  that has equal angular momentum to the actual flow, divided by the crankshaft angular rotational speed [19]:

$$SR = \frac{\omega}{2\pi N} \quad (2.3)$$

where  $N$  is the engine speed.

Traditionally, the swirl ratio is measured on a steady-flow impulse torque swirl meter [19]. In this test rig, a steady flow through the intake port and valve assembly is created. The total torque exerted by the swirl flow on the honeycomb flow straightener as well as the mass flow rate are measured to calculate the swirl ratio. Alternatively, with the aid of optical diagnostics, swirl ratio can be also measured by PIV in an optical engine, as discussed in Chapter 3.

According to a previous study [20], in terms of the effect on the spray, stronger swirl deflects the spray trajectory, increases the spray dispersion angle and volume, and decreases the spray penetration. Thereby, the air entrainment into the spray and the fuel/air mixing are intensified. With one exception [21], most of the studies found that higher swirl ratios reduced ignition delay [22-24]. The effect of swirl on the heat release rate ( $HRR$ , refer to Section 2.1.5) of combustion is also controversial. In a few studies [21, 22, 24], higher premixed-burn peaks and lower  $HRR$  in the burn-out phase are observed with increased swirl levels, while Miles [23] found the opposite trends in a light-duty optical Diesel engine. The main advantage of introducing swirl in the engine is the reduction of soot emissions by enhancing the soot oxidation [21]. The drawbacks lie in more intense heat transfer with the engine walls [25] and lower volumetric efficiency.

In cold weather, high-speed Diesel engines can be difficult to start because the temperature at top dead center (TDC) after compression is not high enough for the auto-ignition of the fuel. In this case, a glow plug is used to provide the necessary heat for ignition, aiding starting the engine. The plug is a pencil-shaped piece of metal with a heating element at the tip. In the cylinder head of the IVG optical Diesel engine, the position for the glow plug is shown in Figure 2.4. Since two intake heating devices exist on the test bench, the bore for glow plugs is used for a pressure sensor.

### 2.1.3 Fuel injection and combustion systems

There are mainly two kinds of Diesel combustion systems, namely indirect injection (IDI) with a divided combustion chamber, and direct injection (DI) with an undivided combustion chamber. An IDI system with a prechamber and a DI system are illustrated in Figure 2.6. In the 80's and early 90's of the last century, the high-speed Diesel engines mainly used divided combustion chambers. The fuel is first injected into a prechamber (or a swirl chamber) under moderate pressure ( $<400$  bar [26]). Part of the fuel is burnt, increasing the temperature and pressure in the prechamber quickly. The rise in pressure blows vaporized fuel and species from partial combustion into the main combustion chamber formed by the cylinder and a recess in the piston head, through one or more channels connecting the two chambers. With the access to more air, the fuel and partially-oxidized fuel continue to burn in the main chamber. This two-stage combustion has low noise but high fuel consumption because of the long combustion duration and high heat loss to the walls. In the 90's, the development of high-pressure injection technology made pre-injection and injection rate shaping possible, lowering combustion noise in the DI combustion system [27]. Also because of the higher fuel efficiency it brings, DI is dominant in modern Diesel engines. The combustion chamber for DI is composed of the piston bowl and the squish area, which is kept as small as possible (height  $< 1$  mm) with a flat fire deck to achieve a high compression ratio [27]. The fuel is injected directly into the piston bowl near TDC and burnt.

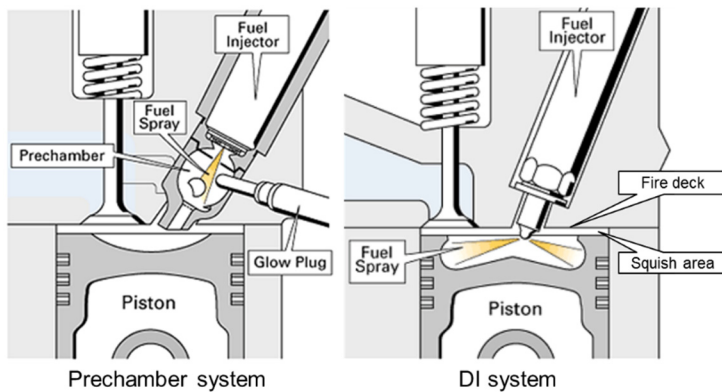


Figure 2.6 Schematics of an IDI prechamber system and a DI system [28].

In a DI combustion system, the piston bowl geometry is critical. For a high-speed Diesel engine, a deep and narrow piston bowl can increase the swirl level near TDC [29], since the intake charge rotates within a smaller cylinder, considering angular momentum conservation. A re-entrant bowl is a type of piston bowl where the top opening is smaller in diameter than the maximum bowl diameter, e.g. in the DI system in Figure 2.6. This type of piston bowl is often used in a light-duty engine to intensify the squish flow near TDC. Both the swirl and squish intensify the fuel/air mixing substantially. The fuel spray is quickly vaporized, and the fuel vapor impinges on the piston wall. If the liquid spray impinges on the piston wall, it will cause a wall-wetting, leading to inefficient combustion and soot production [30]. By contrast, the interaction between the fuel vapor and the wall is beneficial to some extent. Maes [31] investigated Diesel sprays in combustion vessels by both experiment and numerical simulation and found that the spray/wall interaction enhanced fuel/air mixing, resulting in a faster increase of the apparent heat release rate (*AHRR*) and a decreased burn-out duration compared to the free jet. In addition, soot formation was significantly reduced, which was also seen by Pickett and López [32] at a flat wall but not a confined wall in a combustion vessel. Bruneaux [33] found the fuel/air mixing rate was increased and the air entrainment was improved compared to a free jet only at high enough injection pressure, e.g. 2000 bar. For a heavy-duty Diesel engine, the engine speed range is smaller than that for a light-duty engine, and correspondingly the necessary swirl and squish level decreases because of longer time for premixture preparation and combustion at a lower engine speed. Thus, the piston bowl for heavy-duty engines is wider and shallower, usually without a re-entrant edge [27].

The so-called “common rail” fuel injection system is the most common for modern HSDI Diesel engines. It achieves electrically controlled multiple high-pressure injections. The fundamental difference from previous injection systems is that the pressure is generated independently from the injection cycle by a high-pressure pump that delivers the fuel to an accumulator volume or “rail” [34]. The injectors are actuated by electrically controlled valves and inject the fuel at the desired time for the desired duration. The fuel rail and the injectors are connected by short high-pressure tubes. There are mainly two kinds of common rail injectors, solenoid valve injectors and piezo injectors, distinguished by the control-valve type. Compared to the solenoid valve version, the piezo injector is more flexible with multiple injections and able to inject very low amounts of fuel for pre-injection. The injector also weighs less. However, the high cost and difficulty in manufacturing of piezo injectors make them less common than solenoid ones for passenger cars. In a solenoid injector, the needle (see Figure 2.7) is normally closed by the force of the nozzle spring. When the solenoid valve actuates, the needle is lifted by the force of the high-pressure fuel, resulting in fuel injection through the nozzle. To improve mixture formation and reduce injection duration, high injection pressure is desired. The injection pressure of an up-to-date mass-production common rail system has reached 2700 bar [35].

Both piezo and solenoid valve injectors use hole-type nozzles composed of needle and needle seat as shown in Figure 2.7. Hole-type nozzles are further divided into valve-covered orifice (VCO) or sac-hole designs. As seen in Figure 2.7, the sac hole designs have larger volume under the sealing edge in the needle seat that can trap fuel after the needle closes. This part of fuel “dribbles” out after the end of fuel injection and slowly burn in the combustion chamber, resulting in increased hydrocarbon (HC) and soot emissions [36]. The VCO nozzle keeps the trapped volume very small. However, the hole-to-hole distance needs to be long enough to keep the stress low [37], and durability can be a problem. Thus, although sac hole nozzles produce more fuel dribble, they are more commonly used. The number of spray holes depends on the combustion system and air management (e.g. swirl). The sprays should not intermix. At present, seven to nine spray holes with diameters of 105–135  $\mu\text{m}$  are employed in cars and six to eight spray holes with diameters of 150–190  $\mu\text{m}$  in heavy-duty vehicles [37].

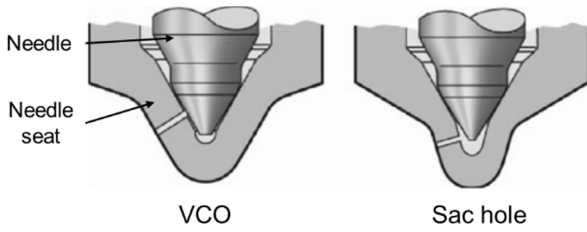


Figure 2.7 VCO and sac hole designs for hole-type nozzles [37].

#### 2.1.4 Diesel spray, ignition, and flame

In a Diesel spray at a quasi-steady state under high-temperature high-pressure ambient conditions, both liquid and gas phase of the fuel exist. The liquid fuel flows out of the nozzle orifice, breaks up to droplets (atomizes), evaporates, and mixes with the surrounding air. Most of the liquid mass is concentrated near the spray axis, while the outer spray regions contain less liquid mass and more fuel vapor. An example for the time evolution of the liquid phase in the spray is shown in Figure 2.8 [38]. Initially, the fuel evaporation is slow and the penetration of the liquid spray keeps increasing. This continues until the liquid phase region penetrates to a point where the total fuel evaporation rate in the spray equals the fuel injection rate. After this, the tip of the liquid region stops penetrating and begins fluctuating (because of turbulence) against a mean axial location. The distance from the nozzle orifice exit to the tip of the liquid spray is defined as the liquid length ( $LL$ ) [39]. Siebers [39] measured the liquid length in a combustion vessel by Mie scattering, defining a threshold at 3% of the maximum intensity along the spray axis. He found that the fuel vaporization in a Diesel spray is controlled by air entrainment, i.e., turbulent mixing processes, instead of the local interphase transport rates of mass, momentum, and the energy, which controls liquid breakup and droplet evaporation. This explains why the liquid length stays constant for different injection pressures. More specifically, the total entrained gas flow rate is proportional to the mass flow of the fuel, when the injection pressure is the only variable. A scaling law for the liquid length was also given by Siebers [40], accounting for the nozzle parameters, fuel, and in-cylinder thermodynamic conditions. For a simpler calculation, Payri et al. [41] postulated an empirical correlation of liquid length based on a Mie scattering experiment in an optically-accessible two stroke engine. It is a power law as a function of the orifice outlet diameter  $d_o$ , orifice area contraction coefficient  $C_a$ , ambient gas density (surrounding the spray)  $\rho_a$ , ambient gas temperature  $T_a$ , and pressure drop  $\Delta p$  across the nozzle, given by

$$LL = C_{LL} \cdot d_o^a \cdot C_a^b \cdot \rho_a^c \cdot T_a^d \cdot \Delta p^e \quad (2.4)$$

where  $C_{LL}$  is a constant.

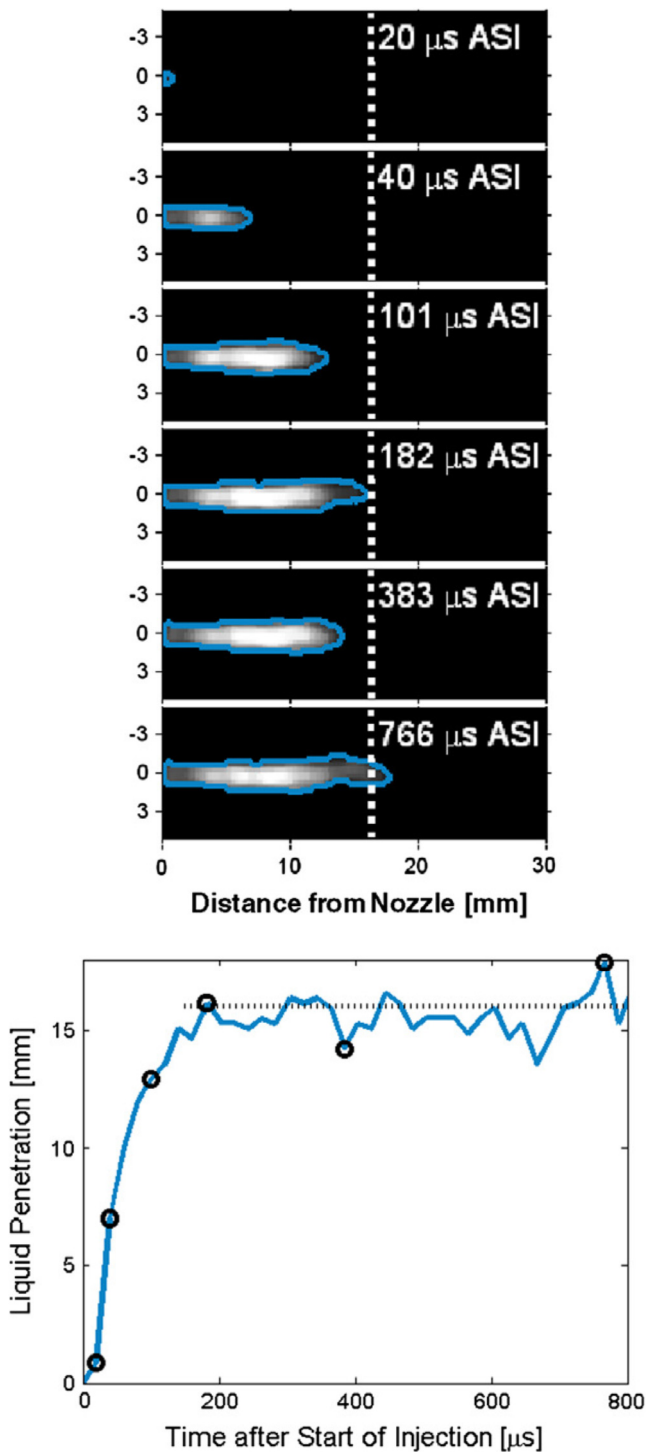


Figure 2.8 (top) Example images in time sequence from Mie scattering and (bottom) the time evolution of liquid length determined from the images [38]. The ensemble-average quasi-steady liquid length is overlaid as a vertical dashed line.

The spray penetration  $s$  is the distance between the nozzle orifice exit and the spray tip, which is mostly defined by the tip of fuel vapor. Naber and Siebers [42] measured the spray penetration in a combustion vessel by schlieren imaging, defining the penetration as the distance along the spray axis  $\mathcal{C}$  to a location where 1/2 of the pixels on an arc of  $\theta/2$  centered on the spray axis are out of the spray region. A schematic is shown in Figure 2.9.  $\theta$  is the spray dispersion angle, defined by

$$\frac{\theta}{2} = \tan^{-1} \frac{A_{p,s/2}}{\left(\frac{s}{2}\right)^2} \quad (2.5)$$

where  $A_{p,s/2}$  is the projected spray area of the upstream half of the spray in an image. Practically,  $\theta$  can be first determined by estimating the penetration to the pixel farthest from the nozzle exit in the spray region.

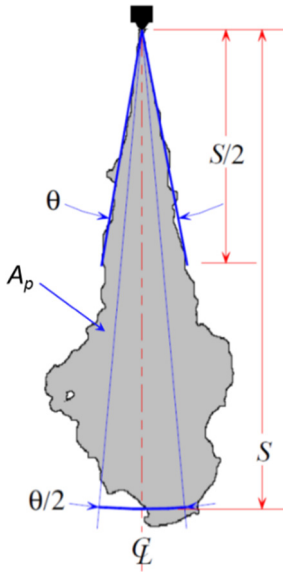


Figure 2.9 Definition of the spray axis ( $\Phi$ ), the spray penetration ( $s$ ), the spray dispersion angle ( $\theta$ ), and the projected area (the gray region  $A_p$ ) according to Naber's and Siebers's method [42].

Theoretically, there is no difference in spray penetration between non-vaporizing and vaporizing sprays at the same boundary conditions, except for gas the contraction from the fuel evaporation (cooling effect) for a vaporizing spray [42]. Therefore, the two-phase Diesel spray can be treated as a gas jet to calculate spray penetration. Again, a scaling law was given by Naber and Siebers [42]. In the short-time limit,  $s$  is roughly proportional to time after start of injection  $t$ . The dimensional form is

$$s = C_v \cdot \sqrt{2 \frac{\Delta p}{\rho_f}} \cdot t \quad (2.6)$$

where  $C_v$  is the orifice velocity coefficient and  $\rho_f$  is the fuel density.

In the long-time limit,  $s$  is roughly proportional to  $t^{0.5}$ :

$$s = \sqrt{\frac{C_v \sqrt{(2 \cdot C_a)}}{a_s \cdot \tan(\theta/2)}} \cdot \sqrt{\frac{\Delta p}{\rho_a}} \cdot d_o \cdot t \quad (2.7)$$

where  $a_s$  is a constant with a value of 0.66.

$\theta$  is a function of the ratio of the density of the ambient air to the fuel, but it is also related to nozzle parameters. An empirical correlation can be written as [42]

$$\tan\left(\frac{\theta}{2}\right) = a_\theta \cdot \left(\frac{\rho_a}{\rho_f}\right)^{0.19} \quad (2.8)$$

where  $a_\theta$  is a parameter dependent on  $d_o$ .

In the transition between the short- and long-time limit, the spray changes from one dominated by the injection momentum to one dominated by entrained air. To calculate  $s$  in the whole time scale, Musculus and Pickett [43, 44] developed a 1D jet model based on Naber's and Siebers's control-volume analysis for steady-state injection [42]. The mixture fraction can be also obtained. An algorithm for this

model can be downloaded from the ECN website [45]. It needs  $\rho_f$ ,  $\rho_a$ ,  $C_a$ ,  $C_v$ ,  $d_o$ ,  $\theta$ , and  $\Delta p$  as inputs, with the profile parameter  $\alpha$  estimated as 1.5.

Diesel spray ignition experiences first a low-temperature and then a high-temperature phase. Both the pressure and optical signal of low-temperature reaction (LTR) are very weak and slowly increasing [46]. The optical signal is mainly attributed to the blue chemiluminescence of  $\text{CH}_2\text{O}^*$  [47-50]. By contrast, high-temperature ignition happens fast, accompanied by strong heat release and light emission due to chemiluminescence [46]. Therefore, to define “ignition delay”, usually high-temperature ignition is used [51]. In direct-injection compression-ignition, such as conventional Diesel combustion, ignition delay is the time duration from start of injection (SOI) to fuel ignition. (Throughout this work, if not specially stated, “ignition” refers to high-temperature ignition.) In previous experiments, researchers exploited different diagnostics for ignition delay measurement. The most common methods are  $\text{OH}^*$  chemiluminescence imaging, non-intensified broadband imaging, as well as traditional pressure-based *HRR* analysis [23, 52-56].

Like the spray metrics, ignition delay is also affected by the thermofluidic conditions in the engine. Higher ambient temperature, ambient density, and oxygen concentration in the ambient gas will cause a shorter ignition delay. A correlation based on an Arrhenius expression for ignition delay (*ID*) under Diesel conditions was found by Pickett et al. [54]. It can be written as

$$ID = A_{ID1} \exp(E_a/RT_a) \rho_a^\alpha Z_{st}^b \quad (2.9)$$

where  $A_{ID1}$  is a pre-exponential constant accounting for nozzle parameters,  $E_a$  the global activation energy,  $R$  the universal gas constant, and  $Z_{st}$  the stoichiometric mixture fraction.

For a Diesel flame in a quasi-steady state, Dec et al. [57, 58] proposed a model for the flame structure based on a series of laser-based imaging diagnostics. As shown in Figure 2.10, low-temperature liquid fuel is injected from the nozzle, heated, and mixed with the entrained air (also including the re-entrained combustion products from downstream), resulting in a fuel-rich fuel/air mixture at the liquid spray tip. This mixture partially burns, producing fuel fragments, CO, and  $\text{H}_2\text{O}$ . The poly-aromatic hydrocarbon (PAH) is a typical type of these fuel fragments and also formed here, in the middle of the jet flame. They are well-known as precursors of soot. Downstream, the temperature is further increased by radiative and convective heat transfer from the flame in the sheath. The jet head is a hot oxygen-depleted region, with conditions favorable for the formation and agglomeration of soot particles. Surrounding the jet is a flame layer, where soot, unburned hydrocarbon (UHC), and CO are converted to  $\text{CO}_2$  and  $\text{H}_2\text{O}$ . The temperature at the surface of the flame downstream is the highest throughout the jet, providing ideal conditions for  $\text{NO}_x$  formation.

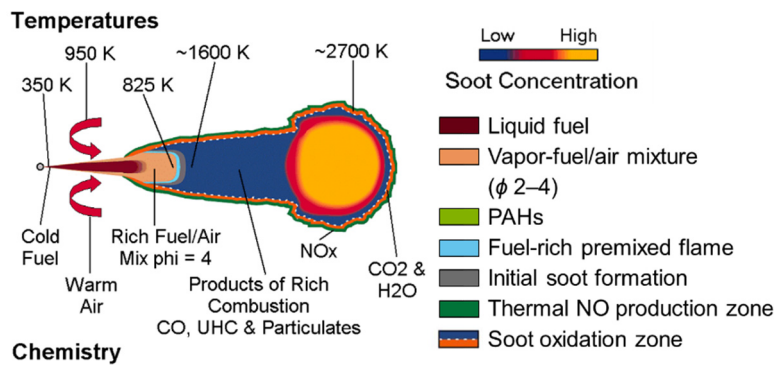


Figure 2.10 Schematic of quasi-steady burning jet according to Dec's model [57, 58].  $\phi$  –fuel/air equivalence ratio.

Since the Diesel jet flame has a certain structure, different species can be detected by optical diagnostics in different locations to evaluate the combustion condition as well as to compare with numerical simulation. Figure 2.11 shows an example from combustion vessels for the single-hole ‘‘Spray A’’ from the ECN [59]. Formaldehyde ( $\text{CH}_2\text{O}$ ) is a good marker of the LTR and detected together with PAH and shown in green. They were not separated from each other in the experiments, because of the overlap of the fluorescence signals in wavelength. In Figure 2.11, the signals of these two species are shown throughout the jet flame. However, theoretically,  $\text{CH}_2\text{O}$  should exist only at the upstream near the liquid spray tip [60], while the PAH is probably located more downstream. The red color shows OH, which is a good marker for high-temperature reaction (HTR). OH exists in the sheath of the jet flame, not in the interior region, as shown in Figure 2.10. There is an overlap region where both OH and  $\text{CH}_2\text{O}$  exist. It is shown in yellow. The above species were all detected with laser-sheet imaging. One group detected the soot volume fraction in line-of-sight imaging [61] in addition, shown in blue, in the more downstream region than  $\text{CH}_2\text{O}$ /PAH.  $\text{OH}^*$  is an electronically excited state of OH, detected also in line-of-sight imaging. It is shown by the white contours.  $\text{OH}^*$  is usually used for measuring the flame lift-off length [62], which is the distance from the orifice exit to the mean flame location. It indicates the amount of entrained air and is closely related with soot production [63, 64].

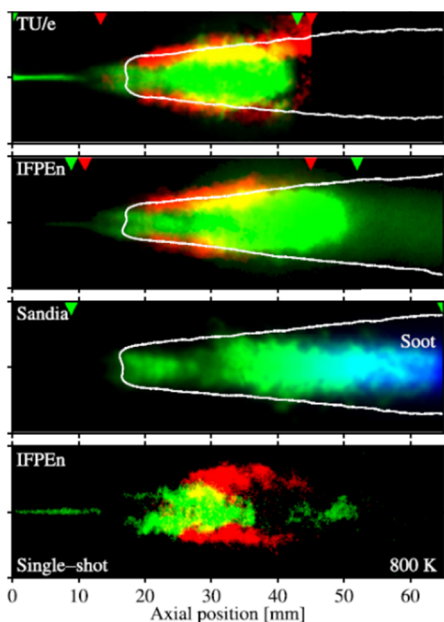


Figure 2.11 Combination of results showing the spatial relation between OH,  $\text{OH}^*$ , formaldehyde/PAH, and soot volume fraction from measurements by several research groups in the ECN [45, 61] (figure taken from [59]). Green –  $\text{CH}_2\text{O}$  and PAH from planar laser-induced fluorescence (PLIF), red – OH from PLIF, and blue – soot volume fraction from light extinction. The white lines show contours of  $\text{OH}^*$  chemiluminescence. The top three panels show ensemble-average images. The bottom panel shows simultaneously acquired single-shot images at an ambient temperature of 800 K, instead of 900 K in the rest.

### 2.1.5 Conventional diagnostics for engine performance

To evaluate and improve the performance of engines, researchers have implemented various techniques for diagnosis. The traditional engineering approach is mostly to treat the engine combustion chamber as a black box and make measurements outside. This includes intake mass flow, temperature and pressure at the intake and exhaust ports as well as in the fuel injection system, oxygen concentration by an oxygen sensor in the exhaust, knock detection through engine body vibration, etc. The in-cylinder pressure measurement is a conventional method of monitoring and analyzing the combustion. To gain

more information, optical diagnostics have been used very often recently. They will be introduced in detail in Section 2.3. For instance, measuring in-cylinder temperature without optical access is very difficult. To measure the wall temperature in the combustion chamber, thermocouples can be inserted on the fire deck, the cylinder liner, and the piston surface [65-67].

The in-cylinder pressure is usually measured by a piezoelectric pressure sensor. It can achieve a sampling rate on the order of 100 kHz. However, piezoelectric transducers respond to pressure differences by outputting a charge referenced to an arbitrary ground, not to the absolute pressure value [68]. Therefore, the cylinder pressure needs to be calibrated with a reference pressure at some point in the engine cycle. Usually, the intake pressure at intake bottom dead center (BDC) is used as the reference pressure, since at this point the in-cylinder pressure is very close to the pressure at the intake port [69]. The manifold pressure sensors are precise for absolute pressure, because they are usually piezoresistive sensors with vacuum chambers. The raw data of cylinder pressure usually contain information of the acoustic resonance in the combustion chamber triggered by combustion [70]. Therefore, a low-pass filter is often used to exclude the resonance signal as well as high-frequency electronic noise.

The heat release rate ( $HRR$ ) is the rate of heat release directly from the fuel combustion in the engine, while the apparent heat release rate ( $AHRR$ ) is the difference between the heat release rate from the fuel and the heat loss rate through the engine. The latter is easier to calculate since a heat transfer model is not needed. According to the first law of thermodynamics, assuming the in-cylinder contents to be an ideal gas, the  $AHRR$  is given by

$$AHRR = \frac{\gamma}{\gamma-1} p_{cyl} \frac{dV_{cyl}}{dt} + \frac{1}{\gamma-1} V_{cyl} \frac{dp_{cyl}}{dt} \quad (2.10)$$

where  $\gamma$  is the specific heat ratio. The crevice flow effects and the sensible enthalpy of the fuel is ignored.

According to Equation (2.10), the  $AHRR$  is composed of two terms, the change rate of the volume and that of the pressure. If an isentropic compression and expansion without combustion is considered, the  $AHRR$  equals zero.

$\gamma$  in an engine slightly decreases during the compression stroke, decreases faster after the start of combustion (SOC), and finally increases when the temperature increases near the end of combustion (EOC) [71]. For a Diesel engine, at the end of compression prior to combustion,  $\gamma$  can be taken as that of air ( $\approx 1.35$ ) [72]. The minimum value during combustion without EGR is approximately 1.3 [71].

An example of  $AHRR$  in a light-duty Diesel engine is shown in Figure 2.12 together with the cylinder pressure trace, from which the  $AHRR$  is calculated. The pressure trace is processed by a low-pass filter with a high-to-low transition at 3 to 5 kHz. Before SOI, the  $AHRR$  is negative because of the heat loss to the walls of combustion chamber. The local peak directly after SOI is probably due to ringing from the low-pass filter. The major peak thereafter is attributed to combustion of the fuel that mixed with air during the ignition delay. This peak is called premixed-burn peak. The next phase is the mixing-controlled burn period, where fuel/air mixing and combustion take place at the same time. Before the end of injection (EOI), the combustion has a quasi-steady phase, with  $AHRR$  nearly unchanged (or slowly increasing [73]). The oscillation here is probably due to the acoustic resonance remaining in the pressure trace after filtering. At EOI, a local peak appears, which can be explained by the entrainment wave [43]. The period after EOI is designated “burn-out” phase, since no fuel is injected any more.

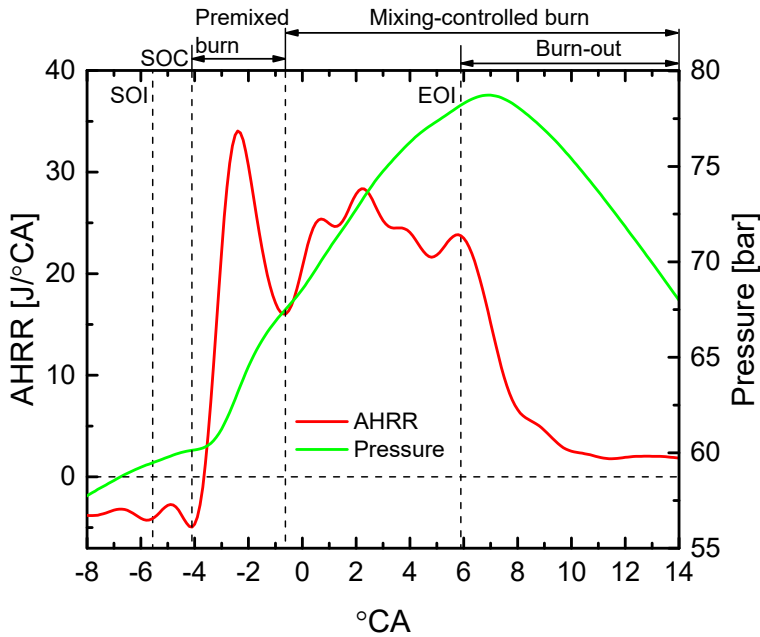


Figure 2.12 Example of cylinder pressure and AHRR trace in a light-duty Diesel engine.

### 2.1.6 Modelling flow and combustion in engines

In the last few decades, with improving computer power, modelling has been an increasingly useful tool for research, design, and development of engines. The flow and combustion in engines can be simulated to investigate a variety of operating conditions, which needs much more time and effort if done by experiment, or is impossible at all. Modelling helps understand the process under study, identify key controlling variables for experiments, predict engine behavior, determine trends and trade-offs, optimize design and control, and provide basis for design innovation [74]. Two main categories of models have been developed. One is based on thermodynamics and low-dimensional fluid dynamics (referred to as thermodynamic models), often zero-dimensional (0D, absence of any flow modelling), quasi-dimensional (e.g. flame propagation or spray penetration distance is considered), or one-dimensional (1D, e.g. for pipe flow out of cylinder). The other (referred to as CFD models) is based on three-dimensional fluid dynamics, providing spatiotemporally resolved information on flow and combustion. The processes outside the cylinder, like intake and exhaust, are usually simulated in a thermodynamic model, while the complex in-cylinder flow and combustion typically need 3D CFD tools to achieve an accurate simulation. As an example for thermodynamic models, GT-POWER from Gamma Technologies is an industry-standard software for 0D/1D engine modelling.

There are three categories of CFD simulations according to the method for treating turbulence [75]. Direct numerical simulation (DNS) solves the Navier-Stokes equations in the computational mesh without modelling the turbulence. This is the most accurate approach but also the most time-consuming. Reynolds-averaged Navier-Stokes (RANS) is the most prevalent method of simulating turbulence. They only compute the time-averaged quantities, not the instantaneous ones. Here the  $k-\varepsilon$  model is widely used to compute the Reynolds stress (accounting for turbulent fluctuations), where  $k$  is the turbulent kinetic energy and  $\varepsilon$  is its dissipation rate. Large eddy simulation (LES) is an approach between RANS and DNS, solving the Navier-Stokes equations only for large eddies, while modelling the small-scale eddies. LES also results in instantaneous information, like DNS.

Figure 2.13 shows an example of RANS simulation results using the  $k-\varepsilon$  model for a reacting Diesel spray, compared to experimental results from laser diagnostics, showing distribution of OH/OH\*, CH<sub>2</sub>O, and C<sub>2</sub>H<sub>2</sub> (only by simulation) at 0.7 ms ASOI (total injection duration 5.0 ms) [73]. Modelling

and optical diagnostics are counterparts of each other and used to understand the complex physical and chemical processes in the “black boxes” of engines. Numerical simulation needs optical diagnostics to validate the underlying models and thus achieve more accurate results.

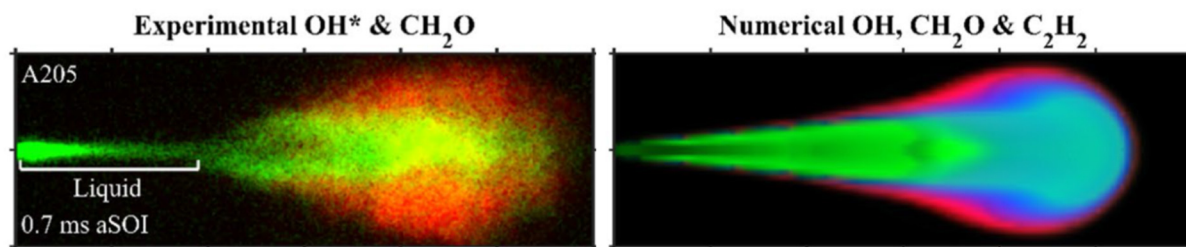


Figure 2.13 (right) Example RANS simulation results using the  $k-\epsilon$  model for a reacting Diesel spray compared to (left) experimental results showing  $\text{OH}^*$  and  $\text{CH}_2\text{O}$  fields [73]. The images are color-coded, green for  $\text{CH}_2\text{O}$ , red for  $\text{OH}$  (modelling) and  $\text{OH}^*$  (experimental and line-of-sight), and blue for  $\text{C}_2\text{H}_2$  (modelling). The experimental  $\text{CH}_2\text{O}$  signal upstream in the spray is an artifact from the elastic light scattering from liquid fuel.  $d_o = 0.205$  mm,  $p_f = 1500$  bar,  $T_a = 900$  K,  $\rho_a = 22.8$  kg/m<sup>3</sup>,  $\text{O}_2$  concentration 15%.

## 2.2 Optically accessible engines

### 2.2.1 Bowditch-type optical engines

As opposed to combustion vessels and rapid compression-expansion machine (RCEM), optically accessible engines have realistic in-cylinder flow fields and sizes of the combustion chamber. The most common type of engines with optical access to the whole combustion chamber is the Bowditch type. It is named after the engineer at General Motors who first proposed and developed it [76]. As shown by the example in Figure 2.14, the Bowditch-type optical engine features an elongated piston with optical access through the piston crown and very often a transparent spacer between the cylinder liner and the cylinder head. For SI optical engines, the spacer can be made of a single piece of “glass” (really, quartz or sapphire). For Diesel versions, the spacer is usually a combination of glass and metal with a cooling system. Sometimes one of the exhaust valves is replaced by a window to view from the engine head [52]. Apart from Bowditch-type, optical accesses via endoscopes [77], borescopes [78], and optical fibers [79] are also possible.

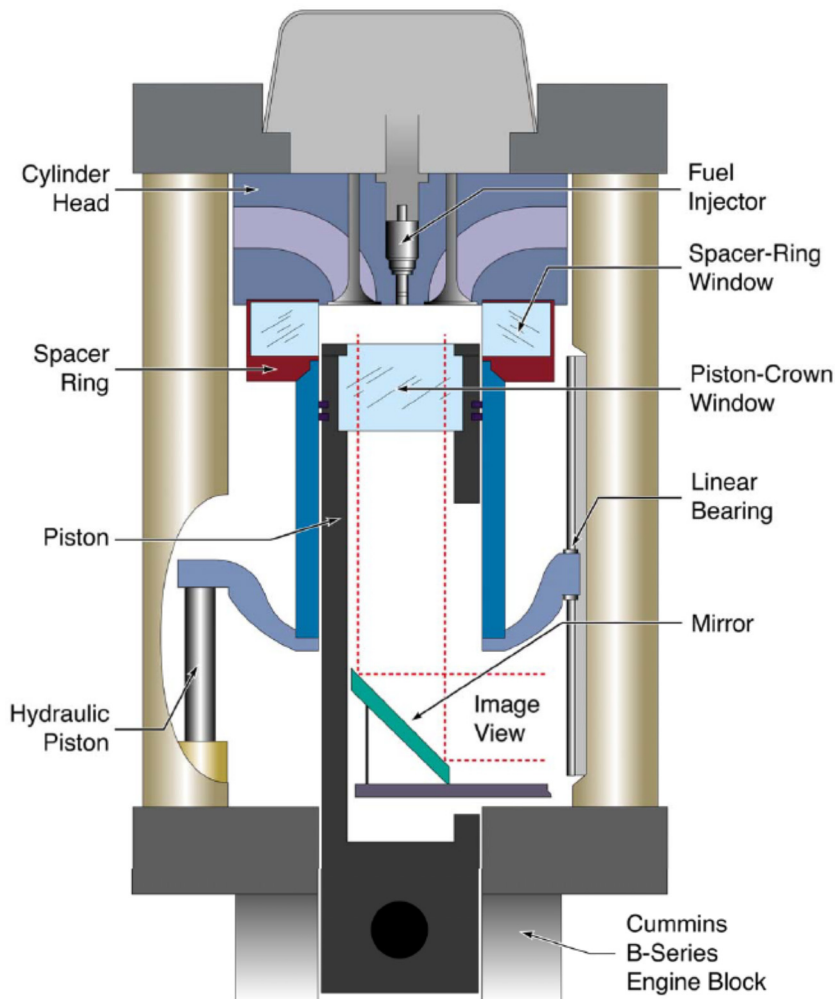


Figure 2.14 Schematic of a Bowditch-type optically accessible HCCI research engine [80].

### 2.2.2 Difference between optically-accessible engines and metal engines

An optically accessible engine is designed to match the in-cylinder thermofluidic conditions in real engines, but differences between them are inevitable. The optical combustion chamber has walls made of quartz or sapphire. These transparent materials are reasonably strong but much more brittle than metal. Also, some of them are not efficiently cooled. Even if they are cooled by water, like the spacer windows, the thermal conductivity of quartz is very low, which leads to a high temperature on the inner surface, and correspondingly makes a difference in heat transfer with the in-cylinder gas, compared with metal walls [81, 82]. The polymer piston rings on the optical piston become hot because of friction and may even melt. All these facts limit the maximum mechanical and thermal load of an optical engine. Often, an operating strategy called “skip-firing” is utilized to keep the thermal load low. This means that one or a few fired cycles for data acquisition are followed by some motored cycles [83]. With skip-firing, the turbocharging and EGR systems as well as emission measurement devices cannot function like on a metal engine test bench. Even with skip-firing, the maximum operating time of a single engine run for an optical engine is still very short compared to that for a metal engine, also due to window fouling. The heavy Bowditch piston assembly limits the maximum engine speed (e.g. 3000 rpm for the IVG optical Diesel engine [84]). The piston rings need to be lower than the spacer window, producing a large crevice volume between the top piston land and the liner [81, 85]. This limits the maximum geometric compression ratio with a certain piston bowl dimension. The oil-free polymer piston rings also result in more blow-by than the production rings in a metal engine, especially when the

rings are cold. Because of the piston window, the piston geometry is usually not the same as that of the metal counterpart. Usually simplified bowl shapes (e.g. cylindrical shape in the IVG optical Diesel engine) are used. A realistic piston geometry is possible but with significantly more effort and cost [23] as well as image deformation.

There are several previous studies on the difference in combustion performance and engine-out emissions between optical engines and metal engines. Aronsson et al. [81] found the optical engine has a shorter ignition delay, an earlier premixed-burn peak in HRR, a later end of combustion, a higher combustion efficiency, and more NO<sub>x</sub> emission. Colban et al. [85] also found a shorter ignition delay in the optical engine, but less NO<sub>x</sub> emission with more unburnt hydrocarbons, CO, and smoke. In addition to measuring the combustion phasing and engine-out emissions, Kashdan et al. [82] performed a finite element analysis (FEA) on deformation of the Bowditch piston in an engine cycle which indicates changes in the clearance volume.

## 2.3 Selected optical diagnostics for IC engines

### 2.3.1 Overview

Although optical diagnostics are often regarded as a novel technique for ICEs, so far a huge variety of them has been being developed. Given enough optical access, most of the in-cylinder physical properties, such as fuel/species/soot concentration, equivalence ratio, fuel droplet diameter, droplet/fluid velocity, gas temperature, etc., can be determined. The optical diagnostics most commonly used in engines are listed in Table 2.1.

Table 2.1 Common optical diagnostics applied in engines.

Diagnostic technique	Physical properties measured	Principle	Example applications with references
Mie scattering	Fuel/droplet concentration	Elastic scattering of light by particles or droplets, whose diameters are larger than the wavelength of the incident light. The overall Mie signal is proportional to the square of the particle/droplet diameter.	Visualization of liquid phase or droplets of fuel spray [52, 86].
Mie scattering interferometry (MSI)	Droplet diameter	The number of fringes due to the interference between the laser light reflected by the droplets and the light refracted is correlated with droplet diameter.	Droplet sizing and distribution near the spark plug prior to ignition in an SI engine [87].
Diffuse back-illumination (DBI)	Particle/droplet concentration	Diffuse light is used for back-illumination to suppress the effect of beam steering. The extinction by droplets or particles is correlated with their average volume fraction along the path of light.	Visualization of liquid phase of the fuel spray [88]; Quantification of soot volume fraction [89].
Tunable diode laser absorption spectroscopy (TDLAS)	Gas composition (H <sub>2</sub> O, CO <sub>2</sub> , CO, hydrocarbons, etc.) and temperature	A quasi-monochromatic and collimated beam from a tunable diode laser passes through the medium being measured. The attenuated light signal is detected by spectrometry. The wavelength-dependent attenuation can be expressed by the Beer-Lambert law, from which the number density of the molecules can be determined with the absorption length and the thermodynamic conditions known. The light-of-sight averaged temperature within the gas volume can be determined with two-line thermometry.	Quantitative measurement of in-cylinder H <sub>2</sub> O concentration during compression stroke in an SI engine [90]; Quantitative measurements of in-cylinder temperature and H <sub>2</sub> O mole fraction in an SI engine [91].
Schlieren (shadowgraph) imaging	Inhomogeneity of refractive index in fluid	For liquid phase: the collimated incident light is scattered by the droplets;	Visualization of liquid or gas phase of the fuel spray [52, 92];

		For gas phase: the collimated incident light is deflected where a gradient of refractive index is present due to different density or composition.	Visualization of spark and premixed flame in an SI engine [93].
Rayleigh scattering	Gas/particle concentration	Elastic scattering of light by particles whose diameters are much smaller than the wavelength of the incident light. The Rayleigh signal is proportional to the sixth power of the particle diameter.	Quantitative measurement of 2D fuel-vapor concentration of a Diesel jet [94]; Local air/fuel ratio in an SI engine [95].
Rayleigh thermometry	Gas temperature	The Rayleigh scattering signal is proportional to the gas density and consequently inversely proportional to the temperature at constant pressure and Rayleigh scattering cross section.	Temperature imaging in homogeneous charge compression ignition (HCCI) and SI combustion [96].
Particle image velocimetry (PIV)	Fluid velocity	The fluid is seeded with particles that are small enough to follow the gas flow. A pair of particle images with a known time interval is taken and the velocity can be determined usually by cross-correlation.	Measurement of flow field in swirl-planes in a light-duty Diesel engine [97].
Particle tracking velocimetry (PTV)	Fluid velocity	Very similar to PIV. The seeding density is lower, and each individual particle is tracked for velocity calculation.	Measurement of in-cylinder flow field during the intake stroke [98].
Laser Doppler anemometry (LDA)	Particle/droplet velocity	Two beams of laser light cross in the flow of the fluid being measured. The two beams interfere and generate straight fringes. As particles/droplets pass through the fringes, they scatter light. The light intensity fluctuates with time. The frequency of the fluctuation is proportional to the particle/droplet velocity.	Measurement of in-cylinder gas velocity [99].
Phase Doppler particle analyzer (PDPA)	Droplet velocity and diameter	Based on the principle of LDA. At least two detectors are used. The droplet diameter is proportional to the phase difference of these signals. Only transparent droplets can be detected.	Measurement of droplet diameter in a flash-boiling spray in an SI engine [100].
Natural chemiluminescence	Presence of excited species	During combustion, light is emitted either directly from excess reaction energy, e.g. CO-O continuum, or indirectly by producing electronically excited species. These species (e.g. OH*, CH*, C <sub>2</sub> *, CH <sub>2</sub> O*) emit photons later when spontaneously returning to electronic ground states.	High-speed imaging of OH* and CH <sub>2</sub> O* in flame-induced auto-ignition and SI knocking combustion [101]; Detection of OH*, CH*, and C <sub>2</sub> * in an SI engine [102]; Flame spectra of partially premixed combustion (PPC) [103].
Natural soot incandescence	Indicator of soot concentration and temperature	The combustion-produced soot is hot and emits strong thermal radiation.	RGB imaging of combustion of flash boiling spray, using the blue channel for chemiluminescence and red channel for soot incandescence [104].
Two-color pyrometry	Soot temperature	The soot radiation can be expressed by the Planck equation and the emissivity is correlated to the line-of-sight integral of soot volume fraction (indicated by the <i>KL</i> factor, see Equation (2.17)). At least two wavelengths are needed to solve for both temperature and concentration.	Measurements of temperature and <i>KL</i> factor of in-cylinder soot in a Diesel engine [105].
Natural infrared (IR) emission	Fuel/species concentration	The emission of C-H stretch vibrations of hot alkynes, aromatics, and aldehydes composing Diesel or gasoline fuels falls in the mid-IR range. The chemiluminescence from some species (e.g. OH, NO <sub>2</sub> , and CH <sub>2</sub> O) also exists in this region.	Imaging of hot fuel and hot large intermediate species before the HTR of reactivity-controlled compression ignition (RCCI) combustion [106].

Infrared absorption-emission pyrometry	Gas temperature	Gases with an asymmetric molecular structure, like CO <sub>2</sub> , CO, H <sub>2</sub> O, and hydrocarbon, absorb and emit infrared radiation in bands. The emissivity is assumed to be equal to the absorptivity, which can be measured by extinction. Then, the temperature can be determined by Planck's law.	Measurement of the mean gas temperature averaged on an optical path of an SI engine [107].
Laser-induced fluorescence (LIF)	Fuel concentration / equivalence ratio	Some substances absorb light and become electronically excited. When the molecules transit to a lower energy state spontaneously, fluorescence is emitted at wavelengths longer than that of the absorbed light ("red-shift"). A fluorescent substance added to a non-fluorescent fluid is called a "tracer".	Measurement of relative concentration of different components in a multi-component gasoline surrogate fuel [108]; Measurement of equivalence ratio under non-reacting conditions in a Diesel engine [109].
Tracer LIF thermometry	Fluid temperature	Both the absorption cross-section and the fluorescence quantum yield of some tracers vary with temperature. Make use of the intensity variation of the fluorescence signal and detect in a single channel → "single-color tracer LIF" Make use of the color shift of the fluorescence signal and detect in two color channels → "two-color tracer LIF" Make use of the color shift of the absorption and excite at two laser wavelengths → "two-line tracer LIF"	Quantitative measurement of in-cylinder temperature stratification in an HCCI engine by single-color tracer LIF [110]; Quantitative measurement of local temperature (together with equivalence ratio) in a fired, methane-fueled engine by two-color tracer LIF [111]; Quantitative measurement of temperature field (together with fuel concentration and equivalence ratio) in an SI engine by two-line tracer LIF [112].
Laser-induced exciplex fluorescence (LIEF)	Fuel concentration / equivalence ratio	Two dopants are used. The fluorescence of the first indicates fuel vapor. The second dopant combines with the excited first dopant and forms an excited complex, which emits more red-shifted light than the fluorescence of the first dopant. This exciplex only exists in the liquid phase. Thus, liquid and vapor phases are measured separately.	Simultaneous detection of liquid phase and quantitative measurement of vapor-fuel/air ratio in an SI engine [113].
CH <sub>2</sub> O-/OH-/PAH-/NO-/CO-/H <sub>2</sub> O-LIF	Species concentration	Some combustion intermediate species or products can be laser-excited to fluoresce	Simultaneous imaging of OH and CH <sub>2</sub> O/PAH for low-temperature combustion strategy in a Diesel engine [114]; Imaging of NO in a DI Diesel engine [115]; Imaging of CO and UHC during PPC combustion [116]; Imaging of water in the residual gas in an SI engine [117].
Laser-induced incandescence (LII)	Soot concentration and particle size	Soot particles absorb the intense laser light, being heated to a temperature well above the surrounding temperature. Soot emits thermal radiation corresponding to the elevated temperature. The radiation signal is correlated with the soot volume fraction. During the cooling down of the soot, heat conduction is the main mechanism. The heat conduction rate is correlated with the surface area. Thereby,	Quantitative measurements of soot volume fraction, number density, and particle size combined with simultaneous scattering measurement in a DI Diesel engine [118]; Quantitative measurements of soot volume fraction, particle size, and its

		the particle size can be determined. Also, the particle size can be obtained by combining the LII signal with the Rayleigh scattering signal.	distribution by time-resolved LII in an HSDI Diesel engine [119].
Phosphor thermometry	Gas/wall temperature	Phosphors are solid materials that emit light, or luminesce, when exposed to light, including phosphorescent materials and fluorescent materials. Phosphor thermometry usually uses phosphorescent materials. They absorb light and re-emit the energy in photons, called "Phosphorescence". Different from fluorescence, this process is relatively slow. Both the lifetime and the spectrum of the emission depend on temperature and can be used for temperature determination. Phosphors can be used as coating on surfaces and as particles seeded in gas.	Measurement of piston surface temperature via phosphor coating based on lifetime of the phosphorescence [66]; Simultaneous measurements of flow field and temperature field by seeded phosphor particles based on the phosphorescence signal at two wavelengths [120].
Spontaneous Raman scattering	Gas composition and temperature	Raman scattering is a non-elastic scattering process. The Stokes signal is red-shifted, while the anti-Stokes signal is blue-shifted. Both signals are very weak. The species concentration can be measured from the Raman signal intensity by spectral integration. The shape of the Raman spectra are dependent on species and temperature, whereby the temperature can be determined.	Measurements of in-cylinder gas density and temperature at two locations in an SI engine. The temperature is determined by the ratio of anti-Stokes to Stokes scattering [121]; Simultaneous measurements of concentrations of O <sub>2</sub> , N <sub>2</sub> , H <sub>2</sub> O, and iso-octane to determine the air/fuel ratios by making use of the polarization of Raman signals in a direct-injection spark-ignition (DISI) engine [122].
Coherent anti-Stokes Raman spectroscopy (CARS)	Gas temperature	Three laser beams are used, namely a pump beam, a Stokes beam, and a probe beam. These beams interact with the molecules being measured and generate a coherent and intensive optical signal at the anti-Stokes frequency. The gas temperature can be determined by recording the CARS beam spectrum and fitting it to the theoretic one.	Simultaneous determination of temperature and relative O <sub>2</sub> -N <sub>2</sub> concentration in an HCCI engine [123].
Laser induced grating spectroscopy (LIGS)	Gas temperature	Two laser beams interfere at the local point being measured. This produces high and low intensity fringes. A thermal grating forms with acoustic oscillation. The evolution of the grating can be recorded by scattering a probe beam off the grating onto a detector. The scattered signal is a coherent with the same oscillation frequency as the grating. Through this frequency, the sound speed and consequently the local temperature can be derived.	Quantitative point measurement of in-cylinder temperature in an SI engine [124].
Laser-induced breakdown spectroscopy (LIBS)	Gas composition	A laser beam is focused on the medium being measured. The medium breaks down into a hot plasma consisting of its constituent atoms, ions, and electrons excited to high energy states. During the cooling down, the atoms and ions emit light. The intensity and shape of the light emission spectrum can be used to deduce the elemental composition of the medium.	Demonstrated that the line area ratios from the LIBS spectrum are correlated with the in-cylinder equivalence ratios in a natural gas engine [125].

Ion current sensing	Ion current	Used mostly in SI combustion, where the ion current arises from chemical reactions that occur during combustion (in the flame front) and charged species produced due to high temperature (in the post-flame).	Measurement of cycle-resolved arrival time of the flame at eight discrete points at the perimeter of the cylinder bore by using a ionization probe in the head gasket in an SI engine [126].
---------------------	-------------	--	--

In this work, PIV and single-color tracer LIF thermometry are used to measure the in-cylinder flow and temperature field, respectively. Mie scattering, schlieren, and DBI are commonly used within the ECN community for fuel spray imaging and a similar method is used here. Natural flame luminosity and multi-spectral imaging are used to determine the ignition delay. In the end, optical flow is used to analyze the flame oscillation during knock. These diagnostics used in this work will be introduced in more detail in the subsequent sections.

### 2.3.2 Particle imaging velocimetry

PIV is a mature technique for quantitative instantaneous flow-field measurements. For 2D imaging, the experimental set-up and computation of a PIV system is shown in Figure 2.15. The fluid is seeded with particles or droplets that follow the flow. Most importantly, the particles should be sufficiently small to faithfully follow the flow dynamics (but cannot be smaller than the wavelength of the illumination light in order to achieve Mie scattering). This behavior can be characterized by the Stokes number, which is defined as the ratio of the characteristic time of the particle to the characteristic time of the flow. When the Stokes number is far smaller than one, the particles can follow fluid streamlines closely. Another requirement for the particles is that they should withstand the high-temperature in the engine. Two pulses of laser sheet are synchronized with the camera. Usually a twin head laser is used, thus producing two laser pulses with adjustable time interval. The scattered light from the two laser pulses are captured by two time-consecutive camera frames, one in each. The time interval of the two laser pulses depends on the flow velocity and the magnification of the imaging system, so as to guarantee that the particles have adequate displacement of pixels in the image during this time interval. In a 2D PIV system, the camera is usually placed orthogonally to the laser sheet. For velocity calculation, the recorded images are divided in small subareas, called “interrogation windows”. Via cross-correlation, one velocity vector can be obtained for each interrogation window. For this reason, the window size should be small enough so that all particles in it have similar velocities. On the other hand, the particles in one window should be sufficient for high-*SNR* cross-correlation results.

There are two categories of correlation function, a standard and a normalized one [127]. In the normalized correlation function, the influence of the spatially-varying foreground or background intensity is suppressed, which would otherwise bias the correlation function in favor of higher intensity. However, the computation time is increased compared to the standard method.

In engines, the PIV can be used to determine the in-cylinder charge motions, such as swirl, tumble, squish, and spray-induced flow [29, 97, 128, 129]. Combined with high-speed lasers and cameras, PIV can be performed at high repetition rates [130]. Not only light scattered by particles can be used for the PIV, but also fluorescence. Lee et al. [131] developed LIF-PIV to measure the ambient air velocity by seeding the air with fluorescent liquid so as to discriminate against the scattered light by the fuel droplets. PIV can be also combined with the phosphor thermometry to measure the flow and temperature field simultaneously [132]. 2D PIV cannot measure the velocity component vertical to the laser sheet. The stereoscopic PIV [133] is applied to determine the 3D flow. In this technique, two cameras are focused on the same laser sheet with different viewing angles. Thereby all the three components can be solved.

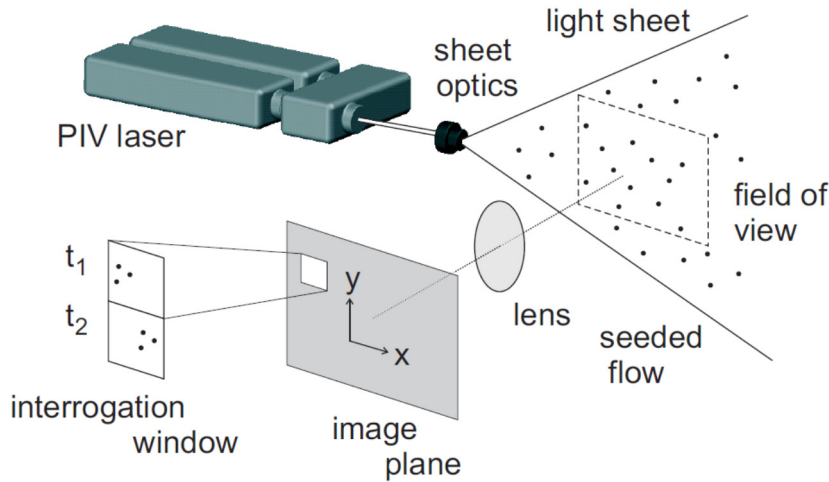


Figure 2.15 General set-up and computation of a 2D PIV system [127].

### 2.3.3 Single-color tracer LIF thermometry

Tracer LIF can be used to measure the in-cylinder temperature where unburned fuel containing an appropriate tracer is present. As introduced in Table 2.1, LIF thermometry can be realized via two-line, single-color, and two-color methods. In this work, single-color tracer LIF thermometry was used to image the temperature inhomogeneity, because single-color signal has a higher sensitivity to temperature variations, achieving a higher *SNR* [134]. The concept was suggested by Koban et al. [135] with toluene excited at 248 or 266 nm as examples. With increasing temperature, the fluorescence signal exhibits a strongly decreasing quantum yield. Ketones, such as acetone and 3-pentanone, are also candidates for single-color tracer LIF [136-138]. Their fluorescence signal is negligibly quenched by oxygen, therefore achieving temperature measurements of air, e.g. in a fired engine [138]. However, the *SNR* and sensitivity of quantum yield to temperature in the case of ketones are worse than with toluene [137]. Anisole, as a good alternative for toluene [139, 140], has even higher fluorescence signal [139]. However, among the tracers that have been investigated so far toluene has the steepest slope on quantum yield against temperature, as shown in Figure 2.16. Naphthalene can be also used for single-color tracer LIF of sprays of heavy fuels, like a Diesel surrogate [141].

At constant-pressure, the LIF signal can be expressed by

$$I(x, y, T) = \eta E_{laser}(x, y) c_{tra}(x, y) \varepsilon_{abs}(T(x, y)) \phi_{qy}(T(x, y)) \quad (2.11)$$

where  $\eta$  is the detection efficiency of the detection system,  $E_{laser}$  the laser energy,  $c_{tra}$  the molar concentration of the tracer,  $\varepsilon_{abs}$  the molar attenuation coefficient of the tracer, and  $\phi_{qy}$  the fluorescence quantum yield.

From Equation (2.11), it seen that the single-color tracer LIF signal is dependent on the laser energy, laser profile, absorption, and tracer number density in addition to the local temperature. Therefore, for single-color tracer LIF thermometry, these factors should be corrected for or uniform across the whole field of view (FOV) [134].

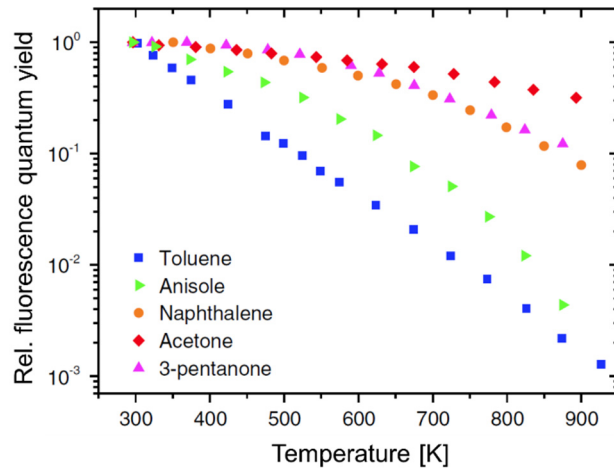


Figure 2.16 Temperature dependence of the fluorescence quantum yield of selected tracers for excitation at 266 nm in 1 bar  $N_2$  normalized to the value at the lowest investigated temperature (300 K) [137].

Single-color tracer LIF thermometry has not been used commonly. All of the documented studies target the in-cylinder temperature measurements in engines. Dec and Hwang [110] first applied toluene single-color tracer LIF thermometry to investigate the local temperature stratification in an HCCI engine, followed by measurements in fired conditions with 3-pentanone as the tracer by Snyder et al. [138], as well as a further investigation of the cold boundary near the wall with toluene by Dronniou and Dec [142]. Kaiser et al. [141] investigated similar phenomena due to wall heat transfer in an SI engine, also with toluene. Strozzi et al. [143] established a model for the absolute LIF signal and solved for the temperature from it. Perterson et al. [134] compared single-color with two-color tracer LIF for in-cylinder gas temperature measurements in an SI engine, and found that the single-color method had lower precision uncertainty and higher sensitivity to temperature gradients, but provided only relative information. Figure 2.17 shows an example of ensemble-average in-cylinder relative-temperature maps during compression and expansion stroke measured by single-color tracer LIF with toluene [142]. The engine piston has a flat top. The FOV is the central vertical plane in the pancake-shaped combustion chamber. The temperature is given relative to the adiabatic-core temperature (see Section 3.1). From the temperature images, the colder boundary layer near the walls and correspondingly the hotter core region can be identified. The temperature fields during compression are much more uniform than those during expansion.

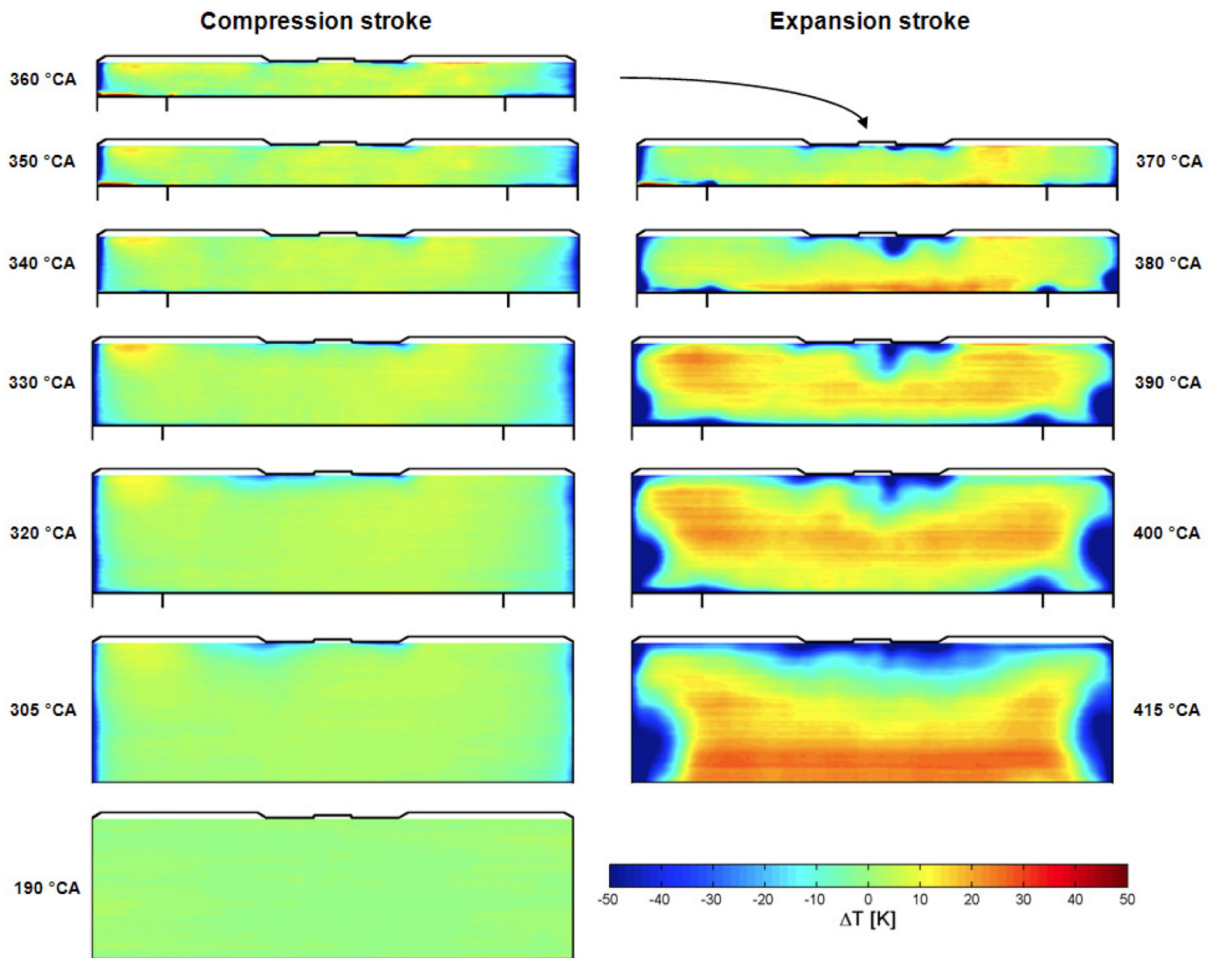


Figure 2.17 Example of ensemble-average relative-temperature images in a central vertical plane in a cylindrical combustion chamber measured by single-color tracer LIF thermometry [142]. The marks at the bottom indicate where the piston-crown is quartz (inner section) and where it is aluminum (outer sections).

### 2.3.4 Mie scattering

Mie scattering, schlieren, and diffuse back-illumination (DBI) are a family of methods for imaging the liquid- or gas-phase of fuel sprays. Mie scattering and DBI image the scattered light or light extinction by the fuel droplets, respectively, while the schlieren method images beam steering from the spatial inhomogeneity in the refractive index in the spray.

Mie scattering is usually utilized to visualize the liquid spray. The Mie-scattering principle and measurement set-up is illustrated in Figure 2.22. The incident light illuminates the spray from one direction, and the scattered light by the fuel droplets is captured by a camera from another direction, often orthogonal. The light source can be a volume or a sheet illumination and either collimated or not. Typical images from Mie scattering are shown in Figure 2.19 [39]. The spray is shown bright in the foreground and the background is dark. To measure the liquid length in the resulting images, a threshold can be set according to the intensity profile along the spray axis. For instance, Siebers [39] selected the threshold to be 3% of the maximum intensity. However, this method is not very robust. Volume or sheet illumination, illumination from the spray head or side, and pixels saturated or not will deliver a different result [144]. However, Mie scattering is a convenient method of visualizing the liquid spray, especially in an engine, where DBI is difficult to realize because of the need of trans-illumination (introduced in

Section 2.3.6). In combination with a schlieren method, a simultaneous measurement of liquid and gas phase of the spray can be achieved [38].

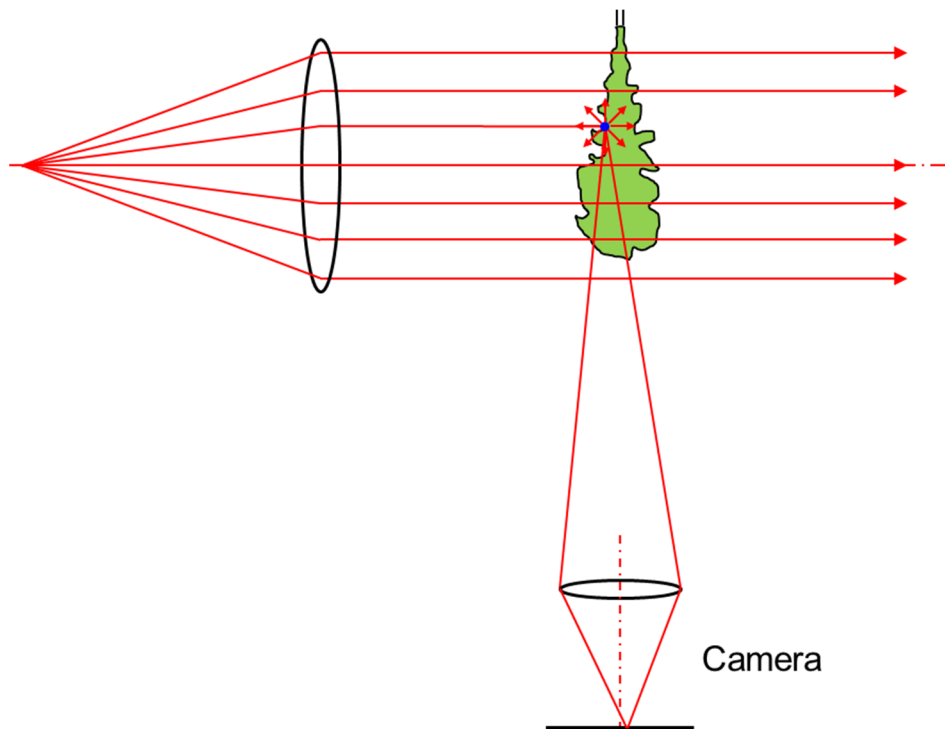


Figure 2.18 Schematics of the Mie-scattering principle and measurement set-up (modified from [145]). The rays for illumination are not necessarily collimated.

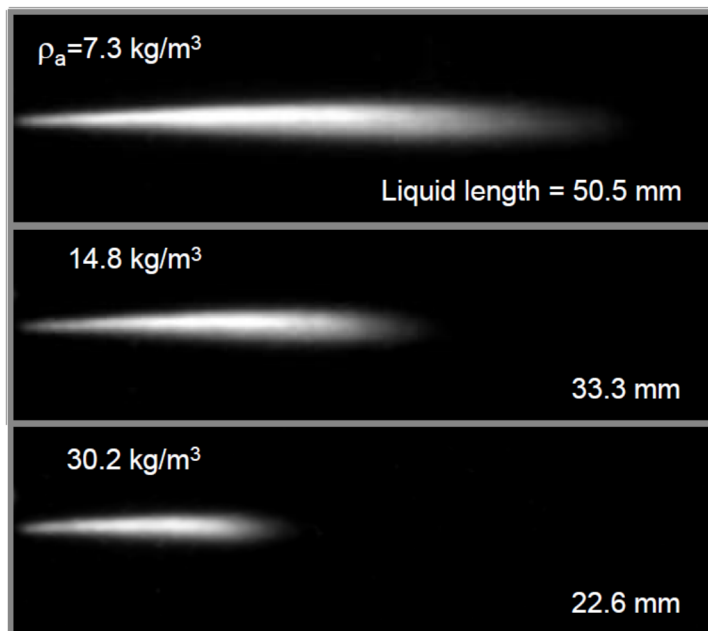


Figure 2.19 Typical images of Diesel spray from Mie scattering obtained at different ambient gas densities in a combustion vessel [39].

### 2.3.5 Schlieren

Schematics of the principle and set-up of schlieren imaging are shown in Figure 2.22. The diverging light of a point light source is collimated by the first convex lens, passing through the probe volume. In this process, the collimated light is attenuated by liquid and refracted at a local gradient of refractive index because of difference in gas density or composition. After focusing by the second convex lens, these local gradients are imaged onto a camera sensor. A diaphragm or a knife edge can be used to block a part of the refracted light at the focus the second convex lens, increasing the sensitivity of the system. This is the most common set-up with a bright background, as shown in Figure 2.22, top graph. Typical schlieren images of spray in a combustion vessel from a bright-field set-up are shown in Figure 2.21 [44]. It is seen that the background is brighter than the spray (foreground). The gradient in the background is from the boundary layers near the windows. In dark-field schlieren imaging (bottom graph in Figure 2.22), a cut-off disc is placed at the focus to block the non-steered light and the steered light is captured, shown as bright features [146, 147].

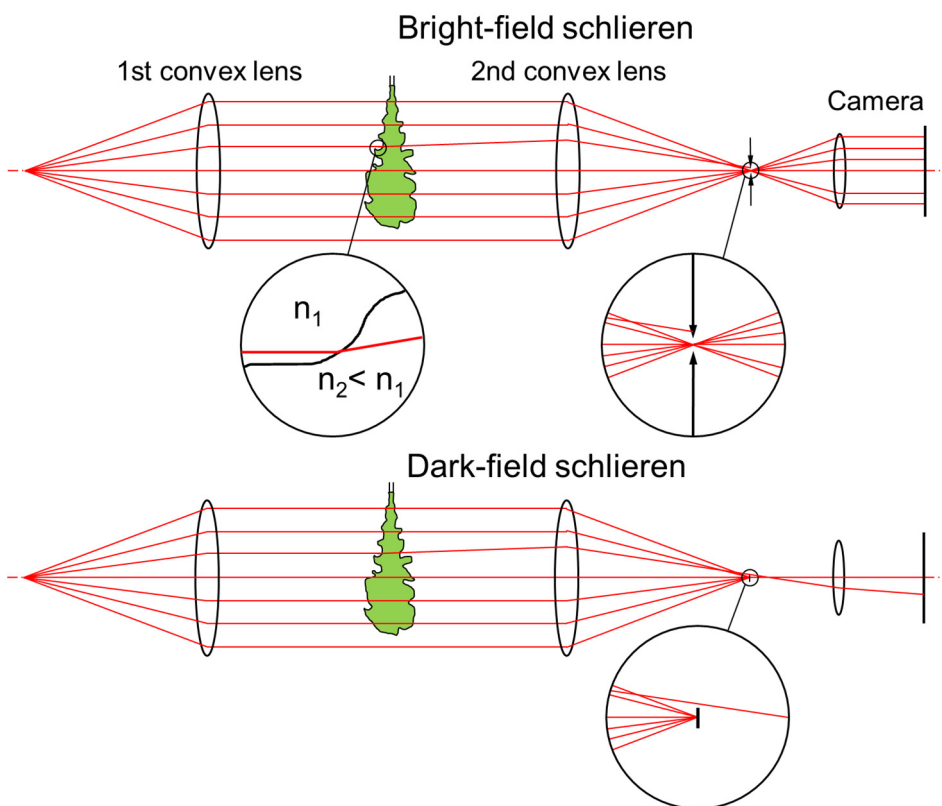


Figure 2.20 Schematics for the principles and set-ups of (top) bright-field and (bottom) dark-field schlieren imaging (modified from [145]).

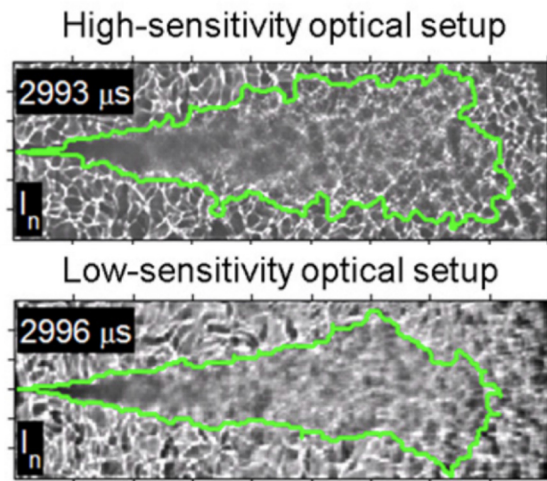


Figure 2.21 Typical bright-field-schlieren images of Diesel spray from two sensitivities of optical setups [44]. Time ASOI is shown at upper left in each image.

For Diesel spray and combustion application, schlieren is mostly used to visualize the fuel vapor [146, 148]. The axial boundary of the fuel vapor at the spray head can be clearly identified by the beam-steering effect, making spray penetration measurement reliable [44]. However, the vapor boundary at the radial periphery exhibits a strong sensitivity to optical setups and image processing routines [44]. This produces an error as high as several degrees with a low-sensitivity system or processing method [44], as seen in Figure 2.21 by comparing the top and bottom graph. An accurate measurement of spray dispersion angle, where the radial distribution of fuel mixture fraction goes to zero, requires a schlieren set-up with a high sensitivity [44]. Apart from this, schlieren imaging can also indicate the low-temperature reaction of a Diesel spray [146, 149]. In this case, the low-temperature heat release increases the temperature of the cold fuel vapor, locally diminishing the beam-steering effect.

### 2.3.6 Diffuse back-illumination

A schematic for the principle and set-up of DBI is shown in Figure 2.22. It is a trans-illumination method. On one side, a diffuser is illuminated by a light source (e.g. an LED) with a field lens, serving as the back illumination of the imaged object, e.g. the fuel spray. An engineered diffuser is preferred since its radiance angle  $\beta$  is spatially constant. The attenuated light is captured by a camera. The light attenuation is due to Mie scattering when imaging transparent fuel droplets, as shown in Figure 2.22. Typical DBI images of fuel spray are shown in Figure 2.23 [150]. The liquid spray is shown as darker than the background. In the case of soot, the light extinction is mostly contributed by absorption [151]. Quantitative measurements of soot volume fraction is out of the scope of this work but representative examples can be found in detail in Ref. [61, 89, 152]. Here, the principle for the liquid volume fraction (LVF) measurement is introduced.

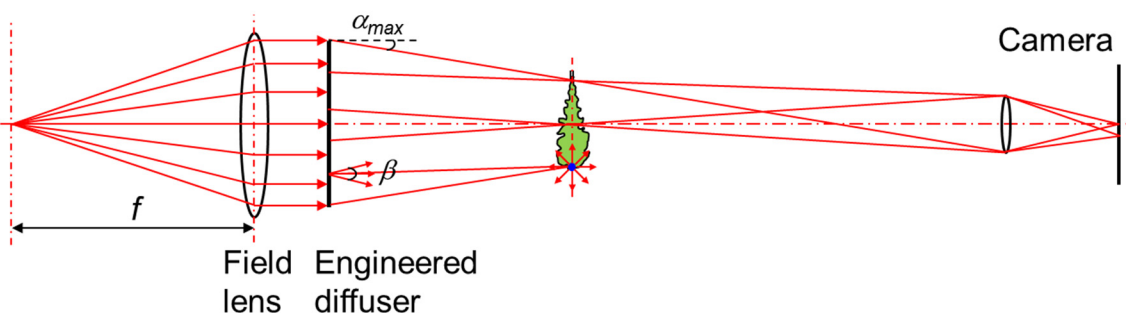


Figure 2.22 Schematic for principle and set-up of DBI (modified from [145]).

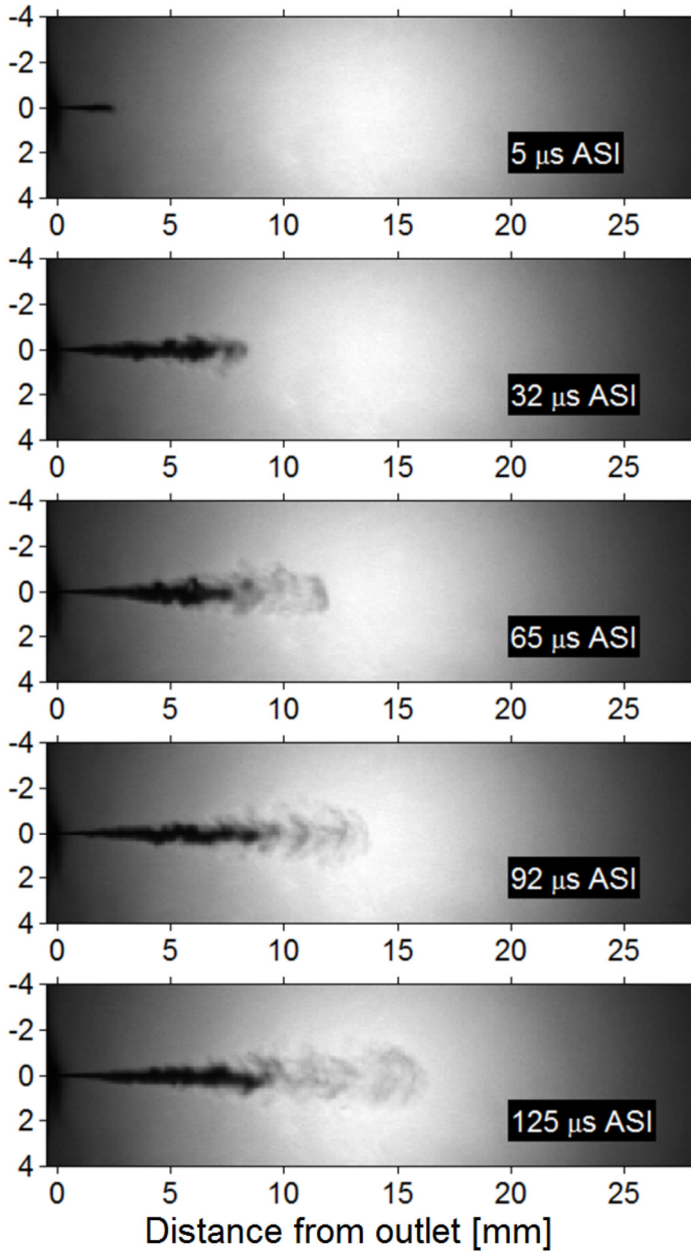


Figure 2.23 Typical DBI images of a Diesel spray at different times after start of injection (ASOI) in a combustion vessel [150].

First, the optical thickness  $\tau$  of the extinction by the droplets is related to the transmitted intensity  $I$  normalized by the baseline intensity without spray  $I_0$  by

$$I/I_0 = e^{-\tau} \quad (2.12)$$

$\tau$  is the extinction integrated along the optical path, related to the *LVF* by

$$\tau = \int_{-y_\infty}^{y_\infty} C_{ext}^* \frac{LVF}{\pi d_d^3/6} dy \quad (2.13)$$

where  $d_d$  is droplet diameter and  $C_{ext}^*$  is the extinction cross-section from Mie-theory, depending upon fuel type, droplet size, wavelength, and camera collection angle. The \* superscript is used because some scattered light within the collection angle is captured by the camera and is not contributing to  $\tau$ . Thus, it is not the complete extinction cross-section.

Assuming a monodisperse droplet-size distribution, Equation (2.13) becomes

$$\tau \frac{\pi d_d^3 / 6}{C_{ext}^*} = \int_{-y_\infty}^{y_\infty} LVF \cdot dy \quad (2.14)$$

Thereby, the projected  $LVF$  along the line-of-sight can be calculated with known fuel type, droplet size, wavelength, and camera collection angle. By thresholding, a liquid length can be obtained. This metric from projected  $LVF$  calculated by DBI is very useful, because the liquid length is not influenced by the absolute illumination intensity. In contrast, the liquid lengths measured by Mie scattering differ with different illumination intensities and schemes [144]. Therefore, using the projected  $LVF$  by DBI achieves a convincing comparison between the results from different research groups. Also, a direct comparison with numerical simulation results is possible. This is why the ECN chose DBI as the standard method for liquid length measurement.

The main concern of DBI for  $LVF$  measurements is the beam-steering effect at the tip of the liquid spray, as seen in Figure 2.23. This is in fact a schlieren phenomenon from the fuel vapor. However, Westlye et al. [153] showed that when  $\beta$  is greater than twice the sum of the largest angle collected  $\alpha_{max}$  (see Figure 2.22) and the largest angle steered, the beam-steering effect is “abated”.

### 2.3.7 Natural flame luminosity

To investigate engine combustion, natural flame luminosity is widely used because of its simplicity and easy post-processing. It is a line-of-sight integrated signal. In engine applications, natural flame luminosity can be classified into three categories, chemiluminescence, soot incandescence, and IR emission, which is less often used than the other two.

Chemiluminescence is the emission of light as a result of a chemical reaction. This can occur either directly or indirectly [83]. In the former case, excess chemical energy is directly emitted as light (photons). An important example for direct chemiluminescence is the CO-O continuum, which comes from the following reaction.



where  $h\nu$  represents the emission of a photon from the reaction.

For direct chemiluminescence, the wavelength of the emitted photon depends on the excess energy in the reaction collision, which is not quantized. Hence, the photon wavelength varies continuously, usually termed “broadband” chemiluminescence. In the case of CO-O continuum, the emission is from UV to blue, ranging roughly from 350 to 450 nm [83].

In indirect chemiluminescence, excess chemical energy is not released immediately, but rather temporarily stored in the electron cloud of one of the product species (an electronic excited state). This species later releases the energy by emitting light when it spontaneously returns to the electronic ground state. Both the excited and ground manifolds can have a multitude of slightly different, yet discrete (quantized) energy states. The spontaneous transition of each excited molecule must occur between discrete quantum states. As a result, the wavelength of the emitted photon corresponds exactly to the energy difference between the two states [83]. Thus, indirect chemiluminescence usually has narrow emission bands, and these bands are characteristic for the corresponding species. Therefore, the chemiluminescence emission bears the spectral “fingerprint” of the excited species. Major excited species and their emission bands are shown in Table 2.2.  $CH^*$  and  $OH^*$  are both commonly used to visualize premixed combustion [47, 154]. Their emission is, mainly concentrated at 431 nm and 309 nm, respectively.  $CH_2O^*$  is another important species and is usually used to track the low-temperature reaction [101]. However, it emits a multi-band signal, making it difficult to separate from other emission sources.

Table 2.2 Strong emission peaks of major combustion species in engines applications [155].

OH*	CHO*	CH <sub>2</sub> O*	CH*	C <sub>2</sub> *	CO <sub>2</sub> *
281–283, 302–309 nm	320, 330, 340, 355, 360, 380, 385 nm	368, 384, 395, 412–457 nm	314, 387–389, 431 nm	470–474, 516, 558–563 nm	2.69–2.77, 4.25–4.3 μm

Chemiluminescence can be detected with a spectrometer or a camera with a species-specific band-pass filter. The advantage of imaging with a camera is visualization of 2D information. However, the band-pass-filtered signal is a sum of the chemiluminescence of the species of interest and other emission sources in that spectral range (e.g. broadband chemiluminescence), which interferes with the signal of interest. An example of the chemiluminescence of a dodecane spray combustion is shown in Figure 2.24 within the spectral range of 275 to 500 nm at different times after ignition [156]. The spectrum is captured in a rapid compression–expansion machine (RCEM) by a spectrograph coupled with a high-speed camera. The soot incandescence has been already subtracted. The narrow peaks of OH\* and CH\* are clearly seen after ignition, and they overlap with the broadband signal (most probably contributed by the CO–O continuum). A common way to obtain the pure emission of the specific species is to fit a curve to the broadband signal and subtract it from the total signal.

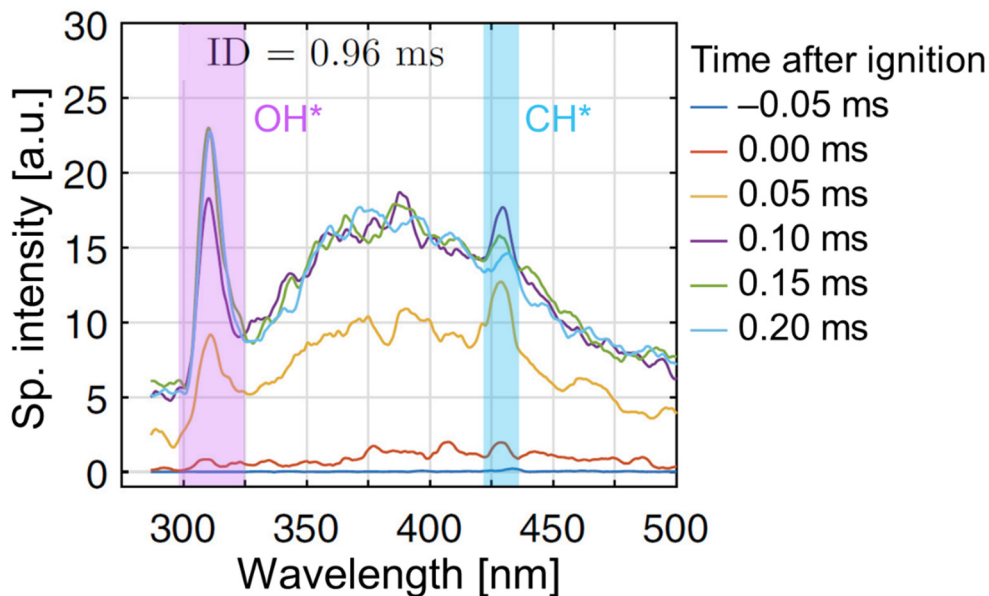


Figure 2.24 Example chemiluminescence spectra of a Dodecane spray combustion in a RCEM at different times after ignition [156].  $T_a = 810$  K (at SOI),  $O_2$  concentration 21%, injection duration 0.58 ms. Sp.: spectral.

Chemiluminescence detection has been used to investigate conventional SI [157] and CI [47] combustion, abnormal combustion like knock [101], and new combustion concepts such as CAI [158] and HCCI [159]. OH\* and visible chemiluminescence have been used to determine the ignition delay (refer to Section 2.1.4). OH\* chemiluminescence has also been imaged to determine the flame lift-off length [62], an important metric in mixing-controlled combustion. The emission ratios between OH\*, CH\*, and C<sub>2</sub>\* have been used to indicate the local equivalence ratio in an SI engine [102].

Soot incandescence is the broadband thermal radiation from hot soot particles. In an aerosol of soot particles, the light emission, absorption, and scattering all exist and affect one another. These processes depend on the soot concentration and light wavelength [83]. For simplicity, the line-of-sight radiation intensity from a soot aerosol can be approximated as a fraction  $\epsilon_{em}$  (emissivity) of the emission of a black body [83], according to the Planck equation

$$I_{soot} = \varepsilon_{em} \frac{C_1}{\lambda^5 [e^{\frac{C_2}{\lambda T}} - 1]} \quad (2.16)$$

where  $I_{soot}$  [ $\text{W}\cdot\text{m}^{-3}$ ] is the monochromatic soot-radiation intensity emitted into a hemisphere at temperature  $T$  [K],  $\lambda$  [ $\mu\text{m}$ ] the wavelength,  $C_1$  the first Planck constant ( $3.7418 \times 10^{-16} \text{ W}\cdot\text{m}^2$ ), and  $C_2$  the second Planck constant ( $1.4388 \times 10^{-2} \text{ m}\cdot\text{K}$ ).

Assuming that scattering is negligible,  $\varepsilon_{em}$  can be semi-empirically estimated by [160]

$$\varepsilon_{em} = 1 - e^{-KL/\lambda^\alpha} \quad (2.17)$$

where  $K$  is an absorption coefficient and proportional to the number density of soot particles,  $L$  is the line-of-sight optical path length.  $KL$  factor is thus proportional to the line-of-sight integral of soot volume fraction (as stated in Table 2.1).  $\alpha$  is a parameter dependent on the physical and optical properties of the soot.

According to Equation (2.16), the broadband soot incandescence signal depends on the soot concentration and soot temperature, both with a positive correlation. At a certain temperature, the radiation curve peaks at a wavelength. According to Wien's displacement law, the wavelength of this peak is inversely proportional to the temperature. Therefore, with a higher temperature, the soot color shifts to shorter-wavelengths. Typical soot temperature for conventional Diesel combustion are expected in the range of 1600 to 2700 K [58], showing a yellow-white color [161]. For a steady-state burning Diesel jet, soot incandescence is four to five orders of magnitude stronger than chemiluminescence [47]. The soot signal even extends into the UV region, interfering with, for example,  $\text{OH}^*$  chemiluminescence [31]. Mueller and Martin [162] show an example of how to interpret natural flame luminosity dominated by soot incandescence. They analyzed all important factors that influence the signal. The signal was found to be proportional to the local soot volume fraction multiplied by a factor that is a strong function of the local temperature for a certain detecting system. This means that only the hottest soot is visible in the images of natural flame luminosity. For a comparison between different datasets, if the temperature is similar, natural flame luminosity can be used to yield estimates of relative in-cylinder soot volume fractions.

Nevertheless, in most of the cases broadband detection of the soot incandescence is only used to provide qualitative information about in-cylinder soot formation and oxidation [83]. The data are difficult to interpret because the soot temperature usually changes across the datasets. Quantitative measurements of soot temperature or concentration need more dedicated diagnostics, such as the two-color method [105], light-extinction method [89], or LII [118].

### 2.3.8 Multi-spectral imaging

Multi-spectral imaging simultaneously collects image data within a limited number of specific broad spectral bands. In combustion, researchers have leveraged this concept to investigate lab-scale bench-top flames [163, 164], combustion in optically accessible combustors and engines [164-167], as well as forest fires [168]. Different optical systems are utilized to separate the spectral bands, including beam splitters and band-pass filters with multiple cameras [164, 165] or a single camera with a relay system capturing two or more different spectral bands on a single frame [105, 167, 169], a rotating filter wheel [168], liquid crystal tunable filters [163], beam-splitting prisms before CCDs [170], etc. In the simplest case, there are only two spectral bands in the imaging system [52, 106, 171-173]. For example, for Spray B in a heavy-duty engine, Eagle et al. [52] performed simultaneous  $\text{OH}^*$  and blue-chemiluminescence high-speed imaging to see if there is a difference in the flame lift-off length determined from each spectral band. Gleis et al. [173] performed simultaneous high-speed imaging of  $\text{OH}^*$  chemiluminescence and soot luminosity to investigate both premixed and mixing-controlled

combustion in direct-injected Diesel and natural-gas dual-fuel combustion. For reactivity-controlled compression ignition (RCCI), Roberts et al. [106] performed simultaneous imaging in the visible and mid-IR regions to capture chemiluminescence (e.g.  $\text{CH}_2\text{O}^*$ ,  $\text{CH}^*$ , and  $\text{C}_2^*$ ) as well as thermal emission from the C-H stretch vibrations of hot hydrocarbons. In addition, with two spectral bands, two-color pyrometry can measure the soot temperature and line-of-sight soot concentration [105, 169, 174]. Two-color pyrometry is based on black-body radiation, utilizing the radiance ratio at two wavelengths to solve for the surface temperature [174]. RGB sensors (see Section 2.4.4) are a special case of multi-spectral imaging. They have significant overlaps between the red, green, and blue spectral bands. Researchers have utilized the blue signal to indicate premixed combustion [104, 175] or  $\text{CH}^*$  [176], the green signal for  $\text{C}_2^*$  [176], and the red signal for mixing-controlled combustion [175] or soot [104]. Two-color pyrometry can be also realized by RGB imaging [177, 178], utilizing two of the three spectral bands. One disadvantage of RGB imaging is the cross-talk between the three color channels. To alleviate this, Jin et al. [179] used a customized double-band-pass filter in front of the camera lens to better separate the  $\text{CH}^*$  and  $\text{C}_2^*$  chemiluminescence. Huang et al. [180] developed digital flame color discrimination (DFCD), converting the images from the RGB color model to a hue–saturation–value (HSV) model, such that the hue is directly correlated with the wavelength. Thereby, the characteristics of flame emission can be analyzed by the distribution in the hue domain. This method was used for lab-scale flames [180-182], as well as gas-turbine [181] and engine combustion [183], where flash-boiling spray combustion was investigated.

The extreme case of multi-spectral imaging is hyperspectral imaging, where images of many narrow spectral bands are recorded [184]. In combustion research, this technique has been applied to lab-scale flames [185-190] and wildfires [184], where fuel type and condition, fire temperature and gaseous emissions, as well as fire severity and ecosystem-recovery potential are analyzed. For example, in a  $\text{CH}_4/\text{H}_2/\text{N}_2$  turbulent non-premixed jet flame and a partially-premixed ethylene flame, Gross et al. [185-187] used an imaging Fourier-transform spectrometer (IFTS) to obtain the temperature, radical and gas fraction. For an ethylene/air laminar diffusion flame, Liu et al. [188, 189] used a commercial hyperspectral imaging system to solve the soot temperature and volume fraction. Targeting practical gas-turbine-engine test facilities with a limited optical access, Hsu et al. [187] developed a fiber-coupled hyperspectral imaging sensor and tested it with laminar methane/air premixed flames.

### 2.3.9 Optical flow

In a broad sense, optical flow can be perceived as the apparent velocities of movement of brightness patterns in an image series [191]. The determination of these velocities can be performed in many ways. One of the most common methods is the differential method based on spatiotemporal derivatives of the image signal, originally proposed by Horn and Schunck [191]. Based on the Horn–Schunck method, researchers have developed various derivatives [192]. Usually these algorithms pose the problem as the optimization of a global “energy” function that is the weighted sum of two terms [192]:

$$E_{Global} = E_{Data} + \lambda_{op} E_{Prior} \quad (2.18)$$

$E_{Data}$  is the “data term” that measures how consistent the derived optical flow is with the input images.  $E_{Prior}$  is the “prior term”, which favors certain flow fields over others. Then the flow field is calculated by optimizing the global energy  $E_{Global}$  with a weighting coefficient  $\lambda_{op}$ .

Other methods to calculate the flow field include frequency-based [193] and region-based matching techniques [194]. Cross-correlation is a well-established region-based matching technique, since it has been optimized through the development of the PIV technique. In fact, PIV is a special case

of optical flow, where distinct particles are added to the flow to favor post-processing with cross-correlation.

Optical flow is mainly used to estimate, detect, or track the object motion as well as to compress videos. For engine-relevant applications, researchers have applied cross-correlation-based optical flow to analyze Diesel flame motion for nearly forty years [195]. Both the ensemble-average flow field and the turbulence intensity [196-199] during the injection- and the post-oxidation events [200-202] have been evaluated. In addition, the swirl ratio can be estimated from the resulting flow field [199, 203]. The velocities inside a Diesel spray has been also estimated using this method [204]. The more complicated differential method has been also applied to investigate the transient velocity field in turbulent gas jets in high-pressure combustion chamber [205] and in an engine [206], as well as the flame-front propagation speed in an SI engine [207]. Apart from flow-field determination, optical flow can be a tool to facilitate the image processing for other diagnostics. For example, Westlye et al. [208] and Bjørgen et al. [209] used a differential method of estimating the position of flame luminosity between two time-consecutive images for determination of soot concentration. Adam [210] leveraged that for locating the gas phase of the spray in schlieren images.

An example for the optical-flow-based analysis on the flame motion is shown in Figure 2.25 [201]. The flame-luminosity images were taken with a high-speed camera in an optical Diesel engine and processed by the PIV cross-correlation algorithm in LaVision DaVis 7. The time interval between two consecutive images is  $28 \mu\text{s}$ . The images and vectors shown in Figure 2.25 were averaged over  $2^\circ\text{CA}$ . The area marked in the right image corresponds to the evaluated area shown in the figure to the left. The red arrows show the stagnation point, where the flame hits the bowl rim. It is seen that the flame is affected by increased swirl ratio, with higher velocity on the leeward side of the flame as a result.

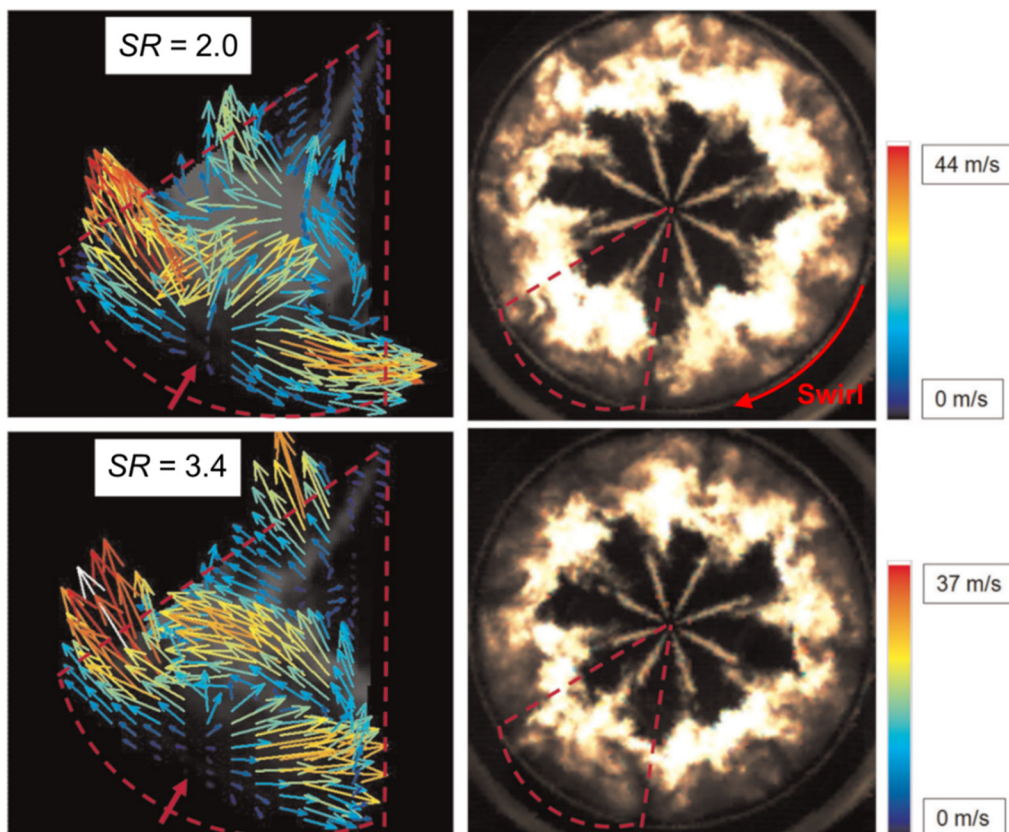


Figure 2.25 Flame-luminosity images and vectors showing the flame motion analyzed by the optical-flow concept at different swirl ratios [201]. Images are taken at  $8^\circ\text{CA}$ ,  $p_f = 1500 \text{ bar}$ .

## 2.4 Illumination and detection in optical diagnostics

### 2.4.1 Overview

For the optical diagnostics shown in Table 2.1, sometimes an additional light source is not needed, e.g. to detect natural flame luminosity. However, most of the techniques require an illumination. Currently, lasers and LEDs are the most popular light sources and to be introduced in Section 2.4.2 and 2.4.3, respectively. Gas-discharge and halogen lamps are often used, as well. These lamps possess broadband emission and are usually used in continuous operation (the strobe light is an example for low-repetition-rate pulsed-operation [211]). UV illumination is possible with a Xenon-mercury or mercury-vapor lamp. Some basic techniques, such as Mie scattering, diffuse back-illumination (DBI), and schlieren imaging, do not need a laser. In some complex optical measurement systems, even three laser beams are needed, such as coherent anti-Stokes Raman spectroscopy (CARS) and laser induced grating spectroscopy (LIGS).

The optical signal can be detected by silicon photodiodes or photomultiplier tubes, which are single-point detectors, as well as cameras, visualizing the signal in a 2D plane. With a spectrometer, the spectral information of the optical signal can be also obtained, providing information on different species resulted from chemical reaction. For imaging in the UV, visible, and near-IR spectral regions, there are two types of cameras, the charge-coupled device (CCD) and the complementary metal-oxide-semiconductor (CMOS) active-pixel sensor. CCDs feature higher quantum efficiencies as well as less dark noise, while CMOSs can run at higher frame rates. The Bayer filter, high-speed imaging, and image intensifier will be also introduced together with these two sensor types, in Section 2.4.4.

### 2.4.2 Laser

Lasers are widely used for optical diagnostics because they are coherent in phase and space (divergence angle about one milliradian [212]), monochromatic (very narrow spectral bandwidth), intense, polarized, and short-pulsed. The word “laser” is an acronym for light amplification by stimulated emission of radiation. Stimulated emission is the core process for laser generation and illustrated in Figure 2.26. An electron in an atom absorbs energy from light or heat, making the atom transit from the ground state ( $E_1$ ) to an excited state ( $E_2$ ). This atom state is metastable and eventually the electron will decay to the ground level. This could happen spontaneously and emit a photon, like chemiluminescence and fluorescence. Otherwise, a photon with the exact energy between the two energy levels ( $\Delta E$ ) can also cause the electron to drop to the ground state, emitting a new photon. This new photon exactly matches the original photon in wavelength, phase, and direction. This stimulated emission occurs repeatedly in a laser, thus increasing the light intensity. A simple laser construction is shown in Figure 2.27, consisting of an active medium, an excitation source, a total-reflection mirror, and a partial-reflection mirror [212]. The excitation source can be a flash lamp, another laser, or an electric circuit, supplying the energy for the state transition of the atoms in the active medium, called “pumping”. Thereafter, stimulated emission takes place. The photon number is amplified between the two mirrors on either end of the active medium (optical feedback). One mirror is partially transparent, emitting light out of the cavity.

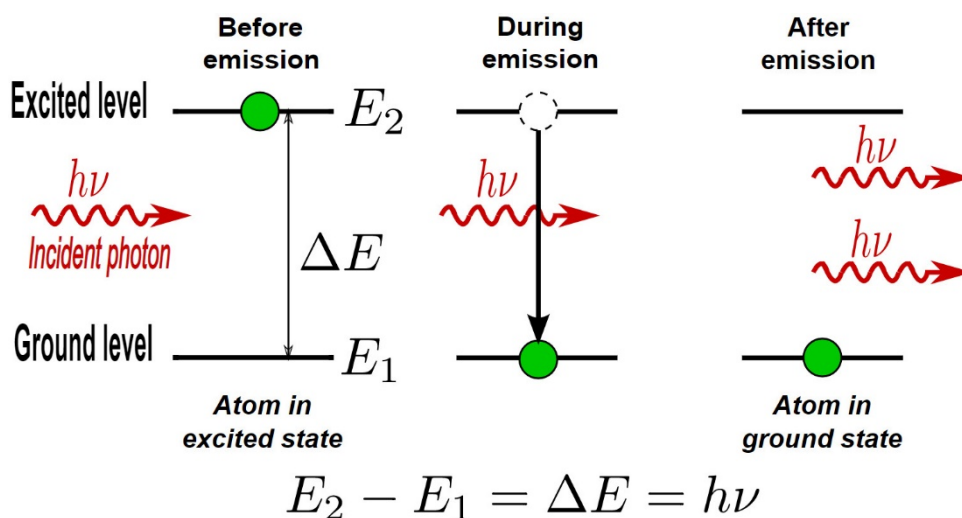


Figure 2.26 Principle of stimulated emission [213].

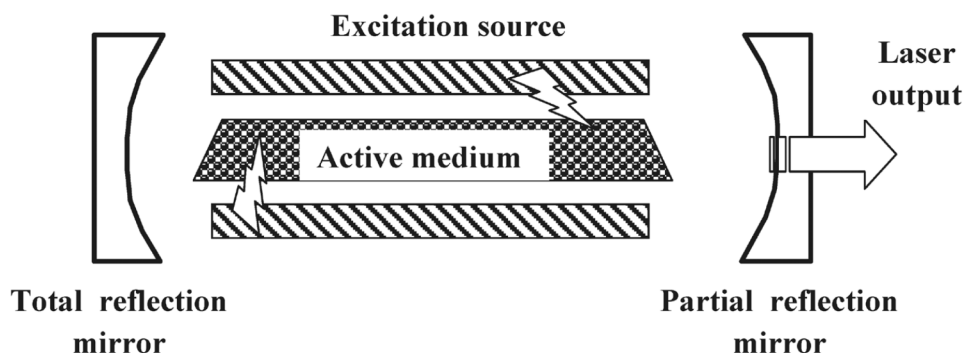


Figure 2.27 Schematic for laser construction [212].

A laser active medium can be solid, liquid, gas, or a relativistic electron beam. The Nd:YAG laser is a typical solid-state laser and usually used in light-scattering, PIV, and LIF measurements [212]. YAG stands for the yttrium-aluminum garnet ( $Y_3Al_5O_{12}$ ) crystal and serves as the host material, while the dopant neodymium ( $Nd^{3+}$ ) is the active medium. The original light emission is at 1064 nm. With non-linear optical crystals, the wavelength can be converted to 532 nm (second harmonic), 355 nm (third harmonic), or 266 nm (fourth harmonic). For Nd:YAG lasers, a Q-switch is usually used to produce an intense short-pulsed output beam ( $\sim 10$  ns) by introducing and removing loss inside the resonator. Typical high-energy pulsed Nd:YAG lasers are operated at a fixed repetition rate at 10 or 20 Hz [212]. High-speed ones with kilohertz repetition rates also exist but with low pulse energy [214]. Diode lasers are another example for solid-state lasers. They are electrically pumped and amplified by an electrical current flowing through a p-n junction of the materials. The emission wavelength depends on the doping material. A common output beam is mid-IR, near-IR, red, green, or blue. The wavelength can be tuned by adjusting the operating temperature, altering the supplying current, or using extra-cavity dispersive optics. Diode lasers usually possess low power, small size, and continuous wave. They are often used in light extinction measurements, like TDLAS [90].

### 2.4.3 Light-emitting diode (LED)

An LED is a semiconductor that emits light when current flows through it. Mass-produced LEDs have been increasingly used for illumination in optical diagnostics due to their advantages and recent improvements. First, LEDs cost little and have high electricity-to-light conversion efficiency, which

contributes to their high luminous flux. Second, today there are LEDs nearly throughout all the wavelength range from deep UV (200 nm) to mid-IR [215, 216]. In addition, LEDs have spectrally relatively narrow emission (typically  $\pm 10\text{--}30$  nm [217]). This is very narrow compared to gas-discharge lamps and halogen lamps, reducing chromatic aberrations. Although LED light is not as monochromatic as a laser beam, it has advantages over lasers for some certain techniques. For instance, using LEDs for schlieren can prevent the appearance of speckle and diffraction effects in the images as in the case of lasers [218]. Last but not least, pulsed and “over-driven” operation makes the LEDs more powerful and flexible. In this scheme, the LED is controlled by a series of TTL pulses and driven by a voltage higher than the rated forward voltage. This is done by a driver based on a capacitor and a MOSFET [219]. Thus, the duty-cycle and the forward voltage/current are in a trade-off to keep the time-average power low. The pulse duration can be as short as 100 ns [218] and the repetition rate can be up to MHz levels [218]. Thereby, the luminous flux per unit time is much higher than driven with a continuous current. In addition, the short pulse duration can “freeze” an object with high velocity. The pulse-to-pulse intensity variation is on the same order of magnitude as the detector (camera) noise permitting quantitative intensity measurements [218]. Therefore, LEDs can be a good alternative to the more expensive and complex lasers.

Wilson et al. [219] utilized an LED for high-speed schlieren imaging in a comparison with a high-intensity discharge lamp. Bröder et al. [220] used an array of over 500 LEDs for DBI, PIV, and PTV of bubbly flows. In engine investigations, LEDs were recently usually used for Mie scattering [52], DBI [150], and schlieren [149] for spray visualization. Red–green–blue (RGB) LEDs have red, green, and blue dies on a single chip, all of which are independently controlled. By combining an RGB LED with an RGB camera, three and even more virtual frames with different spectral ranges and extremely short inter-frame duration can be acquired from a single image. The color information helps identify the time sequence of these virtual frames. This method can achieve high speed imaging for several frames with low cost and has been applied to flow tracking [221] as well as engine diagnostics [88].

#### 2.4.4 *CCD and CMOS sensor*

A CCD is essentially a device for the movement of electrical charge. The array of photon detectors, namely pixels, converts the incoming photons to electron charges. The pixels are p-doped metal–oxide–semiconductor (MOS) capacitors and the photon-to-electron conversion occurs at the semiconductor–oxide interface (an epitaxial layer of silicon). The electric charge generated in each pixel is then moved and stored in a neighbor cell before being transferred to the shift register. In a digital camera, the charge is sampled (to analog voltage signal), digitized in an A/D converter, and usually stored in memory. A CCD sensor can be sensitive within the spectral range from UV to near-IR. Since there is only one A/D converter, the frame rate is very low. To improve this, binning of pixels can be used, which means combining the charges in a number of pixels, e.g.  $4 \times 4$ .

CMOS image sensors are based on complementary and symmetrical pairs of p-type and n-type MOS field-effect transistors (MOSFETs). Each pixel sensor unit cell has a photodetector (typically a pinned photodiode) and one or more active transistors, including a charge-to-voltage converter and often also amplification, noise-correction, and digitization circuits [222]. Thus, the signal is read at each pixel. This provides a faster read-out process and correspondingly a higher recording speed for CMOS sensors compared to CCDs, but also brings more noise and higher non-uniformity across the sensor. In addition, these transistors at each pixel reduce the photosensitive area, reducing the quantum efficiency.

The noise characteristics of CCD and CMOS cameras are very similar to each other. The main types of noise are described in Figure 2.28 [223]. In the process from photons to charges (electrons), first comes the photon noise or shot noise. Since the photons are quantum particles, the pixels on the detector do not receive the same amount of photons at a certain duration of time even with a uniform

light source and an ideal imaging system. Photon noise can be modeled as a Poisson process. The  $SNR$  is equal to the square root of the number of photons. This means that at lower signal, photon noise is more pronounced. The dark current noise also stems from here. It stems from the electrons freed by heat instead of excitation by photons. Thus, there is more dark current noise at higher detector temperature. The fixed pattern “noise” (FPN) is not a real random noise but a background, which is a systematic additive offset. The photon response non-uniformity (PRNU) is the local variation in pixel responsivity. Both the FPN and the PRNU are attributed to differences in the pixels or electronic circuits. For PRNU, the difference to the real value is proportional to the signal and thus the image needs to be divided by a reference image (a so-called “flat field”) to correct it, while for FPN a subtraction is needed. The FPN and the PRNU are more pronounced for CMOS cameras because of the aforementioned charge-to-voltage conversion scheme. When converting the charge to voltage at the sense-node capacitors, the reset noise is generated. It appears when resetting the preceding charge not exactly to zero, due to thermal variation in the reset-transistor channel. The voltage signal is then amplified. Here, amplifier-intrinsic noise and  $1/f$  noise are added. Finally, the quantization noise or digitization noise, which is the difference between the smooth analog signal and quantized digital signal, occurs in the A/D converter.

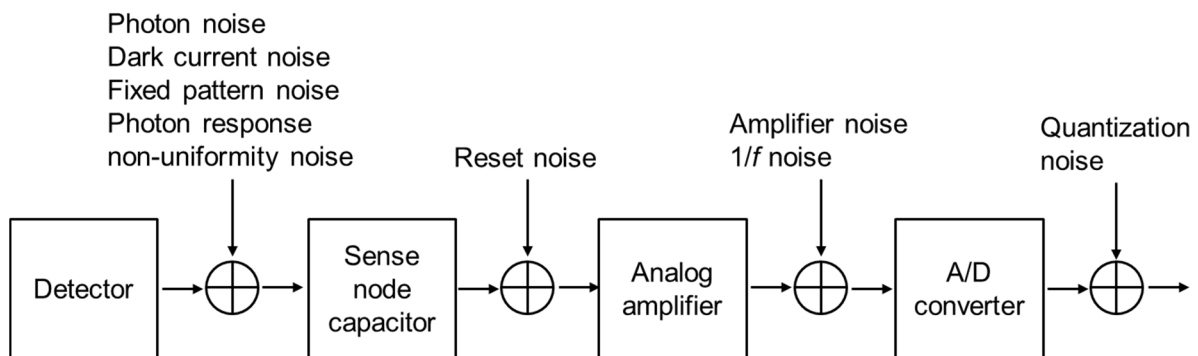


Figure 2.28 Noise model of the CMOS and the CCD [223].

For color imaging, a Bayer filter is most commonly used on the CCD or CMOS sensor. Bayer filter mosaic is a RGB color filter array on a square grid of sensors, shown in Figure 2.29. It is seen that the array is a repetition of four pixels including two green, one red, and one blue. The difference between the RGB pixels is the sensitivity to the light wavelength, namely the quantum efficiency. Different RGB patterns exist, like BGGR, RGBG, GRGB, and RGG. In the raw Bayer pattern image, only one color signal of the three is recorded in each pixel. To obtain a full-color image, demosaicing algorithms are used. A usual demosaicing method is interpolation across the pixels to fill the missing color signals.

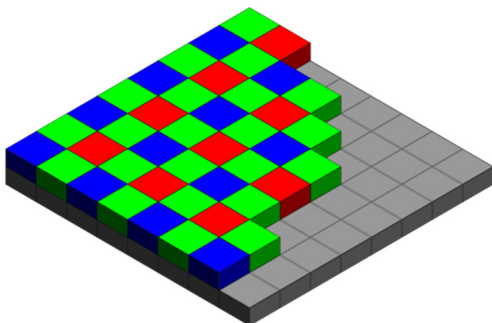


Figure 2.29 Schematic of Bayer filter array [224].

Regarding high-repetition-rate imaging (often imprecisely called “high-speed imaging”), the most commonly-used modern cameras are based on the CMOS sensors. Another type of high-speed camera is multichannel framing cameras with multiple CCD or intensified charge-coupled device (ICCD) sensors. This type of camera uses a beam-splitter or a rotating mirror to distribute the signal to several

sensors, achieving ultra-high-speed imaging. State-of-the-art high-speed cameras can run at tens of kilohertz at full-frame resolution and even faster with reduced resolution [225]. The currently fastest camera (Shimadzu HPV-X2 [226]) can go up to 10 MHz with an unchanged resolution, but only has a maximum storage of 256 frames. This camera is based on a CMOS sensor with storage memories directly under the detector.

For engine-relevant application, high-speed imaging is usually used to capture high-velocity, transient, or turbulent processes, including in-cylinder charge flow [130], internal-/near-nozzle flow [227, 228], needle movement [229], spray development [42], ignition [51], knock [230].

A CMOS sensor is usually not sensitive to UV light. To capture UV light or very weak signal that might hide in the read-out noise, an image intensifier is needed. An image intensifier is usually coupled with relay optics, together called “intensified relay optics” (IRO). A schematic set-up of a 3-stage IRO with camera and camera lens is shown in Figure 2.30 [231]. The light first goes onto the photocathode, converted to electrons. The electrons are multiplied by a micro channel plate (MCP). Then the electrons are converted back to photons by a phosphor screen. This process can be repeated several times. Finally, the signal on the output window is imaged onto the coupled camera sensor. The “gain” is the ratio of the luminous emittance of the phosphor screen to the illuminance incident on the photocathode and controlled by the voltage of the MCP. The on-time (gate) of the intensifier (photocathode) is usually shorter than the exposure time of the camera. A main disadvantage of using an intensifier is its limited spatial resolution.

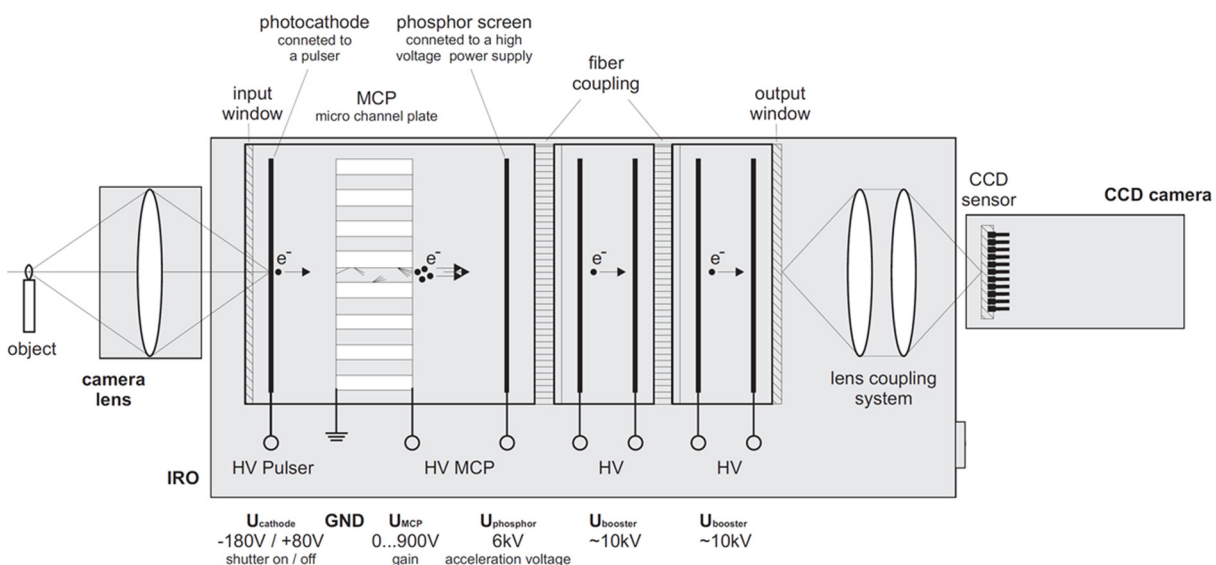


Figure 2.30 Schematic set-up of a 3-stage IRO with camera and camera lens [231].

## 2.5 Engine Combustion Network

### 2.5.1 Concept and structure of the ECN

The ECN [45] is a worldwide collaboration on spray combustion with a common set of standardized injectors and spray conditions, involving both experimental and computational research. The main goal of the ECN is to “establish an internet library of well-documented experiments that are appropriate for model validation and the advancement of scientific understanding of combustion at conditions specific to engines, to provide a framework for collaborative comparisons of measured and modeled results, and to identify priorities for further experimental and computational research” [45]. The ECN involves both experimental and computational research on engine spray combustion. Patterned

after the “International workshop on measurement and computation of turbulent non-premixed flames” (TNF) [232], the network was founded in 2009 by Sandia National Laboratories (SNL) and the French Institute of Petroleum (now IFPEN) with contributions from the Universitat Politècnica de València – CMT-Motores Térmicos (CMT). Research and data contributions are open and participant-funded. ECN participants perform experiments at standardized conditions, enabling a direct comparison of the data. Sets of specific injectors are donated and pre-characterized by Bosch and Delphi. The ECN website [45] serves as an internet library of the resulting data, featuring a searchable interactive data base. About every 18 months, a workshop is organized, where the accumulated data around a certain topic is presented as a direct comparison across facilities and simulations. More than 50 research groups worldwide are participating now, and more than 220 groups are using the ECN work [12]. As shown in Figure 2.31, from 2010 to 2017, the publication and citation numbers of ECN-related work grow drastically, with the maxima in 2017 higher than 25 and 350, respectively [12].

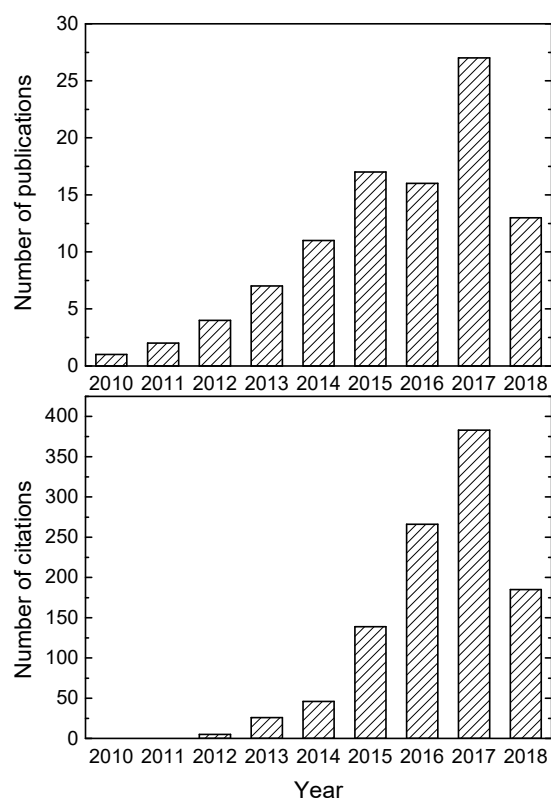


Figure 2.31 Number of publications and citations of ECN-related work from 2010 to 2018 [12]. Data were collected before the end of 2018.

Current active ECN targets are Diesel-types Sprays A (single hole), B, C (single-hole, strong cavitation), D (weak cavitation), and gasoline-type Spray G, with further targets in preparation. Numerical and experimental topics include internal nozzle flow, atomization, evaporation, ignition, combustion, emission formation, and effects of fuel properties.

### 2.5.2 Target conditions and nozzles

The standard operating conditions for Diesel and gasoline spray combustion are shown in Table 2.3. The Diesel condition is a low-temperature combustion condition relevant to engines that use moderate EGR, applicable to all the four different spray targets. The gasoline condition (Spray G) corresponds to a non-reacting early injection case for spray-guided direct injection. The ambient gas should be composed of  $O_2$  (reacting),  $N_2$ , and a small amount of  $CO_2$  and  $H_2O$ , which stems from the pre-burn process in the combustion vessel [233]. Recommendations for parametric variation are also

available on the ECN website [45]. For Diesel, ambient temperature, injection pressure, and injection duration are the preferred parameters to vary to the other ones; for gasoline, several other sets of experimental conditions are given, with the first priorities dedicated to flash boiling and early injection. These alternative conditions are useful for more deliberate model validation and cross checking between experimental facilities.

Table 2.3 Standard ECN operating conditions.

	Diesel	Gasoline
Ambient gas temperature [K]	900	573
Ambient gas pressure [bar]	60	6.0
Ambient gas density [kg/m <sup>3</sup> ]	22.8	3.5
Ambient gas oxygen (by volume)	15% (reacting) 0% (non-reacting)	0%
Fuel	n-dodecane	iso-octane
Fuel injection pressure [bar]	1500	200
Injection duration [ms]	1.5	0.78
Injection mass [mg]	3.5 – 3.7	10
Fuel temperature at nozzle [K]	363	363

The injector specifications for both Diesel and gasoline targets are for modern advanced injection systems with high-pressure capability. The nozzle parameters for Diesel and gasoline are listed in Table 2.4 and Table 2.5, respectively. The single-hole nozzles are designed to simplify the (optical) research in combustion vessels and modelling, while the multi-hole nozzles (Sprays B and G) are closer to (or exactly) mass-production nozzles with realistic internal-nozzle flow conditions. Also, these nozzles are easier for investigation in engines, initially without specifying further flow and boundary conditions. The Spray A and B have a smaller nominal orifice diameter, targeting light-duty Diesel engines, while the Spray C and D with larger orifice diameters target medium-heavy-duty engines. The difference in nozzle geometry between C and D is meant for investigations of the effect of cavitation.

Table 2.4 Nozzle parameters of ECN Diesel targets [234].

	Spray A	Spray B	Spray C	Spray D
Common rail fuel injector	Bosch solenoid-activated, generation 2.4		Bosch 3-22	
Number of holes	1	3	1	1
Nominal orifice outlet diameter [ $\mu\text{m}$ ]	90	90	200	180
Nozzle $K$ factor <sup>a</sup>	1.5	1.5	0	1.5
Orifice orientation relative to injector axis	0°	72.5°	0°	0°
Nozzle shaping	Hydroerosion to $C_d = 0.86$ <sup>b</sup>	Hydroerosion to $C_d = 0.86$	5% hydroerosion	Hydroerosion to $C_d = 0.86$

a.  $K = (d_i - d_o) / 10 \mu\text{m}$ .  $d_i$ : orifice inlet diameter.

b.  $C_d$  is the orifice discharge coefficient.

Table 2.5 Nozzle parameters of ECN Spray G.

Fuel injector	Delphi solenoid-activated
Number of holes	8
Nozzle type	VCO
Nozzle shape	Step hole
Orifice diameter [ $\mu\text{m}$ ]	165
Orifice length [ $\mu\text{m}$ ]	160-180
Orifice orientation relative to injector axis	37°

Currently, some of the Spray A and Spray B nozzles available to the ECN participants are worn, and measurements using the old Spray A nozzles are not recommended. The single-hole spray investigation is focused on Spray C and Spray D. A series of new Spray A nozzles have been manufactured and being characterized in SNL and Argonne National Laboratory (ANL). Non-rotational-symmetric Spray B nozzles (to investigate the effect of spray/spray interaction) are planned.

### 2.5.3 Facilities

The ECN participants utilize combustion vessels [233], rapid compression (expansion) machine [235, 236], optically-accessible engines [52] to measure the spray and combustion characteristics. In addition, beamlines of the Advanced Photon Source (APS) at ANL are used to investigate the spray by, e.g. fuel mass X-ray radiography [237] and ultra-small angle x-ray scattering [238], as well as the nozzle geometry by X-ray tomography [239, 240]; neutron computed tomography measurements of internal-nozzle geometry for Spray G [241] have been also implemented at the High Flux Isotope Reactor at Oak Ridge National Laboratory.

Most of the ECN data were obtained in high-pressure vessels, while only multi-hole injectors were studied in engines. There are mainly two types of combustion vessels, constant-volume preburn (CVP) vessel and constant-pressure flow (CPF) vessel. The former uses a constant-volume vessel, in which a spark ignites a pre-mixed lean combustible gas mixture, producing the required ambient temperature and pressure condition at a certain timing; while in the latter case the ambient gases are compressed and heated upstream of the test session, flowing out (in a low flow rate) to scavenge the injected fuel or combustion products and to maintain the required ambient condition. The active ECN participants, such as SNL, Michigan Technological University, IFPEN, and Eindhoven University of Technology, are using CVPs, while the active CPFs are located in CMT and Caterpillar [233]. The different working principles of these two vessel types produce possibly different boundary conditions for spray combustion research, such as spatial temperature distribution, temperature at the nozzle, and ambient gas composition. In a CPF, usually only  $N_2$  and  $O_2$  are present in the ambient gas.

In engines, the ambient conditions are different from the vessels and more difficult to characterize. Currently, for Spray G, the IVG, University of Michigan, and Technical University of Darmstadt, and for Spray B, the IVG, SNL, and CMT have investigated the ECN targets in optical engines. All of these engines are Bowditch-type.

### 2.5.4 Spray and combustion metrics

To measure the spray and combustion indicators, the ECN regulates standard and detailed diagnostics for experimentalists; to achieve a meaningful comparison between the experimental and modelling results, modelling standards have been also defined to describe these indicators in a consistent way with the experiment. The definition of liquid length is a recent good example. Before ECN 6, experimentalists used Mie scattering or DBI with arbitrary thresholds to measure the liquid length, which was found hard to compare among different facilities as well as with the modelling results. Later on, the current method was proposed so that both experiment and modelling are “measuring” the same physical quantity. However, not all methods can be applied in an experiment. In particular, in engines it is difficult to implement the trans-illumination required for DBI and schlieren imaging, as discussed in Section 2.3.4. The definition of the most important spray and combustion indicators is listed in Table 2.6, where a connection between the experimental and modelling standards can be seen to some extent. The spray indicators are applicable for both Diesel and gasoline targets.

Table 2.6 Experiment and simulation standards for ECN indicators.

<b>Spray and combustion indicators</b>	<b>Experiment (methods and metrics)</b>	<b>Simulation</b>
Liquid penetration length	<b>DBI</b> Convert the extinction to projected liquid volume (two thresholds given).	Integrate the liquid volume fraction along the viewing direction. Same thresholds as for the experiment.
Vapor spray penetration	<b>Schlieren imaging</b> Detect the vapor by the texture in the image temporal derivative. Penetration is defined in Ref. [42].	Defined as the farthest axial distance where the mixture fraction is more than 0.001.
(High-temperature) ignition delay	<b>Optically</b> Broadband chemiluminescence (CL) imaging (non-intensified). Adjust exposure time and filter to detect high-temperature CL. Ignition delay is the first time with a CL signal greater than a threshold of 50% the maximum luminosity. <b>Pressure-based</b> First time at which the low-pass-filtered speed-of-sound corrected pressure increase is larger than a threshold of 0.025 bar (not applicable for CPF vessels).	<b>OH mass fraction</b> First time at which Favre-averaged OH mass fraction reaches 2% of the maximum in the domain after a stable flame is established. <b>Temperature</b> Time of maximum rate of temperature rise.
Lift-off length	<b>OH* CL imaging</b> From the nozzle orifice exit along the spray axis, the first location where OH* intensity profile exceeds a value of 50% of the leveling-off value.	Location where Favre-averaged OH mass fraction reaches 14% of its instantaneous maximum in the domain.

---

## Chapter 3 PIV and LIF for measurements of the in-cylinder flow and temperature fields

---

This chapter is based on PIV measurements and single-color tracer LIF thermometry measurements. The latter is intended as a contribution to the ECN Spray B research. The PIV measurements were performed together with my former colleague, P. Barth, and are partially presented in his dissertation [84]. No other publications are completed yet.

### 3.1 Introduction

In-cylinder charge flow, in the sense of both average and turbulence, plays an important role in the heat transfer with the walls, mixture preparation, ignition, combustion, as well as pollutant formation and destruction in DI Diesel engines [242]. The flow field also influences the temperature field by heat convection. PIV is a mature diagnostic tool to determine the in-cylinder flow field.

As discussed in Section 2.1.2, in an optical engine the swirl ratio can be measured by PIV. During the intake stroke, the aspirated air gains momentum from the piston work. After intake valve closing (IVC), towards combustion TDC, turbulent dissipation decreases the average-velocity gradients such that the flow will tend toward solid-body rotation (also with some tumble motion). By sampling the flow field in a plane, the angular momentum can be determined. The effective angular velocity of the in-cylinder charge can be obtained by assuming a solid-body rotation with the same total angular momentum as in the measured plane. Thereby, the swirl ratio can be determined.

In fact, the swirl ratio changes throughout the engine cycle. The maximum swirl ratio occurs around the maximum piston speed and the maximum valve lift [243, 244]. Thereafter, the swirl ratio decreases because of turbulent dissipation and friction at the engine walls. If a piston bowl is present, the swirl ratio will increase again when the piston is approaching compression TDC [97, 244]. This is because the charge is flowing from the engine cylinder to the piston bowl (squish motion). Neglecting the effect of dissipation and friction, the swirl's angular momentum is conserved. Since the turning radius of the charge decreases, the angular velocity increases correspondingly [29]. The increase depends on the ratio of the bore diameter to the bowl diameter. After TDC, the swirl ratio decreases significantly due to wall friction and turbulent dissipation. Roughly half of the angular momentum generated during the intake process survives compression and persists into the expansion stroke [97].

Usually the swirl center does not coincide exactly with the geometric center of the cylinder, because of tumble motion. Tumble is a charge motion around an axis parallel to the fire deck. A mild tumble usually exists in a Diesel engine, tilting the swirl axis slightly from the longitudinal axis of the cylinder. This tilted axis also precesses against the longitudinal axis, because the tumble axis rotates driven by the high rate of swirl. Therefore, the interaction of swirl and tumble results in an offset of the swirl center that precesses around the geometric center with time [243, 244]. In addition, the swirl ratios measured at different distances to the fire deck are not the same [97, 245]. There is a dispersion of swirl level along the longitudinal axis of the cylinder.

The in-cylinder temperature distribution is as important as the flow. Temperature influences both physical processes, like fuel evaporation, and chemical processes, such as ignition, combustion, and soot oxidation. Throughout the combustion chamber, the temperature is not uniform [142, 246], which is usually termed "thermal stratification". The stratification stems mainly from the gas-wall heat transfer [142, 247]. Not only do cold boundary layers exist, but also the thermal transport brings the cold gas from the boundary layer into the hot gas in the center. Therefore, a volume-averaged bulk temperature ( $T_b$ ) obtained from pressure-trace analysis is not adequate to characterize the boundary condition in

---

Diesel spray combustion. The bulk temperature is a volume average involving both hotter gas in the center and the colder gas in the crevices and boundary layers [142]. However, to analyze the spray and combustion metrics, such as liquid length and ignition delay, the gas temperature near the spray is more characteristic when comparing with the experimental results in combustion vessels and with simulation results. In vessels, the temperature around the fuel spray is more uniform, since the spray-wall distance is greater. In modelling, for simplicity often a uniform-temperature condition is set. Therefore, in the engine experiment, a more characteristic temperature than the bulk temperature needs to be determined. Sometimes an adiabatic “core” region at the center of the combustion chamber is assumed [110, 248]. This core experiences little heat transfer with the boundary layers. The core temperature ( $T_c$ ) is calculated based on the bulk temperature at BDC or IVC via isentropic compression along the measured pressure trace and varying specific heat ratio. In this way, the computed temperature accounts for the overall effects of heat transfer via the measured pressure trace, but not the thermal transport with the boundary layers and the crevices. However, this adiabatic core has been found to be not valid anymore shortly before the compression TDC, due to heat transfer between the core and the boundary layers [110, 142]. In addition, at a higher swirl ratio, turbulence and consequently the thermal transport are intensified, so that an adiabatic core is more unlikely to be valid compared to a low swirl. Thus, for the sake of comparison with the vessel data and simulation data, which is a main objective of the ECN, it is useful to investigate if such an adiabatic core is present, especially at high swirl.

To the author’s knowledge, previous work has not investigated the temperature distribution in a bowl-in-piston combustion chamber. Dec et al. [110, 138, 142] implemented a series of experimental investigations on the temperature stratification in an HCCI engine with a flat piston and a flat roof. Both Kaiser et al. [247] and Peterson et al. [134, 214] investigated in SI engines with flat pistons and pent roofs. Luong et al. [249] investigated in an SI engine with a bowl-in-piston, but not in the bowl. Schmitt et al. [246, 250-253] performed a series of calculations for a cylinder with a flat roof and a flat piston via both direct numerical simulation (DNS) and large eddy simulation (LES).

There are several diagnostics suitable for 2D measurements of the in-cylinder temperature. Absorption-based methods, like TDLAS and infrared absorption-emission pyrometry, provide only the mean temperature along an optical path. Rayleigh thermometry is subject to interference by light reflected from the engine walls, leading to inaccuracies near the walls [254]. LIF and phosphor thermometry are both applicable here. Compared to LIF thermometry, the particles in phosphor thermometry are much larger than the tracer molecules and consequently may influence the spatial resolution. Regarding LIF thermometry, two-line tracer LIF is complex because two lasers are required. Two-color tracer LIF has low precision especially at high temperatures near TDC [134]. By comparison, single-color signal has a higher sensitivity to temperature variations, achieving a higher *SNR* [134]. For the purpose of imaging the spatial temperature distribution in a homogeneous mixture (no fuel injection), single-color tracer LIF is preferable in terms of precision, although it cannot determine the absolute temperature. The absolute temperature (accuracy) is not so important here, since the main objective is the thermal stratification. In similar studies for this purpose, single-color tracer LIF was mostly used [110, 142, 247].

In this chapter, first, the in-cylinder flow fields measured by PIV at both low and high swirl are presented. The swirl ratios for the IVG light-duty optical Diesel engine are determined from the resulting flow fields. In the second part, the temperature field in the piston bowl around TDC is determined via single-color tracer LIF thermometry, again, for both low and high swirl conditions. In the LIF experiment, the engine was operated at ECN-relevant conditions, contributing to the ECN Spray B study in Chapter 4.

## 3.2 In-cylinder flow field

### 3.2.1 Experiment

All the experiments in this work were performed in the light-duty optical Diesel engine at the IVG [84]. It is a typical Bowditch-type optical engine with modern features. A picture of it is shown in Figure 3.1 and a schematic in Figure 3.2. The piston has a cylindrical bowl with a flat bottom made of fused silica, giving optical access to the combustion chamber via the 45° mirror. Four windows, also made of fused silica, are inserted into the spacer (see Section 2.2.1). The windows have a flat outer surface and a curved inner surface (matching the bore diameter), resulting in a negative-lens effect. This engine is designed to match the characteristics of modern passenger-car HSDI Diesel engines. The main engine parameters are listed in Table 3.1.

The engine has two differently shaped intake ports, a fill port and a swirl port. The swirl ratio can be increased by blocking the fill port. In this work, “low swirl” designates the lower swirl level and “high swirl” the higher level. A pressure sensor (Kistler 6058A) with a deviation from linearity less than 0.3% full scale output is used to record the in-cylinder pressure, sampled in AVL IndiCom every 0.1°CA. The intake gas flow and composition are controlled by mass flow controllers for air and nitrogen. There are two intake heaters. The more upstream primary heater can heat the intake air to 250 °C but has a slower response [84], while the secondary heater is closer to the intake port and able to heat the intake air to about 75 °C within 15 s [255]. For more information about the structure of this engine (and test bench), refer to Ref. [84].

The engine operating conditions for the PIV measurement are listed in Table 3.2. The engine was motored at 1000 rpm with air at room temperature and atmospheric pressure. Di-ethyl-hexyl-sebacate ( $C_{26}H_{50}O_4$ ) was used as the seeding fluid. The particles were seeded upstream of the large intake plenum by an aerosol generator from LaVision GmbH, resulting in a particle size expected to range from 0.1 to 1  $\mu\text{m}$  [256].

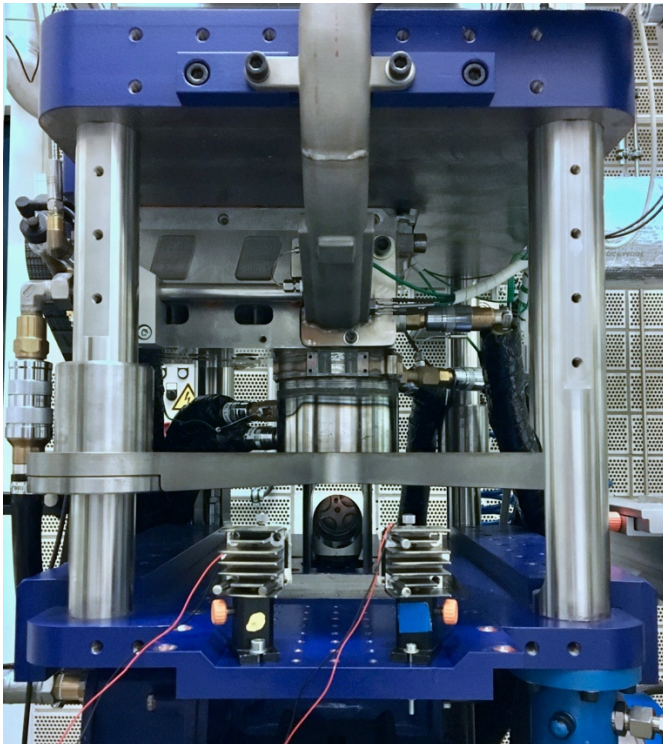


Figure 3.1 Single-cylinder light-duty optically accessible Diesel engine at the IVG.

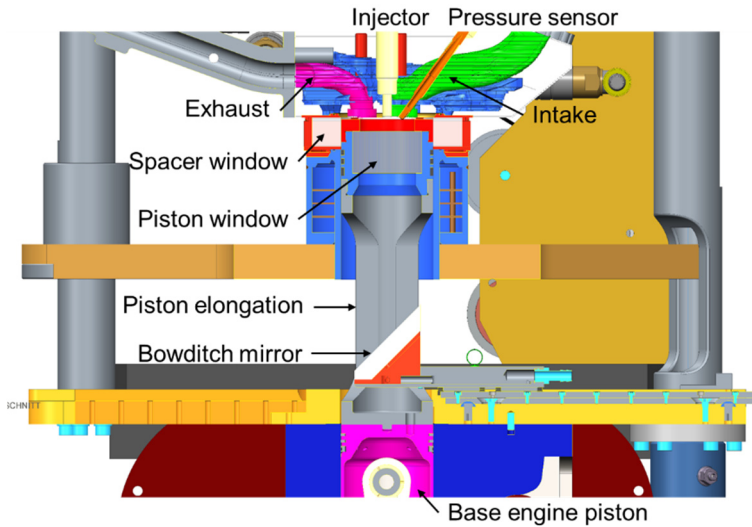


Figure 3.2 Schematic of relevant parts of the engine.

Table 3.1 Engine specifications.

Engine type	Single cylinder, 4 valves, flat roof
Piston bowl	Pancake, 47.4 × 10.4 mm
Piston glass	Fused silica
Squish height	1.2 mm
Bore / Stroke	80 / 80 mm
Conrod length	198 mm
Displacement	402 cm <sup>3</sup>
Geometric compression ratio	15
IVO, IVC	350°CA, -146°CA
EVO, EVC	122°CA, -350°CA

IVO: intake valve opening

IVC: intake valve closing

EVO: exhaust valve opening

EVC: exhaust valve closing

Table 3.2 Engine operating conditions.

Engine speed	1000 rpm
Coolant and oil temperature	60 °C
Intake gas composition	100% air
Intake pressure	1 bar
Intake temperature	20 °C
PIV particles	Di-ethyl-hexyl-sebacate

Figure 3.3 shows the optical arrangement with the parameters for PIV imaging listed in Table 3.3. A frequency-doubled Nd:YAG laser (Nano L135-15 from Litron Lasers) provided a pair of pulses of 532 nm beam at 8.31 Hz repetition rate. The time interval ( $\Delta t$ ) depended on the crank angle where the images were taken. 6  $\mu$ s was used from gas exchange TDC to -161°CA, and beyond 20  $\mu$ s. (The crank angle convention in this dissertation assigns 0°CA to combustion TDC, i.e., crank angles during compression are negative.) Sheet optics from LaVision GmbH, composed of a telescope and a negative cylindrical lens, formed a horizontal laser sheet, which was about 2.5 mm thick at the entrance of the spacer window. The spacer window diverged the laser sheet, so that it covered the entire FOV that could be seen from the bottom of the piston bowl. A CMOS camera (PCO Edge 5.5) imaged the particles through the 45° mirror. The camera was run in a double-frame mode with a recording (image pair) rate

of 4.15 Hz, capturing every second engine cycle at 1000 rpm. A band-pass filter (BrightLine®) centered at 530 nm with a bandwidth of 11 nm was used to only transmit the laser light. The background (BG) images were taken without seeding to account for the reflected laser signal, e.g. from the fire deck. 300 engine cycles were recorded in each dataset. A few horizontal positions were measured within the height of the spacer window (25 mm). At low swirl, images at different crank angles were taken during the intake, compression, and also several in the expansion stroke. The flow field near TDC could not be measured, since the piston blocked the laser sheet. At high swirl, data were taken only during the intake stroke.

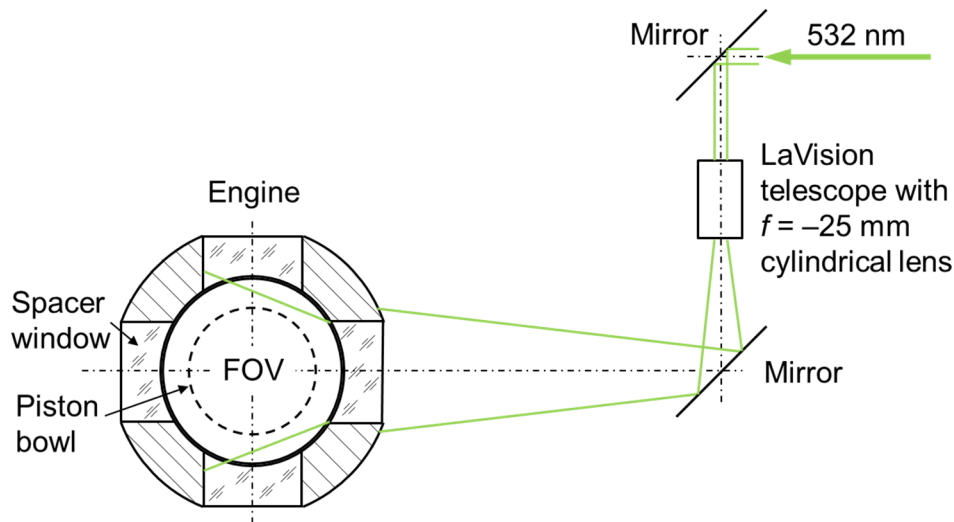


Figure 3.3 Optical arrangement for PIV. FOV: field-of-view.

Table 3.3 PIV parameters.

Laser repetition rate	8.31 Hz	
Laser pulse duration	4 ns	
Camera lens	Tokina 100 mm $f/2.8$	
Filter	530/11 nm BrightLine® band-pass filter	
Recording rate	4.15 Hz	
Image resolution	2560 × 2160 pixels	
Exposure time	10 $\mu$ s (first frame), 20 ms (second frame)	
Size of interrogation window	9.0–10 mm (final pass)	
$\Delta t$ between two laser pulses	6 $\mu$ s, 20 $\mu$ s	
Number of BG image pairs	10	
Number of particle image pairs	300	
	Low swirl	High swirl
Laser sheet position	8 mm, 12 mm, 16 mm, 20 mm, 24 mm below fire deck	8 mm, 12 mm, 16 mm below fire deck
Crank angle where data were taken	From $-315^\circ\text{CA}$ to $-42^\circ\text{CA}$	$-281^\circ\text{CA}$ (max. piston speed during intake)

### 3.2.2 Data post-processing

#### Raw image and background subtraction

A raw particle image of the first frame in an image pair taken at  $-311^\circ\text{CA}$  and 12 mm below the fire deck is shown in Figure 3.4a. It was subtracted by the average background (BG) image (Figure 3.4b). The resulting image is shown in Figure 3.4c. The FOV is a circular area above the piston bowl, in which the valves can be seen, as indicated in Figure 3.4b. The size of the FOV is slightly larger than the piston bowl diameter and expanding as the laser sheet is placed closer to the fire deck and the piston is closer to BDC. In this experiment, the diameter of the FOV is between 48 and 56.5 mm. A geometric mask preserving the FOV (shown by the green circle in Figure 3.4c) was applied before the vector computation.

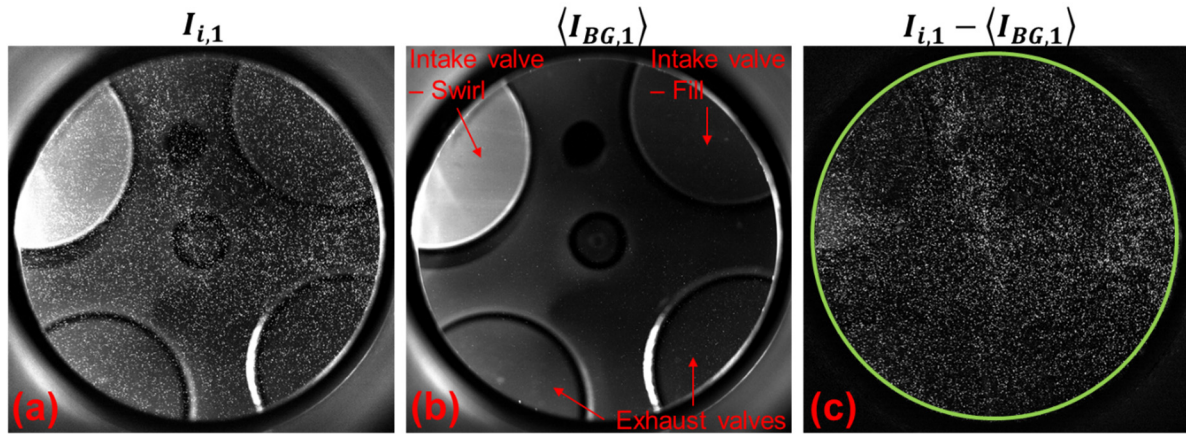


Figure 3.4 Single-shot raw particle image, average BG image, and BG-corrected particle image.

#### Vector computation

The PIV vectors were computed in LaVision DaVis 8.2. The processing parameters were set following the first results presented by in the work of Barth [84] and listed in Table 3.4. A more detailed discussion of these procedures can be found in Ref. [127, 257]. The multi-pass option with window sizes decreasing from  $64 \times 64$  px to  $32 \times 32$  px was used. The overlap of the interrogation windows was 50%, resulting in a vector spacing of 16 px, namely 4.5–5.1 mm. The standard cross-correlation function (see Section 2.3.2) was used, since the spatial variation of the foreground or background intensity is little here. A series of vector discrimination criteria and smoothing were applied in post-processing. The resulting single-shot vector fields were ensemble-averaged with options suppressing spurious vectors. From the single-shot results, the turbulent kinetic energy (*TKE*) was estimated as [257]

$$TKE = \frac{3}{4} v_{std,x}^2 + \frac{3}{4} v_{std,y}^2 \quad (3.1)$$

where  $v_{std,x}$  is the standard deviation of the local velocity in the  $x$  direction, and  $v_{std,y}$  in the  $y$  direction. The factor 3/4 estimates the unknown contribution to the *TKE* by the velocity in the  $z$  direction.

Table 3.4 Processing parameters for PIV vector computation in LaVision DaVis 8.2.

1. Vector calculation – double frames – PIV		
Vector calculation parameters	Iterations	Multi-pass (decreasing size)
	Interrogation window properties	Start: $64 \times 64$ , adaptive PIV, 50% overlap, 2 passes End: $32 \times 32$ , adaptive PIV, 50% overlap, 2 passes
	Other options	High accuracy mode for final pass
Correlation function	All initial pass(es)	Standard I1*I2 (via FFT, no zero-padding)

	Final pass(es)	Standard I1*I2 (via FFT, no zero-padding)
	Deformed interrogation windows	Symmetric shift (both frames)
Multi-pass post-processing	2 × median filter: remove & iteratively replace	Remove if diff. to avg. > 2 * Stdev of neighbors (Re)insert if diff. to avg. < 3 * Stdev of neighbors
	Remove groups with < 5 vectors	
	Fill-up empty places (interpolation)	
	Smoothing 3 × 3	
Vector post-processing	2 × median filter: remove & replace	Remove/replace if diff. to avg. > 2 * Stdev of neighbors
	Remove groups with < 5 vectors	
2. Vector statistics – vector field result		
Vector fields	Average V (velocity)	
	Standard deviation V	
Other options	Require minimum of 4 source vectors at each position to compute result	
	Include only Vs (vectors) inside (preliminary) range: Avg ± 1 Stdev	
3. Vector statistics – scalar field result		
Scalar fields	Turbulent kinetic energy	

### 3.2.3 Results and discussion

Selected ensemble-average vector fields at low swirl 12 mm below the fire deck from  $-281^{\circ}\text{CA}$  (maximum piston speed during the intake stroke) to  $-42^{\circ}\text{CA}$  are shown in Figure 3.5, with the corresponding intake valve lift, piston position from the fire deck, and piston speed indicated in Figure 3.6. One vector field during the compression stroke 24 mm below the fire deck is also illustrated. The vectors are overlaid on their respective average BG image for each dataset. At  $-281^{\circ}\text{CA}$  (image a), the high-velocity regions stem from the fresh airflow out of the intake valves. The function of the beveled valve seat at the swirl port can be seen. From the beveled edge the intake gas flows counterclockwise, providing the initial momentum for the swirl motion. At this time, the gas flow velocity can be as high as 28 m/s at low swirl. Later on, the flow field evolves towards a solid-body rotation. At  $-151^{\circ}\text{CA}$  (image d), after BDC and shortly before IVC, at least at this plane, most of the radial components have dissipated and the gas flows circumferentially. After this, the swirl motion is dominant in the cylinder. However, the swirl center is not always located at the cylinder center and is seemingly moving counterclockwise, following the direction of the swirl. This is consistent with the previous findings where through the cylinder the swirl axis was tilted and precessing with the swirl [243, 244]. Another evidence is that at  $-92^{\circ}\text{CA}$  the swirl center at 12 mm below the fire deck is not projected at the same horizontal position as that at 24 mm. The circumferential velocity of the gas slowly decreases from IVC towards combustion TDC. At  $-42^{\circ}\text{CA}$  (image h), the maximum velocity in the FOV has declined to 8.5 m/s.

At the same crank angles as in Figure 3.5, the *TKE* throughout each dataset is plotted in Figure 3.7, with the spatial mean shown at the upper right of each *TKE* map. It is seen that the *TKE* level decreases over the crank-angle range shown here. Before IVC, high *TKE* occurs at positions with high local velocity gradient, i.e. intense shear flow, e.g. where the fresh air flows in. After IVC, high *TKE* is more located around the center of the swirl, indicating the swirl center is dynamic, consistent with Ref. [243].

The flow fields and their respective *TKE* at  $-281^{\circ}\text{CA}$  at 8, 12, and 16 mm below the fire deck are compared between the two swirl levels in Figure 3.8. It is seen that at high swirl the velocity is nearly twice of that at low swirl (max. 52 m/s at 12 mm below the fire deck), and the spatially-averaged *TKE* is more than twice of that at low swirl. At high swirl, the velocity distribution of the fresh airflow from the swirl valve does not interfere with that from the fill valve. The airflow through the beveled part of

the valve seat has a greater velocity component in the horizontal plane than that through the normal part of the valve seat, as shown in Figure 3.8d. This high velocity gradient against the surrounding airflow produces very high  $TKE$  at high swirl. For both swirl levels, at 8 mm the flow velocity and the  $TKE$  are both higher than those in the lower planes. This is reasonable, because before  $-281^\circ\text{CA}$ , both the intake valve lift and the piston speed are increasing.

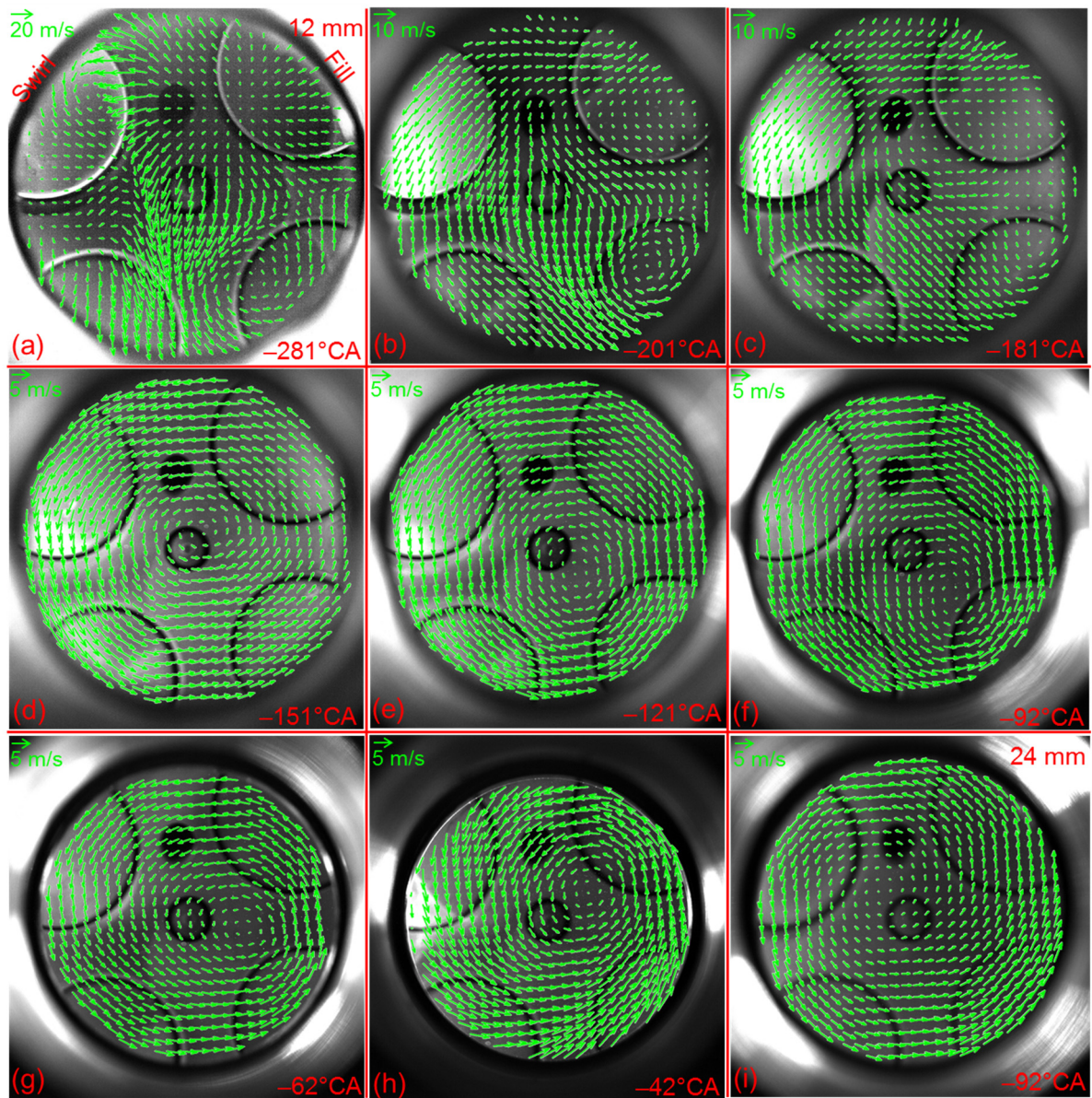


Figure 3.5 Temporal evolution of ensemble-average vector fields during intake and compression stroke at low swirl. All images except for (i) are from 12 mm below the fire deck. (i) is from 12 mm below the fire deck. The background is the average BG image for each dataset. Note that the vector length scaling differs between different images.

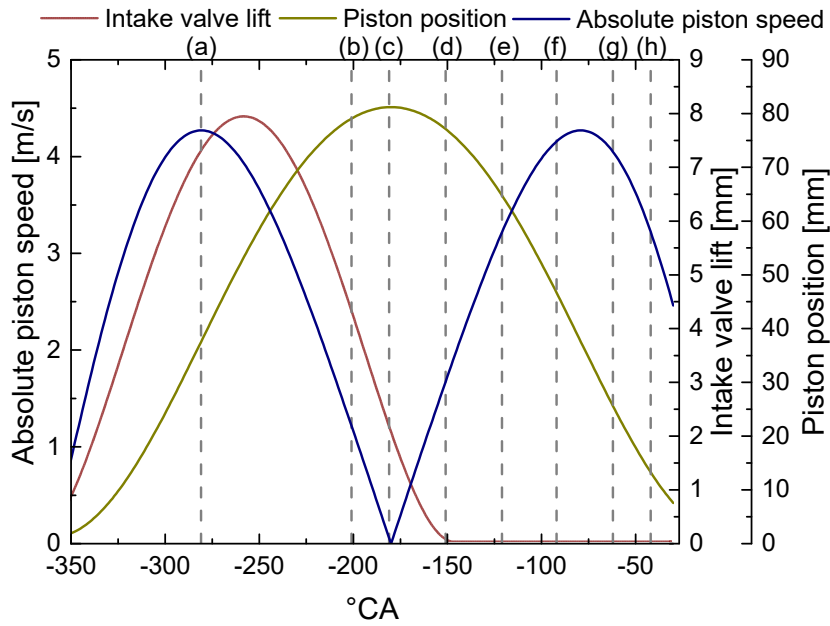


Figure 3.6 Temporal variation of absolute piston speed, intake valve lift, and piston position during intake and compression stroke at 1000 rpm. The letter sequence indicates the timing of the vector fields shown in Figure 3.5.

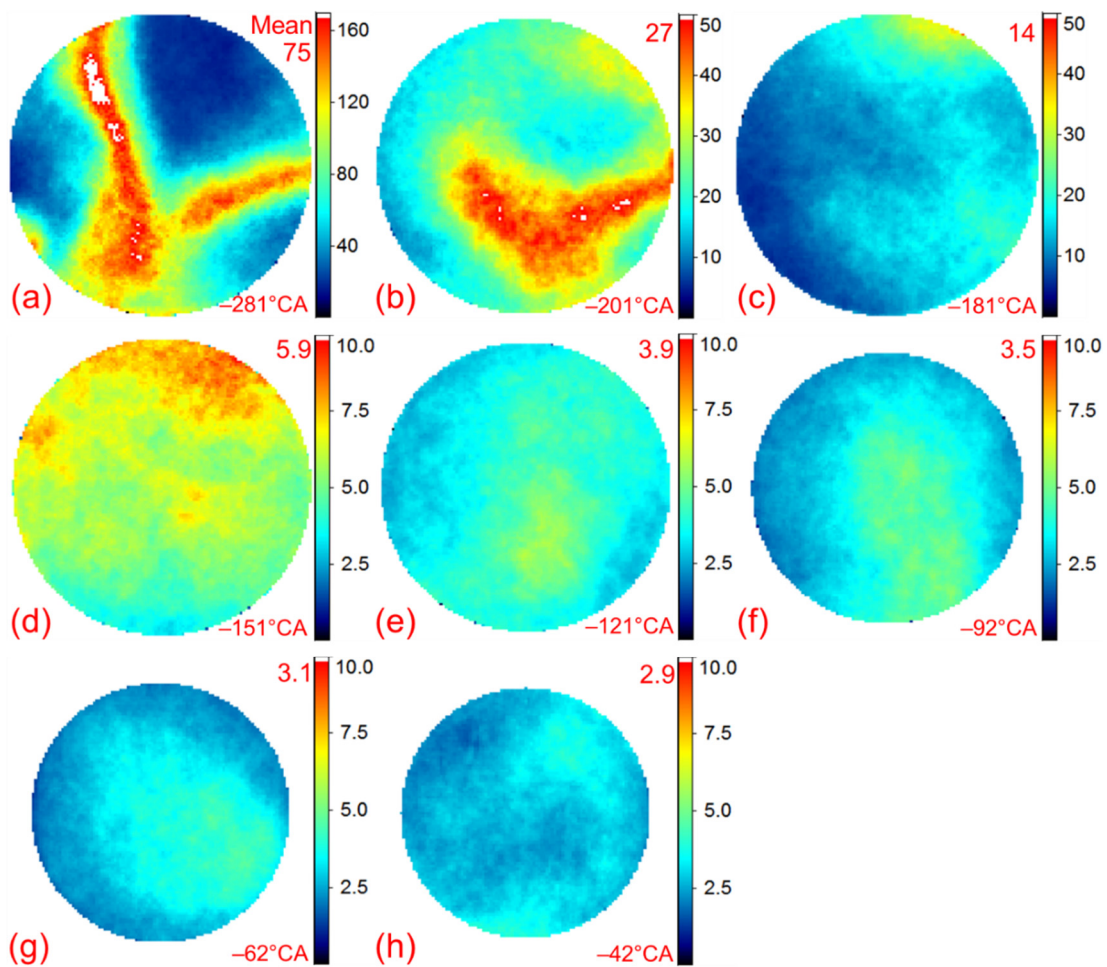


Figure 3.7 Maps of the turbulent kinetic energy (TKE) for the vector fields shown in Figure 3.5 at 12 mm below the fire deck. The number at upper right in each map is the spatially-averaged TKE.

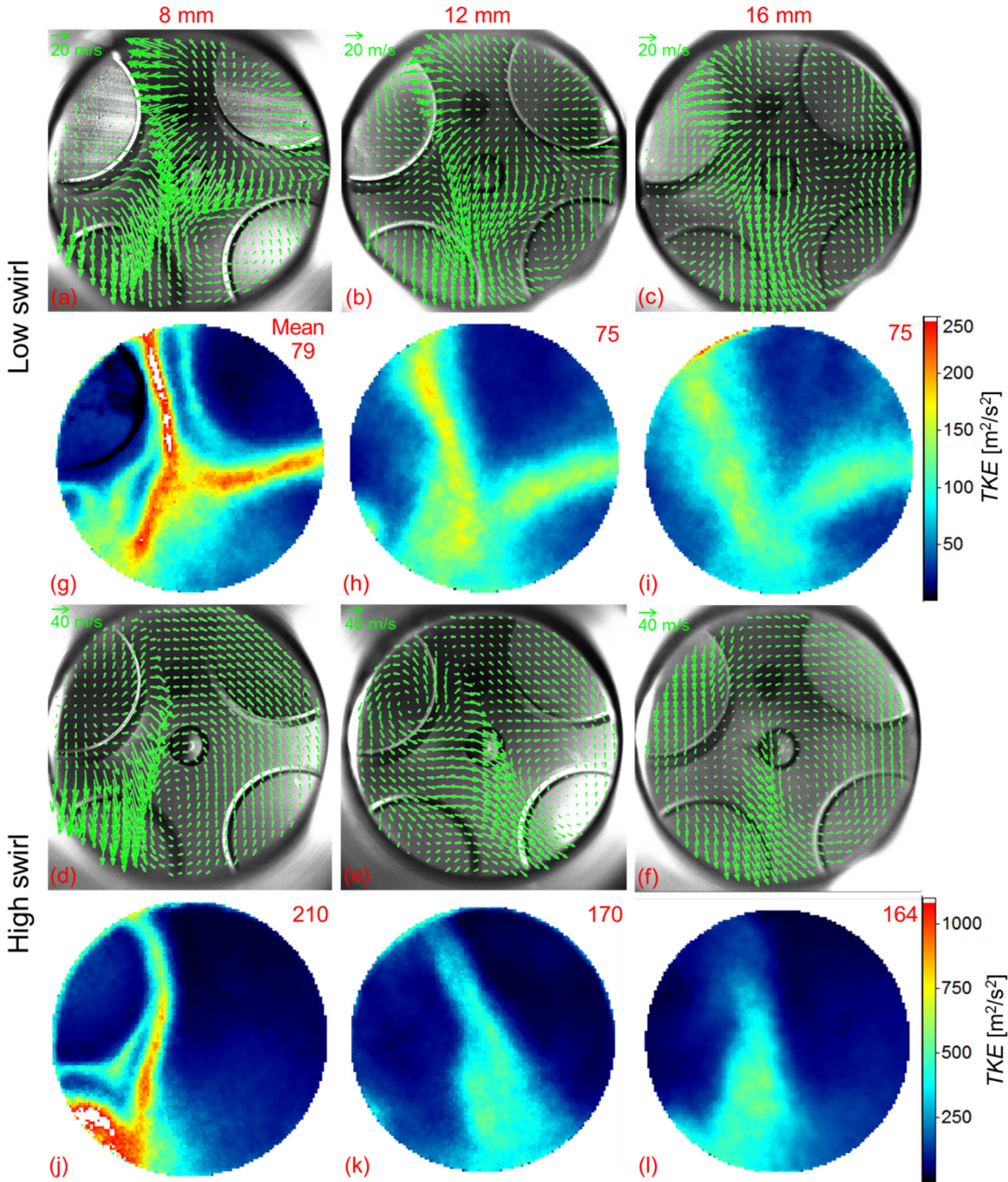


Figure 3.8 Ensemble-average vector fields at  $-281^{\circ}\text{CA}$  at 8 mm, 12 mm, and 16 mm below the fire deck with the respective TKE shown below for both low-swirl and high-swirl.

### 3.2.4 Swirl ratio

As discussed in Section 3.1, to determine the swirl ratio, the effective angular velocity of the swirl motion can be estimated as that of a solid-body rotation with the same total angular momentum as the measured flow field. Here, the flow field was measured within the FOV, which is smaller than the bore diameter, to estimate the angular momentum in the whole cylinder. The total angular momentum in the measured ensemble-average vector field,  $M_{v1}$ , was calculated as the sum of the angular momentum of each vector, as shown in Equation (3.2).

$$M_{v1} = \sum_{i=1}^n r_i v_{\theta,i} \quad (3.2)$$

where  $r$  is the radial distance from the swirl center (here the geometric center of the cylinder is used for simplicity, which might result in a lower momentum) and  $v_\theta$  is the circumferential component of the velocity vectors with respect to the swirl center.

The angular momentum of the corresponding rotating solid body,  $M_{v2}$ , with an angular velocity of  $\omega$  is given by

$$M_{v2} = \sum_{i=1}^n r_i(r_i\omega) = \omega \sum_{i=1}^n r_i^2 \quad (3.3)$$

Since  $M_{v2}$  was assumed equal to  $M_{v1}$ ,  $\omega$  can be obtained as

$$\omega = \frac{\sum_{i=1}^n r_i v_{\theta,i}}{\sum_{i=1}^n r_i^2} \quad (3.4)$$

Finally, the swirl ratio of each dataset was calculated according to Equation (2.3)

$$SR = \frac{\omega}{2\pi N} \quad (2.3)$$

where  $N$  is the engine speed.

At low swirl, the temporal evolution of swirl ratio with crank angle is plotted in Figure 3.9. Two series of datasets measured 12 mm below the fire deck were obtained and are plotted here. The intake valve lift, piston position below the fire deck, and piston speed are normalized by their respective maximum and are plotted here as well. The two series of swirl ratio 12 mm below the fire deck match each other well, increasing drastically after gas exchange TDC, peaking slightly after the timing of the maximum intake valve lift, which is also that of the maximum piston speed, and decreasing afterwards towards combustion TDC. After BDC, the swirl ratio decreases more slowly. Although this is the results in only one horizontal plane, the trend matches the simulation results for the whole in-cylinder charge in Ref. [243, 244] well. The swirl ratio 24 mm below the fire deck behaves differently, peaking around IVC. However, this also matches some experimental data [243] from limited optical access into the cylinder. The swirl ratios at  $-281^\circ\text{CA}$  at other locations also deviate much from those at 12 mm below the fire deck, generally decreasing with increasing distance from the fire deck (within the limited range investigated here). Thus, the swirl ratio throughout the cylinder probably disperses much before IVC. In fact, several vortices were seen in the ensemble-average flow fields at 24 mm from  $-297^\circ\text{CA}$  to  $-251^\circ\text{CA}$ , consistent with the low swirl ratios. Around IVC, the swirl ratios at 12 and 24 mm tend to converge, indicating a less stratified distribution of swirl level throughout the cylinder than before. This is consistent with the phenomenon seen in Figure 3.5 that after IVC the vector field starts to resemble a rotating solid body.

The swirl ratio measured at high swirl is plotted in Figure 3.10. 12 mm below the fire deck, the swirl ratio also increases drastically during the first half of the intake stroke, similar to that with low swirl. However, the swirl level at the maximum piston speed is still pronouncedly lower than the maximum level during the intake. Also, different from the low-swirl case, at  $-281^\circ\text{CA}$ , the swirl ratio increases with increasing distance from the fire deck, although the plane at 8 mm has the highest level of flow velocity among the three positions, as shown in Figure 3.8.

According to Figure 3.9, at IVC, the swirl level of the intake charge is one of the least diverged throughout the cylinder for the crank angle range investigated here. Also, in numerical simulations, the swirl ratio is usually set at IVC as a boundary condition [258-260]. Therefore, the preferable crank angle position to define the swirl ratio is IVC ( $-146^\circ\text{CA}$ ). At low swirl, the swirl ratio is determined by the mean of those at  $-151^\circ\text{CA}$  and  $-141^\circ\text{CA}$  at 12 mm below the fire deck, resulting in 1.4. Unfortunately, the flow field at IVC at high swirl was not measured here. As an alternative, the swirl ratio at the maximum piston speed during intake at 12 mm is used to characterize the swirl level. It is 2.4 at low swirl (mean of the two series) and 6.0 at high swirl.

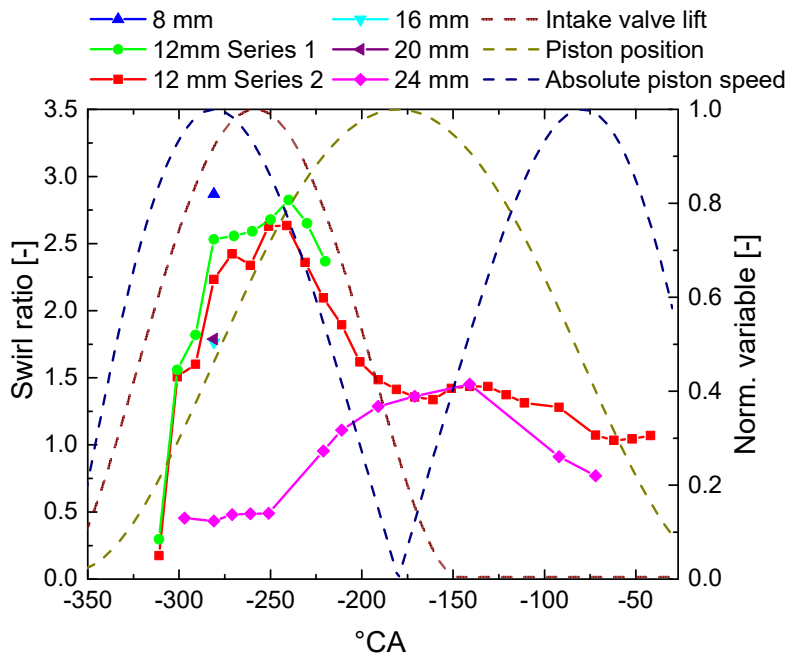


Figure 3.9 Temporal evolution of the swirl ratio with crank angle during intake and compression at low swirl with normalized intake valve lift, piston position, and piston speed as the background.

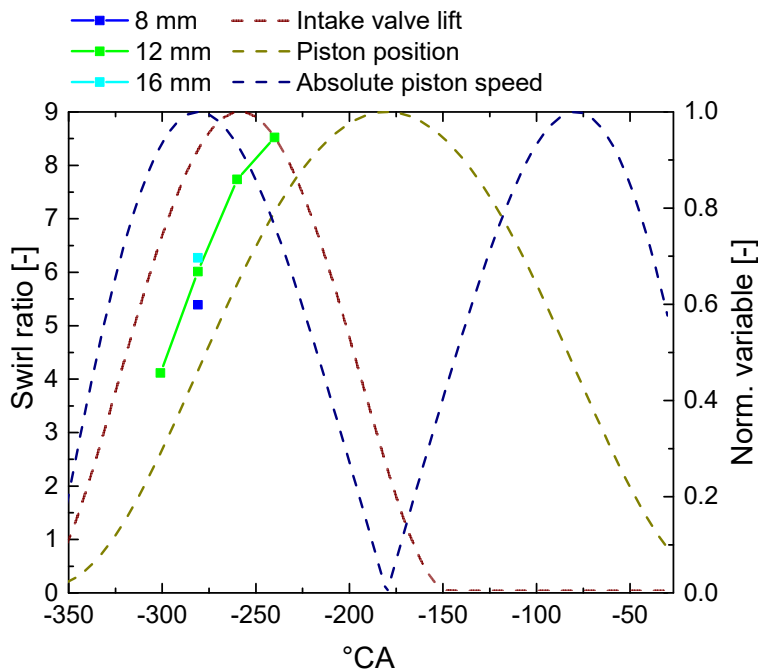


Figure 3.10 Temporal evolution of the swirl ratio with crank angle during intake at high swirl with normalized intake valve lift, piston position, and piston speed as the background.

### 3.3 In-cylinder temperature field

#### 3.3.1 Experiment

For the measurements of temperature fields with single-color tracer LIF, a piston crown with optical access to the bowl was designed and manufactured, as shown in Figure 3.11. The piston rim consists of two metal parts and two windows made of fused silica. The geometry of the cylindrical bowl is  $47.4 \times 10.5$  mm, 0.1 mm deeper than the bowl in the metal-rim piston crown. The squish height here

is 1.1 mm instead of 1.2 mm for the metal-rim piston crown, resulting in a best-fit compression ratio of 12.8 in GT-POWER, instead of 12.3 for the metal-rim piston crown.

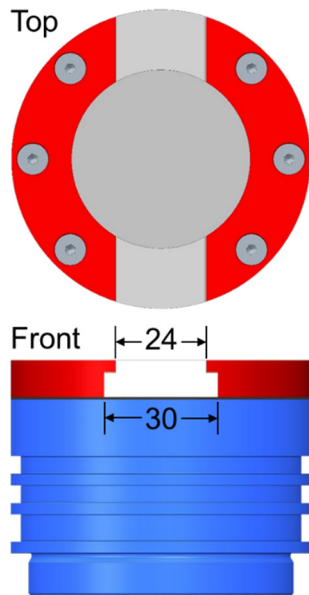


Figure 3.11 Schematic of the piston crown with the optically accessible bowl.

The engine operating conditions are listed in Table 3.5. The engine was motored with nitrogen. The coolant and oil temperature, intake pressure, and intake temperature were chosen according to the ECN specifications (refer to Section 4.2 for detail). Toluene was used as the tracer for LIF measurements, because of the high sensitivity of its fluorescence quantum yield to temperature, as shown in Figure 2.16. The tracer was injected into a small plenum (around 2 L) approximately 310 mm upstream of the intake port in every engine cycle to ensure the perfect mixing required for single-color tracer LIF thermometry. A PFI injector (Siemens, type 7506158) was used. The injection duration was chosen as a compromise between the fluorescence signal and the laser absorption at TDC. According to the injector calibration in Ref. [261], the tracer mass fraction in the intake charge is approximately 0.13%, very similar to that in Ref. [142].

Table 3.5 Engine operating conditions for the LIF thermometry measurement.

	Low swirl	High swirl
Engine speed	1200 rpm	
Swirl ratio at max. piston speed during intake	2.4	6.0
Coolant and oil temperature	85°C	
Intake gas composition	99.87% N <sub>2</sub> + 0.13% toluene (by mass)	
Intake pressure	2.02 bar	2.10 bar
Peak cylinder pressure	ca. 62.5 bar	ca. 62.0 bar
Intake temperature	60 °C	
Tracer	Toluene	
Tracer injection pressure	5 bar	
Tracer injection duration	13°C A	

Figure 3.12 shows the optical arrangement with the parameters for LIF imaging listed in Table 3.6. A frequency-quadrupled Nd:YAG laser (Quanta-Ray) provided a 266 nm pulse at 10 Hz of repetition rate and approximately 20 mJ/pulse of energy. The laser beam was formed into a sheet by a positive and a negative cylindrical lens. A second positive cylindrical lens was used to laterally focus the laser sheet before it entered the engine so as to partially compensate the negative-lens effects of both

the spacer window and the piston-rim window. The beam waist was placed outside of the engine (indicated by a dashed line in Figure 3.12) to avoid window damage and photobleaching [110]. At the beam waist, the laser sheet was about 1-mm thick. The laser sheet in the piston bowl was laterally diverging. Part of the beam was intended to reach the metal rim, in order to investigate possible differences in the heat-transfer characteristics of the hot gas between the fused-silica wall and the metal wall. The laser sheet was placed at 7 mm below the fire deck, which is vertically about the middle of the piston bowl at TDC. It is also nearly the depth where ECN Spray B impinges the wall (about 8 mm below fire deck). A UV-enhanced back-illuminated CCD (ANDOR iKon-M, model number DU934P) captured the toluene fluorescence with a quantum efficiency of about 60% at 290 nm. A band-pass filter centered at 292 nm blocked the scattered laser light and transmitted the fluorescence. Binned  $4 \times 4$  on chip, the camera ran at 5 Hz, capturing every second engine cycle at 1200 rpm. A  $2\times$  pre-amplifier gain was used to intensify the signal. Since the mechanical shutter of the camera was open during the entire engine run, the test cell was kept dark.

Three types of image data with corresponding BG images (without tracer) were taken on each day of data acquisition, namely flat-field (FF), temperature-calibration, and temperature-measurement images. In addition, dark images (with the lens cap on) were also taken to determine the camera's dark noise.

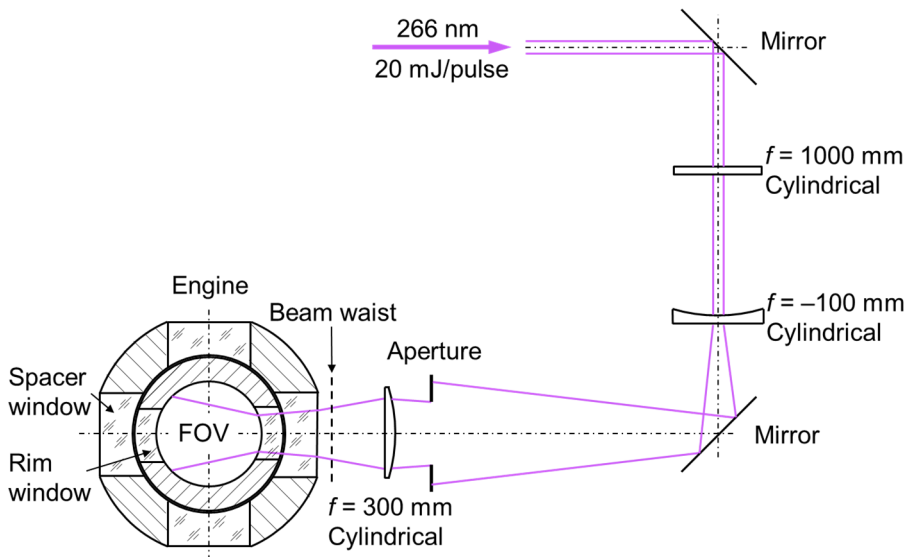


Figure 3.12 Arrangement of optics and engine cylinder for LIF imaging. FOV: field-of-view.

Table 3.6 LIF imaging parameters.

Laser repetition rate	10 Hz
Laser energy <sup>a</sup>	~20 mJ/pulse
Laser pulse length	14.1 ns
Laser sheet position	7 mm below fire deck
Camera lens	Cerco UV 100 mm $f/2.8$
Filter	BP 292/27
Frame rate	5 Hz
Camera binning	$4 \times 4$
Image resolution	$256 \times 256$ pixels
Projected pixel size	0.22 mm/pixel
Camera readout speed	5 MHz
Camera pre-amplifier	$2\times$
Number of dark images	50

	Flat field	T calibration	T measurement
Number of recorded LIF images	50	20	150
Number of recorded BG images	50	20	30
Crank angle where data were taken	N.A.	-146°CA, -96°CA, -47°CA, -33°CA, -21°CA, -2°CA	-1°CA

a. The incoming beam in Figure 3.12.

To correct for laser absorption, local reflectivity of the fire deck, and transverse laser-profile inhomogeneity, a flat-field (FF) correction is required in an LIF experiment. In this experiment, since temperature is to be measured, in the FF images the temperature has to be spatially uniform. However, in a running engine, the temperature is never uniform. Instead, in the standing engine at room temperature a series of FF images was taken with different tracer concentrations. The variation in tracer concentrations was intended to account for that in laser absorption in the images taken in the running engine. The FF images were taken with air as the bath gas. The ratio between the signals with and without oxygen quenching is a constant, if the temperature and oxygen concentration are spatially uniform [262]. FF images at three piston positions were taken: with the laser sheet passing through the lower part and the upper part of the piston-rim window (see Figure 3.11), as well as with the sheet not entering the piston bowl. These different positions account for the different crank angles that will be used for temperature calibration.

The relation between temperature and fluorescence signal was obtained via the increasing temperature during the compression stroke. During one engine run, sets of 20 LIF images each were taken at six crank angles from IVC to TDC. The core temperature was assigned to a region of interest (ROI) near the center of the piston bowl. The core temperature was calculated according to the adiabatic-core assumption, which is not always valid and to be discussed in Section 3.3.3. Images for the temperature calibration were taken at both low and high swirl. For the actual temperature measurements, at -1°CA sets of 150 images each were taken with both swirl levels.

### 3.3.2 Data post-processing

#### *Pressure trace*

In the pressure-trace processing, a low-pass filter with high to low transition from 3 to 5 kHz was used to filter out high-frequency electronic noise and in-cylinder acoustic resonances [230]. The core temperature for each engine run was calculated by isentropic compression along the measured pressure trace, starting from the bulk temperature at IVC computed with GT-POWER (refer to Section 4.3.1 for details).

#### *Raw image*

An example single-shot raw of the FF (left) and the temperature calibration/measurement (right) in the running engine is shown in Figure 3.13. The laser propagates from right to left. Both the scattered laser light and fluorescence were reflected by the fire deck, so that the patterns of the valves, pressure-sensor bore, and injector nozzle are seen. The low-reflectivity region results in low local intensity, e.g. the valve seats. The top-to-bottom large-scale gradient in image brightness is due to transverse laser-profile inhomogeneity. The small-scale stripes in the temperature-calibration/-measurement image are presumably due to beam steering by refractive-index gradients in the boundary layer at the laser-input window, a common issue in high-pressure high-temperature imaging, e.g. Ref. [142]. The decreasing intensity from right to left is due to laser absorption of the tracer. The bright curved pattern, indicated

by a red oval on the FF image, is a focused back reflection from the piston walls (including both glass and metal) [110]. In fact, on the left of the bright curved pattern, there is a second, weaker, triangle-shaped focused back reflection from the spacer window.

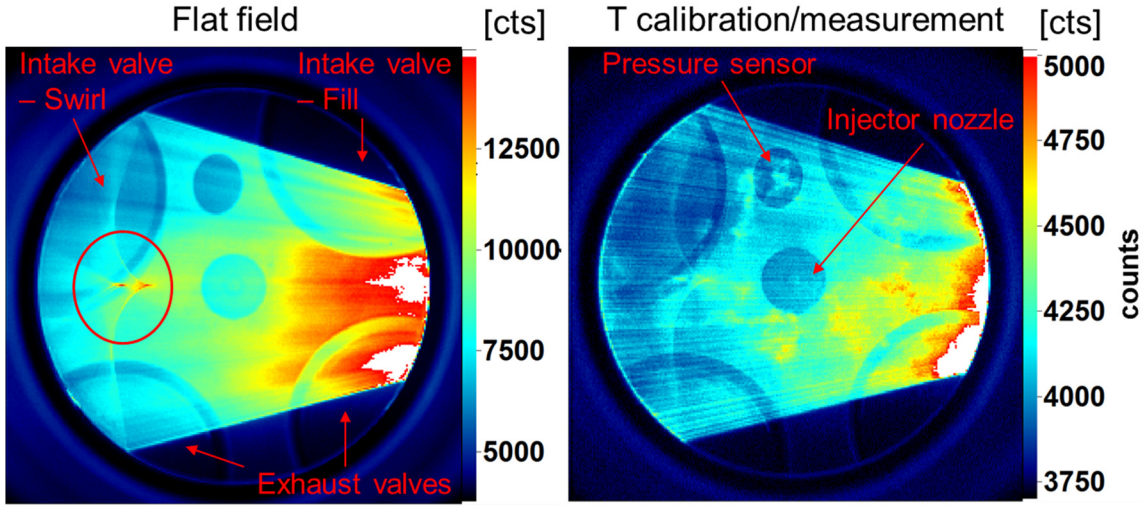


Figure 3.13 (left) Single-shot raw images of flat field and (right) temperature calibration/measurement. The right image is taken at  $-1^\circ\text{CA}$  at high swirl.

### Determination of laser absorption

For optical throughput correction, the temperature-calibration/-measurement images need to be divided by a FF that experiences the same absorption. Here, the local laser energy is a result of the absorption in the optical path in the upstream, the reflection of the scattered laser light, as well as the input laser profile and beam steering. The Beer-Lambert law is

$$I_1 = I_0 \cdot 10^{-c_{tra}\epsilon_{abs}L_{abs}} \quad (3.5)$$

where  $I_1$  is the transmitted-light intensity,  $I_0$  the incident-light intensity,  $L_{abs}$  the optical path length of absorption,  $c_{tra}$  the molar concentration of the tracer, and  $\epsilon_{abs}$  the molar attenuation coefficient of the tracer.

In the flat field or in the adiabatic-core region of the temperature-calibration/-measurement image, both the temperature and tracer concentration are spatially uniform. Thus, substituting Equation (3.5) into (2.11), the LIF signal can be written as

$$I(x, y, T) = \eta \{ [(E_{laser_0} k_{laser}(x, y) k_{div}(x)) \cdot 10^{-c_{tra}\epsilon_{abs}(T)L_{abs}(x, y)}] (1 + k_{ref_l}(x, y)) c_{tra} \epsilon_{abs}(T) \phi_{qy}(T) \} (1 + k_{ref_f}(x, y)) \quad (3.6)$$

where  $E_{laser_0}$  is the incident laser energy at the center of the exit of the laser-input piston-rim window,  $k_{laser}$  the ratio of the laser energy at the exit of the laser-input piston-rim window to  $E_{laser_0}$ ,  $k_{div}$  the ratio of the local laser energy to that at the exit of the laser-input window due to divergence of the laser beam,  $k_{ref_l}$  the ratio of the reflected light of the scattered laser light to the in-laser-sheet light, and  $k_{ref_f}$  the ratio of the reflected fluorescence light to that produced in the laser sheet.

Thus, the local fluorescence signal is strongly influenced by the reflectivity of the fire deck, the absolute absorption level is difficult to isolate. As an alternative, here the relative absorption level is determined. Assuming  $\eta$ ,  $k_{laser}$ ,  $k_{div}$ ,  $k_{ref_l}$ , and  $k_{ref_f}$  are the same for each dataset with the imaging parameters unchanged, if one LIF image (at temperature  $T_2$ ) is divided by another (at temperature  $T_1$ ), the local signal ratio is

$$I_{ratio}(x, y, T_1, T_2) = 10^{-(c_{tra,2}\varepsilon_{abs}(T_2) - c_{tra,1}\varepsilon_{abs}(T_1))L_{abs}(x,y)} \frac{E_{laser\_0,2} c_{tra,2}\varepsilon_{abs}(T_2) \phi_{qy,2}(T_2)}{E_{laser\_0,1} c_{tra,1}\varepsilon_{abs}(T_1) \phi_{qy,1}(T_1)} \quad (3.7)$$

Throughout the flat field or the core region,  $E_{laser\_0,2}/E_{laser\_0,1}$  and  $c_{tra,2}\varepsilon_{abs}(T_2)/c_{tra,1}\varepsilon_{abs}(T_1)$  are constants. As discussed in Section 3.3.1,  $\phi_{qy,2}(T_2)/\phi_{qy,1}(T_1)$  is also a constant regardless of the bath gas, if the temperature and oxygen concentration are both spatially uniform in the region of interest. Therefore, along each ray in the laser sheet, the logarithm of  $I_{ratio}$  is a linear function of  $L_{abs}$ . The slope is  $-(c_{tra,2}\varepsilon_{abs}(T_2) - c_{tra,1}\varepsilon_{abs}(T_1))$ , and can be used to quantify the difference in absorption between two datasets.

To determine the absorption difference between the FF images, first, one FF dataset was selected as a reference,  $I_{FF,0}$ . The BG-corrected average  $I_{FF,0}$  is shown in Figure 3.14a, while the BG-corrected average image of an arbitrary FF dataset,  $I_{FF,i}$ , is shown in Figure 3.14b. The ratio between the latter and the former is shown in Figure 3.14c. There is an obvious gradient form right to left, due to the difference in absorption. The “stripes” from the top down is probably because of difference in  $k_{laser}$  between these two datasets. A thin ROI in the central axis of the laser sheet was taken and averaged in the vertical direction. Then logarithm was calculated and the result is shown in Figure 3.14d. A good linear fit can be made. The slope is the absorption difference between  $I_{FF,i}$  and  $I_{FF,0}$ . The absorption difference between the temperature-calibration/-measurement images and  $I_{FF,0}$  was also determined this way. In this case, the ROI was located such that the boundary layer on the laser input side was avoided.

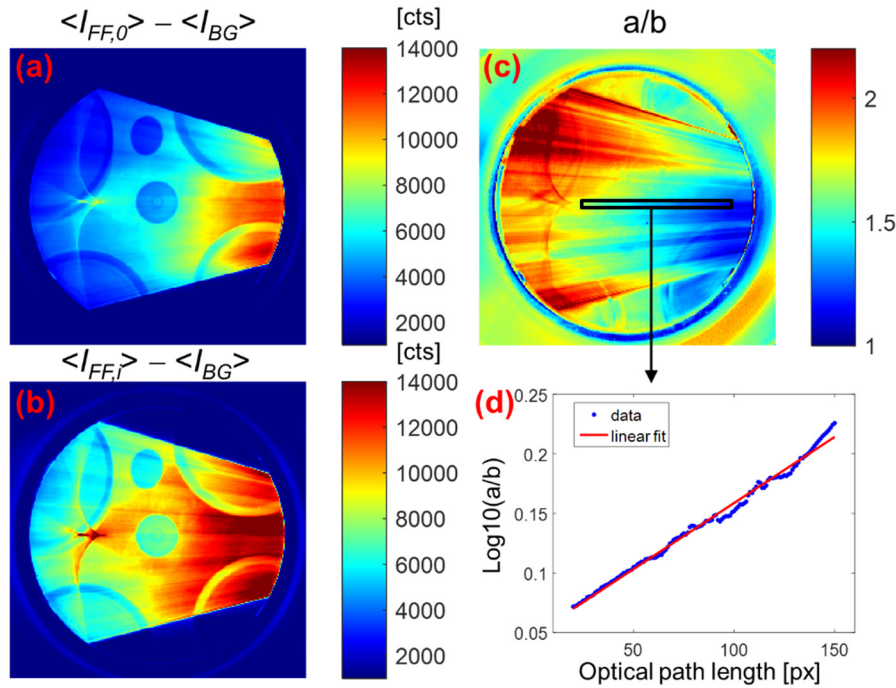


Figure 3.14 Image processing for determining laser absorption. (a) reference FF image after averaging and BG subtraction, (b) an arbitrary FF image after averaging and BG subtraction, (c) ratio of image b to image a, (d) the logarithm of vertical average of the ROI in image c with respect to the optical path length.

### Flat-field correction

Here the FF correction is demonstrated using the temperature-calibration images. The processing routine is illustrated in Figure 3.15. The FF dataset with the absorption level closest to the dataset to be corrected is chosen. In order to eliminate the influence of individual intensity level of FF images, the BG-corrected average FF image was normalized by its  $E_{laser\_0}$  (see Equation (3.6)). It was estimated

from the spatial mean in an ROI 1.5 mm away from the wall, as indicated by the black box in image b. The BG-corrected average image (image a) was divided by this normalized FF image (image b). Then a mask preserving only the FOV was applied on the resulting image. The masked image is shown in image c. According to Equation (3.6), to correct the final absorption difference between the FF and temperature-calibration dataset,  $L_{abs}$  was calculated by assuming a point light source at some distance in front of the laser input window. The absorption-correction factor  $\xi_{abs}$  is calculated as  $10^{(c_{tra}\varepsilon_{abs} - c_{tra,FF}\varepsilon_{abs,FF})L_{abs}}$  and shown in image e. Typical values of the correction factor are in a range of 0.4 to 1.4. By multiplying image c with image d, the absorption-corrected image is shown in image e.

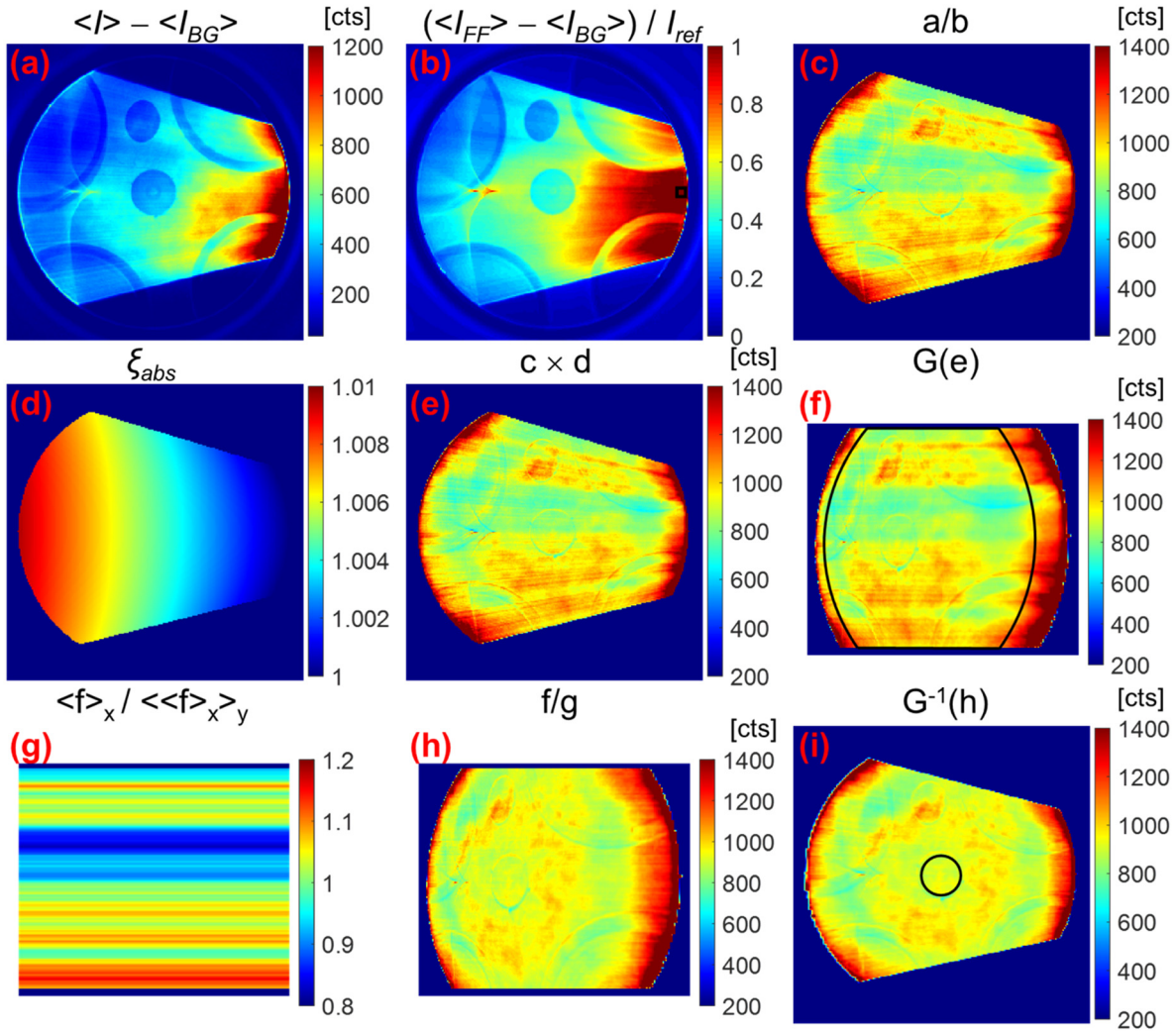


Figure 3.15 Image processing for flat-field correction. “ $\langle \cdot \rangle_x$ ” means spatial averaging in the horizontal direction, while “ $\langle \cdot \rangle_y$ ” means spatial average in the vertical direction. “ $G(\cdot)$ ” and “ $G^{-1}(\cdot)$ ” mean geometric image transformation and inverse transformation, respectively.

In the absorption-corrected image, large-scale stripes remain, probably because the transverse laser profile is different between the FF images (engine standing) and the temperature-calibration images (engine running). During measurements in the running engine, the trigger for the imaging system is changed from the internal trigger to the trigger from the engine timing unit. The small-scale stripes, due to the boundary layers, are more obvious downstream at the left side [142]. To suppress both types of stripes, first, the image was geometrically transformed such that each ray in the laser sheet is horizontal, i.e., as if the beam were collimated, as shown in image f. This was performed by the MATLAB functions

“fitgeotrans” and “imwarp” (transformation type “projective”, interpolation type “linear”). Then the vertical (sheet-transverse) profile of the laser beam was estimated by averaging in the horizontal direction in a ROI excluding the boundary layers (indicated by the black lines in Figure 3.15f). The vertical profile was normalized by its mean, preserving the total laser energy, with the result shown in image g. Upon dividing the transformed image by the normalized vertical profile, most of the large-scale vertical gradients disappeared, but some small-scale gradients still remained, as seen in image h. After this, the image was transformed back to the original geometry, shown in image i.

For the temperature-calibration images, an ROI slightly smaller than the nozzle, indicated by the black circle in Figure 3.15i, was positioned in the adiabatic core. The spatial mean in this ROI was assigned to the corresponding adiabatic-core temperature of this image set. For the temperature-measurement images, the BG-corrected single-shot images were calculated, substituting for Figure 3.15a. The mean intensity in the FOV is used as proxy for the single-shot laser energy, and each image is divided by its FOV mean. The single-shot images for temperature calibration were not processed since only average information was used in this experiment. The rest processing for FF correction in Figure 3.15 is the same for temperature-calibration and temperature-measurement images.

Since the tracer concentration at different crank angles also affects the LIF signal, the FF-corrected image needs a further correction to eliminate the influence of compression. Additionally, at a certain crank angle, the pressure is nearly spatially uniform in the cylinder, while the local gas density is inversely proportional to temperature. Therefore, the FF-corrected images were linearly rescaled to the same pressure instead of volume, accounting for both in-cylinder volume change and local gas density variation in the running engine. The pressure at  $-146^\circ\text{CA}$  (IVC) in the temperature-calibration dataset was used as a reference.

### ***Temperature calibration***

For both swirl ratios (one engine run for each), the core temperature is plotted against the ROI intensity after FF and pressure correction, as shown by the points in Figure 3.16. According to an LIF experiment in a flow cell from the literature [135], the fluorescence intensity of toluene excited at 266 nm decreases exponentially with temperature. Hence the data were fitted based on exponential functions. The fitting equation was of the form

$$T = a_1 e^{-b_1 I} + a_2 e^{-b_2 I} + c \quad (3.8)$$

where  $a_1$ ,  $a_2$ ,  $b_1$ ,  $b_2$ , and  $c$  are fitting coefficients.

The temperature-calibration fits are plotted in Figure 3.16 and the fitting coefficients are listed in Table 3.7. It is seen that in the temperature range of interest (near 900 K at TDC), the temperature has a very high slope against the image intensity compared to the low-temperature range. This indicates that the optical signal is not as sensitive to temperature at high temperature as at low temperature. The two curves nearly coincide with each other, but around 900 K, the low-swirl curve shows lower temperature than the high-swirl curve at the same LIF signal. This is probably because at high swirl, the core temperature is overestimated. The core region at high swirl probably experiences more heat transfer than at low swirl. This will be discussed further in Section 3.3.3. By applying the temperature-calibration curves pixel-wise to the pressure-corrected images, temperature fields are obtained.

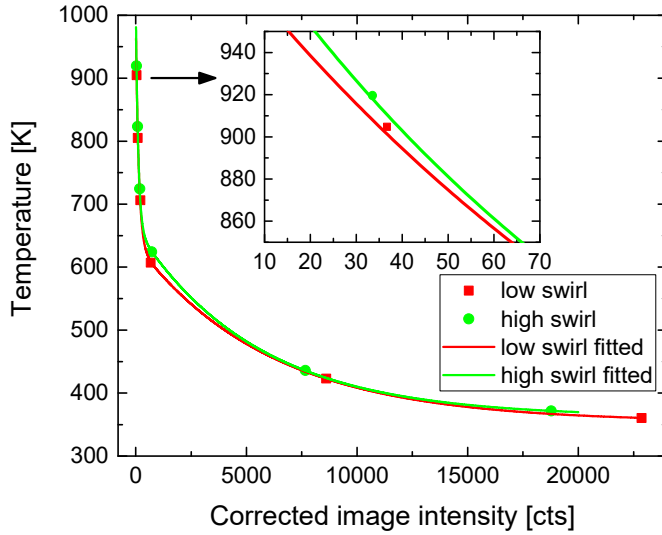


Figure 3.16 Correlation between the core temperature and the corrected image intensity in the adiabatic-core region at both low and high swirl. The reference pressure for each calibration curve is the respective pressure at IVC.

Table 3.7 Fitting coefficients in Equation (3.8).

	Low swirl	High swirl
$a_1$	353.1	350.6
$a_2$	282.7	299.5
$b_1$	$7.683 \times 10^{-3}$	$9.117 \times 10^{-3}$
$b_2$	$1.644 \times 10^{-4}$	$1.831 \times 10^{-4}$
$c$	354.0	362.1

### Measurement uncertainty

The accuracy for single-color tracer LIF in engines is difficult to evaluate [110, 142, 247], since the absolute temperature for temperature calibration is usually estimated by thermodynamics. In this work, the accuracy uncertainties mainly stem from two aspects. The first is the calculation of the temperature at IVC via GT-POWER simulation. The second is due to the possible heat transfer between the core region and the engine walls, which means the adiabatic-core assumption is not valid. Both of these two uncertainties are complex to access. However, the absolute temperature (accuracy) is not so important here, since the main objective of this work is the thermal stratification, i.e. the relative temperature. Therefore, here the measurement uncertainty is evaluated for the precision.

With respect to precision, the shot noise, the shot-to-shot variation in the laser profile and laser energy, and the beam steering caused by boundary layers contribute to the uncertainty. In the image processing, the latter two are addressed (beam steering partially). Here, the measurement uncertainty from the shot noise is determined.

First, the photon transfer curve for the camera used under the current setting was plotted to extract the shot noise model with optical signal as input. The dark noise was determined from the dark images. To evaluate the uncertainty for an image set, the shot noise of the dark-corrected average image of a dataset is determined, resulting in an upper limit and a lower limit by one standard deviation around the average. These two limits then went through the whole processing routine towards temperature. The precision uncertainty was determined by averaging the lower deviation and the higher deviation.

### 3.3.3 Results and discussion

Figure 3.17 shows selected single-shot temperature images relative to their respective mean core temperature (in the ROI in Figure 3.15i). At low swirl, the high-temperature zones at the intake valve seat (left side of the image) and where the red arrow indicates are artifacts from the FF image, presumably due to liquid toluene that was stored in a crack in the laser-exit window. Despite the remaining beam-steering stripes, a clear difference between low swirl and high swirl is evident. At high swirl, more intense temperature stratification is seen, both in the center and near the wall (because of the boundary layer). In addition, at high swirl, especially at the second frame shown in Figure 3.17, a low-temperature swirl structure is identified and indicated by the black arrows.

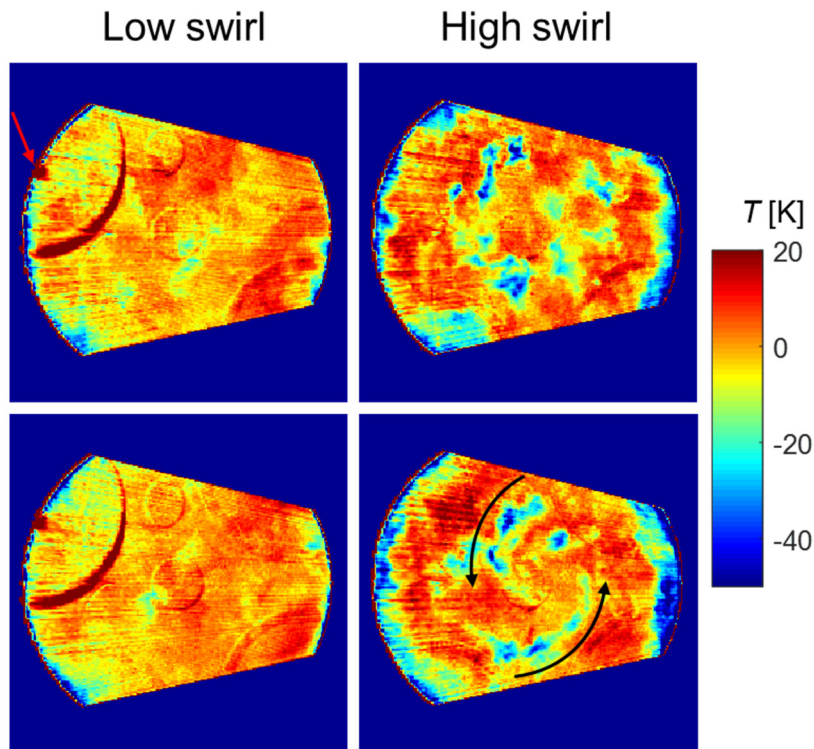


Figure 3.17 Selected single-shot images of relative temperature at low and high swirl. The reference temperature is the core temperature from the ensemble-average temperature image.

The ensemble-average temperatures, again relative to their mean adiabatic-core temperature, are shown in Figure 3.18, top row. The red arrows indicate the width of the laser-exit piston-rim window. At low swirl, the temperature field is relatively flat with a thin boundary layer. In contrast, at high swirl a pronounced ring-shaped low temperature zone exists around the injector nozzle. This is probably attributed to the squish flow. When the piston is approaching TDC, the displaced fluid from the squish volume penetrates inwards and join the swirl flow. At a higher swirl level, a higher centrifugal force is exerted by the swirl flow, so that the inward penetration is shorter [263-265]. Thereafter, the fluid flows downward into the piston bowl and circumferentially with the swirl. If the temperature in the squish volume (height 1.1 mm) is lower than the core temperature, this would result in a “low-temperature ring”. At low swirl, no such a stratification is seen, probably because the temperature in the squish volume is similar to that in the bowl, and/or the squish penetration disperses more. The boundary layer near the wall at high swirl is also thicker than at low swirl, presumably due to stronger heat transfer with the wall [25, 266]. Also, at high swirl the boundary layer appears thinner at the glass wall than at the metal wall, which is consistent with the lower heat conductivity of quartz vs. metal (i.e. the nickel alloy Invar).

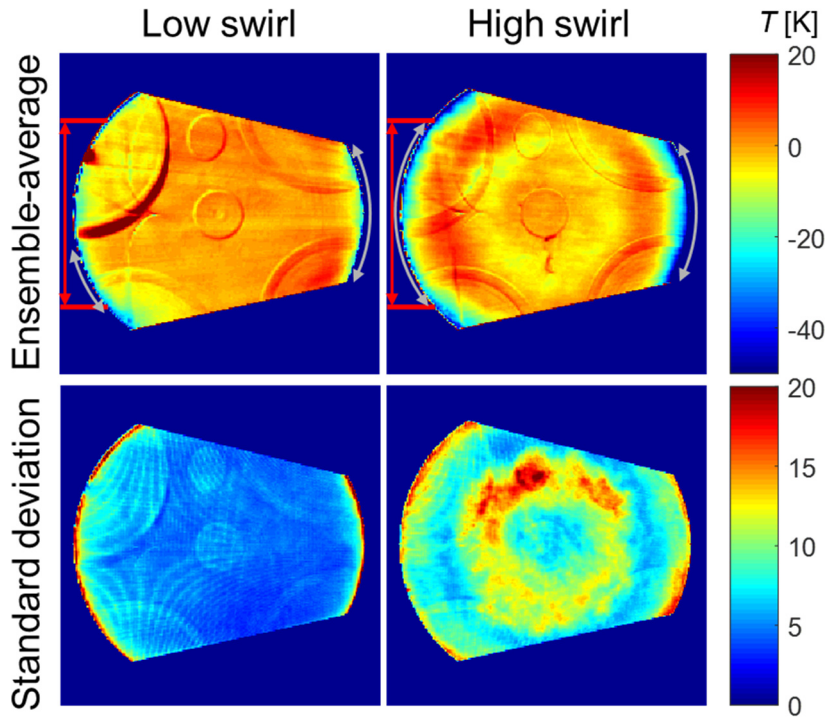


Figure 3.18 Ensemble-average relative temperature and the corresponding standard deviation at low swirl and high swirl. The reference temperature for the average is the mean core temperature. The red arrows indicate the width of the piston-rim window, while the gray arrows indicate the radial angle for extracting the radial temperature profiles shown in Figure 3.20.

The ensemble standard deviations in temperature are also shown in Figure 3.18, bottom row. Their features are consistent with those of the ensemble-average temperatures. The spatial mean of the deviation is 5.6 K at low swirl and 9.8 K at high swirl. At low swirl, much lower fluctuations are seen in the center of the bowl, indicating weaker turbulence, cycle-to-cycle variation, and/or temperature stratification. At both swirl levels, the higher fluctuations are located in the low-temperature regions, namely the boundary layers and – at high swirl – the low-temperature ring. This is consistent with the fluctuations stemming from the boundary layers that are always colder than the core gas. The fringe-like structures in the standard deviation are probably artifacts from the two interpolations in the geometric transformations in the image processing (Figure 3.15f and i).

Figure 3.19 shows the measurement uncertainty due to the shot noise. The uncertainties at the two swirl ratios are very similar, with an approximate spatial mean of 4 K. This is on the same order of magnitude as two previous studies with toluene single-color tracer LIF in compression-ignition engines [110, 142], where the uncertainties are 8.4 K with mean core temperature of 990 K and 7 K with about 900 K, respectively. As expected, regions that are darker in the raw images (see Figure 3.13) have higher temperature uncertainty. The gradient from right to left stems from the laser absorption. The regions of valve seats, pressure-sensor bore, and injector nozzle show higher uncertainty, consistent with the larger standard deviations in temperature at the same locations at low swirl, as seen in Figure 3.18, bottom left. This indicates that these locally higher deviations are not due to stronger turbulence, cycle-to-cycle variation, or thermal stratification, but due to lower signal.

The mean core temperature calculated within the nozzle region (see Figure 3.15i) from LIF thermometry is compared with those calculated via GT-POWER and isentropic compression in Table 3.8. It is seen that the error is around 1 K, which indicates that the LIF measurement is repeatable for different engine runs and the GT-POWER simulation is precise.

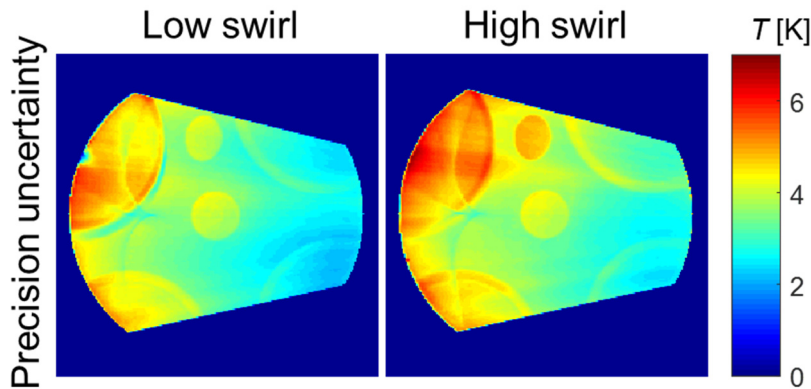


Figure 3.19 Precision uncertainty of the LIF temperature measurement. The uncertainty is determined by averaging the upper and the lower temperature deviation calculated from one standard deviation of the shot noise.

Table 3.8 Temperatures related to LIF thermometry and thermal boundary-layer thickness.

	$T_b$ (GT-POWER)	$T_c$ (thermodynamics)	$T_c$ (LIF)	$T_c$ (LS cal.)	Boundary layer thickness
Low swirl	814 K	887 K	888 K	888 K	1.5 mm
High swirl	811 K	916 K	915 K	908 K	3.0 mm

LS cal.: using the low-swirl temperature calibration.

To obtain an estimate of the radial distribution of the temperature, the ensemble-average absolute temperatures (corresponding to the relative ones shown in Figure 3.18) were averaged circumferentially within the angular ranges indicated by the gray arrows in Figure 3.18. The temperatures in the left half and the right half of each image were computed separately. For low swirl, the left temperature profile was extracted avoiding the valve-seat artifact. The resulting radial profiles are plotted as solid lines in Figure 3.20. The temperatures at the nozzle tip and the nozzle edge are omitted because of an artifact presumably from image misalignment during the FF correction (see Figure 3.15c). The left and right part of the temperature profiles are not symmetric, presumably because the laser absorption is not fully corrected.

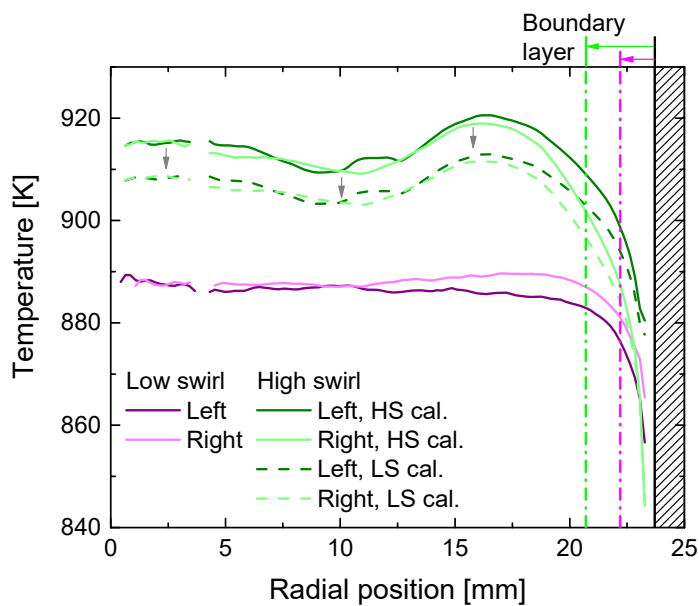


Figure 3.20 Radial temperature profiles at low swirl and high swirl. HS cal.: using the high-swirl temperature-calibration curve. LS cal.: using the low-swirl temperature-calibration curve.

At low swirl, the temperature field is very flat out to a few millimeters from the piston wall. The thickness of a boundary layer defined by  $T/T_c < 0.99$  is 1.5 mm ( $T_c$  for core temperature), indicated by the magenta arrow in Figure 3.20. From Figure 3.18, the standard deviation in temperature in the core region is slight, lower than 5 K (close to the precision uncertainty in Figure 3.19). Thus, at low swirl, the adiabatic-core assumption applies well – a large region with nearly uniform temperature, presumably close to adiabatic, exists in the piston bowl. By contrast, at high swirl, the low-temperature ring seen Figure 3.18 corresponds to a shallow “pit” around  $r = 10.5$  mm. The maximum temperature is located around  $r = 16.5$  mm, designated as the “high-temperature ring” here. This region has probably the least heat transfer with the walls and the presumed cold squish volume, and is closer to adiabatic than the region near the injector nozzle that was used as a reference in the image processing (see Figure 3.15i). The nozzle region also appears influenced by the cold squish flow, having a temperature between the high-temperature and low-temperature ring. Using the temperature in the nozzle region as the core temperature, the boundary layer ( $T/T_c < 0.99$ ) at high swirl is still twice that at low swirl, namely 3.0 mm, shown by the green arrow. Clearly, at high swirl, the ensemble-average temperature in the piston bowl is radially non-uniform due to heat transfer, and the adiabatic-core assumption does not apply here.

In the high-swirl dataset, the temperature in the core region is nearly 30 K higher than in the low-swirl dataset, although the bulk temperatures at the same crank angle calculated via GT-POWER are very close to each other (3 K difference). This is partially because the temperature for the calibration in the high swirl data is already higher than the real temperature, because of the inapplicability of adiabatic-core assumption at high swirl, as discussed in the last paragraph. To estimate the error incurred by this, the temperature calibration for low swirl is used to compute the temperature field at high swirl (assuming that the tracer concentration and laser energy are the same for the different engine runs). The results are plotted in Figure 3.20 as green dashed lines. The core temperature is now 7 K lower (Table 3.8) and radial temperature profiles are overall by about that much lower, but a gap of around 20 K to the low-swirl profiles still exists. This indicates that, in general, for two datasets with different swirl ratios but similar in-cylinder pressures and bulk temperatures at TDC, the core temperature at high swirl is higher than that at low swirl, at least at the central horizontal plane in the piston bowl. Conversely, the boundary layers must be thicker or colder. Concerning the bowl wall, this is consistent with the measurements, and concerning the squish and crevice volume it supports the indirect conclusion made above that this part of the in-cylinder gas is significantly colder than the bowl volume at high swirl.

### 3.4 Summary and conclusions

At both low swirl and high swirl, the flow field in different horizontal planes within the spacer during the intake and (for low swirl) the compression stroke was measured via PIV. The vector fields and  $TKE$  were computed in LaVision DaVis 8.2 and the swirl ratios were calculated from the ensemble-average vector fields by assuming a solid-body rotation with the same angular momentum as the in-cylinder gas. The conclusions are as follows. The initial momentum for the swirl motion is generated at the beveled valve seat. Before IVC, the swirl level disperses much at different axial positions in the cylinder, as also found in Ref. [97, 245]. For the plane 12 mm below the fire deck, the swirl ratio increases drastically from gas exchange TDC and peaks shortly after the timings of the maximum piston speed and intake valve lift, consistent with the simulation results in Ref. [243, 244]. The  $TKE$  is also high around this time, locally concentrated at the regions with high velocity gradients. Around IVC, the airflow starts to resemble a solid-body rotation. The swirl ratios at different vertical positions tend to converge. However, the swirl center is not the geometric center of the cylinder and also not the same across the crank angles and plane locations, which is consistent with Ref. [243, 244]. From IVC towards combustion TDC, the swirl and  $TKE$  level decrease slowly due to the turbulent dissipation and the friction from the engine walls. The high  $TKE$  regions are located around the swirl center, as also found

in Ref. [243]. At high swirl, both the velocity and *TKE* level are much higher than those at low swirl, which was observed at the maximum piston speed. For the plane at 12 mm, at low swirl, the swirl ratio is 2.4 at the maximum piston speed during the intake and 1.4 at IVC, while at high swirl it is 6.0 at the maximum piston speed. Finally, the swirl ratios at the maximum piston speed during the intake are used for now to characterize the swirl level in this engine.

Toluene single-color tracer LIF thermometry was used to measure the in-cylinder temperature field around TDC ( $-1^\circ\text{CA}$ ). The goal was to investigate the difference in temperature distributions between low swirl and high swirl operation, and in particular the applicability of the adiabatic-core assumption for in-cylinder temperature calculations. Image processing was developed to perform an optical-throughput correction, correct for laser absorption and laser-profile variation. The measurement uncertainty due to the shot noise was determined as well. The temperature calibration used the temperature computed according to the adiabatic-core assumption at different crank angles in an engine run. The results show that at low swirl, a large thermally uniform core region exists in the piston bowl, while at high swirl, the ensemble-average temperature field is radially non-uniform, with a ring-shaped low-temperature region probably due to the cold squish flow. The boundary layer at the bowl wall is also about twice as thick as for low swirl. Thus, the adiabatic-core assumption may be reasonably accurate at low swirl, but not at high swirl. At similar bulk temperatures, the high swirl dataset has a higher core temperature in the piston bowl than at low swirl. The difference is about 20 K at a core temperature around 900 K and a cylinder pressure of 60 bar.

Thus, especially at high swirl, the in-cylinder flow and temperature field in an engine is complicated, temporally dynamic, and spatially stratified, consequently very different from that in a combustion vessel for spray combustion studies.

In future work for the in-cylinder flow field, first, the data at high swirl needs to be measured at more crank angles to determine the swirl ratio at IVC. In addition, at both swirl levels, the flow field in the piston bowl around TDC should be measured via a piston crown with optical accesses into the bowl (already designed and manufactured), since this flow field has direct influence on the fuel spray. Regarding the in-cylinder temperature field, the small-scale vertical gradients (see Figure 3.17) could be removed by image processing. To obtain a more accurate temperature calibration, intake temperature could be varied to obtain an in-cylinder temperature variation at the same in-cylinder pressure (e.g. at TDC) [110, 142]. However, it appears most interesting to extend the temperature measurements in space (i.e., different image planes) and time (different crank angles) to better understand the thermofluidics of the charge near TDC.

---

## Chapter 4 Fire-deck retro-reflection with skip-illumination applied to Spray B

---

Most of the results from this chapter have been presented or published in the papers and conferences listed below. After these, more data targeting the difference between low swirl and high swirl were taken and are also included in this chapter.

ECN Workshop 5.13, 2018, oral presentation “Methodology and experimental uncertainty of Spray B measurements in University of Duisburg-Essen”.

THIESEL 2018 – Conference on Thermo- and Fluid Dynamics Processes in Direct Injection Engines, Valencia, Spain, 2018, poster “Time-resolved simultaneous visualization of liquid and gas-phase fuel and combustion by retro-reflection of pulsed LED light in an optically accessible Diesel engine”.

SAE World Congress Experience 2019, Detroit, USA, 2019, SAE technical paper & oral presentation “A Study of ECN ‘Spray B’ in a Light-Duty Optically Accessible Diesel Engine Based on High-Speed Imaging with LED Retro-Reflection”, doi: 10.4271/2019-01-0550.

Encom 2019 – 14th International Congress on Engine Combustion and Alternative Concepts, Waischenfeld, Germany, 2019, conference paper “A brief introduction to the Engine Combustion Network (ECN) and a study of ECN “Spray B” in a light-duty optical Diesel engine”.

### 4.1 Introduction

ECN Spray B injectors have the same nominal orifice outlet diameter and nozzle  $K$  factor specification as those of Spray A, but have three holes with a full included angle of  $145^\circ$ , which makes this spray target more realistic towards production injectors than Spray A. As illustrated in Figure 4.1, from combustion vessels to heavy-duty engines to light-duty engines, the bulk volume of ambient gas decreases and the typical ambient gas motion increases. With walls closer to the fuel spray, the ambient conditions near the spray may be less uniform, as seen in Section 3.3. Spray/wall interaction has more of an effect, and together with increased ambient flow velocities (mainly swirl), the air entrainment into the spray changes, which strongly influences liquid length, spray penetration, and spray dispersion angle [39, 42]. Therefore, it is interesting to investigate such a standardized injector in optically-accessible facilities with different geometries under the same nominal operating conditions. (In this work the term “operating condition” encompasses both the ambient gas condition and the fuel-injection parameters.) Since substantial ECN research has been done in combustion vessels, e.g. Spray A, experiments on Spray B in engines can act as a bridge connecting these basic-science studies with industrial applications in real engines.

Several facilities have previously performed and published studies with one of the Spray B injectors. These facilities are abbreviated as follows:

- The constant-volume preburn (CVP) chamber at Sandia National Laboratories (SNL) – “SNL-CVP”.
  - The large-bore optical engine at SNL – “SNL-LBE”.
  - the constant-pressure flow (CPF) chamber at CMT-Motores Térmicos (CMT) at Universitat Politècnica de València – “CMT-CPF”,
  - The small-bore optical engine at CMT – “CMT-SBE”.
  - The small-bore optical engine at the Institute for Combustion and Gas Dynamics (IVG) at the University of Duisburg-Essen – “IVG-SBE”.
-

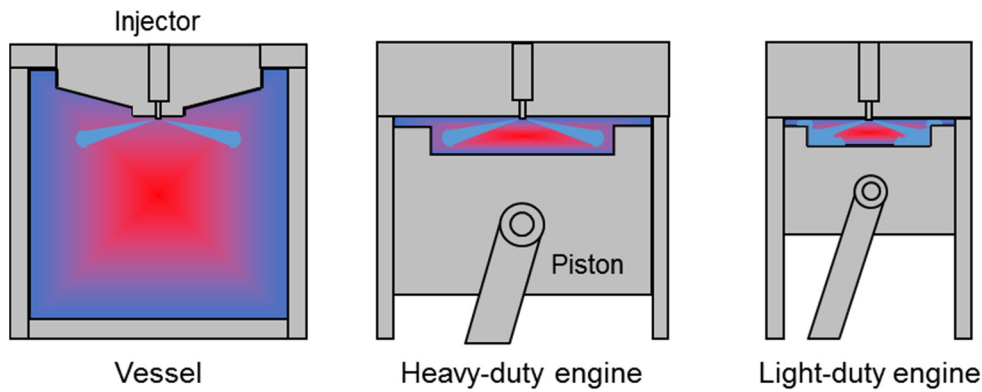


Figure 4.1 Schematic for difference between combustion vessels, heavy-duty engines, and light-duty engines in chamber size and temperature field.

After initial measurements in the SNL-CVP [53, 267] and in the CMT-CPF [55], Spray B injectors were also investigated in the SNL-LBE [52] and the CMT-SBE [56]. The facility parameters and the corresponding measured data with the corresponding diagnostics used are summarized in Table 4.1, also with the data from this work.

Table 4.1 Summary of current ECN Spray B database with diagnostics used for measurements.

Abbreviation	SNL-CVP	CMT-CPF	SNL-LBE	CMT-SBE	IVG-SBE
Facility	Constant-volume preburn chamber	Constant-pressure flow chamber	Large-bore engine	Small-bore engine	Small-bore engine
Dimension <sup>a</sup>	1150 cm <sup>3</sup>	Unknown	97.8 mm	45 mm	47.4 mm
Swirl ratio	N.A.	N.A.	0.5	Unknown	2.4, 6.0
Injector	211201	211200	211199	211200	211201
Liquid length	DBI	Mie scattering	Mie scattering	Mie scattering	Fire-deck retro-reflection
Vapor penetration	Schlieren	Schlieren <sup>b</sup>	Schlieren	×	Fire-deck retro-reflection
Spray dispersion angle	Long-distance microscopy (near-nozzle spreading angle)	×	×	×	Fire-deck retro-reflection
Ignition delay	Non-intensified CL	Schlieren, Non-intensified CL	Pressure-based, OH* CL	Pressure-based, Non-intensified CL, Intensified broadband CL	Non-intensified CL
Ignition location	Non-intensified CL	×	×	Non-intensified CL	Non-intensified CL
Lift-off length	Non-intensified CL, OH* CL	Non-intensified CL, OH* CL	Non-intensified CL, OH* CL	OH* CL	×
HRR	×	×	√	×	√
Hole-to-hole variation	√	×	√	×	√
References	[53, 267]	[55, 268]	[52]	[56]	Current work

a. chamber volume for vessels, piston bowl diameter for engines.

b. work in progress.

CL: chemiluminescence.

The swirl ratio between different engines cannot be directly compared because of probably different diagnostics. The information is only based on publications.

Regarding Spray B measurements in engines, the results from the SNL-LBE did not show any strong outliers compared to previous measurements in vessels [52]. The authors attribute most of the differences between the results from different facilities to the internal injector dynamics (different injector numbers). Neither did the measurement in the CMT-SBE show any remarkable different results from those obtained in the vessels. Vapor spray penetration, hole-to-hole variation, heat release rate ( $HRR$ ), and effect of swirl were unfortunately not investigated in CMT's study. In this work, ECN Spray B injector 211201 was used in the small-bore optically accessible Diesel engine at the IVG, the IVG-SBE. For Diesel spray diagnostics, the ECN recommends diffuse back-illumination (DBI) to measure liquid penetration length [148]. For vapor penetration, schlieren imaging is recommended [148]. However, to perform these two trans-illumination methods in a Bowditch-type optical engine, a window in the fire deck is needed, as for example in Ref. [52]. Alternatively, the reflection of the fire deck (or the metal wall at the same position in a vessel) can be utilized to achieve retro-reflection. In schlieren imaging, single-port collimated illumination and collection can be achieved by a beam splitter. Pastor et al. [269] used an injector holder with a mirror-coating surface and performed such double-pass schlieren in a two-stroke optical Diesel engine to image the transient fuel vapor. Neal and Rothamer [270] inserted a polished stainless-steel mirror into the fire deck and performed "shadowgraphy" with a beam splitter and an uncollimated beam to see the fuel vapor. The liquid fuel was visualized simultaneously by the extinction of the reflected light from both the low-reflective and high-reflective surface. Grochowina et al. [271] also used a polished steel plate next to the injector and performed schlieren imaging in a combustion vessel to detect the fuel vapor and ignition in dual-fuel combustion with Diesel and natural gas.

Similar to the two methods discussed above, also by making use of the retro-reflection from the fire deck, an optical method of quasi-simultaneously imaging both liquid and gas phase of the fuel spray as well as combustion at kHz-rates with uncollimated pulsed LED light was developed here. In addition to the standard Spray A condition (from which the Spray B operating condition is taken), a variation of ambient temperature  $T_a$  and density  $\rho_a$ , fuel rail pressure  $p_f$ , and swirl ratio  $SR$  were investigated. In addition to comparisons with the previous measurements of Spray B, hole-to-hole variation and effect of swirl ratio are analyzed in this work. In Appendix 9.1, the LED fire-deck retro-reflection method is compared to Mie scattering in terms of liquid phase detection, and to collimated schlieren imaging via retro-reflection in terms of gas phase detection.

## 4.2 Experiment

The engine parameters can be found in Table 3.1. Here a piston crown with the full-metal rim was used. The fuel injector was the three-hole ECN Spray B injector 211201, with a nominal orifice outlet diameter of 90  $\mu\text{m}$ . The parameters of this injector are listed in Table 4.2.

Table 4.2 Specifications of ECN injector B211201 [45, 239, 272].

Number of holes	3		
Nominal orifice outlet diameter	0.090 mm		
Nominal nozzle $K$ factor	1.5		
Orifice orientation relative to injector axis	72.5°		
Hole	1	2	3
Hole angular position with respect to fuel supply tube	36.4°	-62.3°	180°
Hole length	737 $\mu\text{m}$	759 $\mu\text{m}$	769 $\mu\text{m}$
Inlet diameter	115 $\mu\text{m}$	117 $\mu\text{m}$	118 $\mu\text{m}$
Outlet diameter	89 $\mu\text{m}$	91 $\mu\text{m}$	92 $\mu\text{m}$
Mean inlet radius of curvature	12 $\pm$ 5 $\mu\text{m}$	10 $\pm$ 5 $\mu\text{m}$	21 $\pm$ 11 $\mu\text{m}$
Orifice area-contraction coefficient ( $C_a$ )	0.98		

Orifice velocity coefficient ( $C_v$ )	0.854	0.893	0.856
Nozzle $K$ factor	0.7	0.9	1.1

The engine operating conditions are listed in Table 4.3, with the baseline targeting the standard Spray B condition [45] underlined. Both non-reacting (inert) and reacting conditions (with 16.5 vol-% oxygen in addition to the standard 15%) were investigated. Although compared to ECN specification  $\text{CO}_2$  and  $\text{H}_2\text{O}$  are missing in the intake gas, all previous Spray B measurements except in the SNL-CVP [53, 267] also used only air and nitrogen. This difference is not expected to cause deviations under non-reacting conditions but may influence ignition [64, 233]. To achieve the standard ECN condition, a closely-spaced series of intake gas temperatures was investigated. To estimate the intake temperatures, first the bulk temperature at BDC was estimated with two methods. One is based on the first law of thermodynamics and Woschni's heat transfer model [273] with the cylinder-wall temperature equal to the engine coolant temperature, while the other is simply taking the arithmetic mean of the intake temperature and the engine coolant temperature. These two methods give a range of bulk temperatures at BDC. The adiabatic-core temperature at TDC [248] was calculated based on the BDC temperature and the measured pressure trace by assuming isentropic compression with the adiabatic index being a function of the gas temperature [71, 274, 275]. After all the measurements had already been completed, the temperature at TDC was re-calculated using GT-POWER (see Section 4.3.1).

The intake pressure was adjusted to keep the maximum in-cylinder pressure in the motored cycles of the skip-fire scheme within 0.5 bar of the pressure calculated according to the target ambient temperature and density, considering non-reacting and reacting conditions. To achieve the least variation of ambient conditions during injection, the (single) injection was scheduled to start just before TDC. The measured injection duration from the images is slightly longer than the ECN standard (1.5 ms), probably due to the injector driver calibration. The fuel temperature at the nozzle is assumed to be the same as the coolant and oil temperature, and both were 5 °C below the ECN specification. The uncertainty in the fuel temperature is influenced by the heat transfer from the hot gas in the combustion chamber [148], which is difficult to account for in an engine. The fuel was pressurized by a pneumatic pump, stabilizing the rail pressure within 50 bar deviation around the target pressure. The engine was skip-fired with fuel injected every 3th or 6th cycle in non-reacting or reacting conditions, respectively. The swirl ratio was varied by blocking the swirl port.

Table 4.3 Engine operating conditions for Spray B measurements by fire-deck retro-reflection.

Engine speed	1200 rpm
Swirl ratio at max. piston speed during intake	2.4, 6.0
Fuel	n-dodecane
Fuel rail pressure ( $p_f$ )	500 bar, 1000 bar, <u>1500 bar</u>
Start of injection (SOI) <sup>a</sup>	-5.56°CA
Duration of solenoid energizing	0.795 ms
Duration of injection <sup>a</sup>	1.59 ms, 11.5°CA (ECN target: 1.5 ms)
Injected fuel quantity <sup>b</sup>	11.3 mg
Coolant and oil temperature	85°C (ECN target: 90°C)
Inject every	3th cycle (non-reacting), 6th cycle (reacting)
Intake gas composition	<u>100% N<sub>2</sub></u> , 15% O <sub>2</sub> + 85% N <sub>2</sub> , 16.5% O <sub>2</sub> + 83.5% N <sub>2</sub> (all by volume)
Target temperature at TDC	<u>900 K</u> , 1000 K
Target density at TDC	15.2 kg/m <sup>3</sup> , <u>22.8 kg/m<sup>3</sup></u>

a. SOI and injection duration are both determined from images at 1500 bar injection pressure.

b. Calculated from the rate of injection data from CMT (1.5 ms injection duration) [272].

Figure 4.2 shows the optical arrangement with the main parameters listed in Table 4.4. The light from two blue LEDs with emission centered at 475 nm was directed by condenser lenses towards the Bowditch mirror. Reflected by the flat cast-aluminum fire deck, the light was captured by a high-speed camera (Photron SA-Z) operating at 112 kHz or 110 kHz frame rate. On its path, the reflected light passed through probe volume twice. This method is very similar to Neal’s and Rothamer’s [270] but here with a rougher fire deck surface and without a beam splitter. To visualize combustion under reacting conditions, the LEDs were run in a skip-illumination mode [276], pulsed in every second camera frame, resulting in “on” and “off” images. This enabled quasi-simultaneous imaging of spray and combustion with better dynamic range than would have been possible with a single-illumination scheme. Two Schott-glass blue filters, a BG-23 stacked with a BG-28 filter (combined peak transmission 40% at 450 nm), were used to suppress most of the soot luminosity. The camera was focused at the fire deck. Two different camera lenses with similar optical parameters were used throughout the measurements. The FOV was in the piston bowl, as shown in the upper left of Figure 4.2.

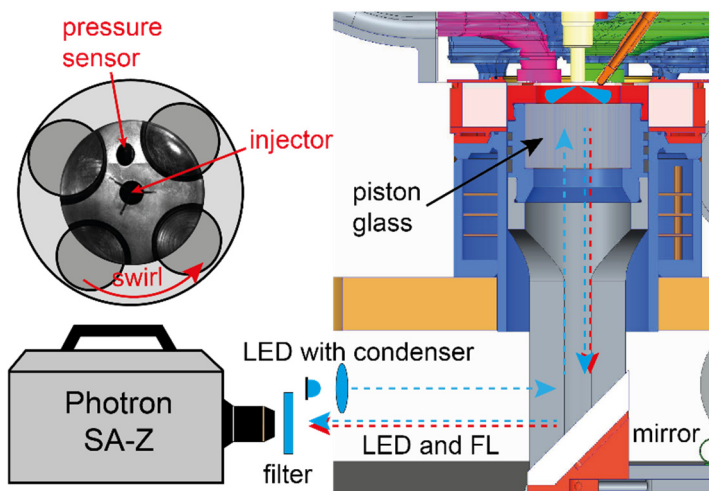


Figure 4.2 Schematic of optics and FOV for fire-deck retro-reflection. FL: flame luminosity.

Table 4.4 Imaging parameters for fire-deck retro-reflection.

	Non-reacting	Reacting
Frame rate	112 kHz or 110 kHz	
Resolution	384 × 360 pixels	
Projected pixel size	0.15 mm/pixel or 0.14 mm/pixel	
LED pulse duration	0.7 μs	2.5 μs
Exposure time	7.5 μs	
Camera lens	Tokina 100 mm <i>f</i> /2.8 or Nikon 105 mm <i>f</i> /2.8	
Filter	None	3-mm BG-28 + 2-mm BG-23
Illumination	All images	Skip (1 on / 1 off)
Recorded cycles	50	25

## 4.3 Data post-processing

### 4.3.1 Pressure-trace processing

First, to filter out high-frequency electronic noise and in-cylinder acoustic resonances [230], a low-pass filter with a transitioning from high to low from 3 to 5 kHz was chosen after checking the power spectral density of the pressure trace (which showed that the first resonance peak occurred at about 4.5 kHz). After this, the apparent heat release rate (*AHRR*) and SOC (in this work targeting high-temperature reaction) were determined using the same algorithm as in Ref. [52] with a constant adiabatic

index of 1.33. SOC was defined as the time of the first zero-crossing after start of injection (SOI) in the  $AHRR$  curve. Hydraulic SOI was determined in each single cycle from the images by setting a region of interest at the nozzle and a threshold on the bright Mie-scattered light from the spray very close to the orifice outlet. The ignition delay was then calculated as the time between SOC and SOI.

The thermodynamic state in the combustion chamber was estimated via a GT-POWER simulation [277]. The “Three-Pressure Analysis”, which calculates the burn rate based on the intake, cylinder, and exhaust pressure traces, was chosen to simulate the last motored cycle just before the fired cycles. In fitting the simulation to the measured pressure traces, the best-fit compression ratio was 12.3 (the geometric compression ratio is 15). The “Leak Path Equivalent Diameter” was set to 0.7 mm, accounting for presumed blow-by in the optical engine, resulting in a blow-by mass fraction between 4% and 5% over all the datasets. The relative deviation of simulated and measured peak cylinder pressure was within 0.3%, and that of the mass flow rate of the intake gas within 0.6%. From the fitted simulation, the in-cylinder bulk temperature trace was obtained. The adiabatic-core temperature was calculated based on the GT-POWER temperature at intake valve closing (IVC) and the measured pressure trace, as described in Section 4.2. Figure 4.3 shows an example of the peak-normalized pressure, density, and temperature traces near TDC. The ambient gas density was calculated via the compressibility-corrected ideal gas law with a compressibility factor of 1.01 both for the core gas and the bulk gas. During fuel injection, the decrease from the maximum in all parameters is within 5%, with the core density being the most sensitive to piston movement (except for the less relevant in-cylinder pressure). Throughout Chapter 4 and Chapter 5, the maximum values are used as the nominal ones.

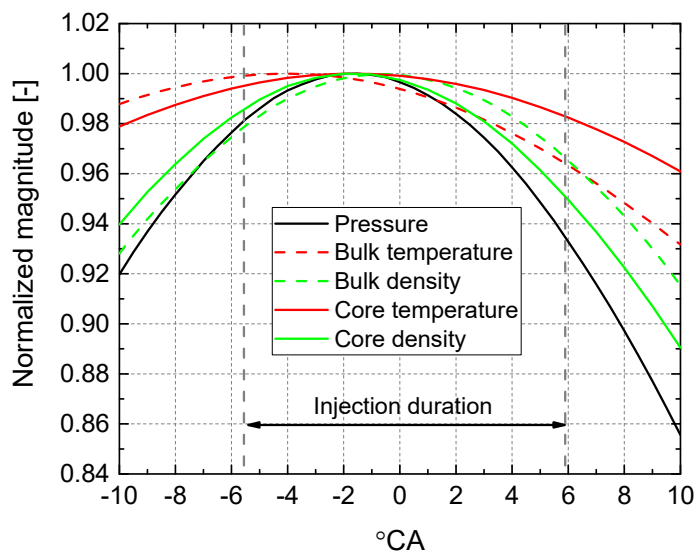


Figure 4.3 Thermodynamic conditions during fuel injection. The pressure data are taken from motored cycles in skip-fired operation. Nominal (maximum) core temperature  $T_c = 956$  K, nominal core density  $\rho_c = 21.7$  kg/m<sup>3</sup>, O<sub>2</sub> concentration 15%.

The cycle-maximum core temperature is plotted against the bulk temperature in Figure 4.4. At low-swirl and standard-density (near 22.8 kg/m<sup>3</sup>) there is a good linear correlation with a mean offset of 76 K between the core and bulk temperature. Lower temperatures have a smaller offset, while higher temperatures have a larger offset. The ambient gas composition and gas density does not exert much influence on the temperature difference. At the same bulk temperature, the datasets at high swirl show higher core temperature. According to the conclusions in Section 3.4, the core temperature calculated by isentropic compression is higher than the real core temperature, but at similar bulk temperatures, the core temperature at high swirl should be higher than that at low swirl, because of the thicker boundary layer and probably lower temperature in the squish region. Therefore, in Figure 4.4, the core temperature

for the high-swirl data should be a little lower than the current values but still generally higher than that for the low-swirl data. Here the bulk temperature is used when necessary to compare between low and high swirl; otherwise the core temperature is used to follow previous ECN studies [52, 267].

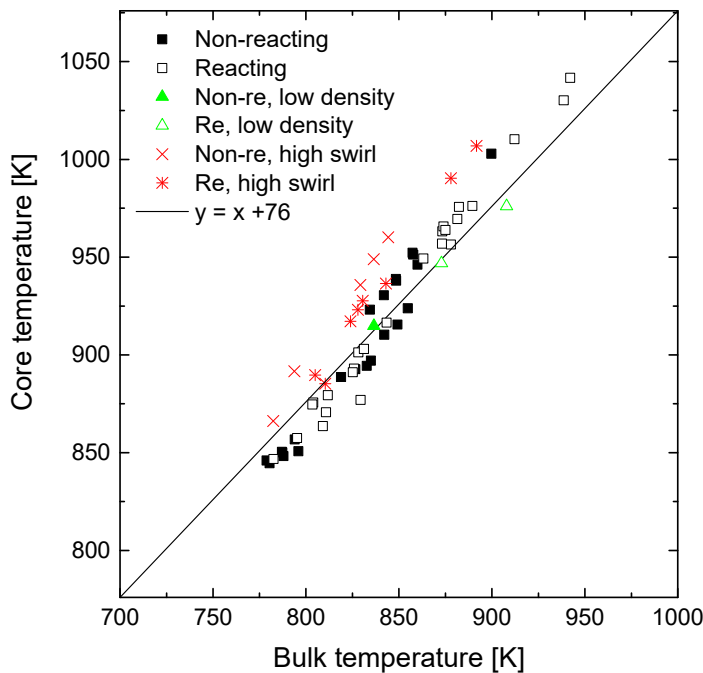


Figure 4.4 Correlation between cycle-maximum bulk temperature and core temperature. The black points represent datasets at a density around the ECN standard density ( $22.8 \text{ kg/m}^3$ ) and at low swirl. The points at high swirl are not considered reliable.

### 4.3.2 Image processing

#### Spray

A raw image taken under non-reacting conditions is shown in Figure 4.5. Compared to the region without spray, dark regions can be clearly seen around the injector showing each of the jets, indicating extinction of the LED light by the liquid-phase spray. This phenomenon is similar to that in DBI [144]. According to Equation (2.12), the optical thickness  $\tau$  here is calculated as

$$\tau = \ln \frac{\langle I_{BG} \rangle - \langle I_{dark} \rangle}{I - \langle I_{dark} \rangle} \quad (4.1)$$

where  $\langle I_{BG} \rangle$  is the average of a set of BG images (before injection, LED on),  $\langle I_{dark} \rangle$  is average of a set of dark images (before injection, LED off), and  $I$  is the spray image.

An example optical-thickness image is shown in Figure 4.5b. For liquid detection, a threshold needs to be set. In SNL's measurement by DBI [267], a threshold of 0.6 was chosen. In fact, the optical thickness depends on the droplet diameter at the spray tip, wavelength of the light source, and the camera collection angle [278]. The current ECN guideline recommends using the projected liquid volume for thresholding, which means individual thresholds of optical thickness should be set for individual experimental apparatus [45, 278]. As shown in Figure 4.6, in the fire-deck retro-reflection imaging, the incident light passes through the spray twice with a reflection in between, while DBI has a single-pass illumination, as shown in Figure 2.22. Detected light stems from both this reflection on the fire deck as well as from backward Mie scattering by the spray. Thus, the relation between optical thickness, which is dependent on the surface condition here, and liquid volume is more difficult to quantify than in conventional single-pass DBI.

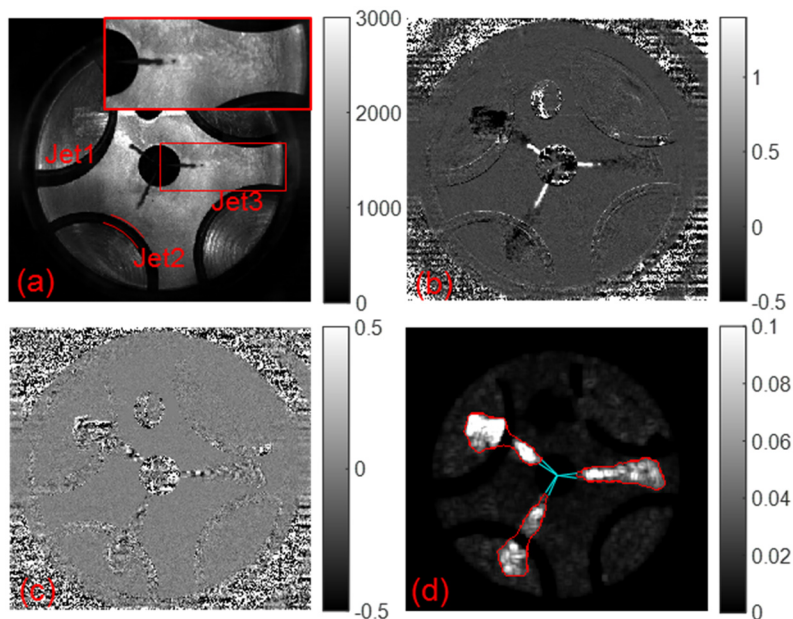


Figure 4.5 Image processing for spray detection. (a) single raw image, (b) resulting optical thickness, (c) time derivative, (d) local standard deviation.

To understand these differences better, Figure 4.7 compares the optical thickness along the spray axis in the average image during the quasi-steady period (see Figure 4.15) with DBI data from Spray A [45]. The initial negative part is due to the non-reflective region around the nozzle. The peak value is lower than that from the DBI signal, indicating more Mie-scattered light was captured. At the spray tip, from 9 to 18 mm from the nozzle exit, a region with negative optical thickness exists in the retro-reflection data, but not in the DBI measurements. This is probably because the light scattered by the droplets was also reflected back by the fire deck, resulting in a redistribution of the retro-reflected light compared to the BG image without spray. Therefore, it does not make much sense to use the same optical thickness, 0.6, as used for the SNL's measurement by DBI [267] to quantify the liquid length. Instead, here the threshold was set to yield the lowest sensitivity of liquid length to the optical thickness. A first estimate of 0.8 was obtained from Otsu's method [279] in a window around the tip of the spray and a sensitivity analysis was then performed around that initial value.

Figure 4.8a shows the results of that sensitivity study. The transient liquid length is determined from the nozzle exit (1.07 mm from the nozzle center measured in the ECN-provided solid model [45]) to the farthest point in the foreground after image segmentation. The quasi-steady liquid length in each engine cycle is calculated by averaging the transient values from 0.5 to 1.4 ms after start of injection (ASOI). The results shown here are the ensemble-average values from an example dataset (non-reacting, core temperature 911 K, core density 22.5 kg/m<sup>3</sup>, 50 cycles). With a threshold of 0.2, excessive spurious signal around the liquid spray tip was detected. All the threshold values between 0.4 and 1.2 seem reasonable choices. As an alternative, the zero-crossing point in the optical thickness of the average image during the quasi-steady period (indicated in Figure 4.7 by a red arrow) was also measured. Figure 4.8b compares the ensemble-average quasi-steady liquid length from different datasets measured by these two metrics. An approximately linear correlation with near-unity slope is seen with an offset of about 1.5 mm, increasing slightly towards longer liquid lengths. In the end, liquid length was calculated by both methods and compared with the results from ECN database, while the results from thresholding at 0.8 are used for internal comparison across different operating conditions.

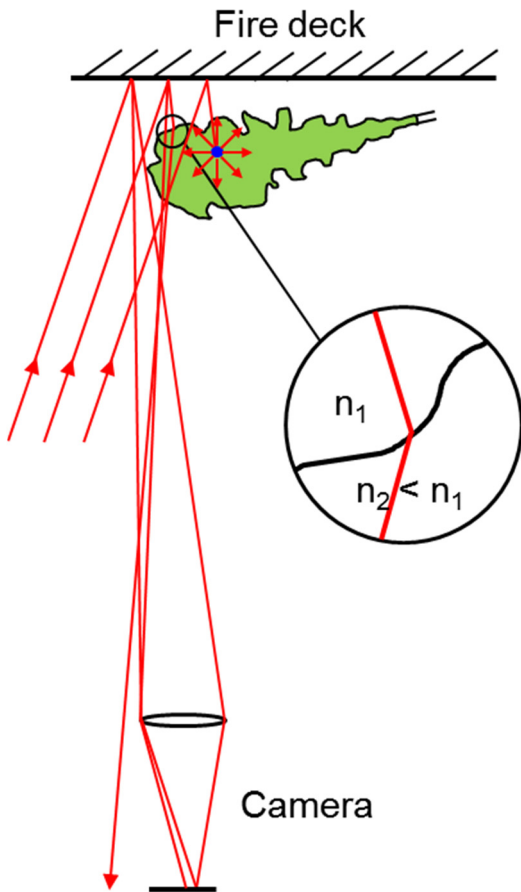


Figure 4.6 Schematic for the signal generation processes fire-deck retro-reflection (modified from [145]).

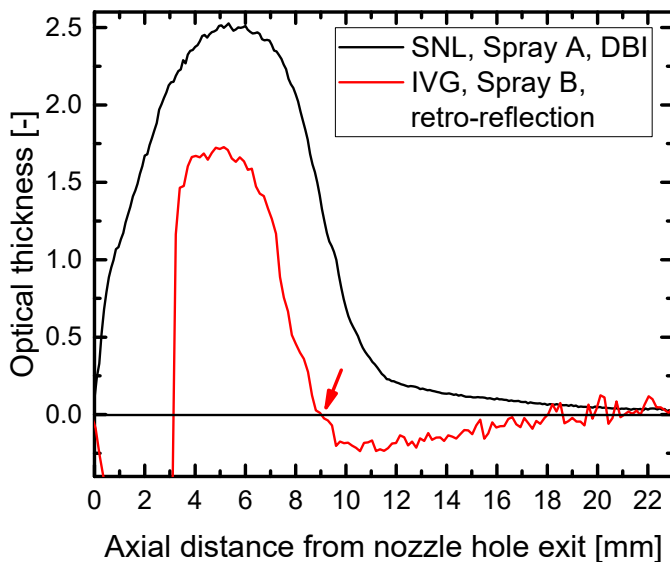


Figure 4.7 Comparison of optical thickness along the spray axis in the average image during the quasi-steady period between DBI (Spray A in SNL's CVP vessel [45]) and fire-deck retro-reflection. The red arrow indicates the zero-crossing point where the liquid length is measured.

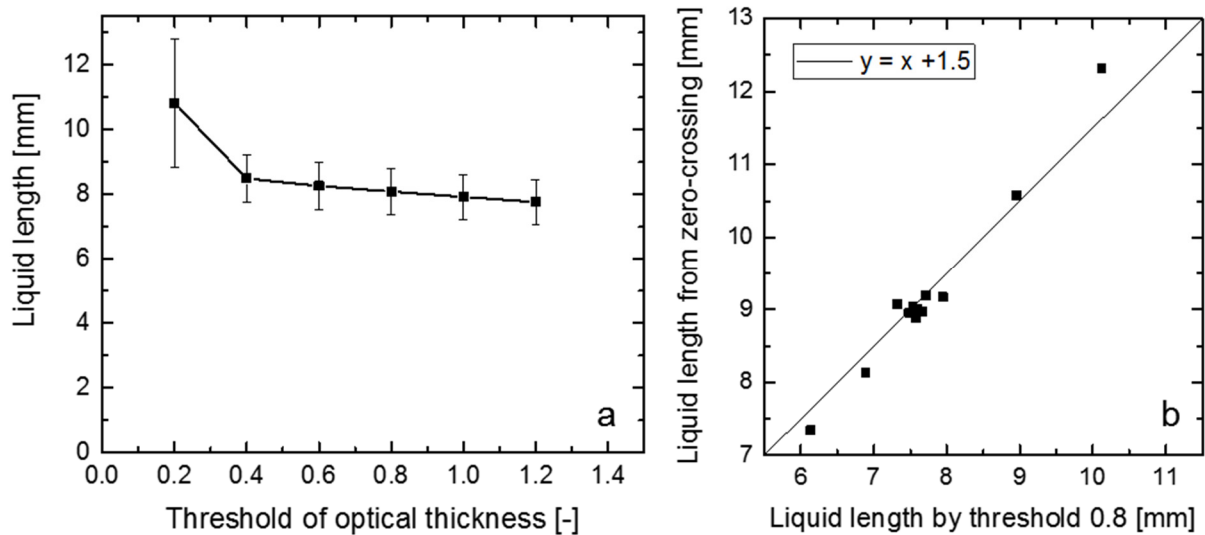


Figure 4.8 (a) Sensitivity of the ensemble-average quasi-steady liquid length to the threshold on the optical thickness used for image segmentation. The error bar indicates one standard deviation across a dataset of 50 cycles. (b) Correlation between the ensemble-average quasi-steady liquid lengths obtained by two different methods (as discussed in the text) for all non-reacting datasets.

As shown in Figure 4.5a, the gas phase of the fuel jet is characterized by a gradient field due to beam steering, similar to, but weaker than a typical schlieren signal. The beam steering in retro-reflection is illustrated in Figure 4.6. Since these gradients undergo fast temporal variation, the time derivative of the BG-normalized image series was calculated [146]. Figure 4.5c shows that the derivative images have an obvious texture where gaseous fuel is expected. This difference in texture was converted into intensity contrast by calculating the local standard deviation across a  $7 \times 7$ -pixel sliding window, with the result shown in Figure 4.5d. A  $5 \times 5$ -pixel median filter was used before and after this step to suppress the background signal (from swirl) and to lessen the contrast within the region with fuel signal. Subsequent thresholding segmented the images into a gaseous-fuel foreground and a surrounding background with low-level fluctuations, presumably due to the boundary layer on the piston window.

Again, the robustness of this segmentation method was examined by a sensitivity analysis. Different thresholds were used for different swirl ratios and different jets (jet 1, 2, or 3). At high swirl, the signal in the background is higher (due to fluctuating boundary layer), requiring higher thresholds; the non-uniform surface condition of the fire deck also makes the sensitivity different for each jet. As an example, the non-reacting jet 3 at low swirl is considered. In this particular case, a threshold of 0.024 was used. Several thresholds around this value were also applied and for each, the ensemble-average vapor penetration traces along with the standard deviation across the dataset is shown in Figure 4.9. It is seen that the variation in both penetration and standard deviation is smallest around 0.024 or perhaps 0.019. From 0.019 to 0.029, the standard deviations are less than 1 mm; at the time of the greatest standard deviation (around 0.23 ms ASOI), the ensemble-average penetration varies less than 0.25 mm. The author concludes that the method is reasonably robust. However, further automation in choosing the threshold would be desirable.

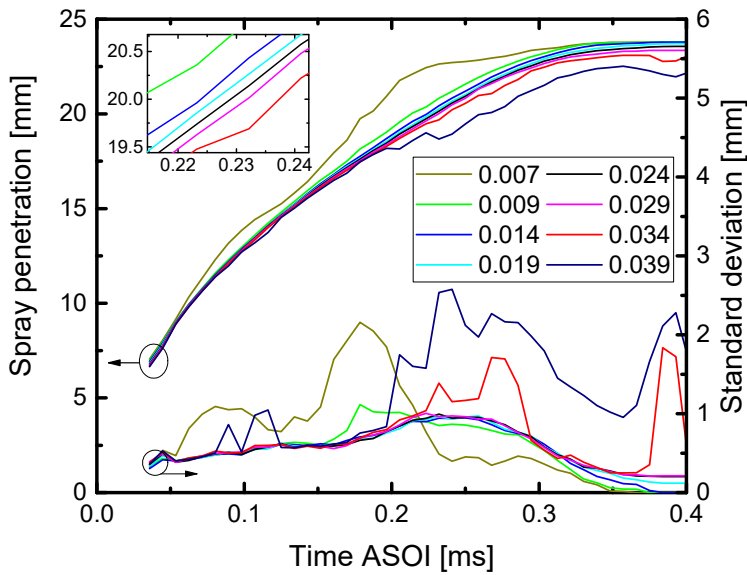


Figure 4.9 Sensitivity of the ensemble-average vapor penetration (jet 3, low swirl) and its standard deviation across the dataset to the threshold used for image segmentation. The threshold used in this work is 0.024 (black curve).

After segmentation, jets 1 and 2 often had gaps corresponding to low reflectance at the seats of the intake and exhaust valves, respectively, as indicated in Figure 4.5a for jet 2 by two red arcs. To obtain complete spray plumes, morphological closing [280] with a “disk” structure was used. The liquid phase was also added. For this, a triangle was used as a proxy for the spray from the nozzle exit to the edge of the injector bore, as indicated by the cyan lines in Figure 4.5d. Thereafter the vapor penetration and the spray dispersion angle were extracted using Siebers’s method [42]. Since the imaging direction is perpendicular to the fire deck, both liquid length and vapor penetration were corrected for the angle between the orifice axis and the fire deck (i.e., divided by  $\cos 17.5^\circ$ ), neglecting the potential effect of spray/wall interaction on the direction of jet propagation (Coanda effect) [267, 281].

### Combustion

Raw images from reacting conditions are shown in Figure 4.10. In “on” frames, mainly the spray is seen, and combustion cannot be identified. These frames were processed in the same way as in the non-reacting case. In the “off” frames, only combustion luminosity is seen. As seen in Figure 4.10a, there are mainly two kinds of noise in the “off” frames. First, there is some non-Gaussian pattern, which is probably camera reset “noise” from the last “on” frame. Since this pattern “noise” is stationary throughout the “off” frames, the average of 30 “off” images before fuel injection was subtracted. The other is the “stripe-like” patterned read-out noise (moving with time), which is typical for some high-speed cameras. To reduce this, a  $13 \times 13$ -pixel median filter was used. To segment the combustion images, a dynamic thresholding method developed in previous work at the IVG [282] was applied (run backward in time, with the free parameter  $SC = 0.2$ ). It makes use of the time correlation in the image series, automatically adjusting the threshold according to the flame luminosity. After image segmentation, the flame luminosity was calculated as the mean intensity of the region corresponding to the foreground.

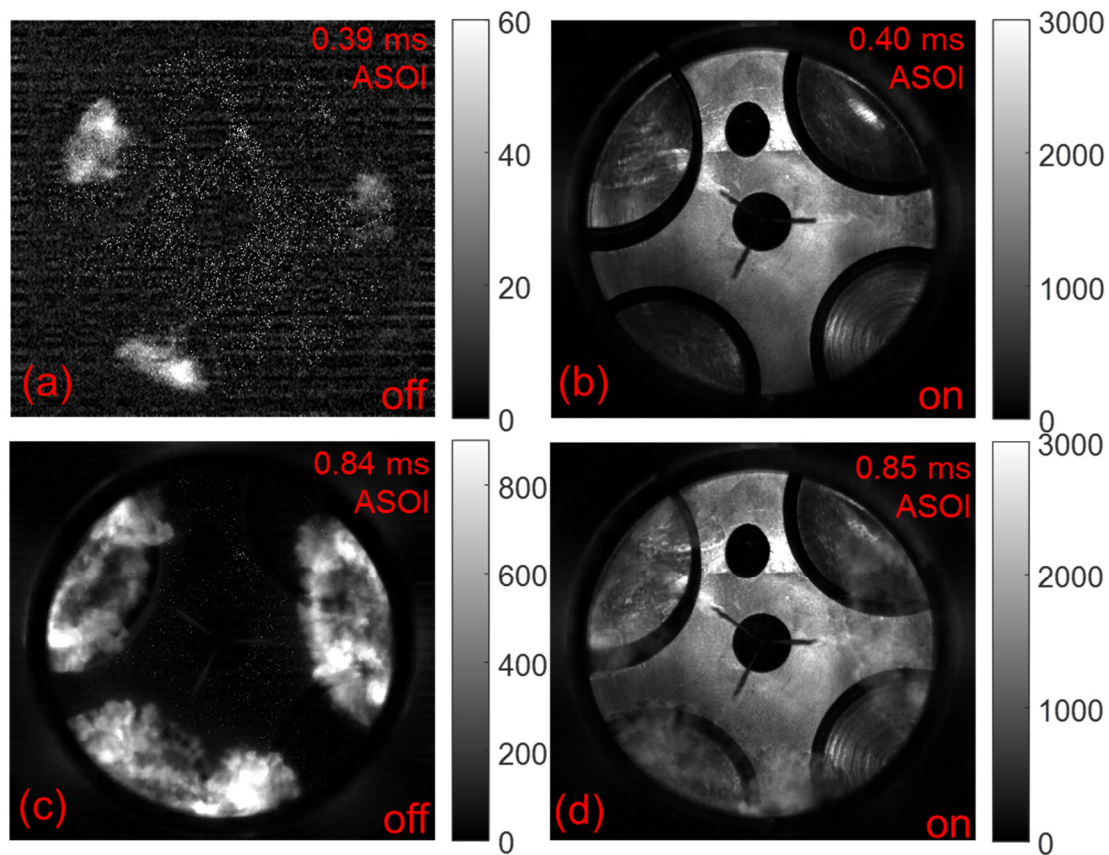


Figure 4.10 Examples of raw images taken in skip-illumination mode under reacting conditions. (a) and (b) are a pair of off/on images just after ignition, (c) and (d) are after significant wall impingement of the now burning jet.

Figure 4.11 shows examples of “on” images under reacting conditions with overlaid contours of liquid and gas-phase fuel and flame. The flame contour is from the preceding “off” frame, yielding a quasi-simultaneous segmentation of spray and combustion. 0.37 ms ASOI, ignition is detected and the ignition locations are seen relative to the fuel spray. The gas phase after spray impingement is not well captured, since fuel/air mixing decreases the temperature and density gradients, as seen here in the head of jet 3. At 0.85 ms ASOI, the flame has expanded not only radially, but also axially backward to the nozzle along the bottom of the piston bowl. This makes measuring the lift-off length with this method inaccurate.

An example of the evolution of flame luminosity and (pressure-based)  $AHRR$  is shown in Figure 4.12. It is seen that the low peak in luminosity before the main combustion event corresponds to the initial premixed-combustion heat release, and therefore probably stems from chemiluminescence. The BG filters were chosen to transmit as much as possible of this presumably blue chemiluminescence. After this peak, the later higher and wider peak of the flame luminosity trace occurs during the mixing-controlled combustion and burn-out. After the  $AHRR$  curve decreases close to zero, which means the main combustion already ended, the flame luminosity still has a relatively large magnitude and declines slowly. This indicates that after the premixed-burn peak, the flame luminosity is mostly contributed by soot luminosity [47], despite the blue Schott-glass filters. In each cycle, the optical SOC was found by thresholding such a time trace. Searching forward in time from this global ignition timing, the individual ignition timing for each jet was also determined. Since in this first jet-specific luminous SOC image, combustion already extended over many pixels (as shown in Figure 4.11), the ignition location for each

jet was estimated by calculating the luminosity-weighted mean of the pixel coordinates within the flame. If more than one flame parcel occurred at SOC, each yielded a separate ignition location.

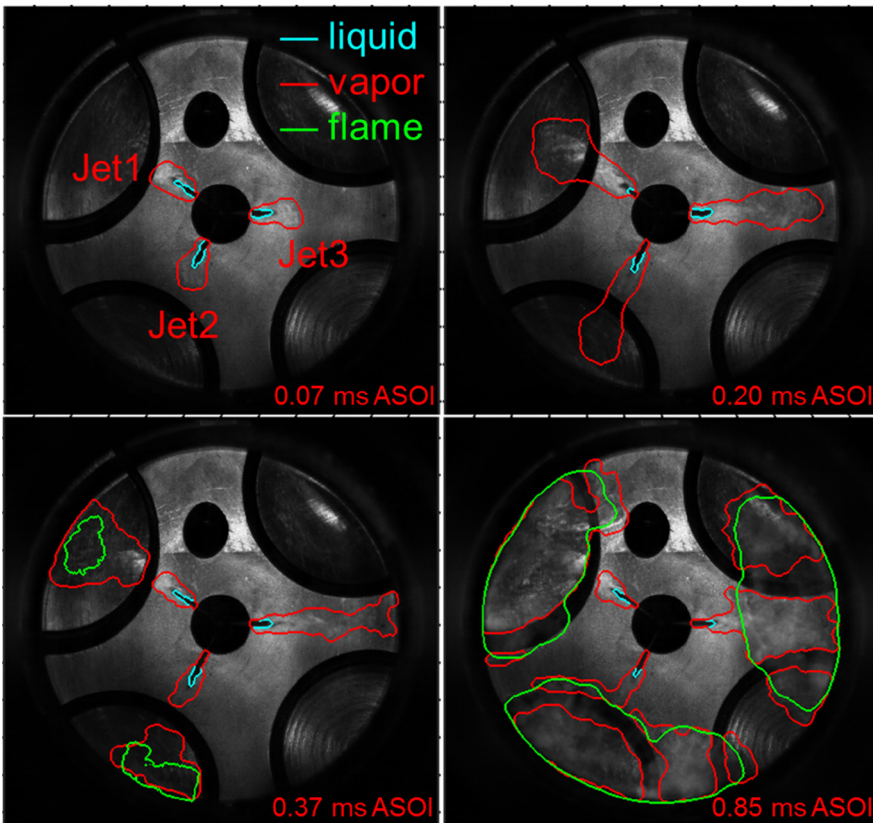


Figure 4.11 Examples of processed images under reacting conditions. Cyan – liquid, red – vapor, green – flame.

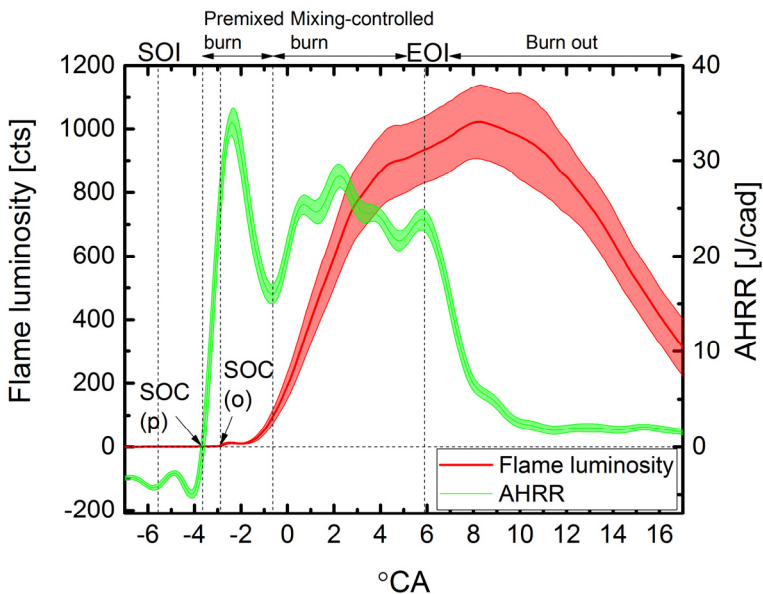


Figure 4.12 Example of flame luminosity evolution and apparent heat release rate from one dataset. The data band indicates one standard deviation.

Figure 4.13 compares the optical ignition delay with the pressure-based one. It shows an approximately linear correlation. With the pressure-based SOC detection by the first zero-crossing of *AHRR* (as introduced in Section 4.3.1), the ignition delays from the datasets with low ambient density

(targeting at  $15.2 \text{ kg/m}^3$ ), shown as red points in Figure 4.13, strongly deviate from this linear correlation. The ensemble-average  $AHRR$  from the filtered and unfiltered pressure trace from one of these datasets are shown in Figure 4.14. A low peak before the premixed combustion phase is clearly seen in both curves. The author attributes this peak not, at least not only, to an artifact from the low-pass filter, but also to a more pronounced low-temperature reaction phase with longer ignition delay compared to that at the standard ECN condition. To detect the start of the high-temperature phase as SOC in these two datasets, the point with the first positive derivative after the low-temperature peak was detected. The updated ignition delay values are shown in green in Figure 4.13 and they now fit much better into the general trend. Overall, the optical delay is on average about  $100 \mu\text{s}$  longer than the pressure-based one, and the offset is greater at longer ignition delays. The reason why the optical methods detects SOC later might be the low sensitivity of the non-intensified imaging system to the chemiluminescence signal. Here, a shorter exposure time and a smaller aperture were used compared to, for example, ignition-delay detection in Spray A [45]. The two Schott BG filters also suppress the signal. Together, this could cause a later detection of SOC. A longer optical ignition delay was also seen in CMT's non-intensified measurement, which did not employ blue filters [56]. Otherwise, the pressure-trace analysis via the  $AHRR$  might have detected the low-temperature heat release, or the  $AHRR$  was advanced by the low-pass filter [52]. However, here the low-pass filter is probably not be the only contributor (the advance by the filter here is shorter than  $0.5^\circ\text{CA}$  or  $69 \mu\text{s}$  as seen in Figure 4.14).

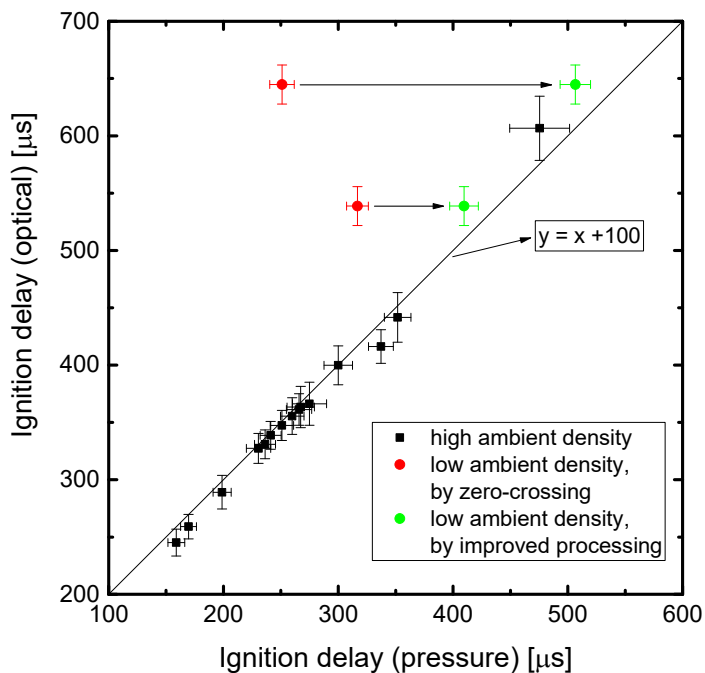


Figure 4.13 Correlation of optical versus pressure-based ignition delay for all reacting datasets. The black and red points were detected by the first zero-crossing of  $AHRR$ , while the green points were detected by the first positive derivative after the low-temperature peak of  $AHRR$ . The error bar indicates one standard deviation.

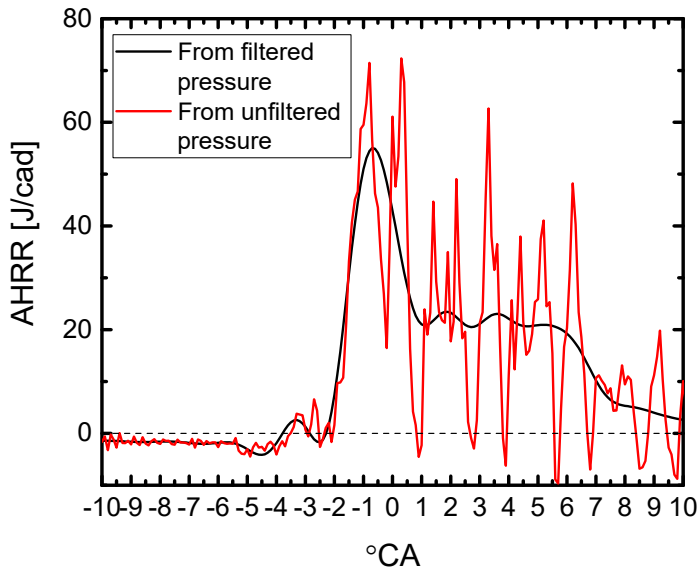


Figure 4.14 Comparison between ensemble-average AHRR from filtered and unfiltered pressure trace at low ambient density.

## 4.4 Results and discussion

### 4.4.1 Temporal evolution of spray

Figure 4.15 shows the ensemble-average liquid spray lengths at both non-reacting and reacting standard Spray B conditions. Since the ambient thermodynamic state is very similar, in the beginning the liquid length behaves also very similarly. Slightly after ignition (as determined from the optical signal), the liquid length under reacting conditions starts to decrease and the gap between the two traces grows. This may be attributed to two reasons. First, the ambient temperature increases due to combustion. Second, the scattered light from flame luminosity reduces the apparent light extinction by the spray droplets. However, the results from the SNL-CVP do not show this deviation [267], which indicates that these two phenomena affect a confined jet but not a free jet. Here, for 1500 bar, 0.5 ms to 1.4 ms ASOI was chosen for calculating the time-averaged liquid length under non-reacting conditions, the same as for Spray A [45], since the liquid length is reasonably stable during this period, instead of the shorter period (1 ms – 1.2 ms ASOI) chosen in the SNL-LBE and the CMT-SBE [52, 56], the liquid-length traces from which will be shown in Section 4.4.4. In this work, at injection pressures of 1000 bar and 500 bar, the quasi-steady period was defined as 0.5 – 1.2 ms ASOI, since the actual injection duration is shorter, 1.50 ms for 1000 bar and 1.41 ms for 500 bar.

Figure 4.16 shows the ensemble-average vapor penetration under both non-reacting and reacting conditions compared to results from a 1D jet model from Musculus and Pickett [43, 44] (see Section 2.1.4). Here, the nozzle diameter is set to 90  $\mu\text{m}$  and the spray dispersion angle is 23°, taken from the previous SNL-CVP study [267]. With this choice of parameters, both experimental traces agree well with the theoretical calculation. Near SOC, the vapor penetration under the reacting condition becomes slightly slower, which is probably due to the post-processing. The penetration measurement in the reacting case was terminated shortly before spray impingement because of window fouling near the piston bowl wall. The location of the fouling biases the ensemble average against greater penetration. Near the bowl wall, the penetration of the non-reacting spray penetrates slower than that from the 1D model. This could be also explained by the bias by the wall limitation. Another reason may be that the boundary layer near the wall or the wall itself influences the air entrainment near the jet head. After impingement at around 23 mm, the part of vapor flowing against the wall is not captured because of the

low sensitivity of the optical method. This is why the vapor penetration seemingly stabilizes after spray impingement.

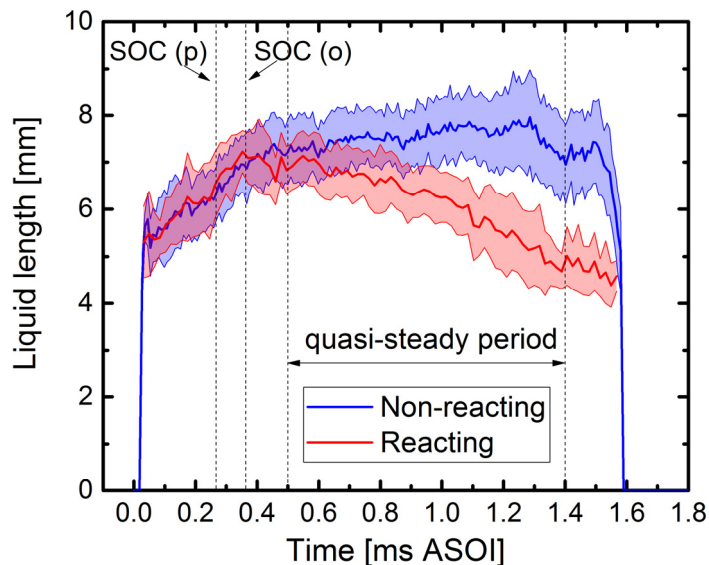


Figure 4.15 Comparison of time-resolved liquid length of jet 3 under non-reacting and reacting conditions. Non-reacting dataset:  $T_a = 943\text{ K}$ ,  $\rho_a = 21.8\text{ kg/m}^3$ , reacting dataset:  $T_a = 942\text{ K}$ ,  $\rho_a = 21.9\text{ kg/m}^3$ ,  $O_2$  concentration 16.5%. The other conditions are the same in both sets. The data band indicates one standard deviation.

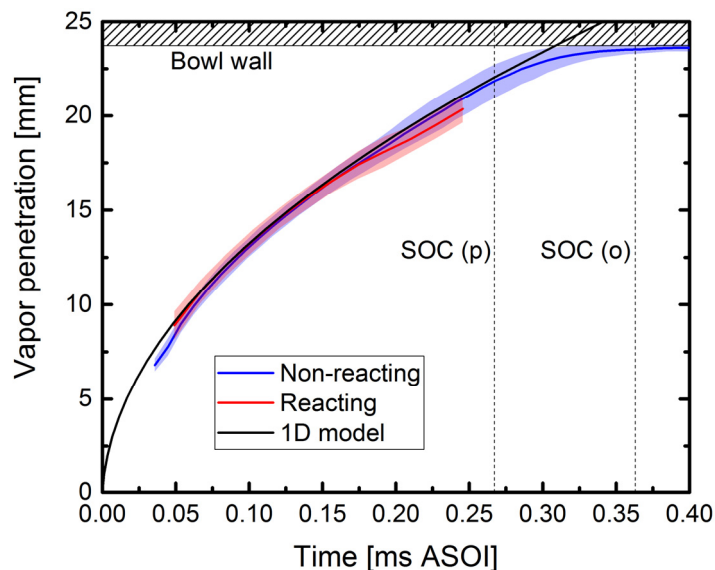


Figure 4.16 Comparison of vapor spray penetration of jet 3 between non-reacting and reacting conditions. The result from a 1D model [26-28] is also plotted, calculated by the nominal orifice diameter  $90\text{ }\mu\text{m}$  and a fixed spray dispersion angle of  $23^\circ$ . Non-reacting conditions:  $T_a = 943\text{ K}$ ,  $\rho_a = 21.8\text{ kg/m}^3$ , reacting conditions:  $T_a = 942\text{ K}$ ,  $\rho_a = 21.9\text{ kg/m}^3$ ,  $O_2$  concentration 16.5%. The data band indicates one standard deviation.

#### 4.4.2 Effect of operating conditions

##### Liquid length

As indicated by the GT-POWER results, the ECN condition is not well achieved in this work, since in an engine the thermodynamic conditions are not as easily controlled as in a combustion vessel. However, the intake temperature variation results in a variation of ambient gas temperature and density (with the same ambient pressure). Thus, here how the spray and combustion characteristics vary across these in-cylinder thermodynamic conditions is analyzed. With correlations derived in previous theoretical studies, the current results can be put in the context of trends from other facilities. Also, the effect of injection pressure and, for the first time for Spray B, that of swirl ratio are investigated.

The liquid length ( $LL$ ) can be expressed as a power law as a function of  $d_o$ ,  $C_a$ ,  $\rho_a$ ,  $T_a$ , and  $\Delta p$ , as shown in Equation (2.4). In the experiment, the in-cylinder pressure at TDC was controlled to meet the standard Spray B condition. Therefore, according to the ideal-gas law,  $\rho_a$  and  $T_a$  are inversely proportional to each other across different datasets. Since  $d_o$  and  $C_a$  are constant, at a given injection pressure, the  $LL$  is solely a power law of  $T_a$ . Taking the core temperature as the horizontal axis (as in previous studies [52, 267]), the ensemble-average  $LL$  during the quasi-steady period measured at ECN standard ambient pressure (61.5 bar) and at low swirl is shown in Figure 4.17 in logarithmic coordinates. The datasets at lower injection pressure are also included. The  $LL$  at 1500 bar injection pressure shows an approximately linear correlation with core temperature. At lower injection pressure,  $LL$  decreases slightly, which was also seen in a two-stroke optical engine [41] (non-ECN nozzle), possibly due to a different fuel temperature in the nozzle, a different  $C_a$ , or a higher liquid volume fraction detected at the same optical thickness threshold because of larger droplet size. Also, in this experiment, the time evolution of liquid length at lower injection pressure undergoes a ramp-down in the later injection phase (to be shown in Figure 4.26), which makes the quasi-steady average lower.

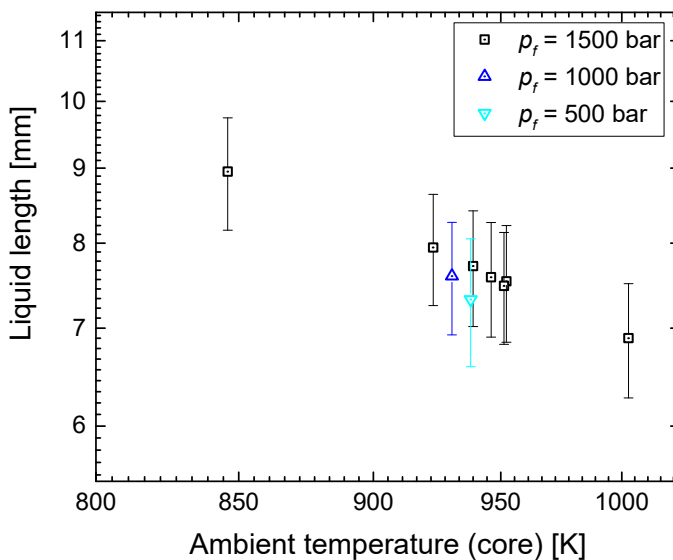


Figure 4.17 Variation of quasi-steady liquid length of jet 3 at low swirl with core ambient temperature at the same ambient pressure (61.5 bar) under non-reacting conditions. The error bar indicates one standard deviation.

At high swirl, the core temperature is unknown. Therefore, the ensemble-average  $LL$  at both swirl levels are compared against the bulk temperature shown in Figure 4.18 in logarithmic coordinates. The  $LL$  at high swirl is lower than that at low swirl. This is consistent with the findings from Chapter 3 that near the ECN standard condition the high-swirl case has a higher core temperature than the low-swirl

case at similar bulk temperatures. Also, swirl increases air entrainment, accelerating evaporation and thus decreasing the liquid length [20, 40].

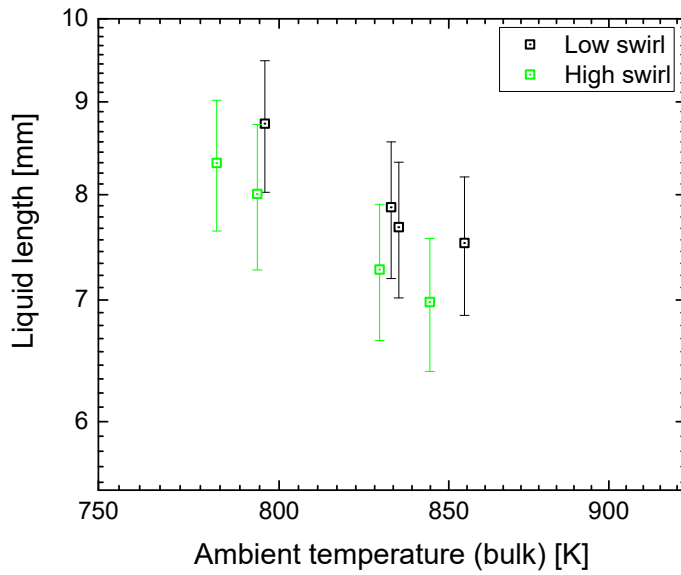


Figure 4.18 Variation of quasi-steady liquid length of jet 3 at low and high swirl with bulk ambient temperature at the same ambient pressure (61.5 bar) under non-reacting conditions.  $p_f = 1500$  bar. The error bar indicates one standard deviation.

### Vapor spray penetration

The ensemble-average vapor penetration measured at ECN standard ambient pressure (61.5 bar) is plotted in Figure 4.19 with the corresponding 1D model results. At an injection pressure of 1500 bar and low swirl, the variation in ambient gas temperature and density at TDC does not cause much difference within the piston bowl radius. In fact, from Naber's and Siebers's work [42], the ambient temperature has negligible influence on vapor penetration, while according to Equation (2.7), the correlation between penetration and ambient density in the long time limit can be rewritten as

$$s = C_v^{0.5} \cdot (2C_a)^{0.25} \cdot [a_s \cdot \tan\left(\frac{\theta}{2}\right)]^{-0.5} \cdot \Delta p^{0.25} \cdot \rho_a^{-0.25} \cdot d_o^{0.5} \cdot t^{0.5} \quad (4.2)$$

Thus, if the  $\tan(\theta/2)$  term is also considered (see Equation (2.8)),  $s$  is proportional to  $\rho_a$  to the power of  $-0.345$ . Therefore, within the density range in this measurement ( $20 - 25 \text{ kg/m}^3$ ) and the piston bowl radius, the difference in vapor penetration is very small, as can be also seen from the 1D model results. The trace at ECN Spray B condition (900 K,  $22.8 \text{ kg/m}^3$ ), if exactly achieved, should also be located in this narrow band. The penetration with high swirl follows the low-swirl traces before around 1.7 ms ASOI and afterwards starts to decrease. The author attributes this is mainly to the diagnostics. Figure 4.20 shows the time differential of the normalized intensity images, where the high-gradient regions indicate presence of fuel vapor. Shortly before impingement, the jet head on the downwind side of the swirl is convected into the upper valve seat region where the reflection of light is weak, causing low detected signal. This makes the jet head appear narrower and the post-processing algorithm terminates earlier (see Siebers's method [42]). At least from this image pair, by visual inspection penetration seems unchanged at high swirl. At 1000 bar injection pressure the penetration agrees well with the 1D model, but not at 500 bar. In the model, the velocity coefficient probably needs to be reduced at lower pressure [41] (the current coefficients are measured at 1500 bar [272]).

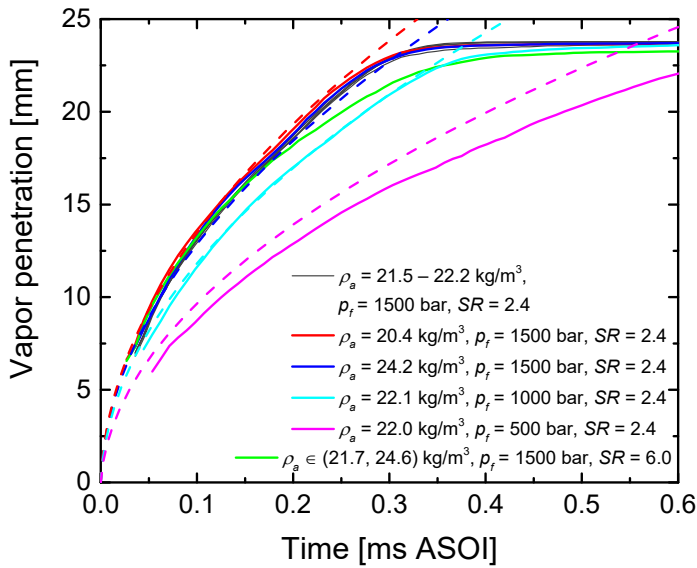


Figure 4.19 Variation of vapor penetration of jet 3 with core ambient density under the same ambient pressure (61.5 bar) under non-reacting conditions. The solid lines are from the experiment, while the dashed lines from calculation. The same color indicates the same operating condition. The 1D model [43, 44] was run with the core density of each dataset, the nominal orifice diameter  $90\ \mu\text{m}$ , and a fixed spray dispersion angle of  $23^\circ$ . The core ambient-density range for the high-swirl case is calculated from the bulk temperature and the adiabatic-core temperature (836, 949) K.

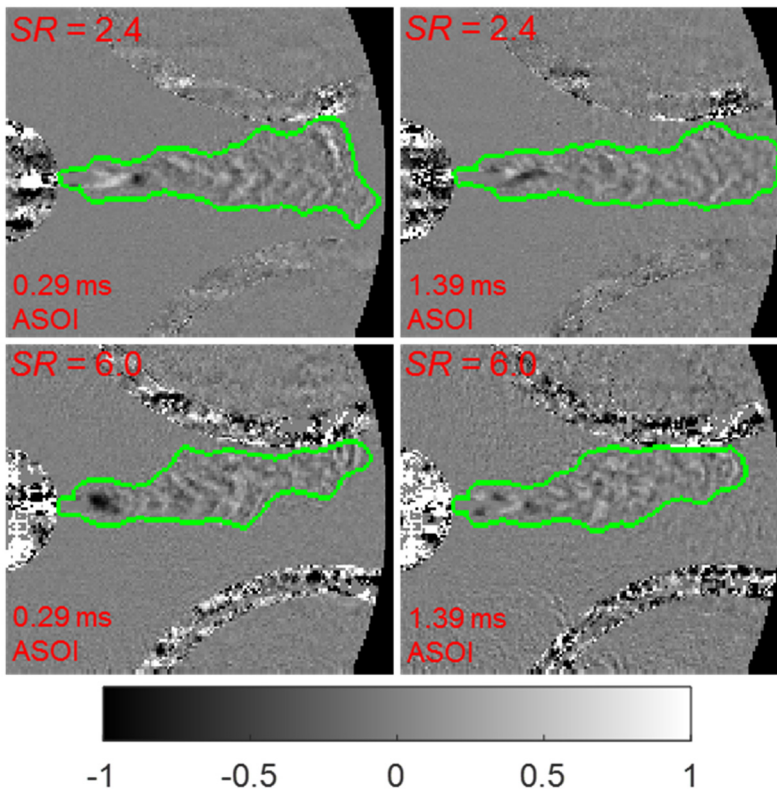


Figure 4.20 Comparison of time differential from single-shot normalized intensity images in low and high swirl under non-reacting conditions. Row 1:  $SR = 2.4$  (low swirl),  $\rho_c = 22.2\ \text{kg/m}^3$ . Row 2:  $SR = 6.0$  (high swirl),  $\rho_c \in (21.7, 24.6)\ \text{kg/m}^3$ . Both:  $p_f = 1500\ \text{bar}$ .

### Spray dispersion angle

The spray dispersion angle in the same datasets as in Figure 4.19 is plotted in Figure 4.21. Like the spray penetration, there is also not much difference among the datasets at 1500 bar injection pressure and low swirl, except for the highest-density case, which could be due to post-processing inaccuracies. Nevertheless, the trend follows the theory [42] – increasing angle with increasing ambient density. From the measured result, in the early phase of the injection (before 0.7 ms ASOI), the dispersion angle at high swirl appears the same as that near the standard ECN conditions but at low swirl. In fact, due to the diagnostic issue shown in Figure 4.20 at 0.29 ms ASOI, the measured spray dispersion angle at high swirl is not very reliable. Later in the injection, the dispersion angle at high swirl starts to overtake the results at similar conditions at low swirl. This could be related to the physical effect of swirl. As seen in Figure 4.20 at 1.39 ms ASOI, the jet at high swirl appears wider in the middle, indicating more intensive air entrainment. From theory [42], the spray dispersion angle during quasi-steady period should not change at different injection pressures. From Figure 4.21, before 0.7 ms ASOI, the spray angle increases with injection pressure, which could be simply explained by the fact that because of the lower momentum the spray at lower injection pressure needs more time to fully develop.

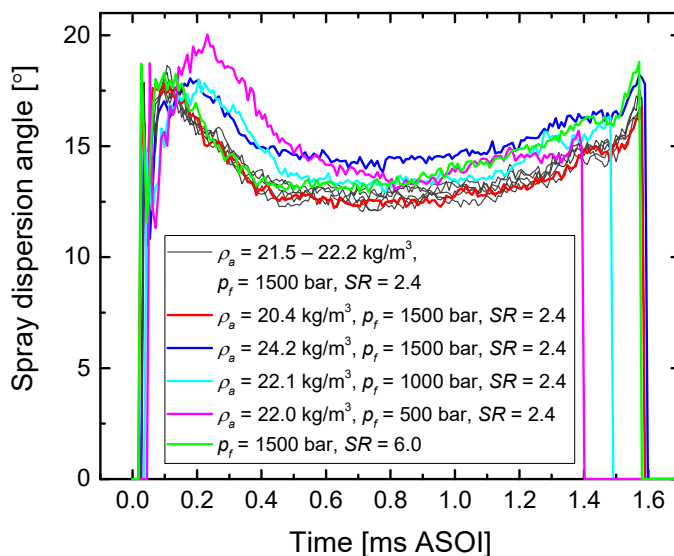


Figure 4.21 Variation of spray dispersion angle of jet 3 with core ambient density under the same ambient pressure (61.5 bar) under non-reacting conditions. For the high-swirl dataset:  $\rho_c \in (21.7, 24.6) \text{ kg/m}^3$ , calculated from the estimated core temperature range (836, 949) K.

### Ignition delay

Figure 4.22 shows the ignition delay under reacting conditions (16.5% O<sub>2</sub>) measured both with the optical and the pressure-based method against both core and bulk temperature. The optical ignition delay is the globally detected one, i.e. in any of the three jets. Under ECN-relevant conditions, higher temperature and lower density exert opposite effects on ignition delay [55]. Figure 4.22 shows that at fixed ambient pressure at TDC, the ignition delay decreases with increasing core temperature. Thus here, temperature is seen to be the dominant factor. Considering the correlation, Equation (2.9) for ignition delay under Diesel conditions, at Diesel conditions, the exponent of  $\rho_a$  is approximately  $-1.3$  and 4000 K is a reasonable choice for  $E_a/R$  according to Ref. [54]. With these values, the ambient temperature is always dominant below 3080 K at fixed ambient pressure. Lower injection pressure causes longer ignition delay, consistent with Ref. [55]. The effect of swirl on ignition delay will be discussed in Section 0 with the multi-spectral data.

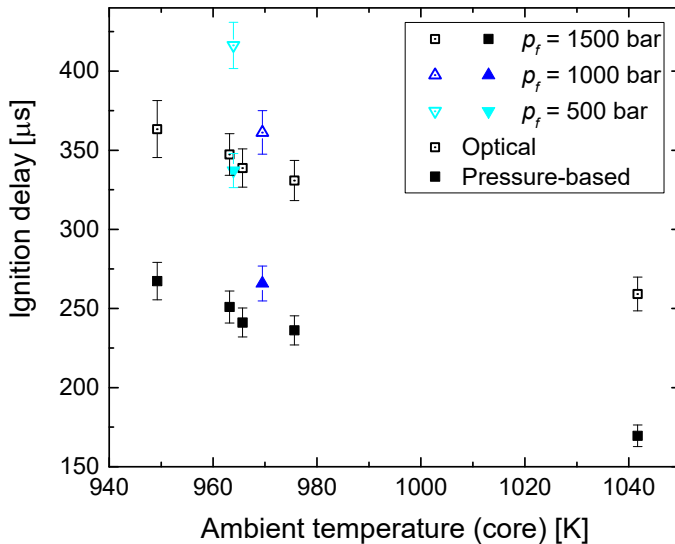


Figure 4.22 Variation of ignition delay with core ambient temperature at the same ambient pressure (59.9 bar) under reacting conditions (16.5%  $O_2$ ). The optical ignition delay is the globally detected one, i.e. in any of the three jets. The error bar indicates one standard deviation.

### Ignition location

In Figure 4.23, the ignition locations are overlaid on the average of the normalized LED-“on” intensity at SOC (optical) of the first 5 cycles (the later cycles start to suffer from excessive window fouling). For the core-temperature variation series (images a – e), with lower ambient temperature and correspondingly longer ignition delay, the ignition location moves farther downstream along the jet axis as well as in the swirl direction. In Figure 4.19 it is seen that the spray starts to impinge on the wall at around 0.35 ms ASOI. Thus, within this temperature variation, the ignition was detected optically well before impingement only for the dataset at 1042 K, but in the rest of the data (at 1500 bar) near or after that event. As discussed in Section 4.3.2, after impingement the fuel vapor is not captured well. That is why in Figure 4.23 the vapor contour appears nearly unchanged with decreasing temperature and ignition seemingly occurs outside of the jet boundary. With high swirl, ignition occurs more downwind (image f). This is also true when comparing with image a, where the ignition delay is similar. At 500 bar injection pressure, ignition occurred before impingement, while at 1000 bar, the chemiluminescence of ignition is detected nearly at the same time as the spray impingement. Generally, if ignition occurred after impingement, all the ignition sites are located near the bowl wall.

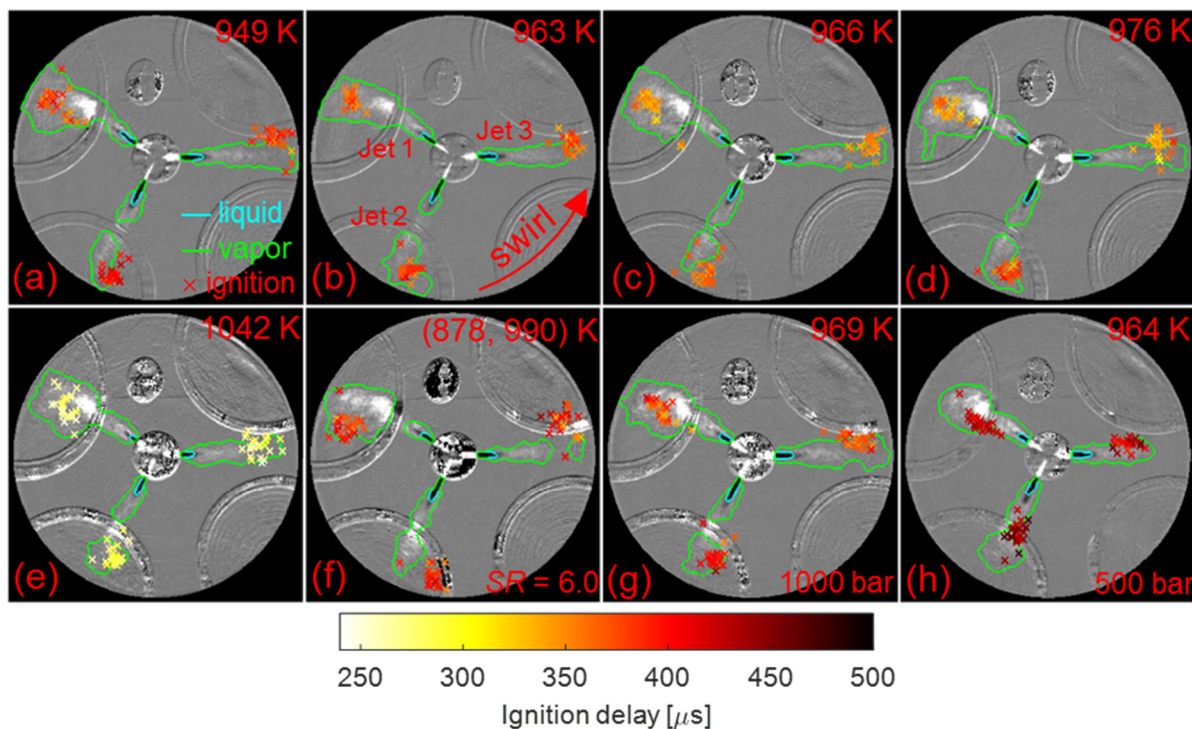


Figure 4.23 Ignition location at different core temperatures (upper right) and at the same ambient pressure (59.9 bar) under reacting conditions (16.5%  $O_2$ ). The ignition location is indicated by crosses, with the color indicating the ignition delay in the corresponding cycle. The spray is shown by the cyan (liquid) and green (vapor) contours. The background is the average image at global ignition normalized by the average image before fuel injection. In the high-swirl dataset, the core temperature is estimated to be between the bulk temperature 878 K and the adiabatic-core temperature 990 K. If not specified, the fuel injection pressure is 1500 bar and the swirl ratio  $SR$  is 2.4 (low swirl).

### Flame luminosity and AHRR

To see in more detail how swirl influences the jet flame, BG-corrected time series of LED-“off” images from two cycles at low and high swirl are shown in Figure 4.24. These two datasets are compared here since they have similar bulk temperatures. The liquid-fuel contour is from the preceding LED-“on” frame, shown in cyan, while the flame contour is shown in red. From the discussion with Figure 4.12, it is known that during the mixing-controlled combustion and burn-out phase, soot luminosity is probably the main contributor to the flame luminosity. Figure 4.24 shows that the luminosity at high swirl covers a smaller area and is concentrated in a thin layer near the bowl wall. The bulk flow moves the impinged jets further downwind and the flame plumes are obviously asymmetric against the liquid spray axis, while the upwind end of each flame plume stays nearly at the same position (as indicated by a green bar). At 0.55 ms ASOI, before the flame expands along the piston bottom, the apparent flame lift-off length of jet 3 (as far as can be told by visual inspection of these non-intensified visible-luminosity image) is longer on the windward side than on the leeward, indicated by green ovals. This asymmetry in lift-off length is much more obvious in the high-swirl cycle. This effect is also observed in the SNL-LBE with a non-ECN nozzle from  $OH^*$  chemiluminescence and  $OH$ -LIF [248], as well as in a heavy-duty engine from  $OH^*$  chemiluminescence [283]. At both swirl ratios, the jets eventually interact, but for low swirl this interaction happens earlier, as indicated by the ovals in Figure 4.24. The three bright and large soot clouds in the image at 2.45 ms ASOI at low swirl are thought to stem from the jet/jet interaction.

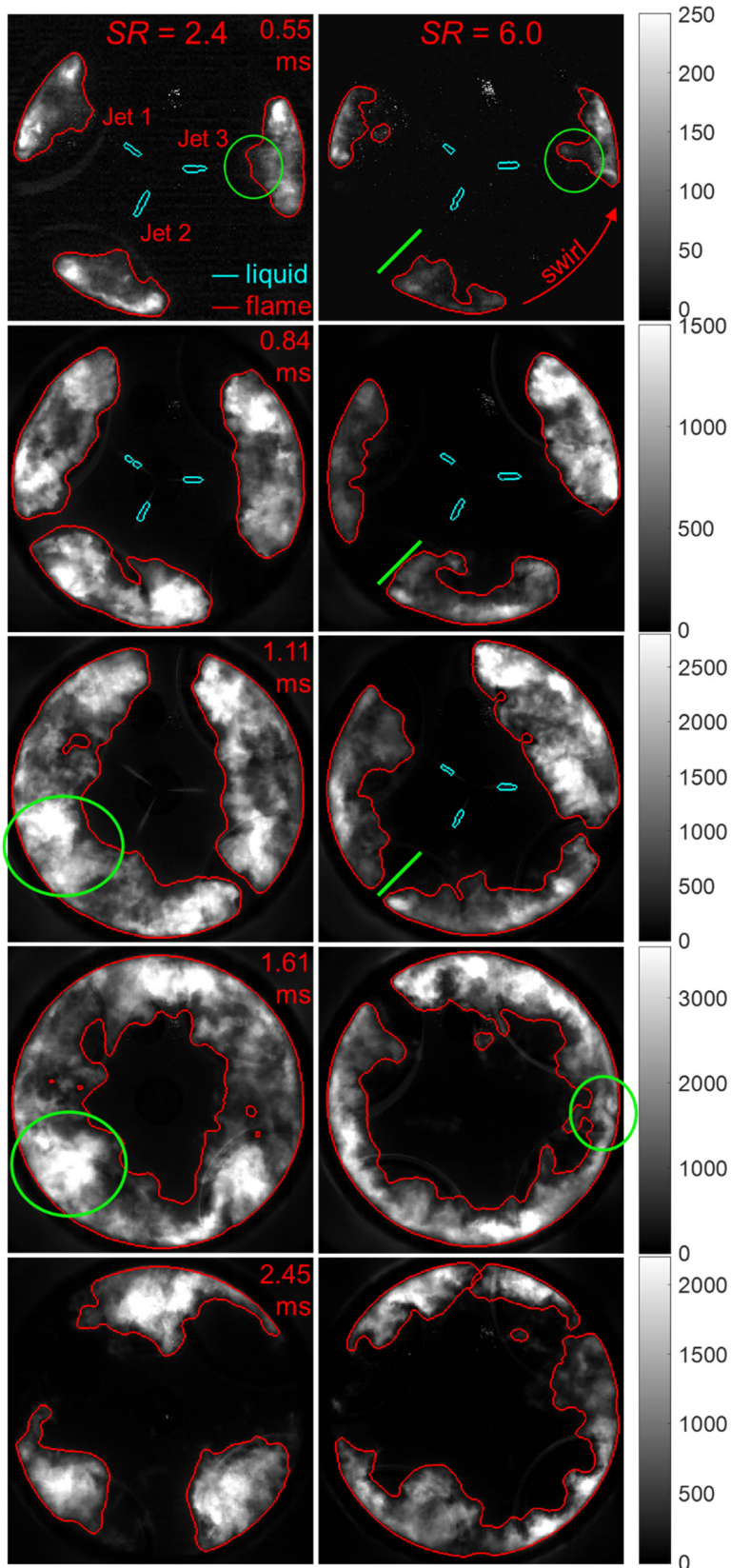


Figure 4.24 Comparison of selected images from two single cycles at low and high swirl. Column 1:  $SR = 2.4$ ,  $T_c = 963$  K,  $T_b = 873$  K. Column 2:  $SR = 6.0$ ,  $T_c$  (adiabatic core assumed) = 990 K,  $T_b = 878$  K. Both:  $p_f = 1500$  bar,  $O_2$  concentration 16.5%. The liquid fuel (from the preceding LED-“on” image) is shown in cyan contours, while the flame in red. The liquid fuel at 1.11 ms ASOI at low swirl

is not well detected but visible through the Mie-scattered light. The green labels mark features discussed in the text.

The time-resolved flame luminosity from the same datasets as in Figure 4.23 is plotted in Figure 4.25, top graph. With higher core temperature (at constant ambient pressure), the flame luminosity in the mixing-controlled burn increases. At high swirl, compared to all datasets at low swirl, the luminosity increases more slowly in the mixing-controlled combustion phase and decreases faster after reaching the peak. This could indicate slower soot production and faster soot oxidation. During most of combustion, the flame luminosity with high swirl is lower than for low swirl at similar operating conditions, except for the peak value. Considering that the flame luminosity is calculated within the flame contour, and Figure 4.24 shows the flame area with high swirl is smaller than that with low swirl, the spatially integrated flame luminosity throughout the areas at low swirl should be always lower. Since the natural soot luminosity is dependent on soot temperature and concentration [284], the high-swirl condition probably yields a lower local temperature or a lower soot amount. The latter (if true) is related to the better fuel/air mixing. Flame lift-off length was not systematically assessed here because the inward redirection of the jet flame by the walls obscures the lift-off point.

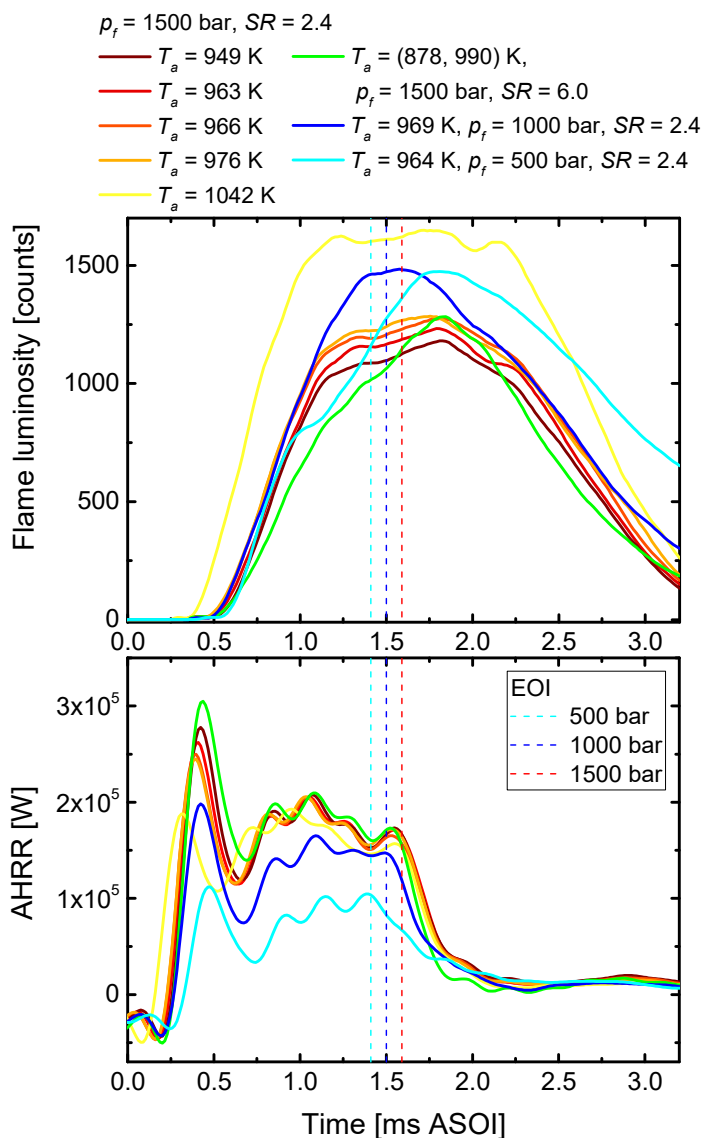


Figure 4.25 Time evolution of the ensemble-average flame luminosity (top) and AHRR (bottom) at the same ambient pressure (59.9 bar) under reacting conditions (16.5% O<sub>2</sub>). In the high-swirl dataset, the

core temperature is estimated to be between the bulk temperature of 878 K and the adiabatic-core temperature of 990 K.

The two lower injection pressures produce higher peak flame luminosities. At injection pressure of 500 bar, the flame luminosity decreases much slower than at higher injection pressure, which indicates slower soot oxidization. It also shows a “delay” period at around 1 ms ASOI, which is not seen in the other datasets and needs to be investigated further.

The *AHRR* of these datasets are plotted in the bottom graph in Figure 4.25. With higher core temperature (at constant ambient pressure), the peak of the heat release during premixed combustion shifts to earlier times and becomes lower, while the later mixing-controlled combustion phase is less influenced, and the burn-out behavior is nearly the same. The high swirl results in a higher premixed-burn peak and a larger proportion of heat release from premixed combustion, consistent with previous studies [24, 201, 285]. At similar ambient conditions, Miles [23] found the opposite trend, probably due to the difference in injection pressure (800 bar) and nozzle-orifice size (not specified, probably larger than the current one). In the burn-out phase (after end of injection, EOI), the *AHRR* with high swirl decreases faster and also to a lower level, indicating a higher soot oxidation rate [201]. With decreasing injection pressure, the *AHRR* is generally lower (because of the lower rate of injection) and shifts to later timing. Also, lower injection pressure causes a lower rate in the burn-out phase (after EOI), indicating that mixing and air entrainment are worse.

#### 4.4.3 Hole-to-hole variation

To investigate the effect of nozzle-hole parameters on the spray characteristics, the time-resolved liquid length, time-averaged liquid length (in the quasi-steady period), and vapor penetration are shown in Figure 4.26, Figure 4.27, and Figure 4.28, respectively. Two injection pressures, 1500 and 500 bar, are also compared to see the effect of fuel pressure on hole-to-hole variation. Because of the importance of the three-hole geometries, the reader may want to review Table 4.2 before this discussion.

In most of the datasets, the liquid length of jet 1 is slightly underestimated. In the underlying images, the spray tip had interference with the non-reflective valve seat, which biased the result against a greater value.

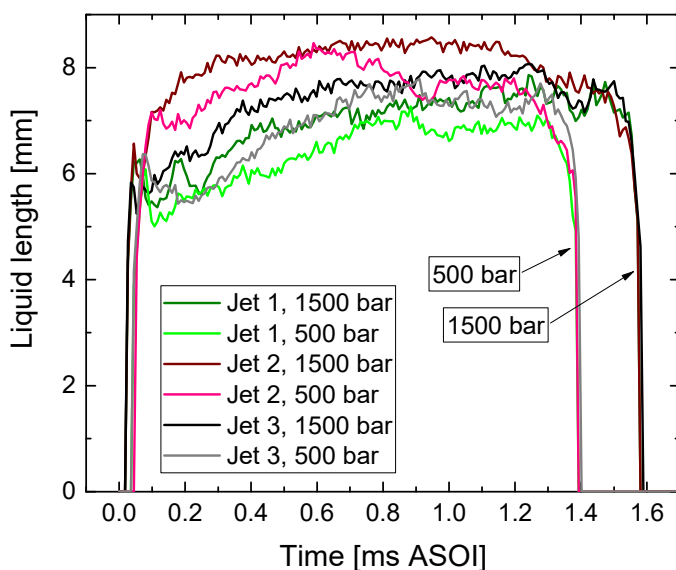


Figure 4.26 Comparison of time-resolved liquid length from different nozzle holes under non-reacting conditions. Dataset 1:  $p_f = 1500$  bar,  $T_a = 939$  K,  $\rho_a = 22.9$  kg/m<sup>3</sup>. Dataset 2:  $p_f = 500$  bar,  $T_a =$

938 K,  $\rho_a = 22.0 \text{ kg/m}^3$ . Both:  $SR = 2.4$ . The liquid length of jet 1 in dataset 1 is slightly underestimated after 0.5 ms ASOI (approximately) because of a diagnostic issue, see text.

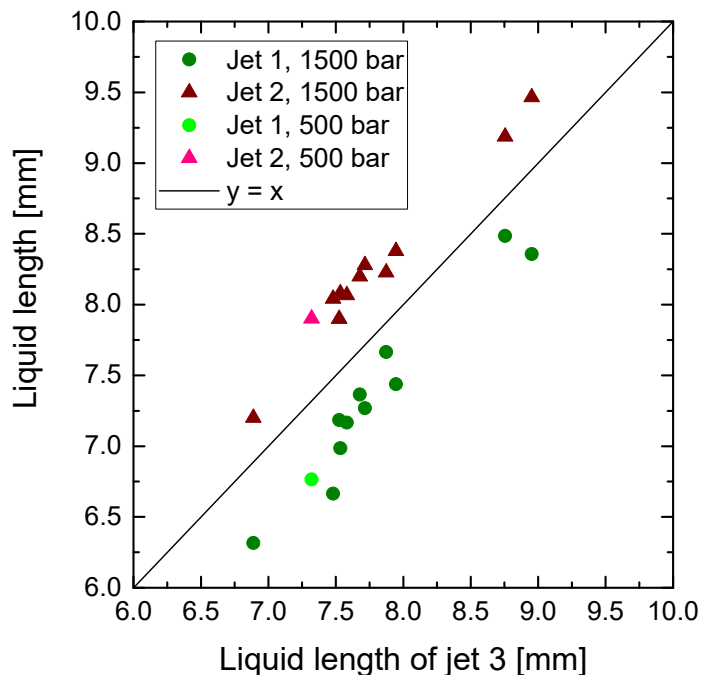


Figure 4.27 Comparison of ensemble-average liquid length during quasi-steady period from different nozzle holes under non-reacting conditions at low swirl and different injection pressures. The data points of jet 1 over 7 mm (approximately) are slightly underestimated because of a diagnostic issue, see text.

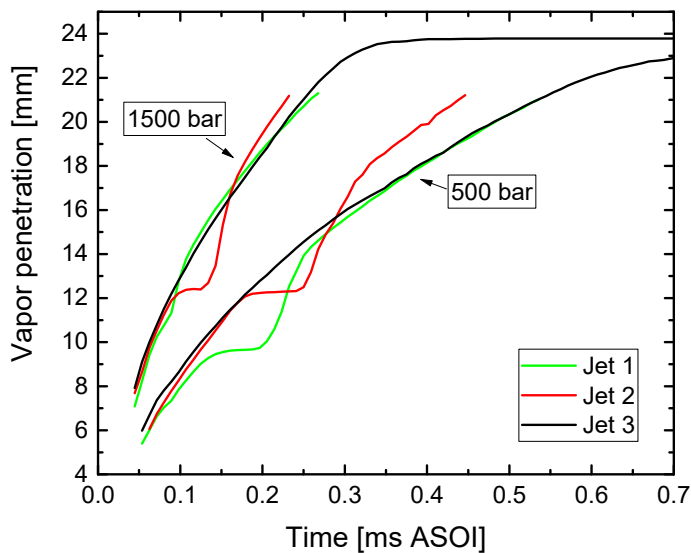


Figure 4.28 Comparison of vapor penetration from different nozzle holes at different injection pressures under non-reacting conditions. Dataset 1:  $p_f = 1500 \text{ bar}$ ,  $T_a = 939 \text{ K}$ ,  $\rho_a = 22.9 \text{ kg/m}^3$ . Dataset 2:  $p_f = 500 \text{ bar}$ ,  $T_a = 938 \text{ K}$ ,  $\rho_a = 22.0 \text{ kg/m}^3$ . Both:  $SR = 2.4$ .

First, it is easy to see that jet 2 has both the longest liquid length and vapor penetration, including the dataset at 500 bar injection pressure. Hole 3 has the largest outlet diameter (see Table 4.2), but it produces shorter liquid length and vapor penetration than jet 2. This could be due to the irregular inlet and outlet geometry of hole 3. Jung et al. [267] discussed this in comparing the liquid length from the same Spray B injector (211201) to that of Spray A, also finding that in this particular case, the outlet

diameter does not dominate liquid length. This was explained by the fact that the orifice exit of hole 3 is not perfectly round compared to the other two holes [45]. An obvious “bump” is seen. X-ray tomography also showed that the inlet radius of curvature of hole 3 has up to three times the deviation around the periphery as those of the other two holes [239]. This could influence cavitation in the orifice and also the discharge coefficient [286, 287].

The liquid length of Diesel spray usually has a ramp-up period, i.e. from SOI to the maximum level [288]. From Figure 4.26, jet 2 has the shortest duration for ramp-up, while jet 1 and 3 show similar durations to each other. This could be explained by hole 2 having the largest orifice outlet diameter and discharge coefficient. At 1500 bar injection pressure, after the ramp-up period, quasi-steady periods are seen with liquid length slightly increasing for all the three jets. At 500 bar injection pressure, after the ramp-up period, no quasi-steady period like that at 1500 bar is seen. Instead, the liquid length undergoes a ramp-down. This could be due to the cooling effect of the spray on the ambient temperature, as will be discussed in Section 4.4.4 with Figure 4.30. For both injection pressures, from 1.25 ms ASOI, the liquid length traces from different nozzle holes coincide. Interestingly, with injection pressure of 500 bar, the liquid length of all jets collapses quickly after the “convergence”, while at injection pressure of 1500 bar there is a short stagnation phase before the final quick decrease, resulting a longer injection duration.

Regarding vapor penetration, as Figure 4.28 shows, at the beginning of injection (below 13 mm penetration), jet 3 has the highest values. This is probably a diagnostic artifact. The gradients in the region of jet 3 near the nozzle appear higher than those in the regions of jet 1 and 2, which causes slightly higher penetration values after using a median filter than by visual inspection. The “recession” in jet 1 and jet 2 appears because near the valve seat, the vapor penetration cannot be captured correctly.

To investigate the effect of nozzle-hole parameters on ignition delay, a comparison of ignition delays from different jets is shown in Figure 4.29. Overall, the ignition delay of jet 2 is the longest, which is consistent with Ref. [53], with those of jet 1 and jet 3 following and very close to each other in most of the datasets. This is also true for the dataset at 500 bar injection pressure. The longer delay in jet 2 could be explained by the larger orifice outlet diameter, consistent with Ref. [54]. Again, jet 3 defies the trend probably due to the irregular orifice surface geometry [45, 239], which could intensify cavitation and turbulence, enhancing mixing and advancing SOC. The outliers indicated by the blue oval is found out possessing the lowest ambient temperatures (below 880 K) among these datasets, where the ignition delay of jet 3 is the longest among the three. This indicates that at lower ambient temperature, the orifice-surface effect might become weaker. The effect of swirl level on the hole-to-hole variation of ignition delay will be discussed in Section 0 with the multi-spectral data.

---

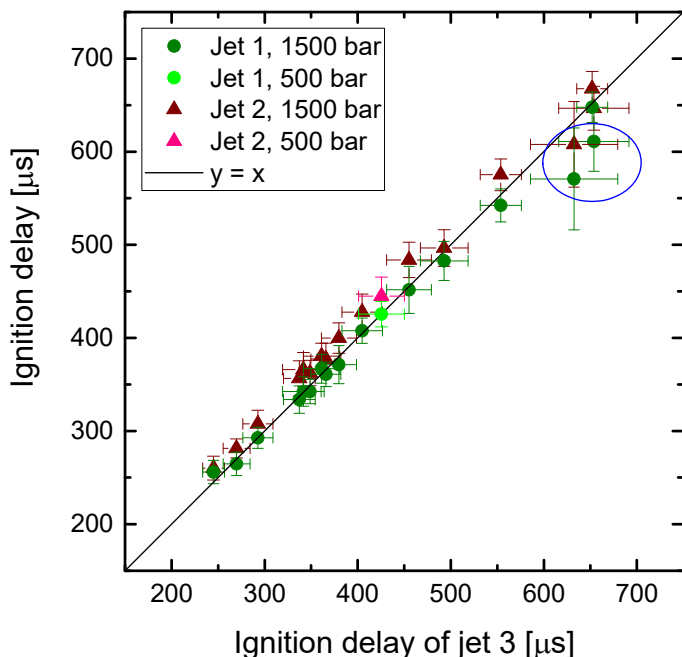


Figure 4.29 Comparison of ignition delay (optical) from different nozzle holes at low swirl and different injection pressures. The error bars represent one standard deviation within each dataset. The blue oval indicates the data points where jet 3 has the latest ignition and  $T_a$  is low.

#### 4.4.4 Comparison with the ECN database

First, the time-resolved liquid lengths are compared among different facilities, as shown in Figure 4.30. The rate-of-injection profile was measured by CMT [272]. The  $LL$  data are normalized with respect to the maximum to alleviate the influence of systematic differences in absolute operating conditions and detection methods. During the ramp-up period, all data from different facilities show a very similar transient behavior. Then, the  $LL$  from the SNL-LBE first starts to slowly decrease. At around 0.9 ms ASOI, the  $LL$  from the CMT-SBE and the SNL-CVP also start to decrease, while that from the IVG-SBE remains nearly constant until around 1.2 ms ASOI, when a sudden drop is seen, which is probably due to closing movements of the needle. In the vessel and the large-bore engine, the  $LL$  decreases more quickly in the later phase (from 0.4 ms to EOI) than in the two small-bore engines. This is probably because in a smaller combustion chamber the faster decrease of the ambient temperature compensates the uncertain physical factor that leads to the liquid-length decrease [267], since the total heat capacity of the ambient gas is lower. Looking back at Figure 4.26, the time evolution of  $LL$  in the IVG-SBE at an injection pressure of 500 bar has a similar ramp-down before EOI to the curve from the SNL-CVP, which can be also explained by this. Specifically, at lower injection pressure, the rate of injection is lower, so less heat flux for fuel evaporation is needed. Thus, the cooling effect on the ambient gas is weaker, making the evolution closer to that in a vessel. The hydraulic end of injection is different in all facilities, probably due to differences between injector drivers. The unique transient immediately after SOI in the SNL-LBE is possibly due to a different injector ramp current, a different injector temperature, or a colder pocket of ambient gas very near the nozzle, as discussed in Ref. [147] for Spray A.

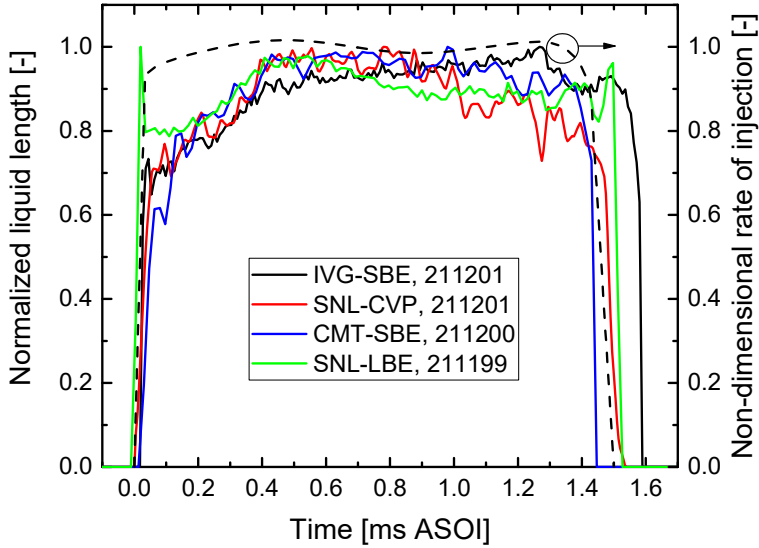


Figure 4.30 Comparison of ensemble-average time-resolved liquid length of jet 3 among different facilities under standard ECN non-reacting conditions. Data are normalized with respect to their maxima.

The ECN regulates the standard ambient gas temperature and density, but the measurement from the IVG engine did not achieve the target accurately. The  $LL$  data used here have a maximum relative error of 6.3% to the standard density. Thus, the correlation used for the data of CMT-SBE [56] is also used here. It is

$$LL_{corr} = LL_{meas} \left( \frac{\rho_{targ}}{\rho_{meas}} \right)^{-0.54} \quad (4.3)$$

The corrected data are plotted with respect to core temperature with the other Spray B data, as shown in Figure 4.31. Again, logarithmic coordinates are used, since under the assumption that Equation (2.4) holds [41], the liquid length obeys a power law against ambient temperature. Some reference lines with the exponent of  $-1.7$  obtained in Ref. [41] are also plotted here to help see the relative differences among the data series. Overall, all the data from different facilities show an approximate power law against temperature. There is a consistency existing composed of the data from the CMT-CPF, the SNL-CVP, and the IVG-SBE by the zero-crossing method for thresholding. However, no useful conclusion can be drawn, since different diagnostic methods were used among these data series. Even the results from the same diagnostic method, e.g. Mie scattering or DBI, are still sensitive to the optical set-up and threshold selection [144, 278].

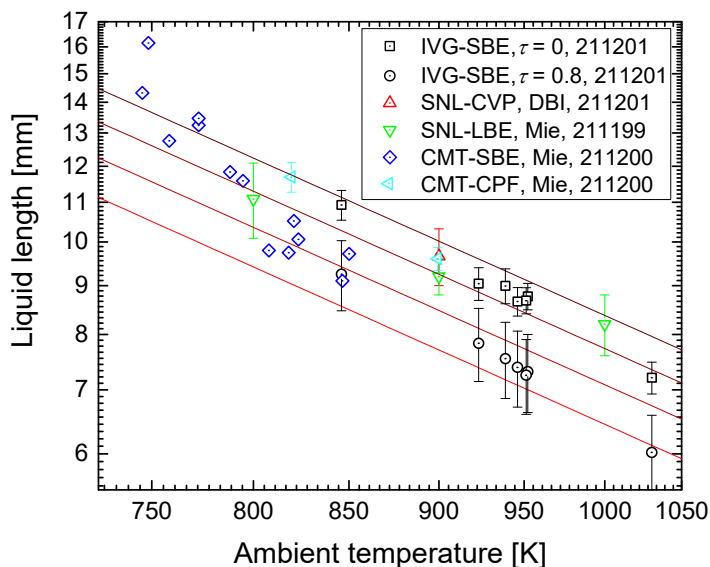


Figure 4.31 Comparison of quasi-steady liquid length of jet 3 among different facilities. The ambient density targets at  $22.8 \text{ kg/m}^3$ . Injection pressure is 1500 bar. The reference lines are obtained using the power-law component of temperature from Ref. [41]. Data points for the IVG-SBE are given for the two different LL metrics discussed in Section 4.3.2, the average of transient values thresholded at 0.8 in single-shot optical thickness images (“ $\tau = 0.8$ ”), and the distance from orifice exit to the zero-crossing point along the spray axis in the average optical thickness image (Figure 4.7, “ $\tau = 0$ ”). The error bar indicates one standard deviation.

If the thermodynamic conditions are characterized accurately, different facilities (mainly in the sense of combustion chamber size and flow field), different nozzles (injector serial numbers), and different diagnostics are the possible reasons that are responsible for data mismatch between different research groups like in Figure 4.31. The effect of different facilities is the final target to be addressed in the ECN community. The effect of different nozzles could be clarified in one single facility comparatively easily. Therefore, the different diagnostics are currently still a barrier preventing the researchers from seeing the difference caused by different facilities. DBI is very difficult to apply in an optical engine without a window in the fire deck. This makes Mie scattering a possible method to be standardized for the comparison between engines and combustion vessels, although it has a few drawbacks [144]. In addition, in Figure 4.31, the data points from combustion vessels are unfortunately not extensive enough to compare the trends with temperature among different data series. Since in engines, it is difficult to achieve the ECN target condition accurately, the author recommends that more vessel data at different ambient temperatures be contributed to the ECN database for comparison with the engine data.

The vapor spray penetration under non-reacting conditions is compared in Figure 4.32. It is seen that both the IVG-SBE and the SNL-CVP data match the 1D model [43, 44] very well, at least in the near field (within 35 mm). There is a small temporal offset between these two datasets at the ambient density of  $22.8 \text{ kg/m}^3$ , probably due to the difference in the definition of SOI. The larger deviation of the penetration in the large-bore engine to the model is partially due to the image processing method [52].

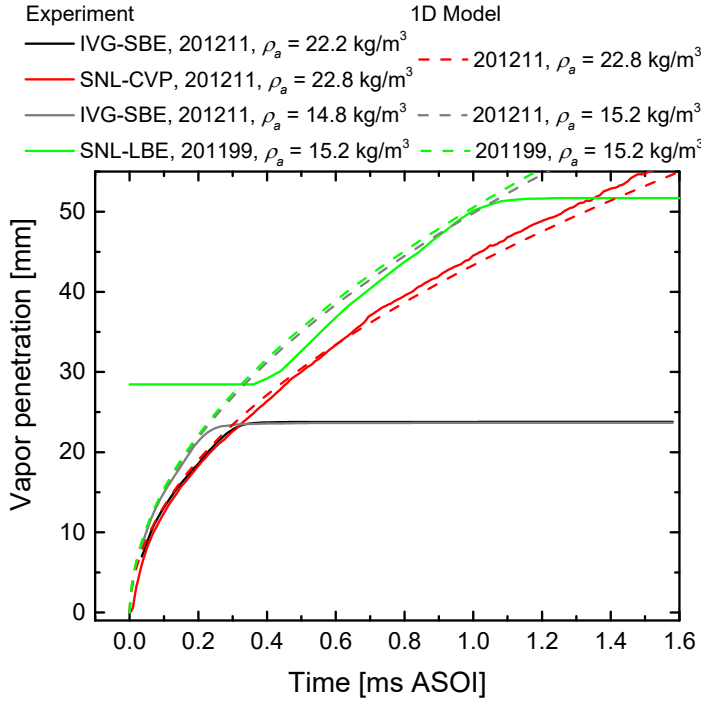


Figure 4.32 Comparison of vapor penetration of jet 3 among different facilities. The ambient temperature targets at 900 K. Injection pressure is 1500 bar. The 1D model results are calculated using the individual parameters of different injectors.

Under reacting conditions, the thermodynamic conditions achieved in this experiment are also deviated from the ECN standard like in the non-reacting case. With reference to the standard density ( $22.8 \text{ kg/m}^3$ ), the data here have a maximum relative error of 6.6%. To correct for this, the correlation from Ref. [54] is used:

$$ID_{corr} = ID_{meas} \left( \frac{\rho_{targ}}{\rho_{meas}} \right)^{-1.3} \quad (4.4)$$

This method is then also used to correct the CMT-SBE data, since the density there has a maximum relative error of 4.4%.

A simpler adaption from Equation (2.9) can be written by combining  $\rho_a$  and  $Z_{st}$  to yield

$$ID = A_{ID2} \exp\left(\frac{E_a}{RT_a}\right) \quad (4.5)$$

where  $A_{ID2}$  is a new pre-exponential constant.

Therefore, in a comparison with the ECN database, to see the variation of ignition delay versus temperature in a linear way, logarithmic spacing is used for the vertical axis and a reciprocal one for the horizontal axis, as shown in Figure 4.33. The slope of the reference lines is obtained from the linear fit to the data from the SNL-CVP, because in a vessel the thermodynamic conditions are better characterized and that data has the widest temperature range. With these reference lines, it is seen that all the data from different facilities show an approximate Arrhenius behavior, which helps to see the relative difference among the datasets.

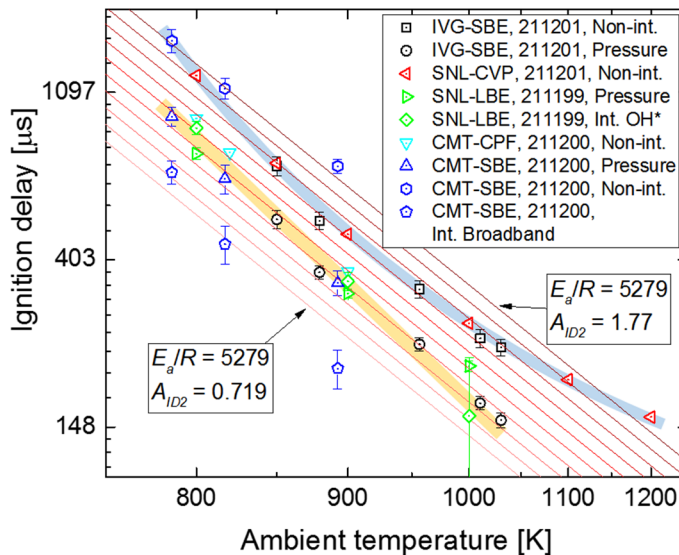


Figure 4.33 Comparison of ignition delay among different facilities. The optical method detects the signal from jet 3, while the pressure-based method detects the global ignition delay. The ambient density targets at  $22.8 \text{ kg/m}^3$ . Injection pressure is 1500 bar. The reference lines are from  $E_a/R$  (see Equation (4.5)) fitted to the SNL-CVP data and a range of  $A_{ID2}$ . The error bar indicates one standard deviation.

As discussed with Figure 4.31, different facilities, different nozzles, and different diagnostics seem to scatter the ignition-delay data a lot as well. However, two consistencies are found here. One is composed of the non-intensified broadband ignition-delay data from the SNL-CVP, the IVG-SBE, and the CMT-SBE (partially), marked by the light blue band, while the other, marked by the yellow band, contains the pressure-based data from the CMT-SBE, the IVG-SBE, and the SNL-LBE (except for the point at 1000 K, which is thought to be inaccurate due to the delay from pressure-wave propagation [52]), as well as intensified ignition-delay data (OH\*) from the SNL-LBE. The non-intensified data from the CMT-SBE are also close to this yellow band. Although there are few outliers, there is a tendency that the non-intensified data, which show longer ignition delay, are mostly located in the light blue band, while the data points based on pressure or OH\* chemiluminescence are in the yellow band. The author thinks the difference in the optical methods stems from two sources if only the high-temperature chemiluminescence is concerned here. The first lies in the sensitivity of the imaging system to combustion luminosity. That means, a different camera, exposure time, aperture, or filter would yield a different result, even if only visible light is detected. The other concern is the possibly different timing of ultraviolet (UV, mainly OH\*) vs. visible chemiluminescence (mainly CO-O continuum, CH\*, and C<sub>2</sub>\*). Therefore, the non-intensified imaging may detect SOC later. In the intensified broadband data from the CMT-SBE, the low-temperature chemiluminescence might have been detected, resulting in much earlier results. The light blue band has a curved shape, indicating the non-intensified ignition delay does not obey the Arrhenius expression of Equation (4.5). In fact, this curved shape is reasonable. At lower temperature, the optical signal becomes weaker and thus the deviation from the actual ignition delay becomes larger; at higher temperature, the absolute offset might be the same, but in logarithmic coordinates the apparent gap becomes larger.

Regarding the pressure-based method, the ignition-delay results might suffer from a low-pass filter artifact [52]. However, referring to the comparison in Ref. [52] and in Figure 4.14, pressure-trace filtering would not cause enough deviation from the results without filtering to account for the difference between the yellow and blue bands. Also, the pressure signal detects the global ignition timing, while the optical signal is only for jet 3. However, for nozzle 211201 (used in the SNL-CVP and the IVG-

SBE), jet 3 is observed to be one of the first to ignite in this work (except for at low temperature), as discussed in Section 4.4.3.

Theoretically, the possible difference caused by different facilities could be attributed to the following reasons. First, in engines the jet/wall interaction enhances fuel/air mixing [32, 33] and the swirl intensifies the air entrainment into the jet [20]. In the IVG datasets, the ignition is optically detected after spray impingement, when the ambient temperature is roughly below 950 K. In addition, to the author's knowledge, there is no heat insulation to help stabilize the nozzle temperature in any of the engines discussed here, which means the fuel temperature at the nozzle tip is influenced by heat transfer from the hot compressed gas, which could shorten ignition delay [289]. The literature shows, however, that the ignition delay is not sensitive to fuel temperature under ECN-relevant conditions [64, 290]. From the results shown here, the difference caused by different facilities could not be determined with certainty (even comparing the same nozzle), at least no large difference is seen compared to the difference from different diagnostics. Similarly, the differences caused by nozzle-to-nozzle variation are also covered by the difference caused by different diagnostics.

To compare the heat release rate ( $HRR$ ), the  $AHRR$  of the motored cycles was subtracted from the  $AHRR$  of the fired cycles. This suppresses the difference in heat transfer to the cylinder walls among different engines to some extent. The  $HRR$  in the IVG-SBE and that in the SNL-LBE are compared in Figure 4.34. Unfortunately, data from the other Spray B participants so far are not available. The pressure trace from the SNL-LBE is filtered with a cut-off frequency of 1.4 kHz, which seems too strong and in particular "smears" the rising edge forward in time. Nevertheless, it is seen that the two engines show the same trend of  $HRR$  with decreasing ambient temperature and density: the premixed-burn peak becomes higher and later, the  $HRR$  of the mixing-controlled combustion phase becomes lower, and more heat release occurs in the burn-out phase. Compared to the  $HRR$  in the large-bore engine, the results from the small-bore engine show higher premixed-burn peaks and lower levels of mixing-controlled combustion under similar conditions. The  $HRR$  traces in the burn-out phase of the two engines decrease with slopes similar to each other. However, in a combustion vessel, the spray impinging on a flat wall yielded a lower premixed-burn peak and higher mixing-controlled  $HRR$  compared to a free jet [73]. Therefore, the jet/wall interaction seems not the main factor that causes the difference in  $HRR$  between the small-bore and large-bore engine, indicating that swirl probably is more relevant, although the small-bore engine data are from the low-swirl condition. Under this assumption, at least the higher premixed-burn peak in the IVG-SBE is consistent with the  $AHRR$  behavior at higher swirl, discussed with Figure 4.25. Comparing the  $HRR$  traces at similar conditions, the integrated heat release throughout time is smaller in the small-bore engine, which might be caused by more intensive heat transfer to the walls during combustion. In the early burn-out phase, directly after EOI, there is a trend of slower  $HRR$  decrease at lower density in the large-bore engine, which cannot be seen in the small-bore engine. The cause needs further investigation.

To summarize, regarding diagnostic-sensitive metrics, e.g. liquid length and ignition delay, if assuming the ECN conditions are well achieved or deviations corrected for, mainly three sources contribute the difference in the results: the different facilities (in particular, nozzle-wall distances and flow field), different nozzles, and different diagnostics, where hole-to-hole variation also plays a role if pressure-based ignition delay is measured. The effect of different nozzles and hole-to-hole variation could be clarified in one single facility. In fact, the difference in hole parameters among the reference holes of different nozzles is of the same magnitude as the differences from hole to hole in a single nozzle [45, 272]. Therefore, the hole-to-hole variation for a single nozzle can give some estimate of the difference caused by different nozzles when comparing the results from different facilities. Thus, to finally see the difference caused by different facilities, the effect of diagnostics should be addressed first.

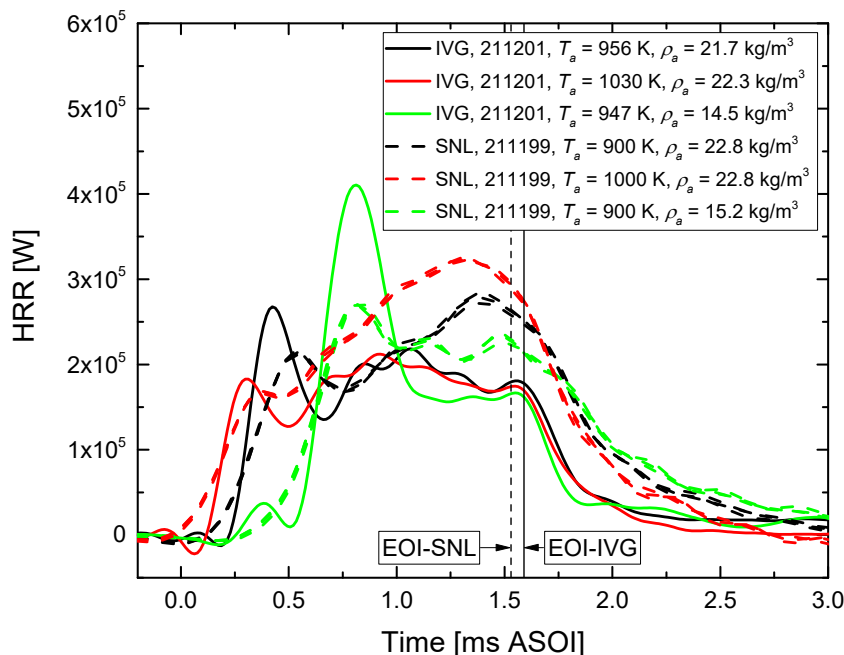


Figure 4.34 Comparison of HRR results from the SNL-LBE and from the IVG-SBE. Injection pressure is 1500 bar. There are three datasets at each operating condition from the SNL-LBE.

## 4.5 Summary and conclusions

With retro-reflection of pulsed LED light from the fire deck, spray and combustion of the ECN Spray B injector 211201 were quasi-simultaneously imaged. Using skip illumination, from the “on” frames, the optical thickness was calculated to identify the liquid phase, while the texture of the time-derivative images indicated the gas phase. From the “off” frames, the flame contour was identified by dynamic thresholding. The optical ignition delay showed a linear correlation with the pressure-based one, and the latter is systematically shorter than the former. Wide-field imaging allowed for studying the nozzle hole-to-hole variation. The lift-off length was not assessed here, since the inward redirection of the jet flame by the walls obscures the lift-off point.

Ambient temperatures and densities were varied to achieve the ECN target at constant ambient pressure. The effects of different injection pressures and swirl ratios were also investigated. The in-cylinder core temperature at TDC was calculated based on the bulk temperature at IVC from GT-POWER and isentropic compression. However, the LIF imaging in Chapter 3 indicated that the core temperature calculated for high-swirl datasets was overestimated.

### 4.5.1 Current results

Liquid length, vapor penetration, spray dispersion angle, ignition delay, flame luminosity, and heat release rate, all show physically reasonable variation with ambient temperature and density as well as with injection pressure, consistent with the empirical correlations and previous studies. At the same bulk temperature but high swirl, the liquid length is lower, consistent with the higher core temperature at high swirl found in Chapter 3. At high swirl, the jet head is observed to be more convected in the down-swirl direction, and ignition also occurs farther downwind. With decreasing core temperature (at constant ambient pressure), the ignition location is farther downstream along the jet axis as well as in the swirl direction, consistent with the longer ignition delay. With a higher swirl ratio, the flame has a lower luminosity level and smaller burning areas. The jet/jet interaction timing is also delayed. Regarding the heat release rate, the premixed-burn peak is higher and wider at high swirl and the rate

decreases faster in the burn-out phase. The effect of swirl on spray penetration and dispersion angle cannot be fully clarified in this work because of the low reflectivity at the valve seat.

Regarding hole-to-hole variation, jet 2 shows the greatest liquid length and gas penetration, even though hole 3 has the largest orifice outlet diameter. This is inconsistent with empirical correlations [41, 42] and probably due to the irregular surface geometry of hole 3. This could also explain that jet 3 ignites at nearly the same time as jet 1 and before jet 2, except for at low temperature.

Comparing the current results to Spray B data from vessels and other engines, it is found that all show a similar ramp-up phase in the time-resolved liquid length, while the ramp-down is different. The data from the combustion vessel show an earlier ramp-down, while the small-bore engines show later ones. The vapor penetration measured here matches well with the data from the Sandia's vessel. The 1D model from Ref. [43, 44] appears to be a good reference for comparison. Compared to the *HRR* in the large-bore engine, the results from the small-bore engine show higher premixed-burn peaks and lower levels of mixing-controlled combustion under similar conditions. Regarding ignition delay, two broad trends are found, depending on the diagnostics used to determine the start of high-temperature combustion. One is non-intensified visible-chemiluminescence imaging, and the other is pressure-based analysis and intensified UV-chemiluminescence ( $\text{OH}^*$ ) imaging. The difference from different facilities (in chamber size and flow field) cannot be clarified here, because it is mixed with the differences in diagnostics and nozzles (injector number). However, the influence of different nozzles could be estimated from the difference between the holes in a single nozzle. This barrier by diagnostics also applies to the comparison of time-averaged liquid length.

#### 4.5.2 Future work

A diagnostic for imaging the fuel vapor with higher sensitivity than the current method needs to be developed, so as to investigate the effect of swirl on spray penetration and dispersion angle, as well as to detect the fuel vapor after spray impingement. To improve the comparison of liquid length with that in the ECN database, Mie-scattering measurements should be performed systematically with carefully selected thresholds. The zero-crossing points of optical thickness by the fire-deck retro-reflection method can be investigated further for liquid-length quantification. The lift-off length is a very important combustion indicator and should be investigated by additional diagnostics. The nominal orifice orientation ( $72.5^\circ$  to the injector axis) of the Spray B injector was used to correct the effect of non-vertical camera viewing angle. Considering that the Coanda effect could deflect the spray axis in an engine [267, 281] and the real orifice orientation to the injector axis of hole 3 is  $1.25^\circ$  less than the nominal one [239], the real spray axis with respect to the fire deck surface should be measured in the engine.

To the ECN community, the author recommends more liquid-length data at different ambient temperatures to be measured in combustion vessels for comparison with engine data, especially by Mie scattering, since in the latter it is hard to achieve an absolute target temperature. Regarding the diagnostic-sensitive metrics for both spray and combustion, the effect of different diagnostic methods as well as that of different nozzles should be clarified first in a vessel. Thereafter, a consistent method should be used in different facilities, over an agreed-on temperature variation, so as to investigate the effect of the facility (chamber size and flow field).

To clarify the effect of sensitivity of the imaging system as well as the possible difference between UV- and visible-light-based ignition-delay measurements, simultaneous intensified  $\text{OH}^*$  and non-intensified broadband imaging is a good solution. This investigation will be shown in the following chapter.

---

## Chapter 5 Multi-spectral high-speed imaging of Spray B

---

The content of this chapter has been or is to be presented or published in:

ECN Workshop 6.8, 2019, oral presentation “Effect of diagnostics on ignition delay measurements for ECN Spray B”.

Zhao, M. and Kaiser, S., “Multi-spectral high-speed imaging of ignition in Diesel combustion in a light-duty compression-ignition engine,” to be submitted to SAE Int. J. Engines, 2020 (manuscript finished).

### 5.1 Introduction

In Section 4.4.4, the ignition delay data from different facilities across the ECN was compared (Figure 4.33). Two data trends were found, differentiated by the diagnostics used. One is composed of the data from non-intensified broadband imaging, while the other contains the data based on pressure-trace analysis as well as those from intensified imaging of OH\*. Although there are few outliers, there is a tendency that the non-intensified imaging yields longer delays than the other two methods. Two sources may contribute to this. The first could be the sensitivity of the imaging system. That is, a different camera, exposure time, aperture, or filter may yield a different result, even if only visible light is detected. The second is the possibly different timing of UV (mainly OH\*) vs. visible-light chemiluminescence (mainly from CO and CO<sub>2</sub> formation, as well as CH\* and C<sub>2</sub>\*). Therefore, the effect of diagnostics on ignition-delay measurement needs to be addressed before the effect of facilities and nozzles can be sorted out.

From the literature, it is not clear which species occurs first in conventional CI of Diesel-like fuels, OH\* or CH\* [47, 154, 291-293]. The issue might lie in the difference between low-temperature and high-temperature ignition. Also, band-pass-filtered imaging is different from baseline-corrected spectroscopy. The former might capture radicals other than OH\* or CH\* (e.g. CHO\* in the case of OH\* [294]). Regarding pressure-trace analysis, Srna et al. [156, 295] recently performed optical investigations on n-dodecane pilot-ignited lean-premixed natural-gas combustion in a rapid compression-expansion machine. Both 2D band-pass OH\* chemiluminescence and 1D flame spectroscopy showed that the *HRR* increases earlier than the OH\* signal, even in pure pilot-injection cases. This is inconsistent with the results from Spray B shown in Figure 4.33. From spectroscopy in conventional Diesel combustion in an optical engine, Klein-Douwel et al. [293] found that *HRR* increases slightly earlier than both CH\* and OH\* signals.

Here, the idea is to *simultaneously* implement the diagnostics that are the basis for the two trends in Figure 4.33. A monochrome intensified camera detects band-pass-filtered OH\* chemiluminescence, while a color camera images visible-light flame luminosity. The temporal evolution of images in different spectral channels is compared with pressure-trace analysis. In addition, imaging systems with higher sensitivity to OH\* chemiluminescence and the broadband visible signal are used to see if higher sensitivity temporally advances the detection of SOC. Finally, since more ignition-delay data are obtained in this experiment, the effects of swirl on ignition delay and its hole-to-hole variation are investigated, continuing Section 4.4.2 and Section 4.4.3, respectively.

### 5.2 Experimental apparatus and conditions

The engine parameters can be found in Table 3.1. Here, a piston crown with a full-metal rim and the ECN Spray B injector 211201 were used. The operating conditions are listed in Table 5.1. Compared to Table 4.3, only the standard Spray B reacting condition was used. A series of intake temperature was investigated to achieve a TDC temperature variation that is favorable for comparison with the ECN

---

database. The swirl ratio was varied. To investigate the effect of diagnostics on the detection of SOC (Section 5.4.1 to Section 5.4.5), only the low-swirl data are used. The high swirl data are used then to understand the effect of swirl level on the ignition delay and ignition location, as well as the hole-to-hole variation of ignition delay at high swirl (Section 5.4.6 to Section 0).

Table 5.1 Engine operating conditions for Spray B measurements by multi-spectral imaging.

Engine speed	1200 rpm
Swirl ratio at max. piston speed during intake	2.4, 6.0
Coolant and oil temperature	85 °C
Fuel	n-dodecane
Fuel rail pressure	1500 bar
Start of injection	-5.56°CA (from image)
Intake O <sub>2</sub> vol.% (N <sub>2</sub> + O <sub>2</sub> )	15%
Duration of injection	1.59 ms, 11.5°CA (from image)
Injection quantity	11.3 mg
Target temperature at TDC	900 K
Target density at TDC	22.8 kg/m <sup>3</sup>
Intake temperature	30 – 130 °C
Skip-fire mode	1 (fired) / 5 (motored)

Figure 5.1 shows the optical arrangement for high-speed imaging with the main parameters listed in Table 5.2. The FOV, which is the piston bowl area, is shown in the upper left. The flame luminosity was first reflected by the Bowditch mirror, and then spectrally separated by a 45° high-reflective (HR) mirror with an edge wavelength of 308 nm. The reflected light was detected through a band-pass filter centered at 312 nm on a monochrome high-speed camera (Photron SA-Z) with an intensifier (LaVision IRO). The combination of the beam splitter and the band-pass filter suppressed the visible light by an optical density of over 5 (measured with a spectrophotometer). The transmitted light was detected by an RGB color camera (Phantom v1612). A 2-mm BG-23 filter was used here to suppress some of the yellow-red soot luminosity. This way, combustion was imaged simultaneously in four color channels, UV, red, green, and blue. Therefore, we designate this method as multi-spectral imaging, although crosstalk between the color channels might exist (to be shown in Figure 5.3).

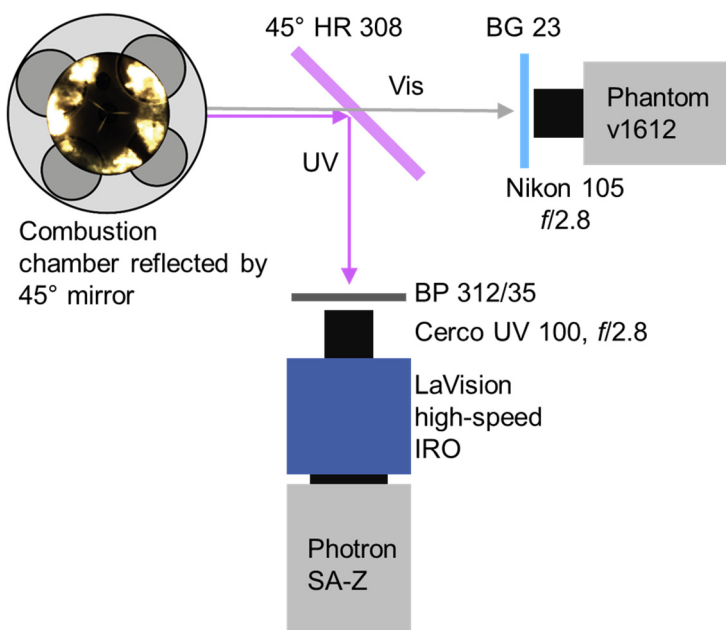


Figure 5.1 Schematic of optics for multi-spectral imaging and FOV.

One might think that with higher sensitivity of the imaging system, SOC would be detected earlier. To investigate if such an effect is significant, also single-camera systems with different sensitivities were compared. For OH\* chemiluminescence, the intensifier gain was increased. This system is designated “high-gain OH\*” here. For visible chemiluminescence, since the maximum exposure time at the given frame rate is already used, an intensifier is used to increase the sensitivity. To eliminate the UV signal and suppress soot luminosity, a combination of GG-375 and BG-28 filters, each 3 mm thick, are used. This system is designated “intensified visible”. The parameters for the three imaging systems above as well as that used in Chapter 4 (here designated as “monochrome” because they use the monochrome camera) are summarized in Table 5.2. In the monochrome system, 1/1 LED skip-illumination was used, such that the “off” frame rate for ignition imaging is 56 kHz.

Table 5.2 Imaging parameters for multi-spectral imaging.

Imaging method	Multi-spectral – RGB	Multi-spectral – UV	High-gain OH*	Intensified visible	Monochrome
Lens	Nikon 105 mm <i>f</i> /2.8	Cerco UV 100 mm <i>f</i> /2.8	LaVision UV 85 mm <i>f</i> /2.8	LaVision UV 85 mm <i>f</i> /2.8	Tokina 100 mm <i>f</i> /2.8
Filters	2-mm BG-23	BP 312/35	BP 312/35	3-mm BG-28 + 3-mm GG-375	3-mm BG-28 + 2-mm BG-23
Camera	Phantom v1612	Photron SA-Z + IRO	Photron SA-Z + IRO	Photron SA-Z + IRO	Photron SA-Z
Imaging trigger	–15°C A		–45.5°C A	–45.5°C A	–10.5°C A
Frame rate	49 kHz		56 kHz	56 kHz	112 kHz (1/1 skip illumination)
Projected pixel size	0.11 mm/pixel	0.10 mm/pixel	0.12 mm/pixel	0.12 mm/pixel	0.15 mm/pixel
Exposure time / Gate	19.4 μs (2 μs)	17.7 μs	14 μs	14 μs	7.5 μs
Intensifier gain (in DaVis software)	N.A.	49	80	70	N.A.
Recorded cycles per dataset	25				

It is useful to evaluate the overall quantum efficiency  $QE$  of the imaging system across the spectrum. The transmittances of the filters and quantum efficiencies of the camera and the intensifier photo cathode are plotted in Figure 5.2. The transmittances of the filters and lenses were measured by a spectrophotometer, while the quantum efficiencies were given by the camera manufacturers. The fused silica piston glass (UV quality SQ0) [296] and the Bowditch mirror (UV-enhanced aluminum coating) [297] are not taken into account, since their transmittance and reflectance, respectively, vary little across the wavelength range of interest here. The overall quantum efficiencies of each color channel – excluding geometric collection efficiencies – are plotted in Figure 5.3. It is seen that the UV channel from 270 nm to 340 nm is well separated from the RGB channels that have significant crosstalk between each other. The blue channel is expected to mainly capture the chemiluminescence from CH\* and broadband CO-O continuum, but also some soot radiation, while the reverse is true for the red channel, and the green channel detects both. Beyond 590 nm the BG-23 filter strongly suppresses the red response. The absolute efficiency of the UV channel is not useful for direct comparison of the absolute signal with the RGB channels, since the signal will be amplified by the intensifier.

Similarly, the overall quantum efficiencies of the intensified visible and the monochrome imaging system (used in Chapter 4) are also plotted in Figure 5.4. Both systems collect light from around 375 nm

to 525 nm, which is determined by the transmission characteristics of the blue Schott-glass filters in each detection train (“blue-biased” visible light). The  $QE$  of the intensified visible system is lower because the  $QE$  of the photo cathode is lower than that of the CMOS sensor (see Figure 5.2).

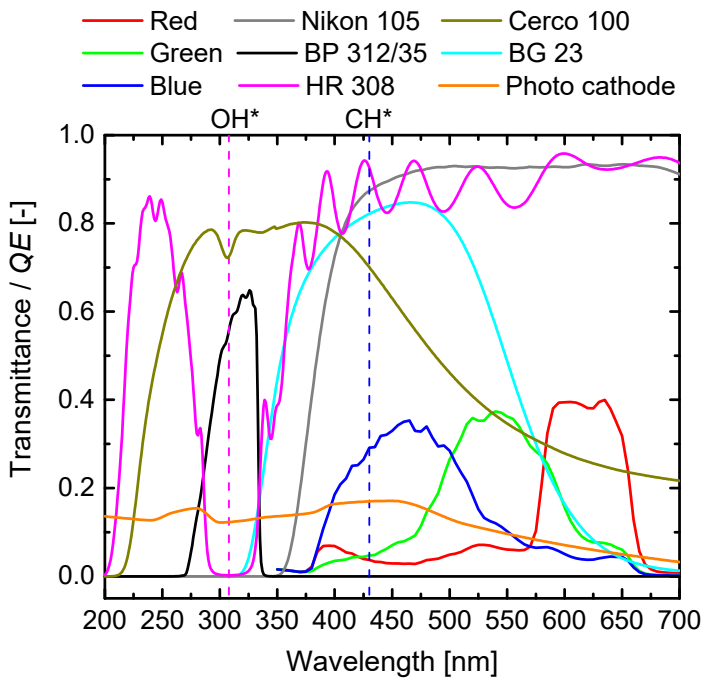


Figure 5.2 Transmittance and quantum efficiency of optics for multi-spectral imaging. The two vertical dashed lines indicate the approximate centers of the strongest  $OH^*$  and  $CH^*$  emission bands.

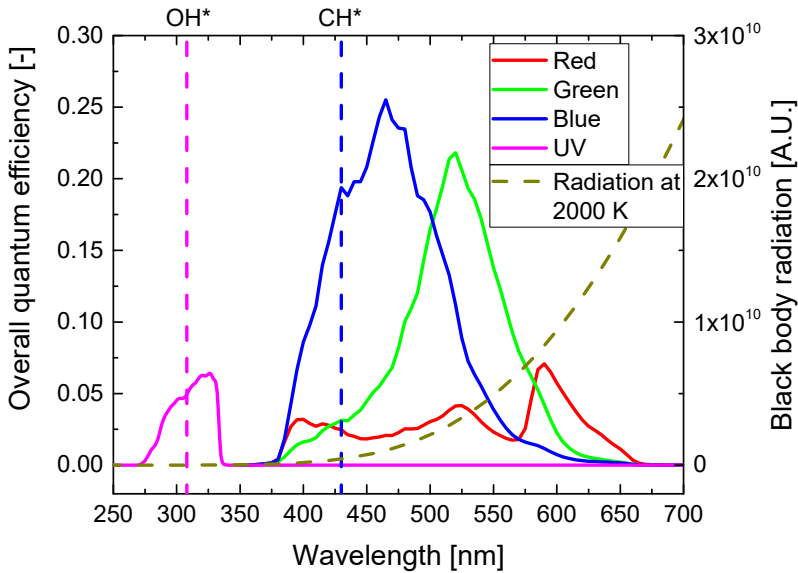


Figure 5.3 Overall quantum efficiency of each channel in multi-spectral imaging. The spectral intensity of black-body radiation at 2000 K is plotted as a reference.

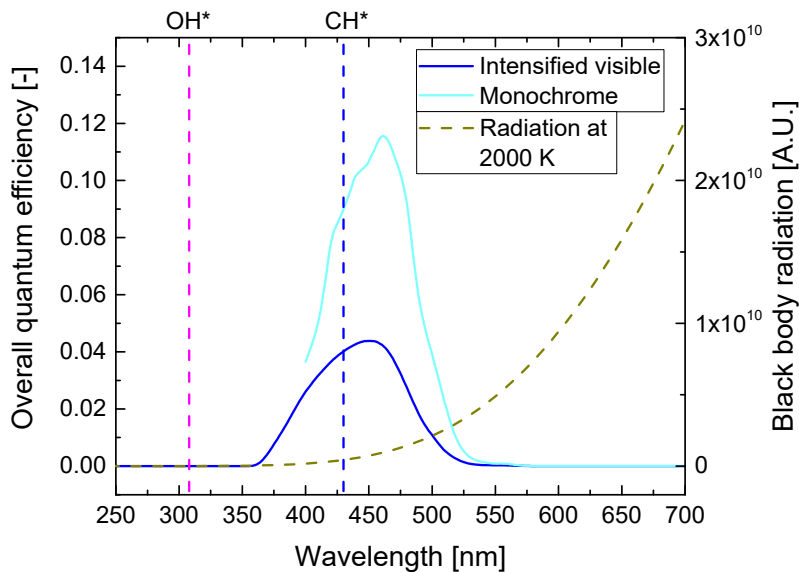


Figure 5.4 Overall quantum efficiencies of the intensified visible and the monochrome imaging system.

## 5.3 Data post-processing

### 5.3.1 Pressure-trace processing

The post-processing for the pressure traces was the same as in Chapter 4. In brief, a low-pass filter with a transitioning from high to low from 3 to 5 kHz was applied and the  $AHRR$  was determined using the same algorithm as in Ref. [52] with a constant adiabatic index of 1.33. The thermodynamic state in the combustion chamber was estimated via a 0/1D GT-POWER simulation. “Three-Pressure Analysis” was used to simulate the last motored cycle just before the fired cycles. From the simulation, the in-cylinder bulk temperature trace was obtained. The adiabatic-core temperature at TDC was calculated based on the bulk temperature at IVC and the measured pressure trace by assuming isentropic compression.

### 5.3.2 Image processing

First, for both RGB and UV images, the average of a set of dark images before SOI was subtracted from the raw images. Noise was suppressed by a  $5 \times 5$ -pixel median filter. To segment the images for the flame areas, the dynamic thresholding method from Ref. [282], was applied (run backward in time, with the free parameter  $SC = 0.3$  for RGB, and  $SC = 0.35$  for UV). After image segmentation, the flame luminosity was calculated as the mean intensity of the foreground. This way, the flame luminosity is more sensitive to small flame areas compared to integrating all the pixels in the whole image. The image segmentation and the corresponding flame luminosity were obtained independently in each of the four color channels. In Figure 5.5, an example for image segmentation is shown at 0.63 ms ASOI.

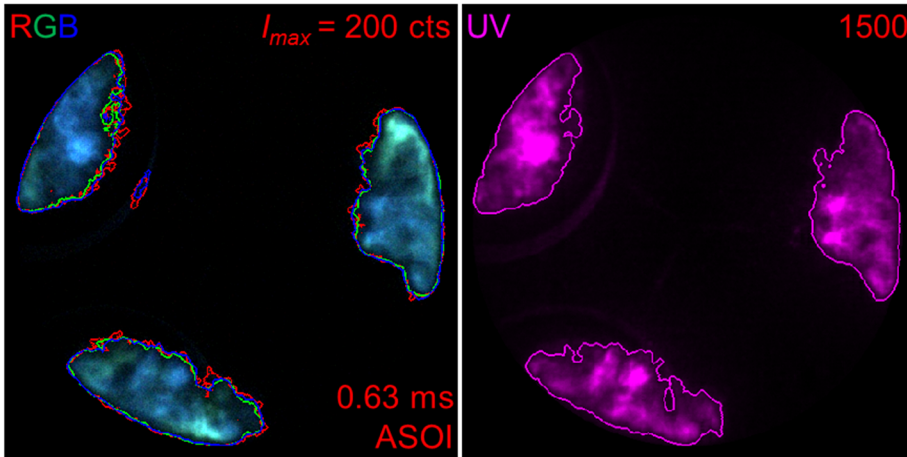


Figure 5.5 An example of the image segmentation in the four color channels. The images have been corrected by average dark images.

## 5.4 Results and discussion

### 5.4.1 Temporal evolution of combustion

Selected images (corrected by dark images) from a single cycle are shown in Figure 5.6. In the RGB images, the blue chemiluminescence exists for only a very short period, until 0.63 ms ASOI approximately. Afterwards, the soot incandescence starts to dominate the light emission within all flame areas. Here the soot appears green because of the suppressed red channel (Figure 5.3). It is also seen that with the current imaging parameters, pronounced saturation areas exist after 0.96 ms ASOI. In terms of flame areas, the UV channel matches well with the RGB channels over most of the sequence. One exception is that at 1.84 ms ASOI, shortly after EOI, burning of the last-injected fuel is seen in the UV channel but not in the RGB channel. Throughout combustion, saturation is not seen in the UV channel.

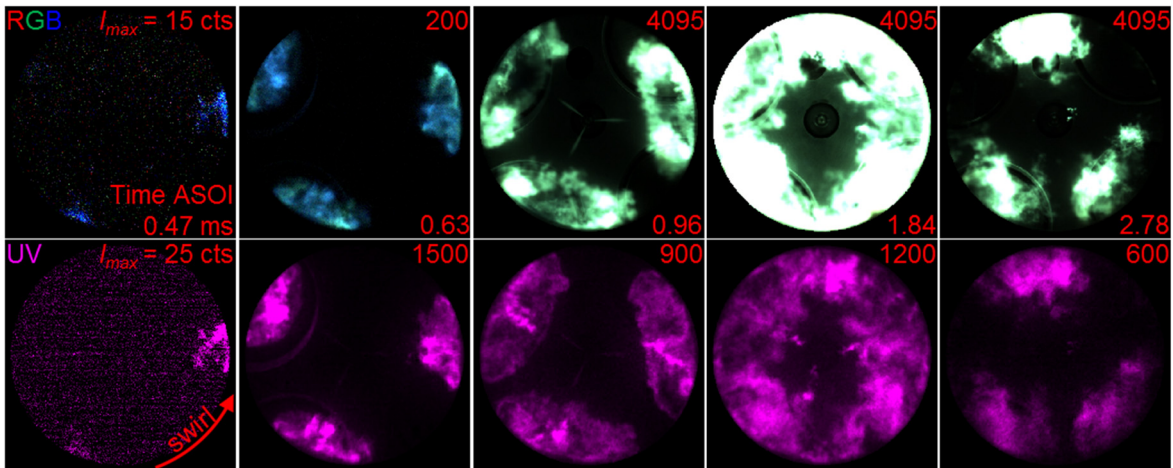


Figure 5.6 Spatiotemporal evolution of Spray B combustion in multi-spectral imaging. The numbers in the upper right indicate the maximum pixel intensity, while the numbers in the lower right indicate time after start of injection.  $T_a = 901$  K,  $\rho_a = 22.7$  kg/m<sup>3</sup>.

The temporal evolution of the ensemble-average flame luminosity and  $AHRR$  from the dataset underlying Figure 5.6 is plotted in Figure 5.7. The traces are normalized by their respective maximum. According to the  $AHRR$  curve, the event can be divided at about 0.8 ms ASOI into two phases, namely premixed burn and mixing-controlled burn. The initial peaks of the optical signals match well with the

premixed-burn peak in the *AHRR* and consequently are attributed to chemiluminescence from the premixed-burn. In the UV trace this peak is very high, even higher than the peak in the later mixing-controlled combustion, while the RGB traces show the contrary. The premixed-burn peaks (around 0.5 ms ASOI) in the RGB traces are very low, with most of light in the blue channel, as can be seen at 0.47 ms ASOI in Figure 5.6. The much stronger signal later (after  $\sim 0.7$  ms ASOI) is attributed to soot incandescence. This disagreement indicates that a visible-light sensitive camera mainly detects soot luminosity even with BG filters, while a UV-light sensitive camera with an OH\* filter mainly detects chemiluminescence. In terms of ignition, the *AHRR* rises first, before the optical signals. If a threshold near zero is used to detect SOC, e.g. zero as used by Eagle et al. [52], too early SOC will be obtained.

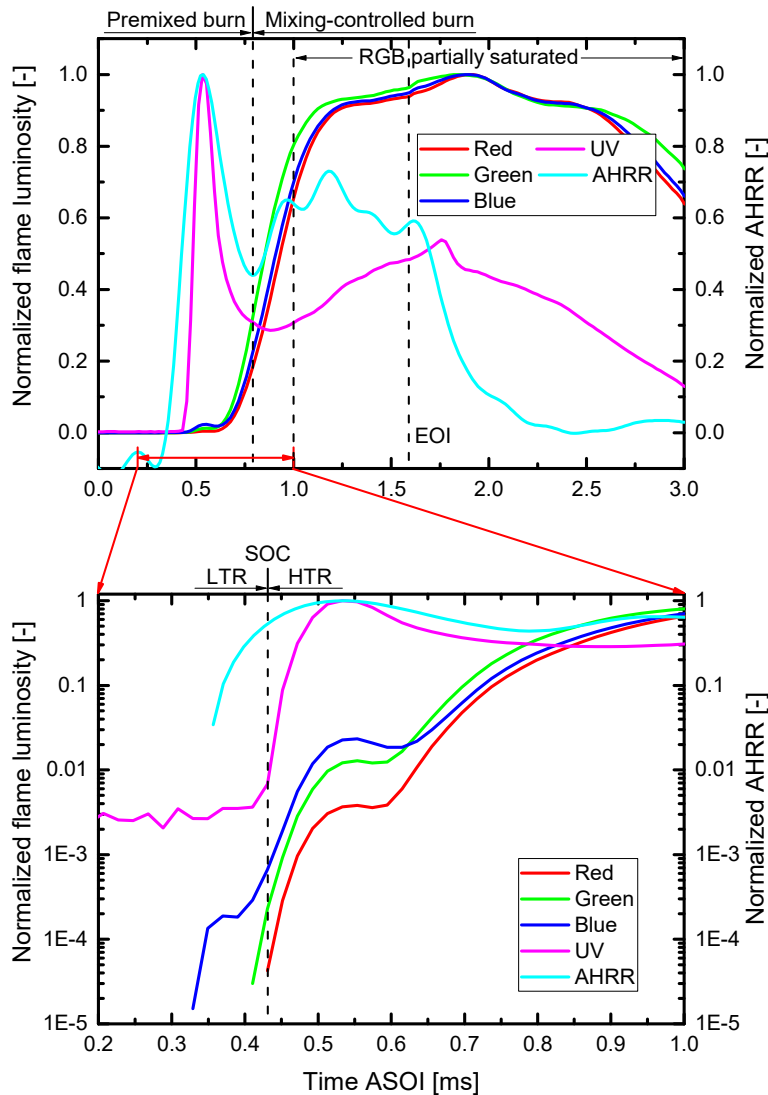


Figure 5.7 Ensemble-average temporal evolution of normalized flame luminosity and *AHRR* of Spray B combustion. Note the logarithmic scale for the vertical axis in the lower plot.  $T_a = 901$  K,  $\rho_a = 22.7$  kg/m<sup>3</sup>.

Figure 5.7 (bottom graph) shows the time between 0.2 and 1.0 ms ASOI, plotting the signals on a logarithmic scale. Among the four optical signals, the blue trace rises first. The other three traces rise at a similar time, around 0.43 ms ASOI. As a preliminary assumption, the time when all four signals are increasing fast is attributed to the time of high-temperature ignition (SOC). Figure 5.8 shows the images before SOC in a single cycle with white flame contours. The flame contours on the RGB images were obtained from the blue channel. During the short time from 0.35 ms to 0.41 ms ASOI, the signal captured

by the blue channel is very weak, but remains at the same location, consistent with the jet position. Therefore, these signals are attributed to the LTR. The flame contours detected in the UV trace are similar. The foreground areas at 0.33 ms ASOI are probably from patterned dark noise. In the RGB images, the dark noise has very little pattern and is mostly suppressed by the median filter before the image segmentation. Therefore, noise is much less detected as “flame luminosity” than in the case of UV images. All these phenomena indicate that the high-temperature ignition indeed occurs when the UV trace increases from the noise level. The  $AHRR$  rises much earlier than this, indicating significant LTR. After the SOC follow the HTR, including high-temperature premixed and then mixing-controlled combustion.

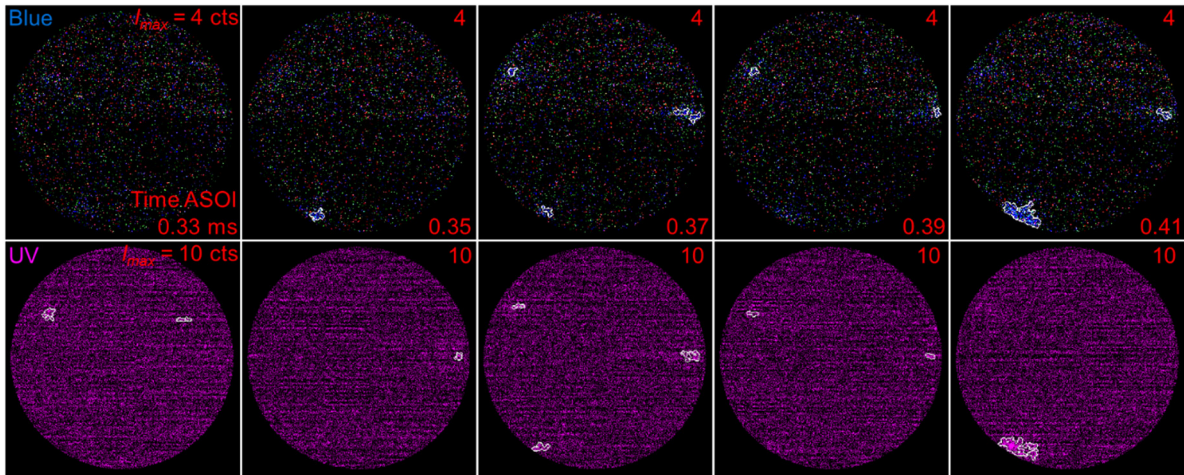


Figure 5.8 Background-corrected images and detected flame areas (shown in white contours) in blue and UV channels during LTR in cycle 2. The background for the blue channel is the RGB image. The numbers at upper right indicate the maximum pixel intensity, while the numbers at lower right indicate time (ms ASOI).  $T_a = 901$  K,  $\rho_a = 22.7$  kg/m<sup>3</sup>.

A clear signature of the high-temperature ignition cannot be found in the  $AHRR$  curve. Therefore, a different metric needs to be derived from the pressure trace if that signal is to be used to locate ignition. Higgins et al. [46] compared the net pressure rise from ignition and combustion of the Diesel spray in a combustion vessel with the flame luminosity trace measured by photomultiplier tubes. To obtain the net pressure rise (or simply, “pressure rise”) in the engine, the average motored pressure trace is subtracted from the fired pressure trace. The pressure trace is not filtered here, since the acoustic resonance could be useful for SOC detection. The normalized ensemble-average pressure rise is added to Figure 5.7, resulting in Figure 5.9. The pressure rise has pronounced acoustic waves. The first fast increase, indicating the first strong pressure wave at the pressure sensor, seems to temporally match well with the fast rise of the UV trace. To suppress the influence of the heat loss to the walls, the  $AHRR$  of the motored cycles is subtracted from that of the fired cycles, resulting in the  $HRR$ , as discussed in Section 4.4.4. The resulting  $HRR$  is plotted in Figure 5.9 instead of  $AHRR$ .

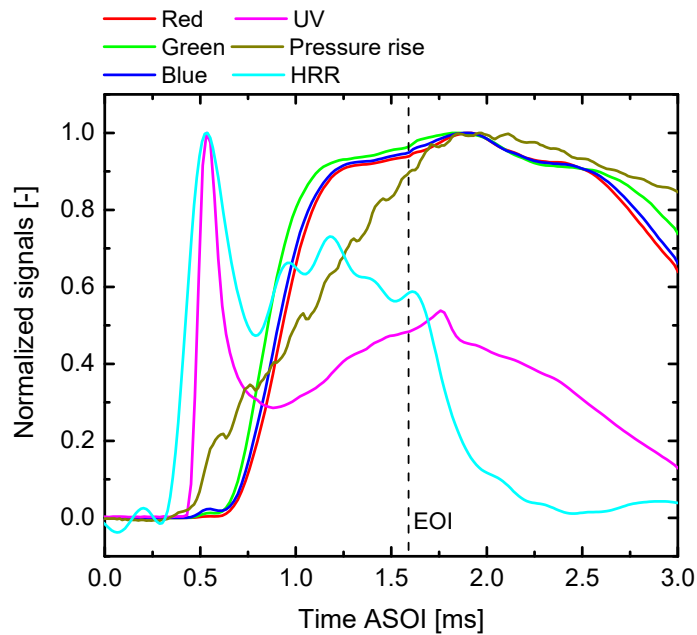


Figure 5.9 Ensemble-average temporal evolution of the normalized flame luminosity, HRR, and net pressure rise of Spray B combustion.  $T_a = 901$  K,  $\rho_a = 22.7$  kg/m<sup>3</sup>.

To find SOC from the pressure rise, the absolute values of different signals are shown in the center plot of Figure 5.10, where the horizontal axis is now scaled narrower to focus on ignition. The initial fast increase in the pressure rise is clearly seen, as well as in the UV and blue traces. This fast increase is used to obtain SOC here. Back-extrapolating (dashed lines) the pressure rise and the UV trace from their respective steepest slopes within that initial fast increase, the zero-crossing points are designated as SOC. They are very close to each other. The small gap is due to the finite speed-of-sound [46, 51]. Assuming an ideal gas with a temperature of 900 K and an adiabatic index of 1.33, and a distance of 20 mm from ignition location to the pressure sensor, the pressure wave needs 34  $\mu$ s to travel to the sensor. This is similar to the gap here (about 20  $\mu$ s). By back-extrapolation, nearly the same SOC from the blue channel is obtained as that from the UV channel. The same observations can be made at lower and higher in-cylinder temperature, as shown in Figure 5.10, top and bottom plots. Therefore, SOC can be found in the ensemble-average pressure rise by back-extrapolation from the steepest increase.

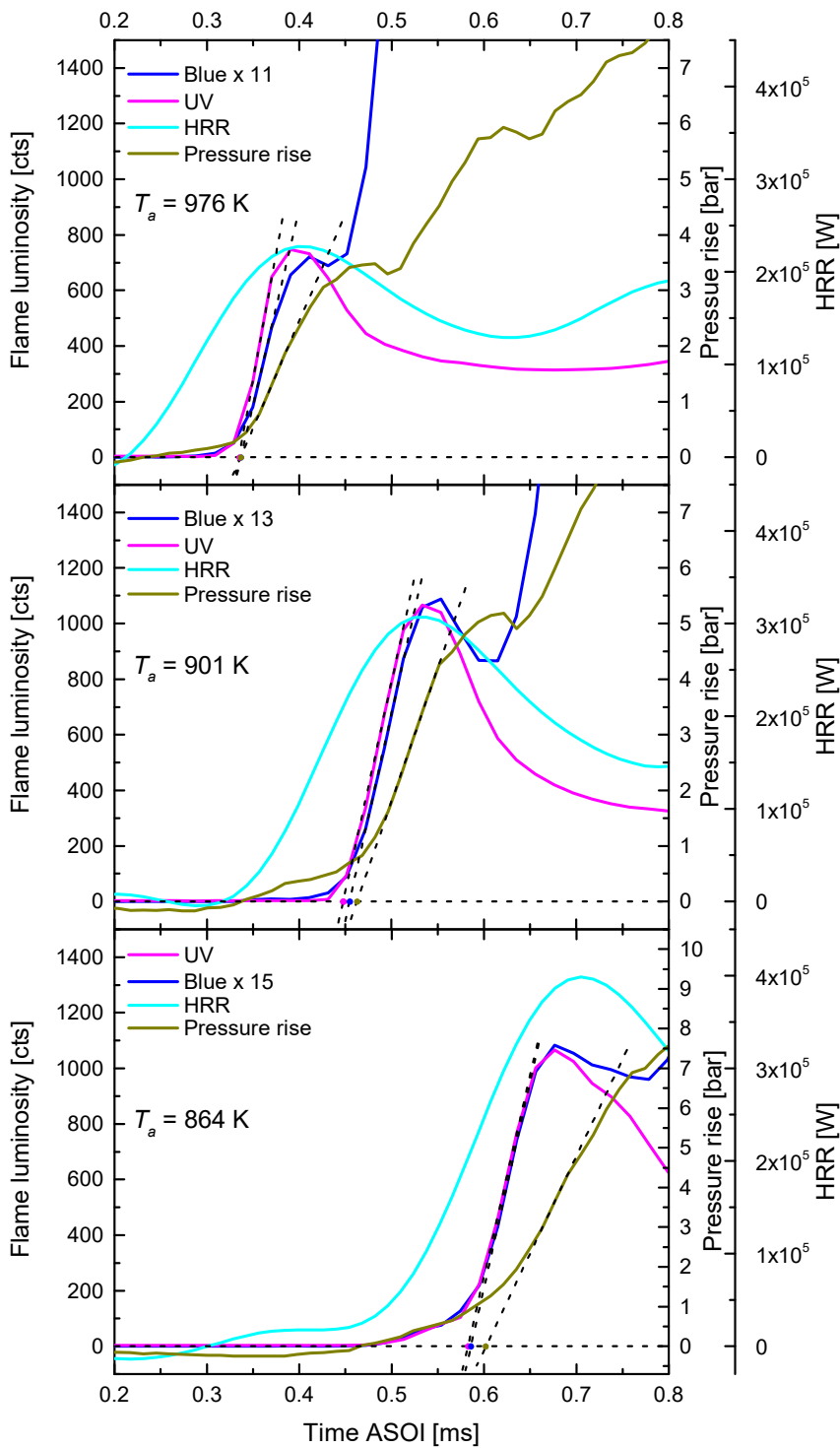


Figure 5.10 Ensemble-average temporal evolution of flame luminosity, HRR, and net pressure rise of Spray B combustion around ignition at different ambient gas temperatures and at the same ambient pressure (59.9 bar). Note that for clarity the blue traces are shown amplified as indicated in the legends.

To check the adequacy of different signals for SOC detection in single cycles, the pressure rise and the optical signals from two typical cycles (number 2 and 18), are plotted in Figure 5.11. If back-extrapolation is used for SOC detection, both the UV and the blue trace are adequate. Pressure rise works in cycle 2. In cycle 18, however, the pressure slowly increases towards high-temperature ignition. A distinct fast increase of pressure rise is not seen, probably due to interaction of the pressure waves

generated from the ignition of different jets. Therefore, the pressure trace is not necessarily adequate for single-cycle SOC detection. Also, a speed-of-sound correction is needed, complicating automatic detection. By principle, pressure-based SOC detection is global, not for a certain jet.

If thresholding is used for SOC detection (simpler to implement), the LTR region should be avoided. This requires high enough thresholds. As the magnified insert for cycle 2 shows, if very low thresholds are used, the blue trace will produce an earlier ignition. The UV trace works better from this point of view.

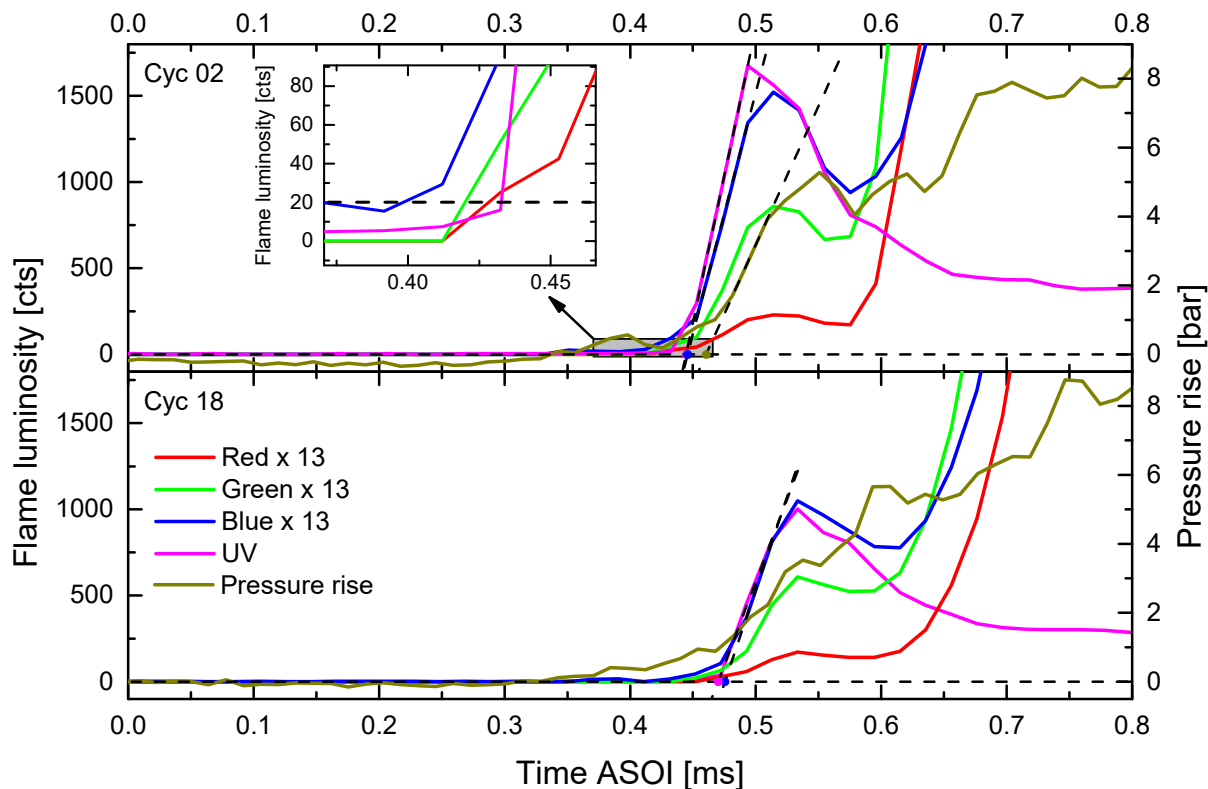


Figure 5.11 Single-cycle evolution of flame luminosity and net pressure rise of Spray B combustion around ignition. The magnified insert for cycle 2 shows the threshold used in the UV channel to detect SOC.  $T_a = 901\text{ K}$ ,  $\rho_a = 22.7\text{ kg/m}^3$ .

#### 5.4.2 Effect of the sensitivity of the imaging system

Figure 5.12 shows the ensemble-average flame luminosity and the pressure rise near ignition for the high-gain OH\* system. Here, the camera sensor partially saturates after ignition. Before local saturation (indicated by the dashed line), the flame luminosity behaves similar to that at the lower gain (UV traces in Figure 5.10, center plot). The only difference is that at the higher gain the system captures more LTR signal. However, the LTR flame luminosity is still very low compared to the later peak value. Figure 5.13 shows a single-cycle image sequence during LTR towards high-temperature ignition. The optical signal is weak and very noisy. The flame area at 0.52 ms ASOI is not detected well, probably because the backward-running algorithm tends to use too high thresholds in a very fast increase of flame luminosity.

In this example, the time gap between optical ignition and pressure-based ignition is not seen. This is probably because of an artifact of a misalignment between the optical and pressure signals. The recorded engine speed from AVL IndiCom was used, which is an average of the speed over a cycle. The actual speed in the compression stroke is lower than that average. If the sequence trigger is very early compared to ignition, the error in the temporal alignment between the optical and pressure signals will

be large. In the high-gain OH\* and intensified visible systems, the sequence trigger was at  $-45.5^\circ\text{CA}$ , while in the multi-spectral system,  $-15^\circ\text{CA}$  was used. Nevertheless, it is concluded that higher sensitivity in OH\* imaging does not yield earlier detected SOC.

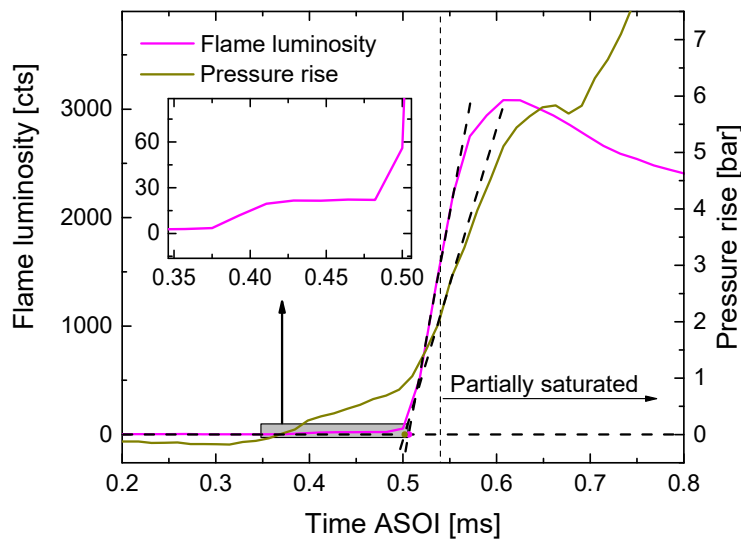


Figure 5.12 Ensemble-average temporal evolution of high-gain OH\* chemiluminescence and net pressure rise of Spray B combustion around ignition.  $T_a = 876\text{ K}$ ,  $\rho_a = 23.4\text{ kg/m}^3$ .

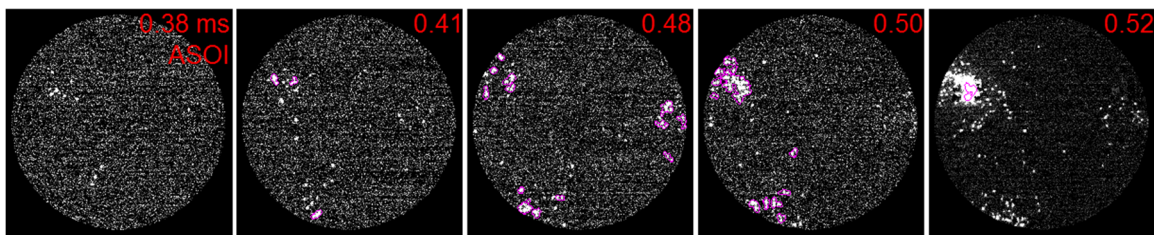


Figure 5.13 BG-corrected high-gain OH\* chemiluminescence images and detected flame areas (magenta contours) during LTR towards high-temperature ignition in cycle 1. The numbers in the upper right show the time ASOI.  $T_a = 876\text{ K}$ ,  $\rho_a = 23.4\text{ kg/m}^3$ .

Next, the effect of increasing the sensitivity of detecting visible light is examined. Figure 5.14 shows the ensemble-average flame luminosity from intensified visible-light imaging and the pressure rise near ignition. Here, the camera sensor also partially saturates after ignition. The flame luminosity, which is mostly blue light according to Figure 5.6 and Figure 5.7, significantly increases at ignition. The back-extrapolated SOC, again, nearly coincides with that from the pressure rise. This indicates that the higher sensitivity of this imaging system also does not advance the detected SOC by back-extrapolation. However, the LTR level of the flame luminosity (before the back-extrapolated SOC) is higher than that in the blue trace in the center plot of Figure 5.10, taking the peak value as a reference. By the same reference, this LTR luminosity is also much higher than that captured by the high-gain OH\* system. The images during LTR towards high-temperature ignition are shown in Figure 5.15. Compared to the band-pass OH\* signal in Figure 5.13, the flame areas are larger and the photon noise is less. Therefore, visible-light (blue) imaging is more sensitive to LTR than band-pass OH\* imaging. Thresholding the spatially integrated time evolution, advanced SOC would be probably obtained.

In term of spatial information, at 0.50 ms ASOI, the flame in jet 3 is not detected, because a single threshold is used for the whole frame and the difference between the flame-luminosity levels of the three jets is large here (this was also found in the high-gain OH\* system). This will cause a later detection of SOC in jet 3, if it does not ignite first, according to the method of SOC detection for individual jets used

here (see Section 4.3.2). Dividing the FOV into three sectors for individual dynamic thresholding could be implemented in the future.

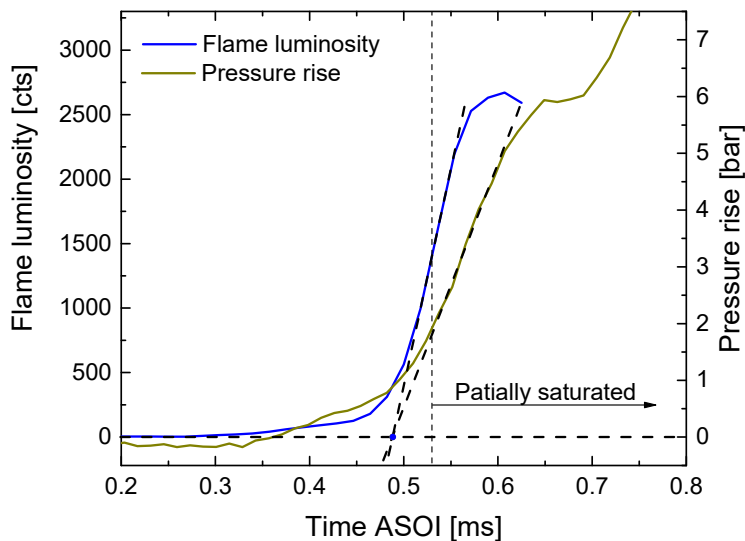


Figure 5.14 Ensemble-average temporal evolution of intensified visible flame luminosity and net pressure rise of Spray B combustion around ignition.  $T_a = 875\text{ K}$ ,  $\rho_a = 23.4\text{ kg/m}^3$ .

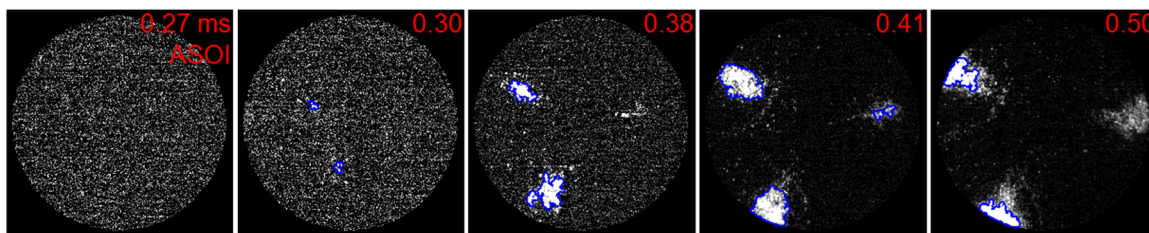


Figure 5.15 BG-corrected intensified visible images and detected flame areas (blue contours) during LTR towards high-temperature ignition in cycle 4. The numbers in the upper right show the time ASOI.  $T_a = 875\text{ K}$ ,  $\rho_a = 23.4\text{ kg/m}^3$ .

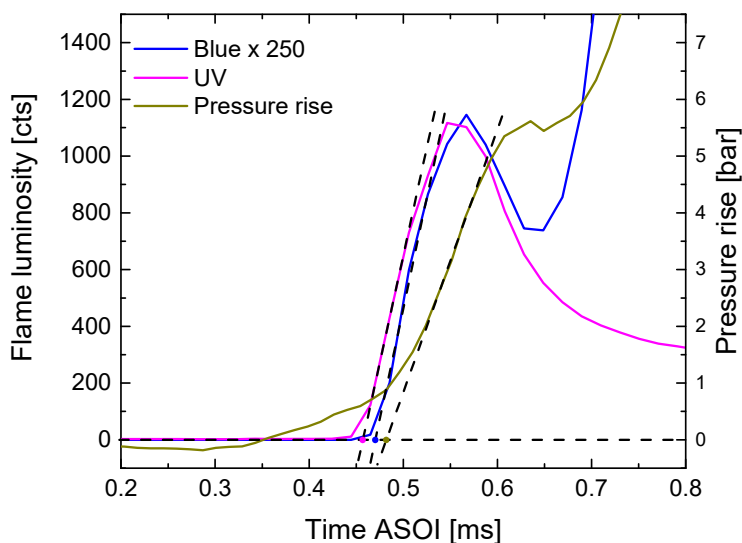


Figure 5.16 Ensemble-average temporal evolution of visible flame luminosity with shortened exposure time and net pressure rise of Spray B combustion around ignition.  $T_a = 893\text{ K}$ ,  $\rho_a = 22.9\text{ kg/m}^3$ .

The flame luminosity in the multi-spectral system locally saturates the RGB sensor. Thus, in some application, one might want to decrease the sensitivity of the imaging system by reducing exposure time or aperture. To investigate the effect of such lower sensitivity on the detection of SOC based on visible-light, the exposure time of the RGB camera was reduced to 2  $\mu\text{s}$ , avoiding saturation. The ensemble-average temporal evolution of flame luminosity and pressure rise are plotted in Figure 5.16. Now, the premixed-burn signal is very weak in the blue trace. The blue trace yields later SOC than the UV trace, regardless of whether back-extrapolation or thresholding (not shown) is used.

### 5.4.3 Monochrome system

As a further comparison, the ensemble-average temporal evolution of flame luminosity and pressure rise from the monochrome system [298] are plotted in Figure 5.17. In this case, a shorter exposure time (7.5  $\mu\text{s}$ ) was used and the overall  $QE$  is about 50% lower than in the blue channel in the multi-spectral system. Nevertheless, with reference to the pressure trace the behavior of the flame luminosity is the same as that of the blue traces in Figure 5.10. The ignition delays measured by these two systems appear directly comparable.

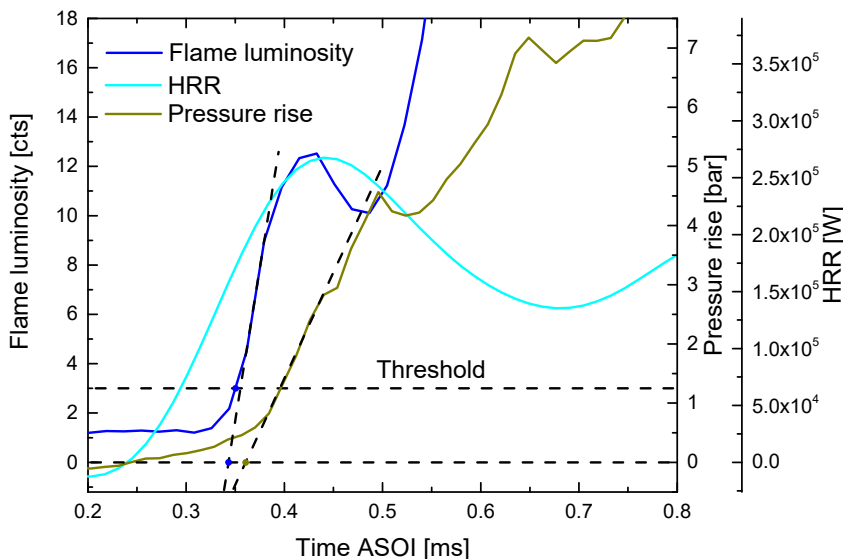


Figure 5.17 Ensemble-average temporal evolution of non-intensified flame luminosity from the monochrome system and net pressure rise of Spray B combustion around ignition.  $T_a = 956 \text{ K}$ ,  $\rho_a = 21.7 \text{ kg/m}^3$ .

### 5.4.4 Discussion

From the temporal evolution of optical and pressure signals of different imaging systems, it can be seen that the band-pass-filtered UV signal is the best for SOC detection due to its significant increase at ignition as well as its low sensitivity to low-temperature reaction (LTR). Both back-extrapolation and thresholding can be applied to quantify the results. Srna et al. [156] found that for both pilot fuel and dual-fuel combustion, at ignition, in the band  $310 \pm 5 \text{ nm}$ , broadband chemiluminescence mainly due to  $\text{CHO}^*$ ,  $\text{CH}_2\text{O}^*$ , and  $\text{CO}_2^*$  is brighter than the  $\text{OH}^*$  signal. Najafabadi et al. [103] also found that for partially-premixed Diesel combustion the  $\text{OH}^*$  signal is a minor part of the band-pass-filtered signal at ignition. In the current experiment, the UV channel collects signal from 270 nm to 340 nm (Figure 5.3). Therefore, the UV channel used here probably also captured more broadband chemiluminescence signal than  $\text{OH}^*$  at ignition. Therefore, one should take caution when comparing the optical signal with the  $\text{OH}^*$  or OH concentration from modelling.

The broadband blue-biased visible signal also has a fast increase at ignition, making SOC detection by back-extrapolation possible, but this chemiluminescence is much weaker than the later soot incandescence. Only reducing the exposure time or aperture to suppress the soot luminosity might cause late detection of SOC. Therefore, Schott BG filters are a good solution to better balance blue chemiluminescence and soot luminosity. A drawback of using the broadband visible signal is that it is more sensitive to LTR signal than the band-pass-filtered UV signal, so that a too low threshold could advance the detected SOC. The ensemble-average unfiltered pressure rise can be a good reference to compare with the optical signal in terms of global ignition delay. However, the single-cycle results do not always show a distinct fast increase. In addition, the delay by the speed of sound needs to be considered. Therefore, the pressure rise cannot be used as a “stand-alone” method for precise SOC detection. Using the  $(A)HRR$  would detect earlier SOC mainly because of LTR heat release. Thus, it is not recommended, especially when comparing with data from other groups or modelling.

#### 5.4.5 Comparison with the ECN database

Here, to obtain ignition delay and compare with the ECN database, the thresholding method is chosen, since most of the ECN data were obtained this way. The UV channel is used because of the low LTR response. To match the ECN modelling standard [299], which is the “first time at which [the] Favre-average OH mass fraction reaches 2% of the maximum in the domain after a stable flame is established” [299], the threshold is taken as 2% of the maximum flame luminosity. In the multi-spectral system the average peak value in the UV channel is approximately 1000 counts for Spray B. Therefore, 20 counts is chosen as a threshold, as shown in the magnified plot in Figure 5.12. The threshold for the monochrome system in Chapter 4 was set to 3 counts, as shown in Figure 5.17. The ECN reference jet for comparison is jet 3. Here, SOC is detected by searching forward for the first frame in which the flame luminosity of jet 3 is higher than the threshold, then subtracting 0.5 from this frame number or 1 in the case of skip-illumination.

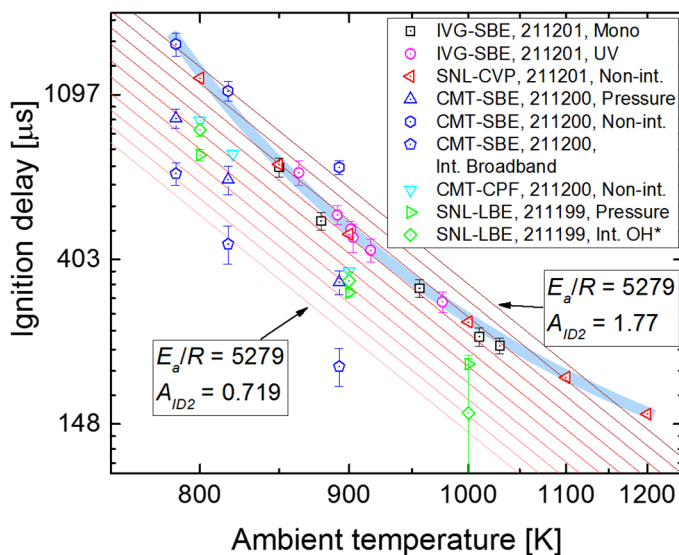


Figure 5.18 Updated comparison of ignition delay among different facilities with UV chemiluminescence results from the IVG-SBE. The optical method detects the signal from jet 3, while the pressure-based method detects the global SOC.  $\rho_a = 22.8 \text{ kg/m}^3$ ,  $p_f = 1500 \text{ bar}$ . The reference lines are from  $E_a/R$  (see Equation (4.5)) fitted to the SNL-CVP data and a range of  $A_{ID2}$ . The error bar indicates one standard deviation.

The results are plotted into Figure 4.33, shown as magenta circles in Figure 5.18. It is seen that these band-pass-filtered UV data match well with the broadband-visible data by monochrome imaging

shown in Chapter 4, as well as the broadband-visible data from SNL's vessel, indicated by the blue band. This shows again, that with the current evaluation procedures the timings of UV and visible chemiluminescence at ignition are the same. The few mismatches between the UV and broadband-visible data from the IVG may be attributed to inaccurate ambient-temperature characterization, LTR signal detected by the visible data, and the inaccurate density correction discussed in Section 4.4.4. Also, as seen in Figure 5.15, the intensified imaging system may detect SOC later when jet 3 does not ignite first, e.g. at low temperature (see Figure 4.29). The advance of the pressure-based and intensified broadband imaging data from CMT's engine and the pressure-based data from SNL's engine is likely due to LTR signal. The reason why the other optical data are located away from the blue band is not clear.

#### 5.4.6 Ignition location

The ignition location for each jet is estimated by calculating the luminosity-weighted mean of the pixel coordinates within the flame, in the first frame in which the flame luminosity exceeds the threshold. If more than one flame parcel occurs at ignition, each yields a separate ignition location. Here, the thresholds for UV and RGB channels are chosen to be just above their respective noise levels, so that the ignition location for each channel is obtained independently. 8 counts is used for UV and 1 count is used for the RGB channels. The results from UV, blue, and red channels at different swirl ratios but similar bulk temperatures (shown in the upper left) are shown in Figure 5.19. The solid circle shows the boundary of the combustion chamber, while the dashed lines show the expected gaseous spray boundary according to the orifice axis with a dispersion angle of  $20^\circ$ . It is seen that at both swirl ratios, the ignition locations from the blue channel occur swirl-upstream within the jets, while the UV and red channels yield more downstream locations. This is because the blue channel detects more of the earlier LTR signal. The red channel here can be regarded as a lower-sensitivity visible imaging system, detecting ignition location further downstream.

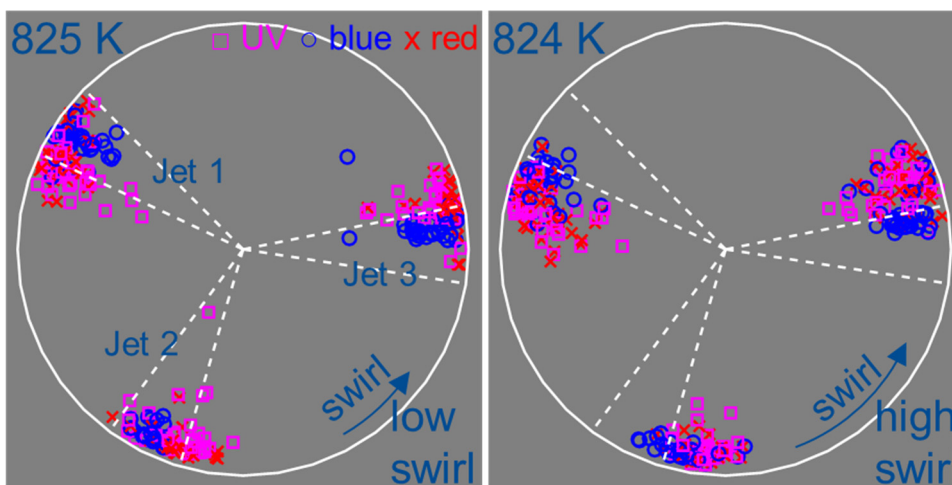


Figure 5.19 Ignition locations in Spray B at different swirl ratios, similar bulk temperatures, and the same ambient pressure (59.9 bar). They are detected in the UV, blue, and red channels independently with thresholds just above the respective noise levels (8 for UV, 1 for blue and red).

### 5.4.7 Effect of swirl ratio on ignition delay

The ignition delays at different swirl ratios measured by multi-spectral imaging are compared against the bulk temperature in Figure 5.20. Here, the optical ignition delay is the globally one, i.e. in any of the three jets. The threshold used for Figure 5.18, 20 counts, was used for the UV channel. The threshold for the blue channel was then chosen to match the ensemble-average results of UV as close as possible from 860 K to 980 K, yielding 14 counts.

In both spectral channels the ignition delay at high swirl is very close to that at low swirl, when comparing at the same bulk temperature. There is a tendency that at low temperature, the ignition delay is slightly shorter at high swirl, probably due to enhanced fuel/air mixing [22-24]. However, here the effect of swirl ratio on ignition delay is generally not as obvious as that on liquid length, as shown in Figure 4.18, although the core temperature at high swirl is higher than at low swirl at similar bulk temperatures (see Figure 3.20). The thicker boundary layer at high swirl (see Figure 3.20) probably exerts more influence on ignition than on fuel evaporation.

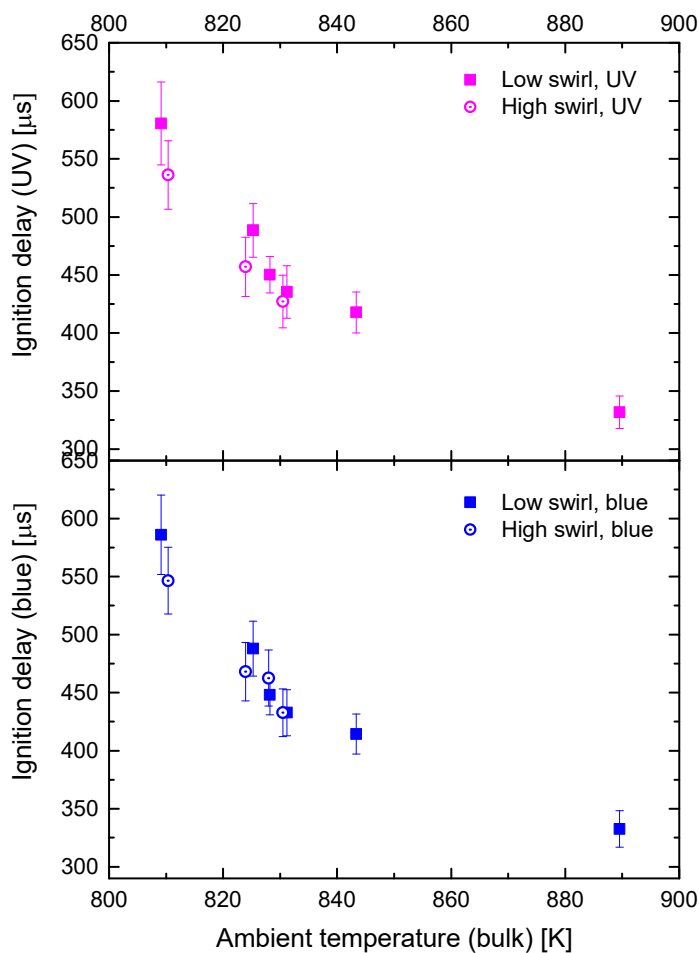


Figure 5.20 Variation of global ignition delay with bulk ambient temperature at the same ambient pressure (59.9 bar) but different swirl ratios. Top: UV channel, bottom: blue channel. The error bar indicates one standard deviation.

### 5.4.8 Hole-to-hole variation of ignition delay

The hole-to-hole variation of ignition delay at high swirl measured by the multi-spectral system and the monochrome system is shown in Figure 5.21. The thresholds for the UV and blue channels are the same as for Figure 5.20, and for the broadband data from the monochrome system the same as that in Chapter 4. Compared to low swirl (see Figure 4.29), the trend is very different here. Jet 1, which issues from the smallest orifice and ignites first at low swirl, ignites last at high swirl according to all imaging methods and throughout the whole temperature range investigated here ( $T_b \approx 800 - 890$  K). This could be due to a spatial inhomogeneity of temperature and flow field at high swirl. However, in the LIF-measured temperature field around TDC at high swirl without fuel injection (Figure 3.18), no such a local difference is found near the jet 1 region, at least near the center of the piston bowl. The difference might stem from other vertical positions, which needs further investigation together with the flow-field measurements. The spray/flow interaction and evaporative cooling cannot be addressed with the current diagnostics. Similarly, comparing Figure 4.29 and Figure 5.20, at lower in-cylinder temperatures (indicated by the longer ignition delay at the same ambient pressure across the data points), jet 3 does not ignite first for both swirl levels, following the theoretical correlation with the orifice outlet diameter, as discussed in Section 4.4.3.

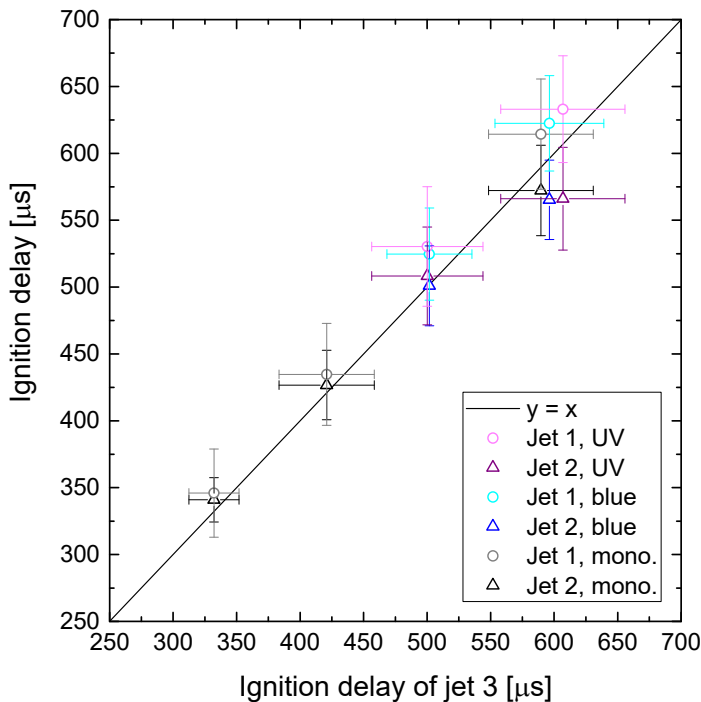


Figure 5.21 Comparison of ignition delay from different nozzle holes at high swirl. The error bars represent one standard deviation within each dataset.

## 5.5 Summary and conclusions

In order to address the remaining question from the ignition delay comparison across the ECN database in Chapter 4, multi-spectral imaging based on two simultaneously running high-speed cameras was implemented for ECN Spray B combustion. Image data in four color channels – UV, red, green, and blue – are obtained. The UV channel is basically band-pass-filtered OH\* chemiluminescence imaging. The RGB channels are Bayer-sensor filtered, with the longer wavelengths partially suppressed by Schott BG filters. In addition, single-camera imaging systems with higher sensitivities are investigated for both the UV and visible signals. The area-averaged flame luminosity in the flame contours, obtained with a dynamic thresholding approach, is used to investigate the temporal behaviors

of different spectral traces at ignition. The applicability of different pressure-derived metrics for detecting the global start of high-temperature combustion was also investigated.

Compared to the non-intensified broadband visible imaging, band-pass-filtered OH\* imaging is less sensitive to low-temperature chemiluminescence and soot incandescence, and more sensitive to the high-temperature chemiluminescence. Nevertheless, these two optical signals match well in terms of detection of the start of high-temperature combustion. Both back-extrapolation and thresholding can be used to quantify the ignition delay, but the threshold should be high enough to be above the low-temperature reaction level. With higher sensitivity (e.g. higher gain, longer exposure time, or larger aperture), for both signals the start of high-temperature combustion detected by back-extrapolation is not advanced. However, the low-temperature reaction level is lifted, especially in the broadband-visible signal. If the sensitivity of the visible imaging system is too low, that could delay the detection of the start of high-temperature combustion. The (apparent) *HRR* curve rises before ignition mainly due to low-temperature reaction. Therefore, it is not recommended using (apparent) *HRR* for detection of the start of high-temperature combustion. As a replacement, the unfiltered net pressure rise due to ignition and combustion matches the optical signals in the first fast increase, considering the delay caused by the finite speed of sound. Nevertheless, the net pressure rise should be not taken as a stand-alone approach due to its single-cycle complexity and the delay by the speed of sound. The above conclusions are from experiments with Spray B, but the author believes they are generally applicable to conventional Diesel combustion. Back to the original question raised in Chapter 4, the ignition delay measured by non-intensified broadband imaging is, in fact, consistent with that measured by the intensified OH\* chemiluminescence imaging. The pressure-based methods used by different research groups yield shorter ignition delay, presumably because of low-temperature reaction.

Continuing the investigation in Chapter 4 on the effect of swirl on the ignition of Spray B in engines by multi-spectral imaging, it is found that there is no pronounced difference in ignition delay between low-swirl and high-swirl operation at the same bulk temperature. It is possible that the various effects of swirl motion, including fuel/air mixing, heat transfer with the engine walls (influencing the temperature field), air entrainment, etc. roughly cancel each other. Interestingly, at high swirl, jet 1 ignites last despite issuing from the smallest-diameter hole, indicating a spatial inhomogeneity in the thermofluidic conditions at high swirl that needs further investigation. At both swirl levels, jet 3 does not ignite first at low ambient temperature (at least  $T_c < 900$  K), while at high temperature it does.

Regarding future work, measurements with the same imaging trigger in different systems could be implemented to yield a more accurate comparison, as discussed with Figure 5.12. The image segmentation for flame areas could be improved by dividing the field-of-view into three sectors before the dynamic thresholding, so that individual thresholds are used for the flame detection of different jets. The current dynamic-thresholding algorithm produces inappropriate thresholds for a fast-increasing flame luminosity. The back-extrapolation approach for detection of the high-temperature combustion from the flame luminosity curves should be automated. In the current multi-spectral system, the green channel captures both chemiluminescence and soot incandescence, and is not very useful. Instead, the green channel could be used to record other physical phenomena, e.g. a green-illuminated fuel spray. Regarding the interesting behavior of the ignition delay of jet 1 at different swirl levels, measurements of temperature and flow field at different vertical positions in the combustion chamber around TDC are needed.

---

---

## Chapter 6 Optical-flow analysis of knock in CI engines

---

This chapter is on the knock measurement by high-speed imaging, inspired by a dataset taken by Barth [84]. It has been published previously as

Zhao, M. and Kaiser, S., “Optical diagnostics for knock in compression-ignition engines via high-speed imaging,” *SAE Int. J. Engines* 11(6): 903-918, 2018, doi: 10.4271/2018-01-0631.

and presented at

28. Deutscher Flammentag – Verbrennung und Feuerung, Darmstadt, Germany, 2017, conference paper & oral presentation “Optical Diagnostics for Diesel Knock Based on High-Speed Imaging and Optical Flow”.

SAE World Congress Experience 2018, Detroit, USA, 2018, SAE technical paper & oral presentation “Optical diagnostics for knock in compression-ignition engines via high-speed imaging”.

### 6.1 Introduction

Knock is a phenomenon of abnormal combustion typically found in SI engines. Auto-ignition in the end gas leads to strong pressure waves in the combustion chamber and audible noise. Similarly, in Diesel engines, very high cylinder-pressure rise-rates, resulting in strong pressure-wave oscillation, destructive engine vibration, and noise are called “Diesel knock”. New concepts of CI combustion, such as HCCI, premixed-charge compression-ignition (PCCI), and PPC, etc., may particularly suffer from knock in high-load operation [300].

There are numerous studies on knock, through analyses of in-cylinder pressure, engine block vibration, heat transfer, gas ionization, and optical diagnostics [301]. The first two methods are the most mature and are widely applied in laboratory and on-board, respectively. As a non-intrusive tool, optical diagnostics have also been utilized to investigate the nature of engine knock. The use of high-speed cinematography for this purpose, at first film-based, dates back to the 1930s [302]. Later studies also leveraged this technique to visualize the flame propagation [303-306] and even the pressure wave [307-309], whose speed could be calculated [303, 305, 306, 308, 309]. PTV was also adopted to measure the flow field during knocking combustion [310].

However, most optical studies were in SI engines, and there is also a recent extensive review paper on SI knock [311]. Research on CI knock by imaging is sparse. Recently, Rusly et al. [230] performed high-speed imaging of soot luminosity during knocking cycles in an optically accessible Diesel engine. Soot pockets were observed to oscillate when knock happened, and a strong correlation was found between their oscillation frequencies and those from the in-cylinder pressure trace. The soot pockets were identified by image segmentation. Their centroids were used to track their movement by visual inspection, yielding the flame oscillation frequencies. Similarly, based on color images Park et al. [312] tracked the centroid of the flame during PCCI combustion to determine the dominant movement frequency in a selected area in the combustion chamber. However, the flame movement is affected by swirl and there might be more than one dominant oscillation frequency.

This frequency-detection method could be improved further by using field-wide calculation of the gas movement via the image processing concept of optical flow, as introduced in 2.3.9. Also, cameras with higher frame rate and higher resolution are available now. The former is important because knock is an extremely fast phenomenon, the latter because analysis by optical flow profits from higher resolution. In this work, the relation between the velocity field derived by optical flow and the pressure trace is investigated, in particular, the relation between the “optical” oscillation and the pressure

---

oscillation. Also investigated is the relation between the optical data and the pressure data in terms of knock onset, knocking time interval, and knock intensity.

## 6.2 Experimental apparatus and conditions

The engine parameters can be found in Table 3.1. Here the piston crown with the full-metal rim was used. The fuel injector was a common-rail solenoid injector (Delphi DFI 1.5) with a 7-hole nozzle. The operating conditions are listed in Table 6.1. The engine was skip-fired with fuel injected every 9th cycle. Therefore, the bulk gas in the fired cycles was pure air without residual burnt gas. Approximately 25 mg of n-dodecane per (fired) cycle were injected. In order to facilitate the occurrence of knock, an early injection timing, a low engine conditioning temperature, low intake temperature and pressure, and a low fuel-injection pressure were used. Pronounced noise and high pressure rise rates indicated knock.

*Table 6.1 Engine operating conditions for knock.*

Engine speed	1000 rpm
Swirl ratio at max. piston speed during intake	2.4
Coolant and oil temperature	60 °C
$p_{mi}$	7.25 ± 0.25 bar
Intake air temperature / pressure	20 °C / 1 bar
Fuel	n-dodecane
Injection pressure	800 bar
Start of injection (from image)	−6.5°CA
Injection duration (from image)	9.1°CA
Injection quantity	25 mg
Global $\phi$	0.73
Skip-fire mode	1 (fired) / 8 (motored)

The optical arrangement and FOV are nearly the same as shown in Figure 4.2, only with the illumination by LEDs not as uniform. Table 6.2 collects the main imaging parameters. A Photron SA-Z high-speed camera captured the natural flame luminosity at 60 000 frames per second (every 0.1°CA at 1000 rpm), the same as the sampling rate of in-cylinder pressure here. Similar to the Spray B measurements, a 2-mm-thick BG-23 filter was used to attenuate soot luminosity in favor of chemiluminescence from the premixed combustion, effectively improving the dynamic range of detection across the combustion event. Two blue LEDs illuminated the fuel spray so that its global characteristics could be monitored. The camera lens and aperture information was not documented, unfortunately. 400 images were recorded in every fired cycle, from −9.9°CA to 30°CA. Two datasets of totally 20 fired cycles were recorded both in pressure and images. Knock occurred in all 20 cycles, i.e., the data were not selected for knocking. In the middle of the experiment, i.e., between the two datasets, the engine was stopped for cleaning. Image recording and vector evaluation were performed in LaVision DaVis 8.2, with further analysis in MATLAB.

*Table 6.2 Imaging parameters for knock.*

Frame rate / exposure time	60 kHz / 6 $\mu$ s
Image resolution	512 × 480 pixels
Image bit depth	12
Projected pixel size	0.11 mm/pixel
Imaging period	400 images from −9.9°CA to 30°CA
Filter	2-mm BG-23
Recorded cycles per dataset	10

## 6.3 Results, analysis, and discussion

### 6.3.1 Temporal evolution of knock

For an overview, Figure 6.1a shows the mean in-cylinder pressure of all 20 fired cycles, while Figure 6.1b shows the individual cycles in the narrower crank-angle range of interest. Here, cycle 6, 11, and 15 are emphasized. All cycles have an extremely high pressure rise rate, high peak pressure, and strong pressure oscillation, but the corresponding values vary greatly. The mean maximum pressure rise rate is  $185 \text{ bar}/^\circ\text{CA}$ . The maximum of  $501 \text{ bar}/^\circ\text{CA}$  occurs in cycle 6, and the minimum of  $67 \text{ bar}/^\circ\text{CA}$  in cycle 11. This magnitude of pressure rise rate is far higher than the criterion for persistent knock occurrence (with cracking sound) defined in previous studies [313], ranging from 5 to  $10 \text{ bar}/^\circ\text{CA}$ . The peak pressure varies from 78.8 bar to 155 bar. The maximum again is in cycle 6, which thus can serve as an example of severe CI knock, while cycle 15 is a more typical cycle. Single-cycle analysis will concentrate on these two cycles.

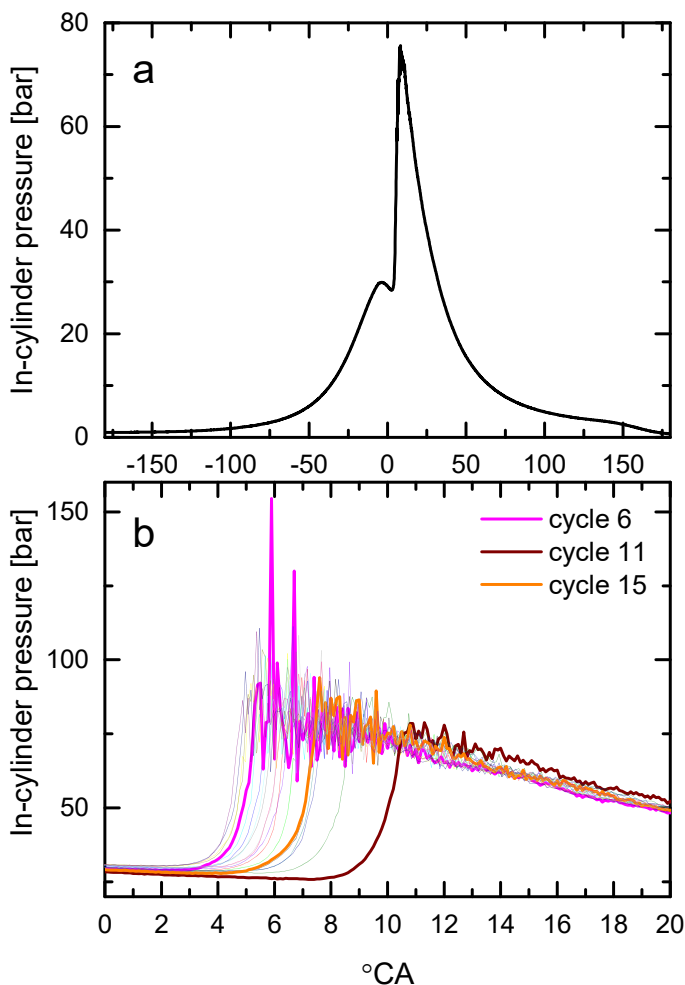


Figure 6.1 (a) Mean in-cylinder pressure of all 20 fired cycles. (b) Single-cycle pressure traces near TDC with cycle 6, cycle 11, and cycle 15 highlighted.

Figure 6.2 shows selected images from cycle 6. The images were corrected for BG by subtracting the mean of the first 30 images (all before injection) in the sequence. The corresponding pressure and  $AHRR$  are plotted in Figure 6.3. At  $2.4^\circ\text{CA}$ , just before EOI, auto-ignition originates on the right side of the piston bowl. Image 1 in Figure 6.2 shows the ignition site at  $2.7^\circ\text{CA}$  (indicated by a red oval), when it has become bright enough to be clearly seen. In fact, this ignition site is composed of several smaller

auto-ignition points. About 60 ms later, as seen in the upper right quadrant of image 2, these auto-ignition points have grown and combined into one bulk flame. Meanwhile the chemiluminescence also becomes brighter, indicating a local acceleration of the combustion reactions. This was also seen by Thirouard et al. [314] in port-fueled controlled auto-ignition (CAI) combustion and by König and Sheppard [315] during the end-gas auto-ignition in an SI engine. Also in image 2, a second auto-ignition site appears in the upper left quadrant (indicated by a red oval). The ignition delay in cycle 6 is 1.47 ms, which would be very long for traditional Diesel combustion. This is mainly due to the low intake temperature and pressure, as well as low wall temperatures, probably. The long ignition delay prompts a large proportion of premixed combustion, and the author thinks this is why knock occurs in this work.

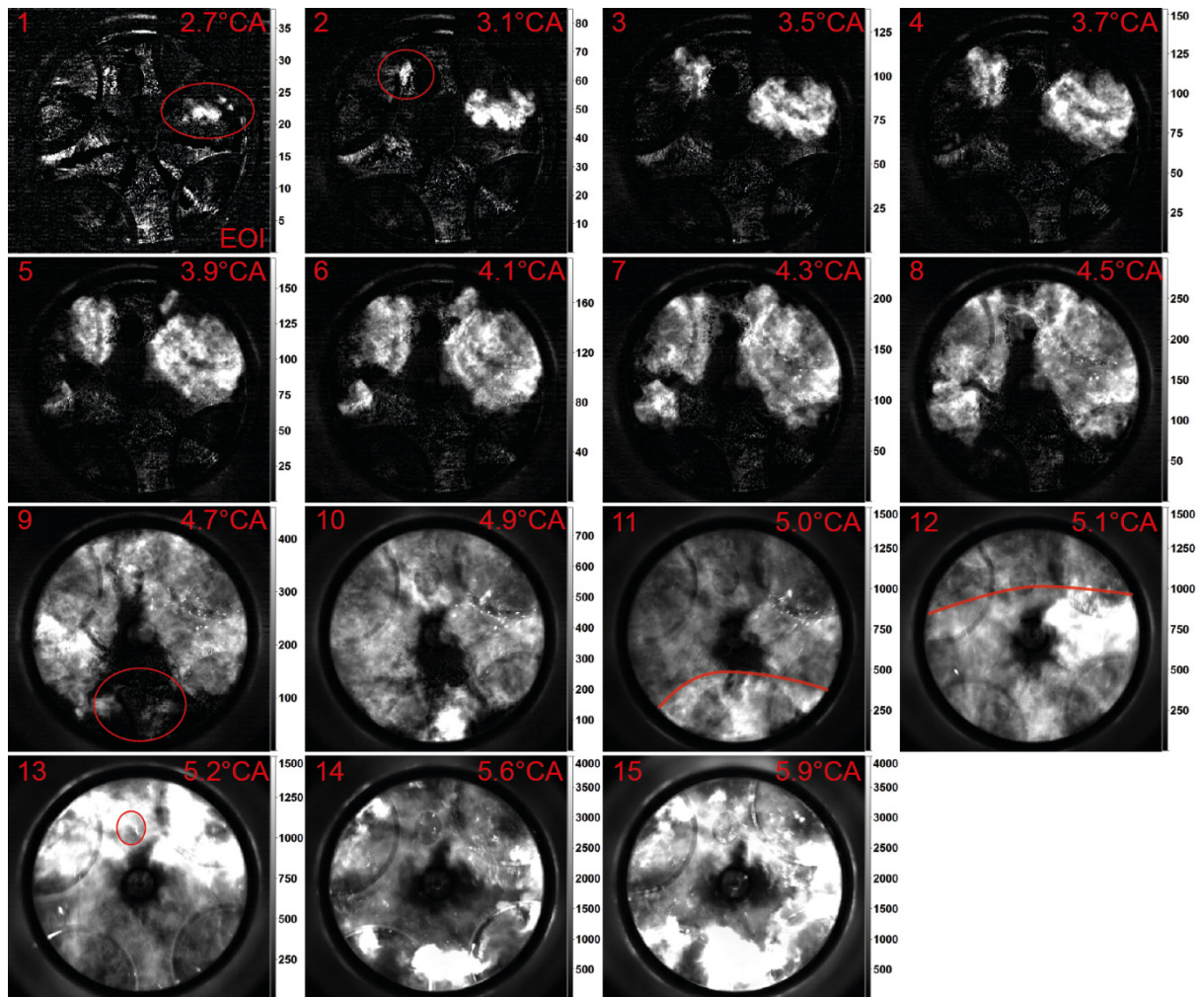


Figure 6.2 Selected images showing ignition and knock in cycle 6. Note that the gray scale (to the right of each image), indicating the flame luminosity, greatly varies throughout the figure. The first image is at EOI, 0.3°CA after ignition as indicated by the onset of flame luminosity. The red ovals and curves mark features discussed in the text.

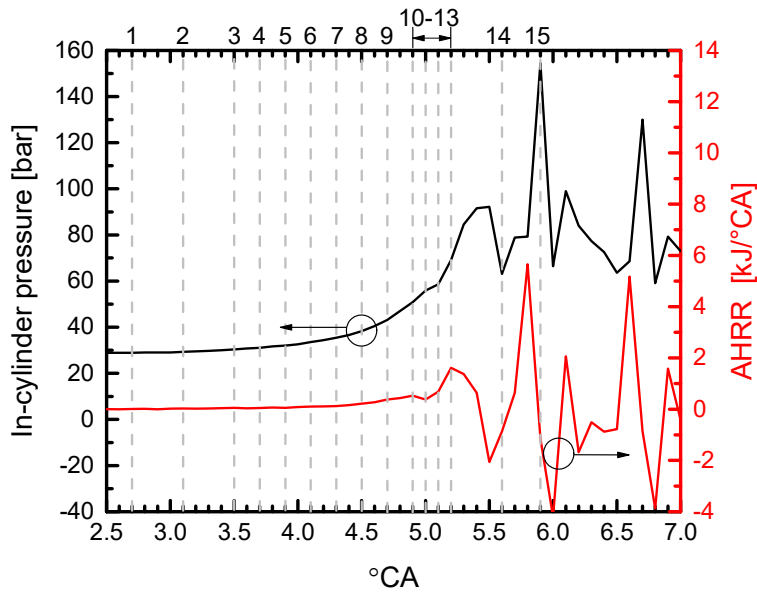


Figure 6.3 Pressure and AHRR in cycle 6. The numbers indicate the timing of the images shown in Figure 6.2.

From image 2 to image 9, the flame develops toward the lower region of the FOV. Both spatially isolated auto-ignition and reaction-front propagation are seen in the image sequence. Kernels first appear by auto-ignition, then expand and merge. The expansion resembles the turbulent flame propagation in SI engines [316]. For HCCI or PCCI combustion, SI-engine-like flame propagation was rarely seen in previous studies [314, 317-320]. For example in the port-fueled controlled auto-ignition (CAI) combustion in Ref. [314], oxidation reactions occurred simultaneously throughout the combustion chamber. The difference may stem from the greater inhomogeneity in this case because of the direct fuel injection. The apparent flame propagation speed (determined by optical flow, see Section 6.3.2) ranges from 20 to 50 m/s, one or two times higher than a typical turbulent flame propagation speed in an SI engine at this engine speed [316, 321]. If it were turbulent (transport-controlled) flame propagation, the high speed could be due to the strong turbulence generated by the high-pressure injection. Another possible regime is spontaneous-ignition propagation [322]. In this case, reaction is chemistry-controlled and only depends on the initial conditions. The reaction-front propagation speed can be one order of magnitude higher than in turbulent flame propagation [101, 323]. This has been experimentally seen during knock in SI engines [101]. Blessinger and Ghandhi [96] investigated the reaction-front structure during HCCI combustion and claimed that probably both of these two regimes existed. To clarify this point, more detailed dedicated investigations would be needed, for example examining the local thermochemical state of the mixture by laser diagnostics.

In the phase of combustion captured by images 2 – 9, auto-ignition outside the flame area does not trigger knock. Instead, new auto-ignition sites just join the larger bulk flame and become part of it. This was also observed by Tanoue et al. [306] investigating knock in SI combustion in a rapid compression-and-expansion machine. This is probably because the auto-ignition in this early phase does not have enough energy to trigger a pressure oscillation. The gas density at the location where auto-ignition occurs is largely affected by the compression by the bulk flame. Thus, the highest energy density occurs in those fuel/air-mixture parcels that ignite last, the “end gas”.

The end gas can be identified in image 9, where most of the mixture is already ignited except for the part in the lower region (indicated by a red oval). The central region also did not ignite, possibly because the mixture close to the injector quickly becomes very lean after injection [324]. From ignition to this point in time, combustion has increased the pressure in the combustion chamber, such that the

remaining end gas is at a high temperature and density. In image 10, the end gas now auto-ignites with much greater luminosity than the auto-ignition sites in the previous frames. In the next image (11), this has triggered an arch-shaped pressure wave (marked by a red line) around a region with elevated luminosity, indicating locally high pressure and *AHRR*. This is the origin of knock.

In the following image (12) in Figure 6.2, the location of the pressure wave is not as clear in the raw image. However, Figure 6.4 shows the vector fields derived by optical flow through two time-consecutive images (see Section 6.3.2) for images 11 and 12 from Figure 6.2 (5.0 and 5.1°CA, respectively). It can be seen that at both crank angles a steep gradient in luminosity coincides with a steep gradient in velocity, clearly dividing each image in two parts, as indicated by the red lines. These gradients indicate the location of the pressure wave [325]. From the locations in the image pair, the speed of the wave propagation is estimated to be 1300 m/s. This indicates a supersonic shock wave, considering the acoustic speed during knock in this case is below 900 m/s (see Section 6.3.2). In fact, the lower part of image 12 in Figure 6.2 appears smeared, consistent with significant gas movement even during the short exposure time of 6  $\mu$ s.

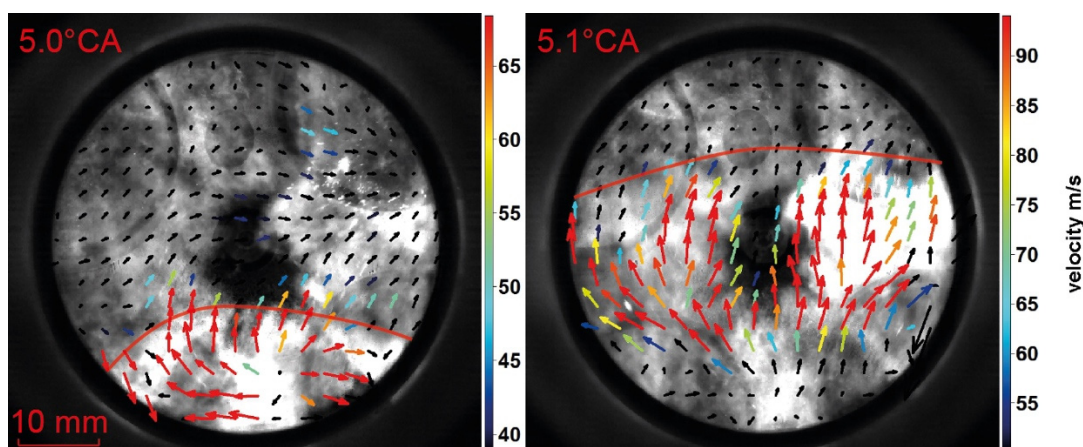


Figure 6.4 Shock-wave propagation in cycle 6. The two images correspond to images 11 and 12 in Figure 6.2, with the overlaid vector fields calculated by optical flow.

In image 13 in Figure 6.2, the upper part of the bulk flame has become brighter than before, and also brighter than the lower part. This could be from chemiluminescence. Higher pressure causes higher temperature and reactant concentration, resulting in faster reaction and brighter chemiluminescence. Another source of the elevated luminosity in image 13 may be soot incandescence, which positively correlates with soot concentration and temperature. Either way, in image 13, a brighter region would indicate higher pressure, temperature, and density. Therefore, until and including image 13, the brightness in the images may be a good indicator of local pressure and temperature. On the other hand, the author attributes the very bright regions near the bottom and the right side of the FOV in image 14 and 15 to soot from the squish region (maybe even from a pool fire). The three images between image 13 and 14, omitted in Figure 6.2, show these bright regions moving into the FOV.

In image 13, the pressure wave is thought to reach the upper brighter region. In fact, the pressure now increases faster than before, and the *AHRR* curve shows a maximum, consistent with the shock wave having reached the pressure sensor (marked by a red oval). Then the pressure trace starts to oscillate, indicating the build-up of a standing wave.

Visual inspection of the image sequences from the other cycles showed that the process of ignition and knock onset is similar in them, but a shock wave only could be identified in cycle 6. Overall, knock in partially premixed CI combustion stems from auto-ignition of the end gas, resembling knock in an SI

engine. In very severe cases, the extremely fast heat release in the end-gas region can cause a shock wave.

In experiments with fiber-based probes detecting near-infrared light from the combustion chamber [326], and also in high-speed OH\* imaging in the UV [327], fast variations of luminosity during knock had been found. Thus, the data here were also examined for such global intensity variations by calculating the mean intensity value over the whole image after BG correction. The temporal variation of this mean intensity is plotted in Figure 6.5. The exceptional character of cycle 6 is obvious. However, in all traces a sharp luminosity increase and subsequent oscillation similar to the pressure trace was found. It is well known that knock onset can be defined by the maximum derivative of the high-pass-filtered pressure signal [328]. Thus, this method was also tried for the image-intensity trace.

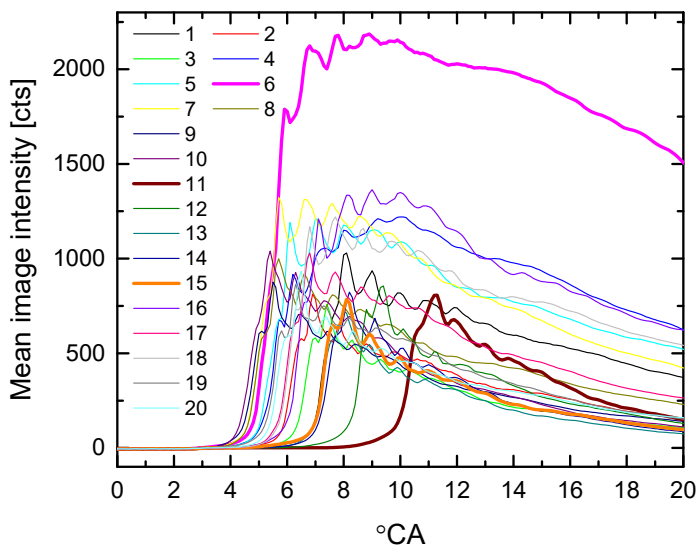


Figure 6.5 Temporal variation of mean image intensity of all 20 fired cycles. The numbers in the legend are serial numbers of each cycle.

Taking cycle 15 with medium knock intensity as an example, a schematic of the processing method is shown in Figure 6.6. A Kaiser-window finite impulse response (FIR) high-pass filter [329, 330] (MATLAB “kaiserord”, “fir1”) with a cut-on frequency of 3 kHz was applied to the mean intensity trace. Then the first derivative of this filtered intensity was calculated. It has multiple peaks. Knock onset was estimated as the timing of the first peak that exceeds 20% of the maximum derivative value. For downstream processing, it is also necessary to find the end of knock, which was defined here as the time when the absolute value of the intensity derivative was attenuated to 5% of the maximum. Thereby, in cycle 15, knock was optically determined to occur from 7.2°CA to 12.1°CA, while from the pressure signal it was from 7.2°CA to 17°CA using the same definition (see Section 6.3.2). Thus, the onset of knock determined from mean intensity of images acquired by broadband detection of visible light is very consistent with that determined from pressure. This is also true for the other cycles. The earlier end in the optical result implies that the luminosity-intensity oscillation decays faster.

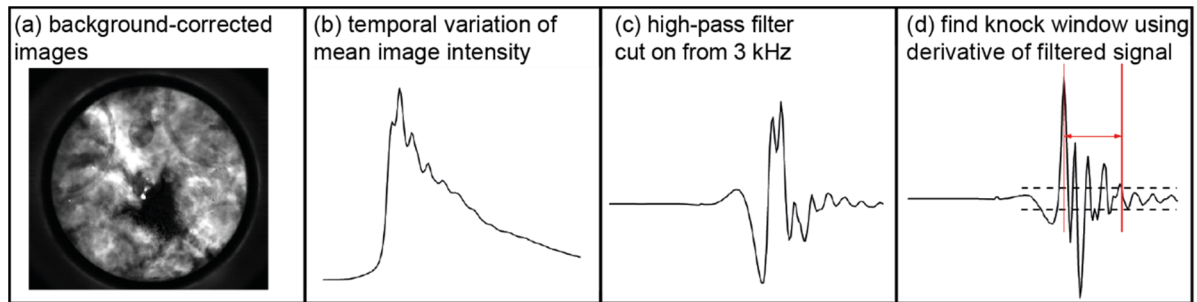


Figure 6.6 Procedure for determining the knock period from the image series.

### 6.3.2 Knocking frequency analysis

#### Pressure-trace analysis

Figure 6.7a shows an example pressure trace (cycle 15). In order to extract the frequency information, processing similar to Ref. [328] was implemented in MATLAB. The knocking time window was determined individually for every cycle using the same procedure as for the image-intensity trace, as described in Section 6.3.1. First, the pressure trace sampled at 60 kHz in IndiCom went through the 3 kHz FIR high-pass filter, then the knocking time “window” was established by peak-finding and determining the 5%-decay time. For cycle 15, the pressure trace during the knock window shown in Figure 6.7b. Within this time window, to prevent spectral leakage and to attenuate the strong amplitude in the beginning of the knock, a 75% tapered cosine bell window [242] (MATLAB “tukeywin”) was applied. The window function is also shown in Figure 6.7b. Finally, the Thomson's multitaper power spectral density (PSD) [331] (MATLAB “pmtm”) of this trace was calculated.

Figure 6.8 shows the PSD of cycle 15 within a range from 3 to 25 kHz, the latter being just below of what can be resolved with 60 kHz data rate without suffering from excessive noise and aliasing. There are two strong peaks at 9.50 kHz and 20.2 kHz, a weaker peak at 15.1 kHz, and several even weaker peaks at low frequencies.

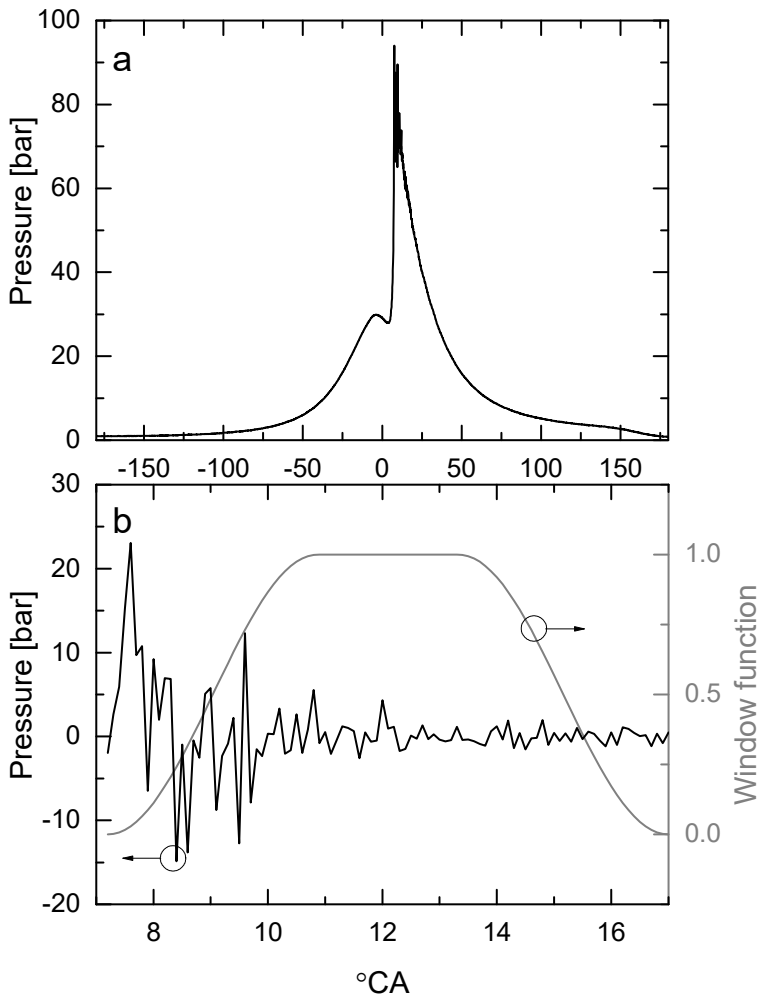


Figure 6.7 Pre-processing for pressure-trace analysis (cycle 15). (a) Acquired pressure trace, (b) high-pass-filtered signal in the knocking window and the time window function.

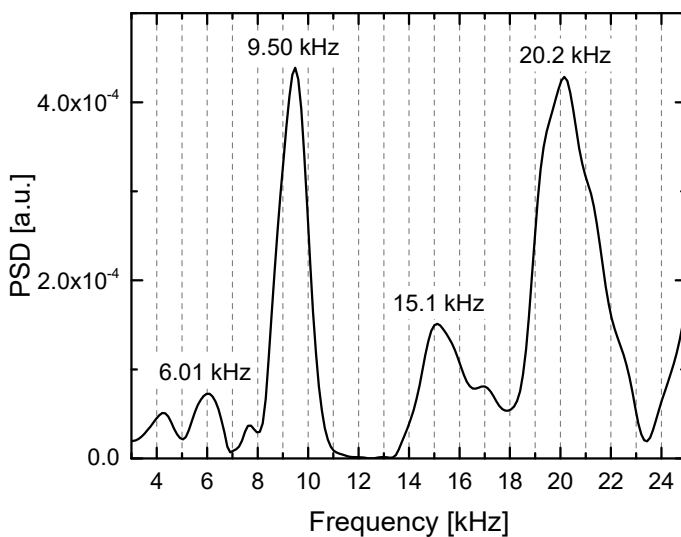


Figure 6.8 PSD of the pressure signal of cycle 15.

It is well known that during Diesel knock the in-cylinder pressure oscillations stem from acoustic resonance in the gas in the combustion chamber's cavity [70, 332-335]. Recent work showed this also to be true for HCCI knock [313, 336]. Here, the combustion chamber basically has an inverted top-hat

shape, including the cylindrical piston bowl and the squish region. During knock (slightly after TDC), the height of the squish region is less than 4 mm in most of the 20 cycles, small compared to the depth of the piston bowl, 10.4 mm. Also, the auto-ignition of the end gas, which triggers knock, is located in the piston bowl. Therefore, acoustical resonance mainly occurs in the piston bowl. According to classical acoustic theory [337], in a rigid duct with plane ends, the possible resonant frequencies  $f_r$  in different modes are given by

$$f_r = c_s \left[ \left( \frac{\alpha_{mn}}{B} \right)^2 + \left( \frac{p}{2l_{cyl}} \right)^2 \right]^{0.5} \quad (6.1)$$

where  $c_s$  is the speed of sound in the gas,  $B$  and  $l_{cyl}$  are the diameter and the length of the cylindrical cavity, respectively, and  $m$ ,  $n$ , and  $p$  are natural numbers denoting the circumferential, radial, and axial vibration mode numbers, respectively. The characteristic values  $\alpha_{mn}$  are the roots of the first-order derivative of the Bessel function. For the first four modes, the values of  $\alpha_{mn}$  are listed in Table 6.3 [337]. Also, a cross-sectional schematic of these modes is shown in Figure 6.9 [70], where the positive and negative signs indicate a representative pressure amplitude at some point in time.

Table 6.3 Resonance modes with values of  $\alpha_{mn}$  (taken from Ref. [337]) and theoretical frequency range in this work.

Modes	$\alpha_{mn}$	Frequency range
(1, 0)	0.5861	[8.96, 10.6] kHz
(2, 0)	0.9722	[14.9, 17.6] kHz
(3, 0)	1.3373	[20.5, 24.3] kHz
(0, 1)	1.2197	[18.7, 22.1] kHz

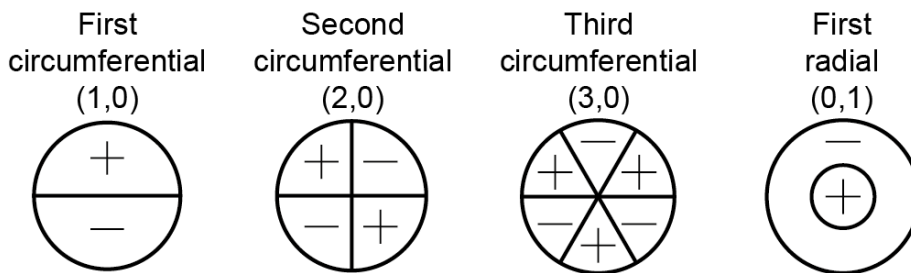


Figure 6.9 Schematic of transverse acoustic resonance modes in a cylindrical cavity [70].

Because the length of the cavity in this engine, namely the depth of the piston bowl, is only about one-fifth of the diameter, the axial modes are neglected here [338]. Equation (6.1) can then be simplified to

$$f_r = c_s \frac{\alpha_{mn}}{B} \quad (6.2)$$

To calculate the possible resonant frequencies, the speed of sound needs to be estimated. In an ideal gas, it is given by

$$c_s = \sqrt{\gamma R_s T} \quad (6.3)$$

where  $R_s$  is the specific gas constant, and  $T$  is the temperature of the gas.

The bulk in-cylinder temperature was estimated from the pressure trace by the ideal-gas law. The trapped mass was estimated from the *HRR* taking the injected fuel into account [339]. The knocking time window was determined for each individual single cycle based on the pressure variation, as described in Section 6.3.1. From this, the lowest and the highest temperature during knocking were determined for every cycle. For simplicity, a representative temperature range was estimated by averaging the single-cycle extrema, yielding 1450 to 2000 K.

The local gas composition during knock is between the two extremes of pure air and the products of stoichiometric combustion. From this range in gas composition and temperature, a corresponding range of  $\gamma$  and  $R_s$  was calculated according to the thermodynamic model of Lapuerta et al. [71]. With these thermodynamic parameters, the range of  $c_s$  was estimated as 730 to 860 m/s according to Equation (6.3). The lower limit occurs with the lower temperature and fully burnt gas, while the upper limit occurs with the higher temperature and pure air (a conservative estimate, since higher temperatures are actually likely to occur when more fuel is already burned). Inserting this range into Equation (6.2) yields the theoretical frequency ranges for the first four resonant modes listed in Table 6.3. Higher-order modes are outside of the frequency window (3 to 25 kHz) considered here.

Comparing the PSD of the pressure in cycle 15 (Figure 6.8) with the theoretical calculation, it is seen that the peaks at 9.50 kHz and 15.1 kHz mainly stem from the first and second circumferential modes of resonance. From the absolute frequency, the peak at 20.2 kHz cannot be conclusively assigned. Nevertheless, the ratio between different resonant frequencies is more characteristic for a system than their absolute values [70]. Taking 9.50 kHz as a known dominant frequency, the dominant frequencies for modes (3, 0) and (0, 1) are 21.7 kHz and 19.8 kHz. Therefore, it seems the first radial mode (0, 1) is closest to the peak at 20.2 kHz. However, these two characteristic frequencies are so close to each other that the resolution here (in this cycle 0.6 kHz, generally, dependent on the sample length in each cycle) is not high enough to distinguish them. The author will come back to this issue when discussing the optical results. The weaker peak at 6.01 kHz is probably due to the resonance in the squish region, since first-order circumferential resonance in that cavity theoretically occurs between 5.3 and 6.3 kHz. The other weak peak at 4.22 kHz may be due to the interaction of spectral leakage from low frequencies and the edge of the high-pass filter.

### Optical diagnostics

The flame movement was quantified as an optical-flow field, calculated in DaVis 8.2 based on image cross-correlation. Figure 6.10 shows the procedure. The processing parameters in DaVis are listed in Table 6.4. The cross-correlation algorithm used here is optimized for PIV technique, but the author found it also usable for optical flow, in which not images of particles, but instead a continuous scalar “pattern” is used.

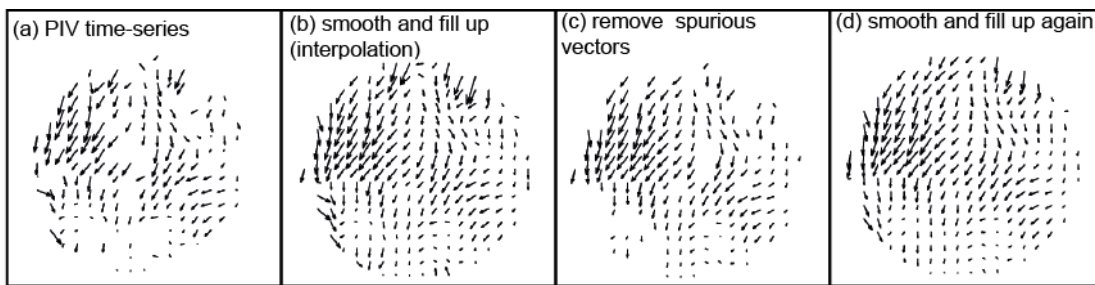


Figure 6.10 Procedure for flow-field calculation.

Table 6.4 Processing parameters for optical-flow calculation in DaVis 8.2.

1. PIV time-series		
Vector calculation parameters	Iterations	Multi-pass (decreasing size)
	Interrogation window properties	Start: $32 \times 32$ , adaptive PIV, 50% overlap, 3 passes End: $24 \times 24$ , adaptive PIV, 50% overlap, 3 passes
	Other options	High accuracy mode for final pass
Correlation function	All initial pass(es)	Standard I1*I2 (via FFT, no zero-padding)
	Final pass(es)	Standard I1*I2 (via FFT, no zero-padding)
	Deformed interrogation windows	Symmetric shift (both frames)

Multi-pass post-processing	Delete vector if peak ratio $Q < 1.5$	
	1 × median filter: remove & iteratively replace	Remove if diff. to avg. $> 2 * \text{Stdev of neighbors}$ (Re)insert if diff. to avg. $< 3 * \text{Stdev of neighbors}$
	Denoising	3 × 3
Vector post-processing	1 × median filter: universal outlier detection	Remove if residual $> 2$ , filter region: 3 × 3 (Re)insert if residual $< 0.1$ , min number of vectors: 5
	Delete vector	If correlation value $< 0.7$
		If peak ratio $Q < 2$
<b>2. Smooth and fill up</b>		
Vector post-processing	Fill-up empty spaces (interpolation)	
	Fill-up all	
	Smoothing	Optimal
	Make mask permanent	
<b>3. Remove spurious vectors</b>		
Vector post-processing	1 × median filter: universal outlier detection	Remove if residual $> 2$ , filter region: 11 × 11 (Re)insert if residual $< 2$ , min number of vectors: 1

The vector calculation was performed with pairs of BG-corrected time-consecutive frames (DaVis “PIV time-series”), here with  $0.1^\circ\text{CA}$  interval. Regions outside of the piston bowl were masked out. In multi-pass iterations, the interrogation areas were decreased in size from  $32 \times 32$  to  $24 \times 24$  pixels, overlapping 50%. In post-processing, vectors with correlation values less than 0.7 or peak ratios less than 2 were deleted. Also, vectors whose “normalized residual” [127] was greater than 2 were removed (DaVis option “universal outlier detection”). Thereafter, the vector field was smoothed and empty spaces were filled up via interpolation. However, among the newly filled-in vectors there were still some vectors with large deviation from their neighbors. Thus another “universal outlier detection” followed by smoothing and filling was used.

For cycle 15, Figure 6.11 shows the resulting vector fields with the flame luminosity in the background. Generally speaking, the flow fields show back-and-forth “sloshing” in the piston bowl, similar to the phenomenon observed by Rusly et al. [230]. (This is also clearly visible in the raw data when viewing the image sequence in slow-motion). The end gas in this cycle is located in the lower-right region of the piston bowl. When knock occurs, the vectors show the gas moving rapidly to the opposite side of the cavity, consistent with the observations made in Figure 6.2 (cycle 6), but without the sharply delineated gradient front encountered in cycle 6. The vector fields from  $7.3$  to  $7.6^\circ\text{CA}$  show maximum velocity magnitudes decaying from 290 m/s to 90 m/s. This is far lower than the speed of sound, which at that time is about 700 m/s. After this initial period, the median velocity stabilizes at around 50 m/s, while the speed of sound increases. Even in cycle 6, the most extreme cycle, the maximum velocity was 280 m/s, indicating that the gas movement is always subsonic.

Regarding every single vector (representing  $12 \times 12$  pixels) as a signal in a time-series, the oscillation frequency can be extracted. The procedure is shown in Figure 6.12. First, considering the low luminosity in the center, and less convincing vectors near the bowl wall, vectors in these areas were masked out. The vector fields were then imported into MATLAB for further processing. The vectors were decomposed into circumferential and radial components, taking the center of the piston bowl as the coordinate origin. Similarly to the pressure analysis, a 25% tapered cosine bell window (steeper edges than in the pressure case) was applied in the time domain. At each of the 762 vector locations, the circumferential and radial Thomson's multitaper PSDs were calculated over the time series in the knocking time window determined from the mean image intensity, as discussed in Section 6.3.1.

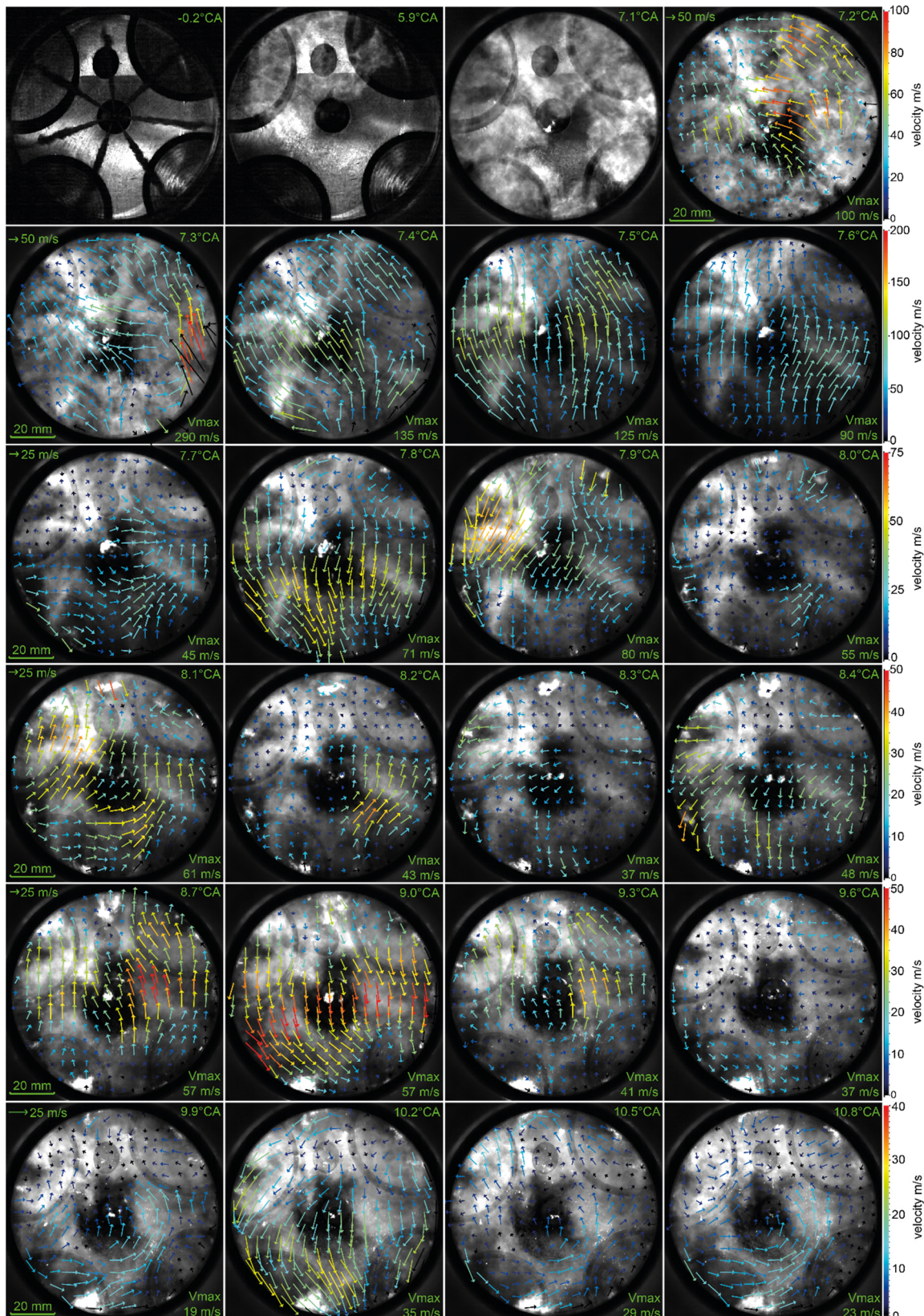


Figure 6.11 BG-corrected luminosity and (during knocking) optical-flow vector fields in cycle 15. Every 2nd vector in each dimension is shown. Note that in each row the color scale for the velocity magnitude is different. Selected crank angles, as indicated in each image, with irregular time spacings are shown. In the first row three raw images and one flow field before knock onset are shown for reference.

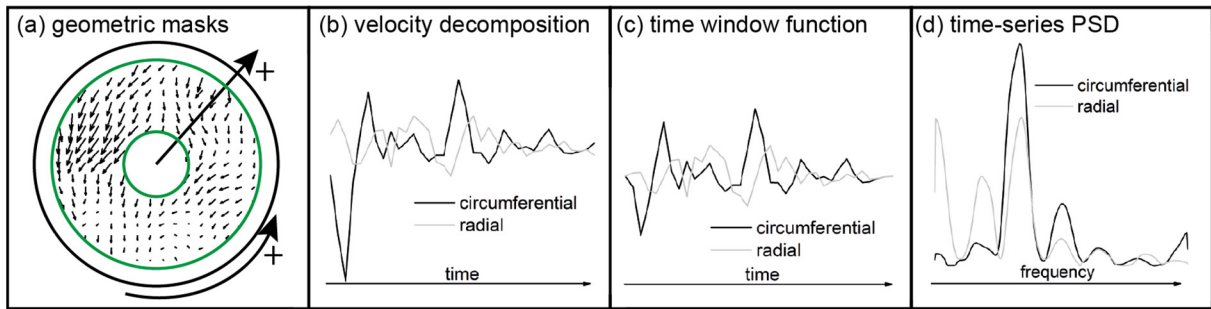


Figure 6.12 Procedure for flow-field PSD analysis.

Figure 6.13 shows the vector-derived PSD averaged over all locations within the masked FOV in comparison with the PSD of the pressure signal in cycle 15. In both velocity PSDs, there are four peaks at about 5, 10, 15, and 20 kHz. The strongest peak in the circumferential velocity PSD occurs at 9.96 kHz, which is very close to the first dominant pressure frequency at 9.50 kHz. Another smaller peak is located at 14.7 kHz, corresponding to the second dominant frequency from pressure analysis, 15.1 kHz. Surprisingly, in both pressure and velocity PSDs, coinciding peaks at 5.5 to 6 kHz appear. This feature may be attributable to resonance in the squish region, as discussed in the “Pressure-trace analysis”. In fact, from 8.1 to 8.4°CA slower-moving glowing particles and incandescent soot can be seen in the images, indicating low-frequency oscillations.

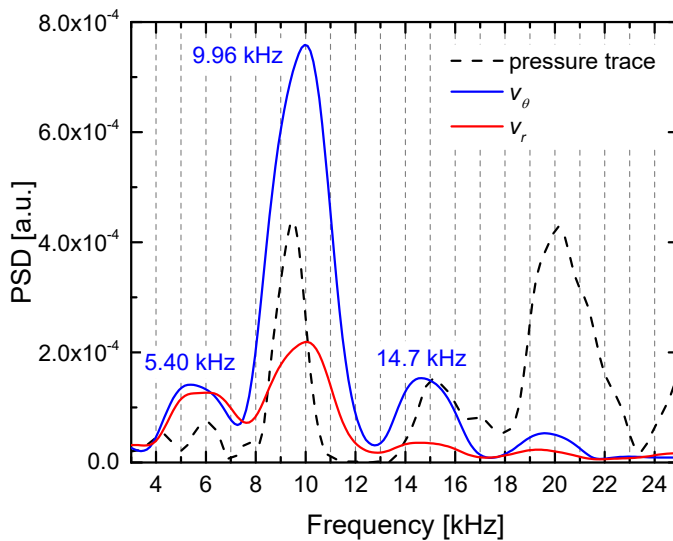


Figure 6.13 Single-cycle (cycle 15) spatial mean of the time-series PSDs of circumferential ( $v_\theta$ ) and radial velocity ( $v_r$ ), with the PSD of the pressure trace for comparison. Note that the (arbitrary) units of pressure PSD and velocity PSDs differ.

To better interpret the peaks in the velocity PSDs, how the gas in cavity resonance moves with respect to the nodal lines has to be considered. The sketches in Figure 6.14 show the direction of the gas movement in the first circumferential and radial modes. The gas movement is always normal to the isobaric lines. In the radial modes, the gas everywhere moves radially, while in circumferential modes, the gas moves both radially and circumferentially. As a result, the radial vector component  $v_r$  stems from both kinds of modes, while the circumferential component  $v_\theta$  stems only from the circumferential modes.

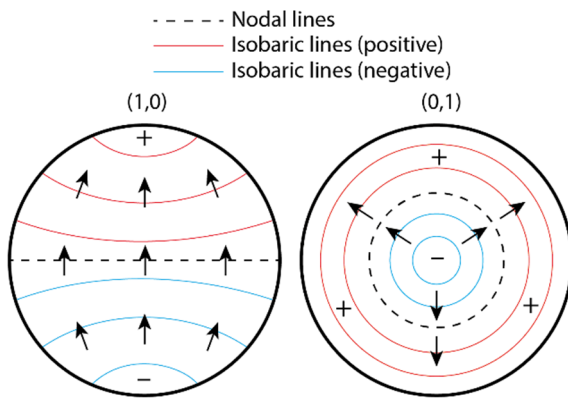


Figure 6.14 Schematic of the gas motion and nodal lines in the first circumferential (1, 0) and radial (0, 1) modes of resonance.

Compared to the PSD of circumferential vector components, the PSD of radial components is very similar in structure, which is expected, since it also includes information on circumferential resonance. The peak near 20 kHz, which the author could not clearly assign from pressure trace analysis, appears in both velocity PSDs. This suggests that this peak more likely stems from the third circumferential mode (3, 0) than from the first radial mode (0, 1). The fact that the radial values are generally lower indicates most information on circumferential oscillation appears in circumferential vectors. Note that swirl motion in the cylinder, a concern in Ref. [230], does not influence the PSD analysis much here, because the velocity from swirl varies at much lower frequencies (if at all) than the knock frequencies.

To examine the cycle-to-cycle variation of the results, the pressure and optical-flow PSDs of all cycles are shown in Figure 6.15. In results derived from the optical data, good cycle-to-cycle consistency is seen, whereas the pressure PSDs show much larger variation. This is mainly because of the limitations of a single-point signal. With one pressure sensor, the signal intensity is very dependent on the position of the sensor, because cavity resonance is a standing wave. In fact, if the sensor happens to be located exactly at the nodal line, there is no signal at all. The optical method is spatially resolved and therefore not influenced by the cyclically varying position of nodal lines. Also, in pressure, cycle 6 has much larger PSD values than the other cycles, while in optical results this is not the case. This difference is likely to be an artifact that is due to pixel saturation at the locally high image intensities in this cycle.

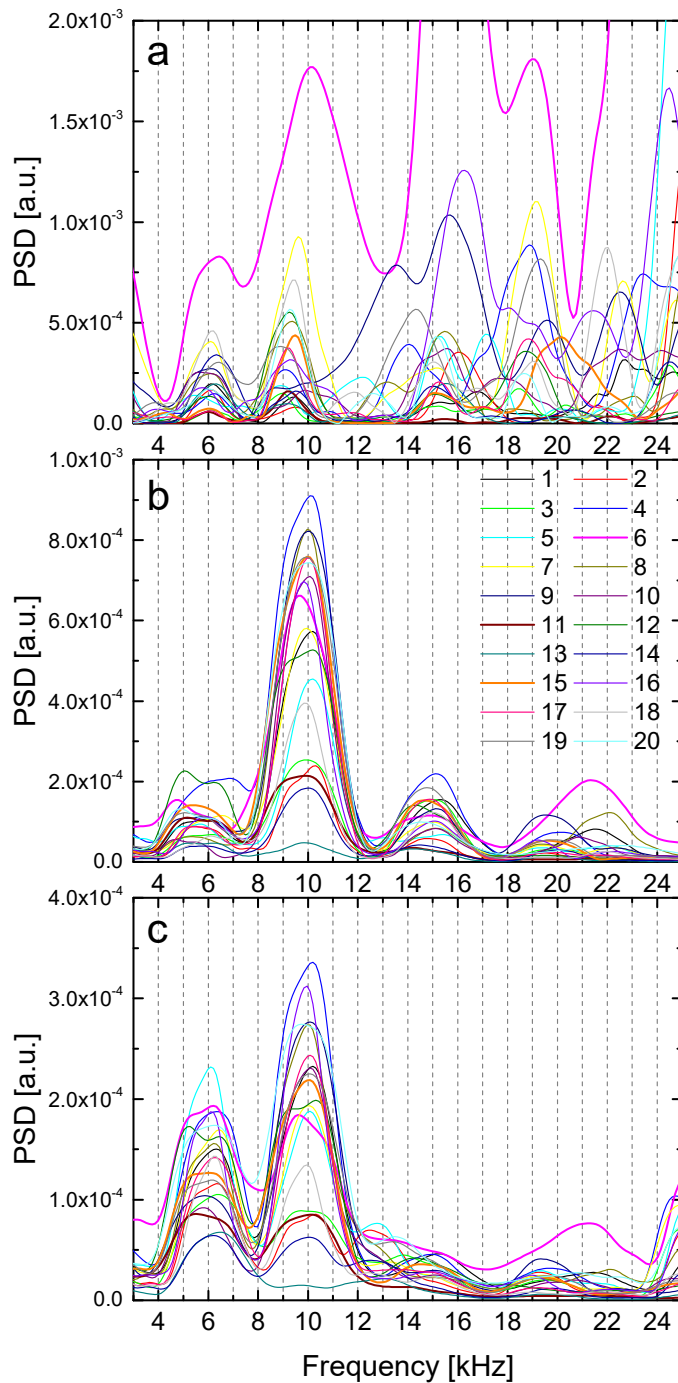


Figure 6.15 PSDs of all 20 fired cycles. (a) From pressure trace, (b) from circumferential components  $v_\theta$ , (c) from radial components  $v_r$ . Note that only the units of  $v_\theta$ -derived PSDs and  $v_r$ -derived PSDs are consistent.

### 6.3.3 Spatial origin of knock

Through the analysis of the temporal variation of the mean image intensity, the temporal origin of knock had been determined. It is also interesting to determine the spatial origin. From visual inspection, the initial movement of the luminosity features in the images seems to always start from the end gas, propagating to the opposite end of the bowl. To validate this conclusion, the second vector field after knock onset is spatially averaged into one single vector. The second vector field is used here because in the very first frame, the energy from the knock has not been fully transferred to the gas in the cavity. The spatially averaged vectors in each cycle are shown in Figure 6.16. The BG-corrected images

two or three frames before knock onset, indicating the position of the end gas, are shown in the background. In all the cycles, the vectors are aligned with the position of non-luminescent pocket of end gas. This means the initial vectors can be used to estimate the spatial origin of knock in an automated fashion. It is likely that a more refined analysis could actually pinpoint the spatial knock origin.

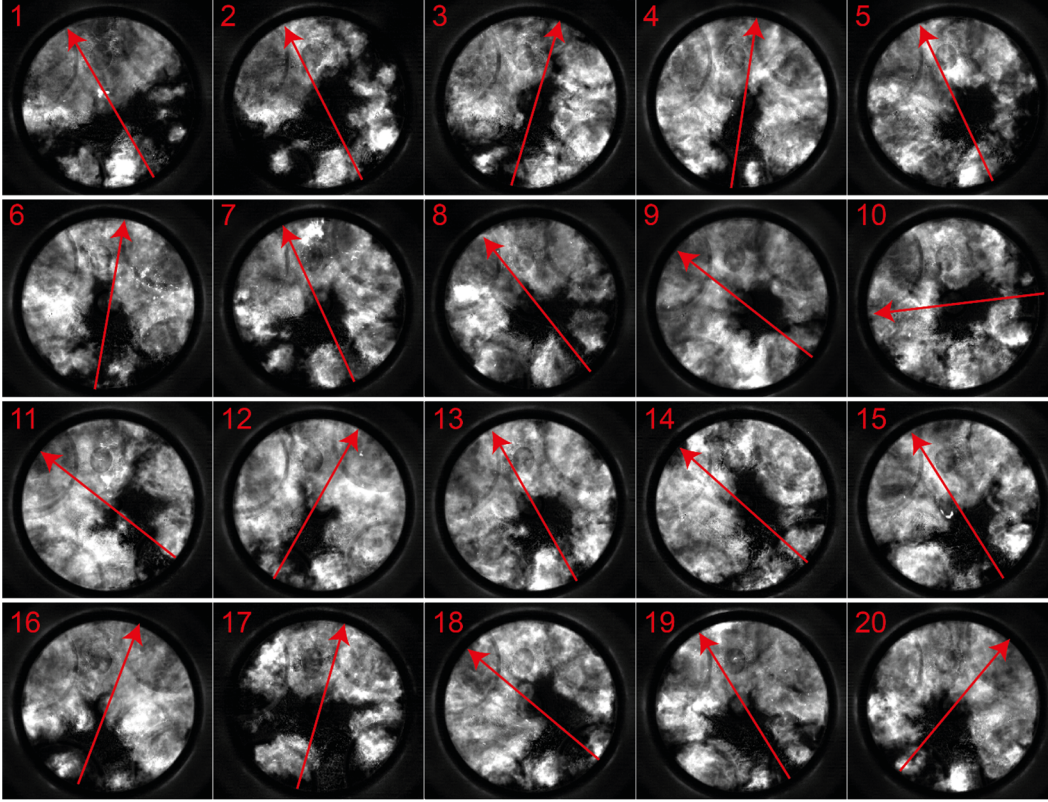


Figure 6.16 The spatial average of all vectors from the second vector field after knock onset, with an image shortly before knock in the background. Note that the vectors are rescaled to the same length.

### 6.3.4 Knock intensity

In classical pressure-trace analysis, various metrics for knock intensity have been proposed, including the maximum pressure rise rate, the integral of modulus of pressure oscillations (*IMPO*), and the maximum amplitude of pressure oscillations (*MAPO*) [338, 340]. In the optical measurements, based on resonance theory it is not hard to imagine that the velocity of the gas in the cavity positively correlates with the intensity of pressure oscillation. Thus, *IMPO* was calculated as the integral of the modulus of the high-pass-filtered pressure signal within a certain time window [340], which is chosen as 15°CA after the knock onset:

$$IMPO = \int_{onset}^{onset+W_t} |\tilde{p}_{cyl}| dCA \quad (6.4)$$

where  $\tilde{p}_{cyl}$  is the filtered pressure,  $W_t$  the time window,  $CA$  the crank angle.

Correspondingly, a knock intensity  $KI_{opt}$  was determined from the optical-flow signal  $v$ , as expressed by Equation (6.5). The modulus of the vectors was integrated first image-wide and then temporally within a window of 20 frames after knock onset. This window is much shorter than that chosen for the pressure signal, because the initial knock period shows large velocity magnitude and therefore is not much influenced by noise and swirl.

$$KI_{opt} = \sum_{onset}^{onset+W_t} \sum |v| \quad (6.5)$$

Figure 6.17 shows the correlation between  $IMPO$  and  $KI_{opt}$ . Linear fitting was conducted without cycle 6 (shown in green), since in this severely knocking cycle, significant parts of the image are saturated by soot incandescence, and the vectors obtained in these regions are biased towards lower magnitudes. The rest of the data shows a reasonable proportionality between these two indices.

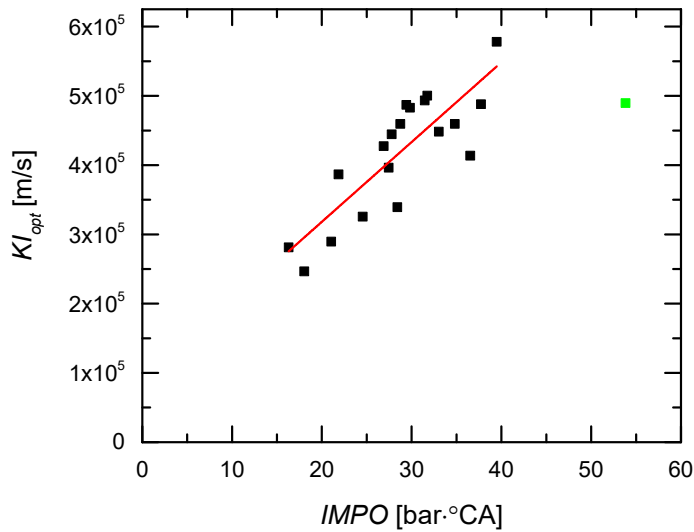


Figure 6.17 Correlation between optically determined knock intensity and pressure-determined knock intensity. Cycle 6 is shown in green and not considered for fitting.

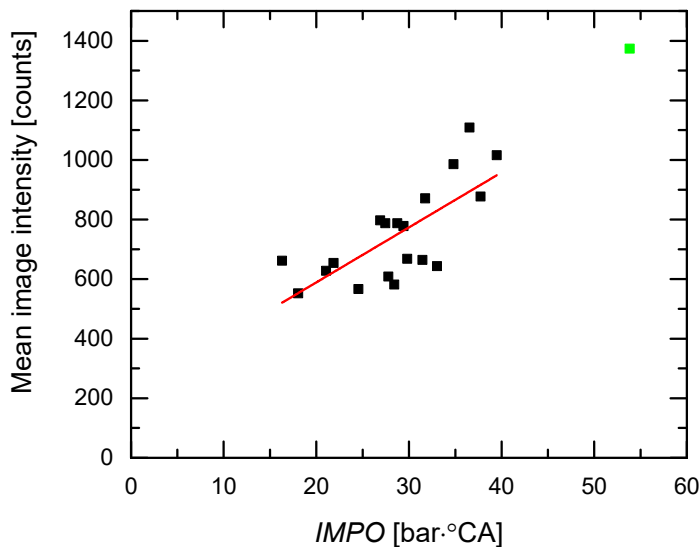


Figure 6.18 Correlation between the temporally averaged image-wide mean intensity and knock intensity. Cycle 6 is shown in green and not considered for fitting.

In SI engines, compared to normal combustion, knock is usually accompanied with elevated luminosity [315, 326, 338]. In fact, cycle 6, with the highest pressure rise rate, also shows very high luminosity as shown in Figure 6.1b. Therefore, it is interesting to see if the image intensity in general correlates with knock intensity in this CI case. Here, the image intensity is represented by the temporally-averaged image-wide mean intensity over 20 frames starting from knock onset. The correlation with  $IMPO$  is shown in Figure 6.18. It can be seen that there is a positive correlation, indicating higher chemiluminescence and soot luminosity during heavier knock. A linear fit was used in Figure 6.18, but actually the data points may better be represented by a power dependency, since soot incandescence increases with the fourth power of temperature.

## 6.4 Summary and conclusions

At very high repetition rates, images of luminosity during compression-ignition knock as well as the in-cylinder pressure were recorded. N-dodecane was used as a Diesel surrogate. The spatiotemporal evolution of knock was examined. A series of post-processing tools was developed to obtain temporal and spatial origin of knock, flow fields, knock frequency information, and knock intensity from the images. The optical results were compared to those from the pressure traces.

The chosen operating conditions and fuel result in a very long ignition delay, promoting the occurrence of knock. Knock in this compression-ignition experiment originates from the auto-ignition of end gas, like in spark-ignition engines. During the flame development, sequential auto-ignition sites occur and expand in a way seemingly similar to turbulent flame propagation in spark-ignition engines, but with higher propagation speed. The auto-ignition points outside the flame area do not trigger knock until the end gas auto-ignites. In one extreme case, a shock wave occurred. The temporal variation of mean image intensity can define an accurate knock onset timing, as can the pressure trace, while the spatial knock origin can be estimated from the first few velocity fields after knock onset. The velocity fields were calculated by optical flow based on cross-correlation. During knock, the gas was observed to slosh back and forth. The movement was more intense in the first few images, followed by stable oscillation. The gas velocity was always below the speed of sound. Through power-spectral-density analysis of the vector-field time-series, the dominant oscillation frequencies were found. These frequencies from the flame (or gas) oscillation are consistent with those from the in-cylinder pressure and from theoretical calculation. Compared to the pressure-signal analysis, the optical method shows less cycle-to-cycle variation. This is because it is spatially resolved and not influenced by the cyclically varying position of nodal lines. The knock intensity was defined by the vector magnitude during knock and shows good linear correlation with the integral of modulus of pressure oscillations. Also, the image-wide luminosity positively correlates with knock intensity.

With regards to future work, to improve the experiment, even higher sampling rates of both pressure trace and images are recommended to alleviate the influence of aliasing and spectral leakage. Also, time-frequency analysis [341] could be applied then to investigate temporal variation of frequencies during knock. Pixel saturation and image smearing should be avoided by stronger blue-biased filtering and a shorter exposure time, respectively. In addition, more cycles are desirable to clarify the statistical correlation of knock intensities defined by different methods. Laser-based diagnostics can be implemented to investigate the regime in which the reaction front propagates. In vector analysis, simultaneous spatial and temporal interpolation, which is needed to fill the vector gaps, could improve the power-spectral-density results. The temporal oscillation of the image intensity, as shown in Figure 6.5, could be also investigated to extract the resonant frequency information. For this, dividing the field-of-view into grids like the vector field might help increase the sensitivity. A refined analysis could be performed to pinpoint the spatial knock origin automatically. This experiment used n-dodecane, which has a higher cetane number than most commercial Diesel fuels. Further studies could investigate the effect of a fuel with more realistic auto-ignition properties.

---

## Chapter 7 Summary, conclusions, and future work

---

### 7.1 Summary and conclusions

In this work, ignition and combustion of Diesel sprays were investigated in a light-duty optically accessible Diesel engine. Much of the investigations was centered on Spray B, an injector and set of thermodynamic conditions standardized by the Engine Combustion Network.

In order to determine the in-cylinder flow field, PIV was performed for both low-swirl and high-swirl conditions. The initial momentum for the swirl motion is found to be generated at the beveled valve seat. Before IVC, the swirl level is very stratified at different axial positions in the cylinder, also varying temporally, with the maximum shortly after the maximum intake valve lift. Around IVC, the airflow starts to resemble a solid-body rotation with similar swirl levels at different vertical positions. Afterwards, the swirl level decreases slowly, and high turbulent kinetic energy is found mainly at the swirl center. The swirl ratio at IVC is thus the most useful to characterize the swirl level for this engine. However, because of the shortage of data at high swirl, the swirl ratios at the maximum piston speed during the intake are used for now, being 2.4 at low swirl and 6.0 at high swirl.

Regarding the in-cylinder temperature field at the Engine-Combustion-Network-relevant conditions, single-color tracer LIF thermometry was performed near TDC, and a method for flat-field correction in the standing engine was developed. At low swirl, a large thermally uniform core region is found in the piston bowl, while at high swirl, the ensemble-average temperature field is prominently radially stratified with a thicker boundary layer, showing a ring-shaped low-temperature region. Thus, the adiabatic-core theory is much more accurate at low swirl than at high swirl. At similar bulk temperatures, high-swirl yields a higher core temperature in the piston bowl than low swirl. Thus, especially at high swirl, the in-cylinder flow and temperature field in the engine is complex, temporally dynamic, and spatially stratified, and consequently very different from that in a high-temperature high-pressure combustion vessel.

Engine Combustion Network Spray B (three jets) was investigated in a small-bore optical Diesel engine. To obtain the basic spray and combustion indicators, “fire-deck retro-reflection” with pulsed LED light was developed, quasi-simultaneously imaging both liquid and gas phase of the fuel spray as well as combustion, all with relatively modest effort. The optical thickness and time derivative were calculated to identify the liquid and gas phase, respectively. The results, including liquid length, vapor penetration, spray dispersion angle, ignition delay, ignition location, flame luminosity, and heat release rate, all show physically reasonable variation with ambient temperature and density as well as with injection pressure, providing a database for CFD validation.

Regarding the effect of swirl, at the same bulk temperature, the liquid length is lower at high swirl, consistent with the higher core temperature found via LIF as well as the improved air entrainment, while the ignition delay is not evidently shortened, which may be related to the thicker boundary layer near the bowl’s side wall. The jet head is convected farther in the down-swirl direction, leading to an ignition location also farther downwind. The *HRR* shows a higher and wider premixed-burn peak and decreases faster in the burn-out phase. The effect of swirl on spray penetration and dispersion angle cannot be fully clarified in this work because of the low reflectivity at the valve seat.

As to the hole-to-hole variation for the Engine Combustion Network Spray B injector 211201, several phenomena were found against the previous semi-empirical correlations [41, 42] and an experimental study [54]. Hole 3 has the largest orifice outlet diameter, but jet 3 does not show the highest liquid length and gas penetration, probably due to the irregular surface geometry of hole 3. The hole-to-

---

hole variation of ignition delay is even more complex, depending on the swirl level and ambient gas temperature.

Comparing the current results to other Spray B data from vessels and engines, reasonable agreement is seen in the time-resolved liquid length, spray penetration, and *HRR*. However, for the time-averaged liquid length and ignition delay, the different diagnostics used by different groups make it hard to see the potential differences caused by different facilities (different in the sense of combustion chamber size and flow field).

Two broad trends in ignition delay – dependent on the diagnostics – are found within the Engine Combustion Network Spray B database, one in data from non-intensified visible-chemiluminescence imaging, and the other from pressure-based analysis and OH\* - chemiluminescence imaging. To clarify this, multi-spectral imaging based on two simultaneously running high-speed cameras was performed. One camera is intensified with a band-pass filter for OH\* and the other has a non-intensified Bayer-RGB sensor blue-biased with a Schott BG filter. The time evolution of the area-averaged flame luminosity in the flame contours in each of the four color channels, UV, blue, green, and red, is obtained by dynamic thresholding [282]. The results show that the OH\* - chemiluminescence and visible-chemiluminescence signal actually match each other at ignition around the Engine Combustion Network standard condition. The seemingly advanced ignition in the pressure-based results, mostly by (apparent) *HRR* analysis, are probably due to the low-temperature reaction. Band-pass-filtered UV imaging is found less sensitive to the low-temperature chemiluminescence but more sensitive to the high-temperature chemiluminescence, compared to non-intensified visible-chemiluminescence imaging. Both back-extrapolation and thresholding of the flame-luminosity trace can be used to quantify the ignition delay, but the threshold should be high enough to be above the low-temperature-reaction level. The (apparent) *HRR* trace does not match the flame-luminosity traces at ignition, but the unfiltered net-pressure-rise trace does. However, it suffers from single-cycle complexities and a delay by the finite speed of sound.

Also with blue-biased high-speed imaging, flame-luminosity images during compression-ignition knock were recorded. Here, a 7-hole injector was used. A very long ignition delay promoted the occurrence of knock at the end-gas region. With the concept of optical flow, the flow fields of flame due to the in-cylinder acoustic resonance were determined based on image cross-correlation. A series of post-processing tools was developed to obtain the temporal and spatial origin of knock, knock frequency, and knock intensity from the images. The optical results match well with those from the pressure traces. During the flame development, both sequential auto-ignition and flame propagation exist. In one extreme case, a shock wave occurred. The mean image intensity also temporally oscillates, like the pressure trace, and helps define the knock onset and duration. Through spectral analysis of the vector-field time-series, the dominant oscillation frequencies were found. They are consistent with those from the in-cylinder pressure trace and from theoretical calculation.

## 7.2 Future work

The flow field at high swirl needs to be measured at more crank angles to determine the swirl ratio at IVC. At both swirl levels, both the flow and temperature field in the piston bowl around TDC should be measured at different vertical positions, to investigate the low-temperature ring (see Figure 3.18) as well as why jet 1 ignites later compared to the other jets at high swirl. Regarding the single-color tracer LIF method, the small-scale vertical gradients (see Figure 3.17) could be removed by image processing, improving the measurement precision.

For the Engine Combustion Network Spray B study, a diagnostic for the fuel vapor not based on the retro-reflection by the fire deck needs to be developed to investigate the effect of swirl on spray

---

penetration and dispersion angle, as well as to detect the fuel vapor after spray impingement. To improve the comparison of liquid length with that in the Engine Combustion Network database, Mie-scattering measurements should be performed systematically with carefully selected thresholds. The zero-crossing points of optical thickness by the fire-deck retro-reflection method can be investigated further for liquid length quantification. The flame lift-off length is a very important combustion indicator and should be investigated by additional diagnostics and with higher spatial resolution than available in the bowl-wide imaging used here. To the Engine Combustion Network community, the author recommends that more liquid-length data at different ambient temperatures be measured in combustion vessels for comparison with engine data, especially by Mie scattering, since in the latter it is hard to achieve an absolute target temperature. Regarding the diagnostic-sensitive metrics for both spray and combustion, the effect of different diagnostic methods as well as that of different nozzles should be clarified in a vessel first. Thereafter, a consistent method should be used in different facilities, over an agreed-on temperature variation, to investigate the effect of the facility (chamber size and flow field).

Regarding the approach to ignition-delay detection used in this work, the image segmentation for flame areas could be improved by dividing the field-of-view into three sectors before the dynamic thresholding, so that individual thresholds are used for the flame detection of different jets. The current dynamic-thresholding algorithm produces too high a threshold for a fast-increasing flame luminosity, which needs further improvement. The back-extrapolation approach for detecting ignition from the flame-luminosity traces should be automated. In the current multi-spectral system, the green channel captures both chemiluminescence and soot incandescence, and is not very useful. It could be assigned to, e.g., green-illuminated spray imaging. Unfortunately the color separation in this high-speed camera, like that of most current Bayer-type RGB sensors, is not very good, with much overlap between color channels.

Finally, to improve the knock experiment, even higher sampling rates of both pressure trace and images are recommended to alleviate the influence of aliasing and spectral leakage. Pixel saturation and image smearing should be avoided by a shorter exposure time. In addition, more cycles are desirable to clarify the statistical correlation of knock intensities defined by different methods. Laser-based diagnostics can be implemented to investigate the regime in which the reaction front propagates. In vector analysis, simultaneous spatial and temporal interpolation, which is needed to fill the vector gaps, could improve the power-spectral-density results. The temporal oscillation of the image intensity, as shown in Figure 6.5, could be also investigated to extract the resonant frequency information. For this, dividing the field-of-view into grids like the vector field might help increase the sensitivity. A refined analysis could be performed to automatically pinpoint the spatial origin of knock.

---

---

## Chapter 8 Bibliography

---

### 8.1 Posters, presentations, and publications

#### 8.1.1 *Peer-reviewed journal papers*

Published:

Zhao, M. and Kaiser, S., “A Study of ECN ‘Spray B’ in a Light-Duty Optically Accessible Diesel Engine Based on High-Speed Imaging with LED Retro-Reflection,” SAE Technical Paper 2019-01-0550, 2019, doi: 10.4271/2019-01-0550.

Zhao, M. and Kaiser, S., “Optical diagnostics for knock in compression-ignition engines via high-speed imaging,” SAE Int. J. Engines 11(6): 903-918, 2018, doi: 10.4271/2018-01-0631.

In preparation:

Zhao, M. and Kaiser, S., “Multi-spectral high-speed imaging of ignition in Diesel combustion in a light-duty compression-ignition engine,” to be submitted to SAE Int. J. Engines, 2020.

#### 8.1.2 *Conferences*

Zhao, M. and Kaiser, S., “A brief introduction to the Engine Combustion Network (ECN) and a study of ECN “Spray B” in a light-duty optical Diesel engine”, conference paper at Encom 2019 – 14th International Congress on Engine Combustion and Alternative Concepts. 2019: Waischenfeld, Germany.

Zhao, M. and Kaiser, S., “Hyperspectral high-speed imaging of Diesel and dual-fuel combustion”, poster at the 2019 Gordon Research Conference on Laser Diagnostics in Energy and Combustion Science. 2019: Les Diablerets, Switzerland.

Zhao, M. and Kaiser, S., “A Study of ECN ‘Spray B’ in a Light-Duty Optically Accessible Diesel Engine Based on High-Speed Imaging with LED Retro-Reflection”, SAE technical paper & oral presentation at SAE World Congress Experience 2019. 2019: Detroit, USA.

Zhao, M. and Kaiser, S., “Time-resolved simultaneous visualization of liquid and gas-phase fuel and combustion by retro-reflection of pulsed LED light in an optically accessible Diesel engine”, poster at THIESEL 2018 – Conference on Thermo- and Fluid Dynamics Processes in Direct Injection Engines. 2018: Valencia, Spain.

Zhao, M. and Kaiser, S., “Optical diagnostics for knock in compression-ignition engines via high-speed imaging”, SAE technical paper & oral presentation at SAE World Congress Experience 2018. 2018: Detroit, USA.

Zhao, M. and Kaiser, S., “Optical Diagnostics for Diesel Knock Based on High-Speed Imaging and Optical Flow”, conference paper & oral presentation at the 28. Deutscher Flammentag – Verbrennung und Feuerung. 2017: Darmstadt, Germany.

#### 8.1.3 *ECN workshops*

ECN Workshop 6.8, 2019, oral presentation “Effect of diagnostics on ignition delay measurements for ECN Spray B”.

ECN Workshop 5.13, 2018, oral presentation “Methodology and experimental uncertainty of Spray B measurements in University of Duisburg-Essen”.

---

ECN Workshop 5.3, 2017, oral presentation “Test bench setup and first measurements for Spray B in a light-duty optical engine”.

ECN Workshop 4.9, 2016, oral presentation “Preparations for Spray B engine experiments”.

## 8.2 Supervised student theses

Kee Tian Tee, “Design and testing of an intake-air heater for an optically accessible Diesel engine”, bachelor’s thesis, 2018.

Guanyu Wang, “Development of a 1D simulation model for an optically accessible Diesel engine in GT-POWER”, bachelor’s thesis, 2018.

Simon Lohwasser, “Design of the piping system for a single-cylinder research engine in PTC Creo”, bachelor’s thesis, 2018.

Muhammad Irfan Tahir, “Optical studies of spray characteristics in an optical diesel engine via schlieren imaging with corrective lenses”, master’s thesis, 2017.

Jan Niklas Bühnen, “Conversion of an automotive Diesel engine to single-cylinder operation, set-up on a test bench, and first experiments”, master’s thesis, 2017.

## 8.3 References

1. "Germany Moves to Ban Internal Combustion Engine by 2030", <https://www.traditionalpractices.com/2019/03/13/germany-moves-to-ban-internal-combustion-engine-by-2030/>, accessed Sept. 30, 2019.
  2. "Nine Countries Say They'll Ban Internal Combustion Engines. So Far, It's Just Words.", <https://qz.com/1341155/nine-countries-say-they-will-ban-internal-combustion-engines-none-have-a-law-to-do-so/>, accessed Sept. 30, 2019.
  3. "Signal of Change / Diesel and Petrol Cars Will No Longer be Sold in Hainan Province of China", <https://thefuturescentre.org/signals-of-change/222351/diesel-and-petrol-cars-will-no-longer-be-sold-hainan-province-china>, accessed Sept. 30, 2019.
  4. "The Electric Car Revolution is Coming. This is What Has to Happen First", <https://edition.cnn.com/2019/07/18/cars/electric-car-market-sales/index.html>, accessed Sept. 30, 2019.
  5. "Electric Vehicle Outlook 2019". 2019, Bloomberg New Energy Finance.
  6. Janek, J., and Zeier, W.G., "A Solid Future for Battery Development", *Nature Energy* 1(9), 2016, doi:[10.1038/nenergy.2016.141](https://doi.org/10.1038/nenergy.2016.141).
  7. "Specific Energy and Energy Density of Fuels", <https://neutrium.net/properties/specific-energy-and-energy-density-of-fuels/>, accessed Sept. 30, 2019.
  8. "Busting 7 of the Most Common Myths about Electric Cars", [https://www.greencarreports.com/news/1122838\\_busting-7-of-the-most-common-myths-about-electric-cars](https://www.greencarreports.com/news/1122838_busting-7-of-the-most-common-myths-about-electric-cars), accessed Mar. 11, 2020.
  9. "Commercial Motor Vehicle Classification", <https://www.thebalancesmb.com/commercial-motor-vehicle-classification-2221025>, accessed Sept. 30, 2019.
-

10. "Support – Supercharging", <https://www.tesla.com/support/supercharging>, accessed Sept. 30, 2019.
  11. "Global Transport Scenarios 2050". 2011, World Energy Council: United Kingdom.
  12. Pickett, L.M. "Introduction to ECN 6". in *ECN Workshop 6*. 2018. Valencia, Spain: Engine Combustion Network.
  13. Krüger, C., "How High Fidelity Simulation and Diagnostic Tools Can be Used for the Development of Hybrid Powertrains (oral only)", in *THIESEL 2018 Conference on Thermo- and Fluid Dynamic Processes in Direct Injection Engines*. 2018: Valencia, Spain.
  14. Mollenhauer, K., and Tschöke, H., "Handbook of Diesel Engines", 1st Edition, Springer-Verlag Berlin Heidelberg, 2010, p. 4, doi: [10.1007/978-3-540-89083-6](https://doi.org/10.1007/978-3-540-89083-6), ISBN: 978-3-540-89082-9.
  15. Mollenhauer, K., and Tschöke, H., "Handbook of Diesel Engines", 1st Edition, Springer-Verlag Berlin Heidelberg, 2010, p. 9, doi: [10.1007/978-3-540-89083-6](https://doi.org/10.1007/978-3-540-89083-6), ISBN: 978-3-540-89082-9.
  16. Wei, H., Zhu, T., Shu, G., Tan, L., and Wang, Y., "Gasoline engine exhaust gas recirculation – A review", *Applied Energy* 99:534-544, 2012, doi:[10.1016/j.apenergy.2012.05.011](https://doi.org/10.1016/j.apenergy.2012.05.011).
  17. "Selbststudienprogramm 465 – Der 1,2l-3-Zylinder-TDI-Motor mit Common-Rail-Einspritzsystem – Konstruktion und Funktion". 2010, VOLKSWAGEN AG: Wolfsburg.
  18. Mollenhauer, K., and Tschöke, H., "Handbook of Diesel Engines", 1st Edition, Springer-Verlag Berlin Heidelberg, 2010, p. 62-64, doi: [10.1007/978-3-540-89083-6](https://doi.org/10.1007/978-3-540-89083-6), ISBN: 978-3-540-89082-9.
  19. Heywood, J., "Internal combustion engine fundamentals", New York, McGraw-Hill Education, 1988, p. 343-345, ISBN: 007028637X.
  20. Desantes, J.M., Arrègle, J., López, J.J., and García, J.M., "Turbulent gas jets and diesel-like sprays in a crossflow: A study on axis deflection and air entrainment", *Fuel* 85(14-15):2120-2132, 2006, doi:[10.1016/j.fuel.2006.03.025](https://doi.org/10.1016/j.fuel.2006.03.025).
  21. Dembinski, H.W.R., "In-cylinder Flow Characterisation of Heavy Duty Diesel Engines Using Combustion Image Velocimetry". 2013, Dissertation, Stockholm, KTH Royal Institute of Technology.
  22. Timoney, D.J., "Effects of important Variables on Measured Heat Release Rates in a D.I. Diesel", SAE Technical Paper 870271, 1987, doi:[10.4271/870271](https://doi.org/10.4271/870271).
  23. Miles, P.C., "The Influence of Swirl on HSDI Diesel Combustion at Moderate Speed and Load", SAE Technical Paper 2000-01-1829, 2000, doi:[10.4271/2000-01-1829](https://doi.org/10.4271/2000-01-1829).
  24. Benajes, J., Molina, S., García, J.M., and Riesco, J.M., "The effect of swirl on combustion and exhaust emissions in heavy-duty diesel engines", *Proceedings of the Institution of Mechanical Engineers, Part D: Journal of Automobile Engineering* 218(10):1141-1148, 2004, doi:[10.1177/095440700421801009](https://doi.org/10.1177/095440700421801009).
  25. Van Gerpen, J.H., Huang, C.-w., and Borman, G.L., "The Effects of Swirl and Injection Parameters on Diesel Combustion and Heat Transfer", SAE Technical Paper 850265, 1985, doi:[10.4271/850265](https://doi.org/10.4271/850265).
-

26. Van Basshuysen, R., and Schaefer, F., "Internal Combustion Engine Handbook", Warrendale, PA, USA, SAE International, 2004, p. 463, ISBN: ISBN 0-7680-1139-6.
  27. Mollenhauer, K., and Tschöke, H., "Handbook of Diesel Engines", 1st Edition, Springer-Verlag Berlin Heidelberg, 2010, p. 70, doi: [10.1007/978-3-540-89083-6](https://doi.org/10.1007/978-3-540-89083-6), ISBN: 978-3-540-89082-9.
  28. "Overview of the Diesel Engine Operation". 2010, National Biodiesel Board.
  29. Deslandes, W., Dupont, A., Baby, X., Charnay, G., and Boree, J., "PIV Measurements of Internal Aerodynamic of Diesel Combustion Chamber", SAE Technical Paper 2003-01-3083, 2003, doi:[10.4271/2003-01-3083](https://doi.org/10.4271/2003-01-3083).
  30. Buchwald, R., Brauer, M., Blechstein, A., Sommer, A., and Kahrstedt, J., "Adaption of Injection System Parameters to Homogeneous Diesel Combustion", SAE Technical Paper 2004-01-0936, 2004, doi:[10.4271/2004-01-0936](https://doi.org/10.4271/2004-01-0936).
  31. Maes, N., "The Life of a Spray". 2019, Dissertation, Eindhoven, Eindhoven University of Technology.
  32. Pickett, L.M., and López, J.J., "Jet-Wall Interaction Effects on Diesel Combustion and Soot Formation", SAE Technical Paper 2005-01-0921, 2005, doi:[10.4271/2005-01-0921](https://doi.org/10.4271/2005-01-0921).
  33. Bruneaux, G., "Mixing Process in High Pressure Diesel Jets by Normalized Laser Induced Exciplex Fluorescence Part II: Wall Impinging Versus Free Jet", SAE Technical Paper 2005-01-2097, 2005, doi:[10.4271/2005-01-2097](https://doi.org/10.4271/2005-01-2097).
  34. Mollenhauer, K., and Tschöke, H., "Handbook of Diesel Engines", 1st Edition, Springer-Verlag Berlin Heidelberg, 2010, p. 145, doi: [10.1007/978-3-540-89083-6](https://doi.org/10.1007/978-3-540-89083-6), ISBN: 978-3-540-89082-9.
  35. "Common-Rail System with Piezo Injectors – Diesel Injection System CRS3-27 for a Maximum Pressure up to 2 700 bar", <https://www.bosch-mobility-solutions.com/en/products-and-services/passenger-cars-and-light-commercial-vehicles/powertrain-systems/common-rail-system-piezo/>, accessed Oct. 07, 2019.
  36. Eagle, E., and Musculus, M., "Cinema-Stereo Imaging of Fuel Dribble after the End of Injection in an Optical Heavy-Duty Diesel Engine", in *THIESEL 2014 Conference on Thermo- and Fluid Dynamic Processes in Direct Injection Engines*. 2014: Valencia, Spain.
  37. Mollenhauer, K., and Tschöke, H., "Handbook of Diesel Engines", 1st Edition, Springer-Verlag Berlin Heidelberg, 2010, p. 131-133, doi: [10.1007/978-3-540-89083-6](https://doi.org/10.1007/978-3-540-89083-6), ISBN: 978-3-540-89082-9.
  38. Kook, S., and Pickett, L.M., "Liquid length and vapor penetration of conventional, Fischer-Tropsch, coal-derived, and surrogate fuel sprays at high-temperature and high-pressure ambient conditions", *Fuel* 93:539-548, 2012, doi:[10.1016/j.fuel.2011.10.004](https://doi.org/10.1016/j.fuel.2011.10.004).
  39. Siebers, D.L., "Liquid-Phase Fuel Penetration in Diesel Sprays", SAE Technical Paper 980809, 1998, doi:[10.4271/980809](https://doi.org/10.4271/980809).
  40. Siebers, D.L., "Scaling Liquid-Phase Fuel Penetration in Diesel Sprays Based on Mixing-Limited Vaporization", SAE Technical Paper 1999-01-0528, 1999, doi:[10.4271/1999-01-0528](https://doi.org/10.4271/1999-01-0528).
-

41. Payri, R., Salvador, F.J., Gimeno, J., and Zapata, L.D., "Diesel nozzle geometry influence on spray liquid-phase fuel penetration in evaporative conditions", *Fuel* 87(7):1165-1176, 2008, doi:[10.1016/j.fuel.2007.05.058](https://doi.org/10.1016/j.fuel.2007.05.058).
  42. Naber, J.D., and Siebers, D.L., "Effects of Gas Density and Vaporization on Penetration and Dispersion of Diesel Sprays", SAE Technical Paper 960034, 1996, doi:[10.4271/960034](https://doi.org/10.4271/960034).
  43. Musculus, M.P.B., and Kattke, K., "Entrainment Waves in Diesel Jets", *SAE International Journal of Engines* 2(1):1170-1193, 2009, doi:[10.4271/2009-01-1355](https://doi.org/10.4271/2009-01-1355).
  44. Pickett, L.M., Manin, J., Genzale, C.L., Siebers, D.L., Musculus, M.P.B., and Idicheria, C.A., "Relationship Between Diesel Fuel Spray Vapor Penetration/Dispersion and Local Fuel Mixture Fraction", *SAE International Journal of Engines* 4(1):764-799, 2011, doi:[10.4271/2011-01-0686](https://doi.org/10.4271/2011-01-0686).
  45. "Engine combustion network", <https://ecn.sandia.gov/>, accessed Oct. 1, 2018.
  46. Higgins, B., Siebers, D.L., and Aradi, A., "Diesel-Spray Ignition and Premixed-Burn Behavior", 1, 2000, doi:[10.4271/2000-01-0940](https://doi.org/10.4271/2000-01-0940).
  47. Dec, J.E., and Espey, C., "Chemiluminescence Imaging of Autoignition in a DI Diesel Engine", SAE Technical Paper 982685, 1998, doi:[10.4271/982685](https://doi.org/10.4271/982685).
  48. Jansons, M., Brar, A., Estefanous, F., Florea, R., Taraza, D., Henein, N., and Bryzik, W., "Experimental Investigation of Single and Two-Stage Ignition in a Diesel Engine", SAE Technical Paper 2008-01-1071, 2008, doi:[10.4271/2008-01-1071](https://doi.org/10.4271/2008-01-1071).
  49. Yu, X., Zha, K., Luo, X., Taraza, D., and Jansons, M., "Simulation and Experimental Measurement of CO<sub>2</sub><sup>\*</sup>, OH<sup>\*</sup> and CH<sub>2</sub>O<sup>\*</sup> Chemiluminescence from an Optical Diesel Engine Fueled with n-Heptane", SAE Technical Paper 2013-24-0010, 2013, doi:[10.4271/2013-24-0010](https://doi.org/10.4271/2013-24-0010).
  50. Kosaka, H., Drewes, V.H., Catalfamo, L., Aradi, A.A., Iida, N., and Kamimoto, T., "Two-Dimensional Imaging of Formaldehyde Formed During the Ignition Process of a Diesel Fuel Spray", SAE Technical Paper 2000-01-0236, 2000, doi:[10.4271/2000-01-0236](https://doi.org/10.4271/2000-01-0236).
  51. Lillo, P.M., Pickett, L.M., Persson, H., Andersson, O., and Kook, S., "Diesel Spray Ignition Detection and Spatial/Temporal Correction", *SAE International Journal of Engines* 5(3):1330-1346, 2012, doi:[10.4271/2012-01-1239](https://doi.org/10.4271/2012-01-1239).
  52. Eagle, W.E., Malbec, L.-M., and Musculus, M.P.B., "Measurements of Liquid Length, Vapor Penetration, Ignition Delay, and Flame Lift-Off Length for the Engine Combustion Network 'Spray B' in a 2.34 L Heavy-Duty Optical Diesel Engine", *SAE International Journal of Engines* 9(2):910-931, 2016, doi:[10.4271/2016-01-0743](https://doi.org/10.4271/2016-01-0743).
  53. Jung, Y., Manin, J., Skeen, S.A., and Pickett, L.M., "Assessment of the Ignition and Lift-off Characteristics of a Diesel Spray with a Transient Spreading Angle", SAE Technical Paper 2015-01-1828, 2015, doi:[10.4271/2015-01-1828](https://doi.org/10.4271/2015-01-1828).
  54. Pickett, L.M., Siebers, D.L., and Idicheria, C.A., "Relationship Between Ignition Processes and the Lift-Off Length of Diesel Fuel Jets", SAE Technical Paper 2005-01-3843, 2005, doi:[10.4271/2005-01-3843](https://doi.org/10.4271/2005-01-3843).
-

- 
55. Payri, R., Salvador, F.J., Manin, J., and Viera, A., "Diesel ignition delay and lift-off length through different methodologies using a multi-hole injector", *Applied Energy* 162:541-550, 2016, doi:[10.1016/j.apenergy.2015.10.118](https://doi.org/10.1016/j.apenergy.2015.10.118).
  56. Garcia-Oliver, J.M., Garcia, A., Novella, R., and Morales López, A., "An Investigation of the Engine Combustion Network 'Spray B' in a Light Duty Single Cylinder Optical Engine", SAE Technical Paper 2018-01-0220, 2018, doi:[10.4271/2018-01-0220](https://doi.org/10.4271/2018-01-0220).
  57. Dec, J.E., "A Conceptual Model of DI Diesel Combustion Based on Laser-Sheet Imaging", SAE Technical Paper 970873, 1997, doi:[10.4271/970873](https://doi.org/10.4271/970873).
  58. Flynn, P.F., Durrett, R.P., Hunter, G.L., zur Loye, A.O., Akinyemi, O.C., Dec, J.E., and Westbrook, C.K., "Diesel Combustion: An Integrated View Combining Laser Diagnostics, Chemical Kinetics, And Empirical Validation", SAE Technical Paper 1999-01-0509, 1999, doi:[10.4271/1999-01-0509](https://doi.org/10.4271/1999-01-0509).
  59. Maes, N., Meijer, M., Dam, N., et al., "Characterization of Spray A flame structure for parametric variations in ECN constant-volume vessels using chemiluminescence and laser-induced fluorescence", *Combustion and Flame* 174:138-151, 2016, doi:[doi.org/10.1016/j.combustflame.2016.09.005](https://doi.org/10.1016/j.combustflame.2016.09.005).
  60. Maes, N., Bakker, P.C., Dam, N., and Somers, B., "Transient Flame Development in a Constant-Volume Vessel Using a Split-Scheme Injection Strategy", *SAE International Journal of Fuels and Lubricants* 10(2):318-327, 2017, doi:[10.4271/2017-01-0815](https://doi.org/10.4271/2017-01-0815).
  61. Manin, J., Pickett, L.M., and Skeen, S.A., "Two-Color Diffused Back-Illumination Imaging as a Diagnostic for Time-Resolved Soot Measurements in Reacting Sprays", *SAE International Journal of Engines* 6(4):1908-1921, 2013, doi:[10.4271/2013-01-2548](https://doi.org/10.4271/2013-01-2548).
  62. Higgins, B., and Siebers, D.L., "Measurement of the Flame Lift-Off Location on DI Diesel Sprays Using OH Chemiluminescence", SAE Technical Paper 2001-01-0918, 2001, doi:[10.4271/2001-01-0918](https://doi.org/10.4271/2001-01-0918).
  63. Chomiak, J., and Karlsson, A., "Flame liftoff in diesel sprays", *Symposium (International) on Combustion* 26(2):2557-2564, 1996, doi:[10.1016/s0082-0784\(96\)80088-9](https://doi.org/10.1016/s0082-0784(96)80088-9).
  64. Pei, Y., Davis, M.J., Pickett, L.M., and Som, S., "Engine Combustion Network (ECN): Global sensitivity analysis of Spray A for different combustion vessels", *Combustion and Flame* 162(6):2337-2347, 2015, doi:[10.1016/j.combustflame.2015.01.024](https://doi.org/10.1016/j.combustflame.2015.01.024).
  65. Selim, M.Y.E., and Elfeky, S.M.S., "Effects of diesel/water emulsion on heat flow and thermal loading in a precombustion chamber diesel engine", *Applied Thermal Engineering* 21(15):1565-1582, 2001, doi:[10.1016/s1359-4311\(01\)00019-9](https://doi.org/10.1016/s1359-4311(01)00019-9).
  66. Husberg, T., Gjirja, S., Denbratt, I., Omrane, A., Aldén, M., and Engström, J., "Piston Temperature Measurement by Use of Thermographic Phosphors and Thermocouples in a Heavy-Duty Diesel Engine Run Under Partly Premixed Conditions", SAE Technical Paper 2005-01-1646, 2005, doi:[10.4271/2005-01-1646](https://doi.org/10.4271/2005-01-1646).
  67. Luo, X., Yu, X., and Jansons, M., "Simultaneous In-Cylinder Surface Temperature Measurements with Thermocouple, Laser-induced Phosphorescence, and Dual Wavelength Infrared Diagnostic Techniques in an Optical Engine", SAE Technical Paper 2015-01-1658, 2015, doi:[10.4271/2015-01-1658](https://doi.org/10.4271/2015-01-1658).
-

68. Zhao, H., and Ladommatos, N., "Engine Combustion Instrumentation and Diagnostics", Warrendale, PA, U.S.A., SAE International, 2001, p. 73-75, ISBN: 0-7680-0665-1.
  69. Randolph, A.L., "Methods of Processing Cylinder-Pressure Transducer Signals to Maximize Data Accuracy", SAE Technical Paper 900170, 1990, doi:[10.4271/900170](https://doi.org/10.4271/900170).
  70. Hickling, R., Feldmaier, D., and Sung, S., "Knock - induced cavity resonances in open chamber diesel engines", *The Journal of the Acoustical Society of America* 65(6):1474-1479, 1979, doi:[10.1121/1.382910](https://doi.org/10.1121/1.382910).
  71. Lapuerta, M., Armas, O., and Hernández, J., "Diagnosis of DI Diesel combustion from in-cylinder pressure signal by estimation of mean thermodynamic properties of the gas", *Applied Thermal Engineering* 19(5):513-529, 1999, doi:[10.1016/S1359-4311\(98\)00075-1](https://doi.org/10.1016/S1359-4311(98)00075-1).
  72. Zhao, H., and Ladommatos, N., "Engine Combustion Instrumentation and Diagnostics", Warrendale, PA, U.S.A., SAE International, 2001, p. 100-101, ISBN: 0-7680-0665-1.
  73. Maes, N., Dam, N., Somers, B., Lucchini, T., D'Errico, G., and Hardy, G., "Heavy-Duty Diesel Engine Spray Combustion Processes: Experiments and Numerical Simulations", SAE Technical Paper 2018-01-1689, 2018, doi:[10.4271/2018-01-1689](https://doi.org/10.4271/2018-01-1689).
  74. Heywood, J., "Internal combustion engine fundamentals", New York, McGraw-Hill Education, 1988, p. 748-750, ISBN: 007028637X.
  75. Reitz, R.D., and Sun, Y., "18 - Advanced computational fluid dynamics modeling of direct injection engines", in *Advanced Direct Injection Combustion Engine Technologies and Development*, H. Zhao, Editor. 2010, Woodhead Publishing: Boca Raton, Boston, New York, Washington, DC. p. 678-680.
  76. Bowditch, F.W., "A New Tool for Combustion Research A Quartz Piston Engine", SAE Technical Paper 610002, 1961, doi:[10.4271/610002](https://doi.org/10.4271/610002).
  77. Goschütz, M., Schulz, C., and Kaiser, S.A., "Endoscopic Imaging of Early Flame Propagation in a Near-Production Engine", *SAE International Journal of Engines* 7(1):351-365, 2014, doi:[10.4271/2014-01-1178](https://doi.org/10.4271/2014-01-1178).
  78. Fujino, R., Aoyagi, Y., Osada, H., Yamaguchi, T., and Mizuno, S., "Direct Observation of Clean Diesel Combustion using a Bore Scope in a Single Cylinder HDDE", SAE Technical Paper 2009-01-0645, 2009, doi:[10.4271/2009-01-0645](https://doi.org/10.4271/2009-01-0645).
  79. Spicher, U., Schmitz, G., and Kollmeier, H.-P., "Application of a New Optical Fiber Technique for Flame Propagation Diagnostics in IC Engines", SAE Technical Paper 881637, 1988, doi:[10.4271/881637](https://doi.org/10.4271/881637).
  80. Dec, J.E., Hwang, W., and Sjöberg, M., "An Investigation of Thermal Stratification in HCCI Engines Using Chemiluminescence Imaging", SAE Technical Paper 2006-01-1518, 2006, doi:[10.4271/2006-01-1518](https://doi.org/10.4271/2006-01-1518).
  81. Aronsson, U., Chartier, C., Horn, U., Andersson, Ö., Johansson, B., and Egnell, R., "Heat Release Comparison Between Optical and All-Metal HSDI Diesel Engines", SAE Technical Paper 2008-01-1062, 2008, doi:[10.4271/2008-01-1062](https://doi.org/10.4271/2008-01-1062).
-

82. Kashdan, J.T., and Thirouard, B., "A Comparison of Combustion and Emissions Behaviour in Optical and Metal Single-Cylinder Diesel Engines", *SAE International Journal of Engines* 2(1):1857-1872, 2009, doi:[10.4271/2009-01-1963](https://doi.org/10.4271/2009-01-1963).
  83. Musculus, M.P.B., Pickett, L.M., and Kaiser, S.A., "Fundamentals", in *Encyclopedia of Automotive Engineering*, D. Crolla, et al., Editors. 2014, John Wiley & Sons. p. 1-21.
  84. Barth, P., "Konstruktion und Inbetriebnahme eines optisch zugänglichen Hochlast-Verbrennungsmotors mit zugehörigem Prüfstand". 2016, Dissertation, Duisburg, Essen, Universität Duisburg-Essen.
  85. Colban, W.F., Kim, D., Miles, P.C., et al., "A Detailed Comparison of Emissions and Combustion Performance Between Optical and Metal Single-Cylinder Diesel Engines at Low Temperature Combustion Conditions", *SAE International Journal of Fuels and Lubricants* 1(1):505-519, 2008, doi:[10.4271/2008-01-1066](https://doi.org/10.4271/2008-01-1066).
  86. Espey, C., and Dec, J.E., "The Effect of TDC Temperature and Density on the Liquid-Phase Fuel Penetration in a D. I. Diesel Engine", SAE Technical Paper 952456, 1995, doi:[10.4271/952456](https://doi.org/10.4271/952456).
  87. Mounaïm-Rousselle, C., and Pajot, O., "Droplet Sizing by Mie Scattering Interferometry in a Spark Ignition Engine", *Particle & Particle Systems Characterization* 16(4):160-168, 1999, doi:[10.1002/\(sici\)1521-4117\(199908\)16:4<160::aid-ppsc160>3.0.co;2-g](https://doi.org/10.1002/(sici)1521-4117(199908)16:4<160::aid-ppsc160>3.0.co;2-g).
  88. Geschwindner, C., Kranz, P., Welch, C., Schmidt, M., Böhm, B., Kaiser, S.A., and De la Morena, J., "Analysis of the interaction of Spray G and in-cylinder flow in two optical engines for late gasoline direct injection", *International Journal of Engine Research*:146808741988153, 2019, doi:[10.1177/1468087419881535](https://doi.org/10.1177/1468087419881535).
  89. Lind, T., Roberts, G., Eagle, W., Rousselle, C., Andersson, Ö., and Musculus, M.P.B., "Mechanisms of Post-Injection Soot-Reduction Revealed by Visible and Diffused Back-Illumination Soot Extinction Imaging", SAE Technical Paper 2018-01-0232, 2018, doi:[10.4271/2018-01-0232](https://doi.org/10.4271/2018-01-0232).
  90. Witzel, O., Klein, A., Wagner, S., Meffert, C., Schulz, C., and Ebert, V., "High-speed tunable diode laser absorption spectroscopy for sampling-free in-cylinder water vapor concentration measurements in an optical IC engine", *Applied Physics B* 109(3):521-532, 2012, doi:[10.1007/s00340-012-5225-0](https://doi.org/10.1007/s00340-012-5225-0).
  91. Bürkle, S., Biondo, L., Ding, C.-P., Honza, R., Ebert, V., Böhm, B., and Wagner, S., "In-Cylinder Temperature Measurements in a Motored IC Engine using TDLAS", *Flow, Turbulence and Combustion* 101(1):139-159, 2018, doi:[10.1007/s10494-017-9886-y](https://doi.org/10.1007/s10494-017-9886-y).
  92. Izadi Najafabadi, M., Dam, N., Somers, B., and Johansson, B., "Ignition Sensitivity Study of Partially Premixed Combustion by Using Shadowgraphy and OH\* Chemiluminescence Methods", SAE Technical Paper 2016-01-0761, 2016, doi:[10.4271/2016-01-0761](https://doi.org/10.4271/2016-01-0761).
  93. Kozuka, K., Ozasa, T., Fujikawa, T., and Saito, A., "Schlieren Observation of Spark-Ignited Premixed Charge Combustion Phenomena Using a Transparent Collimating Cylinder Engine", *Journal of Engineering for Gas Turbines and Power* 125(1):336-343, 2003, doi:[10.1115/1.1496774](https://doi.org/10.1115/1.1496774).
-

94. Espey, C., Dec, J.E., Litzinger, T.A., and Santavicca, D.A., "Quantitative 2-D Fuel Vapor Concentration Imaging in a Firing D.I. Diesel Engine Using Planar Laser-Induced Rayleigh Scattering", 1, 1994, doi:[10.4271/940682](https://doi.org/10.4271/940682).
  95. Arcoumanis, C., and Enotiadis, A.C., "In-cylinder fuel distribution in a port-injected model engine using Rayleigh scattering", *Experiments in Fluids* 11(6):375-387, 1991, doi:[10.1007/bf00211792](https://doi.org/10.1007/bf00211792).
  96. Blessinger, M., and Ghandhi, J., "Investigation of the Combustion Front Structure during Homogeneous Charge Compression Ignition Combustion via Laser Rayleigh Scattering Thermometry", *SAE International Journal of Engines* 9(2):950-963, 2016, doi:[10.4271/2016-01-0746](https://doi.org/10.4271/2016-01-0746).
  97. Petersen, B., and Miles, P.C., "PIV Measurements in the Swirl-Plane of a Motored Light-Duty Diesel Engine", *SAE International Journal of Engines* 4(1):1623-1641, 2011, doi:[10.4271/2011-01-1285](https://doi.org/10.4271/2011-01-1285).
  98. Khalighi, B., "Intake-Generated Swirl and Tumble Motions in a 4-Valve Engine with Various Intake Configurations-Flow Visualization and Particle Tracking Velocimetry", SAE Technical Paper 900059, 1990, doi:[10.4271/900059](https://doi.org/10.4271/900059).
  99. Cole, J.B., and Swords, M.D., "Laser Doppler anemometry measurements in an engine", *Appl Opt* 18(10):1539-45, 1979, doi:[10.1364/AO.18.001539](https://doi.org/10.1364/AO.18.001539).
  100. Guo, H., Ma, X., Li, Y., Liang, S., Wang, Z., Xu, H., and Wang, J., "Effect of flash boiling on microscopic and macroscopic spray characteristics in optical GDI engine", *Fuel* 190:79-89, 2017, doi:[10.1016/j.fuel.2016.11.043](https://doi.org/10.1016/j.fuel.2016.11.043).
  101. Ma, X., Wang, Z., Jiang, C., Jiang, Y., Xu, H., and Wang, J., "An optical study of in-cylinder CH<sub>2</sub>O and OH chemiluminescence in flame-induced reaction front propagation using high speed imaging", *Fuel* 134:603-610, 2014, doi:[10.1016/j.fuel.2014.06.002](https://doi.org/10.1016/j.fuel.2014.06.002).
  102. Ikeda, Y., Kaneko, M., and Nakajima, T., "Local A/F Measurement by Chemiluminescence OH\*, CH\* and C<sub>2</sub>\* in SI Engine", SAE Technical Paper 2001-01-0919, 2001, doi:[10.4271/2001-01-0919](https://doi.org/10.4271/2001-01-0919).
  103. Najafabadi, M.I., Egelmeers, L., Somers, B., Deen, N., Johansson, B., and Dam, N., "The influence of charge stratification on the spectral signature of partially premixed combustion in a light-duty optical engine", *Applied Physics B* 123(4):108, 2017, doi:[10.1007/s00340-017-6688-9](https://doi.org/10.1007/s00340-017-6688-9).
  104. Yang, J., Dong, X., Wu, Q., and Xu, M., "Influence of flash boiling spray on the combustion characteristics of a spark-ignition direct-injection optical engine under cold start", *Combustion and Flame* 188:66-76, 2018, doi:[10.1016/j.combustflame.2017.09.019](https://doi.org/10.1016/j.combustflame.2017.09.019).
  105. Hampson, G.J., and Reitz, R.D., "Two-Color Imaging of In-Cylinder Soot Concentration and Temperature in a Heavy-Duty DI Diesel Engine with Comparison to Multidimensional Modeling for Single and Split Injections", SAE Technical Paper 980524, 1998, doi:[10.4271/980524](https://doi.org/10.4271/980524).
  106. Roberts, G., Rousselle, C.M., Musculus, M., Wissink, M., Curran, S., and Eagle, E., "RCCI Combustion Regime Transitions in a Single-Cylinder Optical Engine and a Multi-Cylinder Metal Engine", *SAE International Journal of Engines* 10(5):2392-2413, 2017, doi:[10.4271/2017-24-0088](https://doi.org/10.4271/2017-24-0088).
-

107. Takagi, H., Ohno, T., and Asanuma, T., "Temperature Measurements of Combustion Gas in a Spark Ignition Engine by Infrared Monochromatic Pyrometry", SAE Technical Paper 900483, 1990, doi:[10.4271/900483](https://doi.org/10.4271/900483).
  108. Kranz, P., and Kaiser, S.A., "LIF-based imaging of preferential evaporation of a multi-component gasoline surrogate in a direct-injection engine", *Proceedings of the Combustion Institute* 37(2):1365-1372, 2019, doi:[10.1016/j.proci.2018.06.214](https://doi.org/10.1016/j.proci.2018.06.214).
  109. Sahoo, D., Petersen, B., and Miles, P.C., "Measurement of Equivalence Ratio in a Light-Duty Low Temperature Combustion Diesel Engine by Planar Laser Induced Fluorescence of a Fuel Tracer", *SAE International Journal of Engines* 4(2):2312-2325, 2011, doi:[10.4271/2011-24-0064](https://doi.org/10.4271/2011-24-0064).
  110. Dec, J.E., and Hwang, W., "Characterizing the Development of Thermal Stratification in an HCCI Engine Using Planar-Imaging Thermometry", *SAE International Journal of Engines* 2(1):421-438, 2009, doi:[10.4271/2009-01-0650](https://doi.org/10.4271/2009-01-0650).
  111. Kranz, P., Fuhrmann, D., Goschütz, M., et al., "In-Cylinder LIF Imaging, IR-Absorption Point Measurements, and a CFD Simulation to Evaluate Mixture Formation in a CNG-Fueled Engine", *SAE International Journal of Engines* 11(6):1221-1238, 2018, doi:[10.4271/2018-01-0633](https://doi.org/10.4271/2018-01-0633).
  112. Einecke, S., Schulz, C., and Sick, V., "Measurement of temperature, fuel concentration and equivalence ratio fields using tracer LIF in IC engine combustion", *Applied Physics B* 71(5):717-723, 2014, doi:[10.1007/s003400000383](https://doi.org/10.1007/s003400000383).
  113. Fröba, A.P., Rabenstein, F., Münch, K.U., and Leipertz, A., "Mixture of triethylamine (TEA) and benzene as a new seeding material for the quantitative two-dimensional laser-induced exciplex fluorescence imaging of vapor and liquid fuel inside SI engines", *Combustion and Flame* 112(1-2):199-209, 1998, doi:[10.1016/s0010-2180\(97\)81768-3](https://doi.org/10.1016/s0010-2180(97)81768-3).
  114. Genzale, C.L., Reitz, R.D., and Musculus, M.P.B., "Effects of Piston Bowl Geometry on Mixture Development and Late-Injection Low-Temperature Combustion in a Heavy-Duty Diesel Engine", *SAE International Journal of Engines* 1(1):913-937, 2008, doi:[10.4271/2008-01-1330](https://doi.org/10.4271/2008-01-1330).
  115. Dec, J.E., and Canaan, R.E., "PLIF Imaging of NO Formation in a DI Diesel Engine", SAE Technical Paper 980147, 1998, doi:[10.4271/980147](https://doi.org/10.4271/980147).
  116. Kim, D., Ekoto, I., Colban, W.F., and Miles, P.C., "In-cylinder CO and UHC Imaging in a Light-Duty Diesel Engine during PPCI Low-Temperature Combustion", *SAE International Journal of Fuels and Lubricants* 1(1):933-956, 2008, doi:[10.4271/2008-01-1602](https://doi.org/10.4271/2008-01-1602).
  117. Johansson, B., Neij, H., Juhlin, G., and Aldén, M., "Residual Gas Visualization with Laser Induced Fluorescence", SAE Technical Paper 952463, 1995, doi:[10.4271/952463](https://doi.org/10.4271/952463).
  118. Pinson, J.A., Mitchell, D.L., Santoro, R.J., and Litzinger, T.A., "Quantitative, Planar Soot Measurements in a D.I. Diesel Engine Using Laser-induced Incandescence and Light Scattering", SAE Technical Paper 932650, 1993, doi:[10.4271/932650](https://doi.org/10.4271/932650).
  119. Menkiel, B., Donkerbroek, A., Uitz, R., Cracknell, R., and Ganippa, L., "Measurement of in-cylinder soot particles and their distribution in an optical HSDI diesel engine using time resolved laser induced incandescence (TR-LII)", *Combustion and Flame* 159(9):2985-2998, 2012, doi:[10.1016/j.combustflame.2012.03.008](https://doi.org/10.1016/j.combustflame.2012.03.008).
-

120. Neal, N.J., Jordan, J., and Rothamer, D., "Simultaneous Measurements of In-Cylinder Temperature and Velocity Distribution in a Small-Bore Diesel Engine Using Thermographic Phosphors", *SAE International Journal of Engines* 6(1):300-318, 2013, doi:[10.4271/2013-01-0562](https://doi.org/10.4271/2013-01-0562).
  121. Smith, J.R., "Temperature and Density Measurements in an Engine by Pulsed Raman Spectroscopy", SAE Technical Paper 800137, 1980, doi:[10.4271/800137](https://doi.org/10.4271/800137).
  122. Egermann, J., Koebecke, W., Ipp, W., and Leipertz, A., "Investigation of the mixture formation inside a gasoline direct injection engine by means of linear Raman spectroscopy", *Proceedings of the Combustion Institute* 28(1):1145-1152, 2000, doi:[10.1016/s0082-0784\(00\)80324-0](https://doi.org/10.1016/s0082-0784(00)80324-0).
  123. Weikl, M.C., Beyrau, F., and Leipertz, A., "Simultaneous temperature and exhaust-gas recirculation-measurements in a homogeneous charge-compression ignition engine by use of pure rotational coherent anti-Stokes Raman spectroscopy", *Appl Opt* 45(15):3646-51, 2006, doi:[10.1364/ao.45.003646](https://doi.org/10.1364/ao.45.003646).
  124. Scott, B., Willman, C., Williams, B., Ewart, P., Stone, R., and Richardson, D., "In-Cylinder Temperature Measurements Using Laser Induced Grating Spectroscopy and Two-Colour PLIF", *SAE International Journal of Engines* 10(4):2191-2201, 2017, doi:[10.4271/2017-24-0045](https://doi.org/10.4271/2017-24-0045).
  125. Joshi, S., Olsen, D.B., Dumitrescu, C., Puzinauskas, P.V., and Yalin, A.P., "Laser-induced breakdown spectroscopy for in-cylinder equivalence ratio measurements in laser-ignited natural gas engines", *Appl Spectrosc* 63(5):549-54, 2009, doi:[10.1366/000370209788346869](https://doi.org/10.1366/000370209788346869).
  126. Witze, P.O., "Cycle-Resolved Multipoint Ionization Probe Measurements in a Spark Ignition Engine", SAE Technical Paper 892099, 1989, doi:[10.4271/892099](https://doi.org/10.4271/892099).
  127. "Product-Manual for DaVis 8.2 - FlowMaster". 2014, LaVision GmbH: Göttingen, Germany.
  128. Zeng, W., Sjöberg, M., Reuss, D.L., and Hu, Z., "High-speed PIV, spray, combustion luminosity, and infrared fuel-vapor imaging for probing tumble-flow-induced asymmetry of gasoline distribution in a spray-guided stratified-charge DISI engine", *Proceedings of the Combustion Institute* 36(3):3459-3466, 2017, doi:[10.1016/j.proci.2016.08.047](https://doi.org/10.1016/j.proci.2016.08.047).
  129. Peterson, B., Baum, E., Ding, C.P., Michaelis, D., Dreizler, A., and Böhm, B., "Assessment and application of tomographic PIV for the spray-induced flow in an IC engine", *Proceedings of the Combustion Institute* 36(3):3467-3475, 2017, doi:[10.1016/j.proci.2016.06.114](https://doi.org/10.1016/j.proci.2016.06.114).
  130. Disch, C., Kubach, H., Spicher, U., Pfeil, J., Altenschmidt, F., and Schaupp, U., "Investigations of Spray-Induced Vortex Structures during Multiple Injections of a DISI Engine in Stratified Operation Using High-Speed-PIV", SAE Technical Paper 2013-01-0563, 2013, doi:[10.4271/2013-01-0563](https://doi.org/10.4271/2013-01-0563).
  131. Lee, J., Yamakawa, M., Isshiki, S., and Nishida, K., "An Analysis of Droplets and Ambient Air Interaction in a D.I. Gasoline Spray Using LIF-PIV Technique", SAE Technical Paper 2002-01-0743, 2002, doi:[10.4271/2002-01-0743](https://doi.org/10.4271/2002-01-0743).
  132. Abram, C., Fond, B., Heyes, A.L., and Beyrau, F., "High-speed planar thermometry and velocimetry using thermographic phosphor particles", *Applied Physics B* 111(2):155-160, 2013, doi:[10.1007/s00340-013-5411-8](https://doi.org/10.1007/s00340-013-5411-8).
-

133. Calendini, P.O., Duverger, T., Lecerf, A., and Trinite, M., "In-Cylinder Velocity Measurements with Stereoscopic Particle Image Velocimetry in a SI engine", SAE Technical Paper 2000-01-1798, 2000, doi:[10.4271/2000-01-1798](https://doi.org/10.4271/2000-01-1798).
  134. Peterson, B., Baum, E., Böhm, B., Sick, V., and Dreizler, A., "Evaluation of toluene LIF thermometry detection strategies applied in an internal combustion engine", *Applied Physics B* 117(1):151-175, 2014, doi:[10.1007/s00340-014-5815-0](https://doi.org/10.1007/s00340-014-5815-0).
  135. Koban, W., Koch, J.D., Hanson, R.K., and Schulz, C., "Absorption and Fluorescence of Toluene Vapor at Elevated Temperatures", *Physical Chemistry Chemical Physics* 6(11):2940, 2004, doi:[10.1039/b400997e](https://doi.org/10.1039/b400997e).
  136. Thurber, M.C., Grisch, F., Kirby, B.J., Votsmeier, M., and Hanson, R.K., "Measurements and modeling of acetone laser-induced fluorescence with implications for temperature-imaging diagnostics", *Applied Optics* 37(21):4963, 1998, doi:[10.1364/ao.37.004963](https://doi.org/10.1364/ao.37.004963).
  137. Faust, S., Goschütz, M., Kaiser, S.A., Dreier, T., and Schulz, C., "A comparison of selected organic tracers for quantitative scalar imaging in the gas phase via laser-induced fluorescence", *Applied Physics B* 117(1):183-194, 2014, doi:[10.1007/s00340-014-5818-x](https://doi.org/10.1007/s00340-014-5818-x).
  138. Snyder, J., Dronniou, N., Dec, J.E., and Hanson, R., "PLIF Measurements of Thermal Stratification in an HCCI Engine under Fired Operation", *SAE International Journal of Engines* 4(1):1669-1688, 2011, doi:[10.4271/2011-01-1291](https://doi.org/10.4271/2011-01-1291).
  139. Faust, S., Dreier, T., and Schulz, C., "Photo-physical properties of anisole: temperature, pressure, and bath gas composition dependence of fluorescence spectra and lifetimes", *Applied Physics B* 112(2):203-213, 2013, doi:[10.1007/s00340-013-5420-7](https://doi.org/10.1007/s00340-013-5420-7).
  140. Tran, K.H., Morin, C., Kühni, M., and Guibert, P., "Fluorescence spectroscopy of anisole at elevated temperatures and pressures", *Applied Physics B* 115(4):461-470, 2013, doi:[10.1007/s00340-013-5626-8](https://doi.org/10.1007/s00340-013-5626-8).
  141. Kaiser, S.A., and Long, M.B., "Quantitative planar laser-induced fluorescence of naphthalenes as fuel tracers", *Proceedings of the Combustion Institute* 30(1):1555-1563, 2005, doi:[10.1016/j.proci.2004.08.263](https://doi.org/10.1016/j.proci.2004.08.263).
  142. Dronniou, N., and Dec, J.E., "Investigating the Development of Thermal Stratification from the Near-Wall Regions to the Bulk-Gas in an HCCI Engine with Planar Imaging Thermometry", *SAE International Journal of Engines* 5(3):1046-1074, 2012, doi:[10.4271/2012-01-1111](https://doi.org/10.4271/2012-01-1111).
  143. Strozzi, C., Sotton, J., Mura, A., and Bellenoue, M., "Characterization of a two-dimensional temperature field within a rapid compression machine using a toluene planar laser-induced fluorescence imaging technique", *Measurement Science and Technology* 20(12):125403, 2009, doi:[10.1088/0957-0233/20/12/125403](https://doi.org/10.1088/0957-0233/20/12/125403).
  144. Pickett, L.M., Genzale, C.L., Manin, J., Malbec, L., and Hermant, L., "Measurement uncertainty of liquid penetration in evaporating diesel sprays", in *ILASS2011-III*. 2011.
  145. Kaiser, S.A., "Quantitative Imaging in Flows – 2. Diagnostic Techniques". University lecture, 2014, Universität Duisburg-Essen: Duisburg, Germany.
  146. Pickett, L.M., Kook, S., and Williams, T.C., "Visualization of Diesel Spray Penetration, Cool-Flame, Ignition, High-Temperature Combustion, and Soot Formation Using High-Speed
-

- Imaging", *SAE International Journal of Engines* 2(1):439-459, 2009, doi:[10.4271/2009-01-0658](https://doi.org/10.4271/2009-01-0658).
147. Pickett, L.M., Genzale, C.L., Bruneaux, G., Malbec, L.-M., Hermant, L., Christiansen, C., and Schramm, J., "Comparison of Diesel Spray Combustion in Different High-Temperature, High-Pressure Facilities", *SAE International Journal of Engines* 3(2):156-181, 2010, doi:[10.4271/2010-01-2106](https://doi.org/10.4271/2010-01-2106).
  148. Bardi, M., Payri, R., Malbec, L.M., et al., "Engine Combustion Network: Comparison of Spray Development, Vaporization, and Combustion in Different Combustion Vessels", *Atomization and Sprays* 22(10):807-842, 2012, doi:[10.1615/AtomizSpr.2013005837](https://doi.org/10.1615/AtomizSpr.2013005837).
  149. Skeen, S.A., Manin, J., and Pickett, L.M., "Simultaneous formaldehyde PLIF and high-speed schlieren imaging for ignition visualization in high-pressure spray flames", *Proceedings of the Combustion Institute* 35(3):3167-3174, 2015, doi:[10.1016/j.proci.2014.06.040](https://doi.org/10.1016/j.proci.2014.06.040).
  150. Manin, J., Bardi, M., and Pickett, L.M., "Evaluation of the liquid length via diffused back-illumination imaging in vaporizing diesel sprays", in *Comodia 2012*. 2012: Fukuoka, Japan.
  151. Zhao, H., "Laser Diagnostics and Optical Measurement Techniques in Internal Combustion Engines", Warrendale, PA, U.S.A., SAE International, 2012, p. 322-324, ISBN: 978-0-7680-5782-9.
  152. Skeen, S., Yasutomi, K., Cenker, E., Adamson, B., Hansen, N., and Pickett, L., "Standardized Optical Constants for Soot Quantification in High-Pressure Sprays", *SAE International Journal of Engines* 11(6):805-816, 2018, doi:[10.4271/2018-01-0233](https://doi.org/10.4271/2018-01-0233).
  153. Westlye, F.R., Penney, K., Ivarsson, A., Pickett, L.M., Manin, J., and Skeen, S.A., "Diffuse back-illumination setup for high temporally resolved extinction imaging", *Appl Opt* 56(17):5028-5038, 2017, doi:[10.1364/AO.56.005028](https://doi.org/10.1364/AO.56.005028).
  154. Payri, R., Salvador, F.J., Gimeno, J., and de la Morena, J., "Effects of nozzle geometry on direct injection diesel engine combustion process", *Applied Thermal Engineering* 29(10):2051-2060, 2009, doi:[10.1016/j.applthermaleng.2008.10.009](https://doi.org/10.1016/j.applthermaleng.2008.10.009).
  155. Zhao, H., and Ladommatos, N., "Engine Combustion Instrumentation and Diagnostics", Warrendale, PA, U.S.A., SAE International, 2001, p. 242-243, ISBN: 0-7680-0665-1.
  156. Srna, A., Bombach, R., Herrmann, K., and Bruneaux, G., "Characterization of the spectral signature of dual-fuel combustion luminosity: implications for evaluation of natural luminosity imaging", *Applied Physics B* 125(7):120, 2019, doi:[10.1007/s00340-019-7222-z](https://doi.org/10.1007/s00340-019-7222-z).
  157. Smith, J.D., and Sick, V., "Crank-Angle Resolved Imaging of Fuel Distribution, Ignition and Combustion in a Direct-Injection Spark-Ignition Engine", SAE Technical Paper 2005-01-3753, 2005, doi:[10.4271/2005-01-3753](https://doi.org/10.4271/2005-01-3753).
  158. Yang, C., Zhao, H., and Megaritis, T., "In-Cylinder Studies of CAI Combustion with Negative Valve Overlap and Simultaneous Chemiluminescence Analysis", SAE Technical Paper 2009-01-1103, 2009, doi:[10.4271/2009-01-1103](https://doi.org/10.4271/2009-01-1103).
  159. Iijima, A., and Shoji, H., "A Study of HCCI Combustion Characteristics Using Spectroscopic Techniques", SAE Technical Paper 2007-01-1886, 2007, doi:[10.4271/2007-01-1886](https://doi.org/10.4271/2007-01-1886).
-

160. Hottel, H.C., and Broughton, F.P., "Determination of True Temperature and Total Radiation from Luminous Gas Flames", *Industrial & Engineering Chemistry Analytical Edition* 4(2):166-175, 1932, doi:[10.1021/ac50078a004](https://doi.org/10.1021/ac50078a004).
  161. Zhao, H., "Laser Diagnostics and Optical Measurement Techniques in Internal Combustion Engines", Warrendale, PA, U.S.A., SAE International, 2012, p. 241-242, ISBN: 978-0-7680-5782-9.
  162. Mueller, C.J., and Martin, G.C., "Effects of Oxygenated Compounds on Combustion and Soot Evolution in a DI Diesel Engine: Broadband Natural Luminosity Imaging", SAE Technical Paper 2002-01-1631, 2002, doi:[10.4271/2002-01-1631](https://doi.org/10.4271/2002-01-1631).
  163. Ni, M., Zhang, H., Wang, F., Xie, Z., Huang, Q., Yan, J., and Cen, K., "Study on the detection of three-dimensional soot temperature and volume fraction fields of a laminar flame by multispectral imaging system", *Applied Thermal Engineering* 96:421-431, 2016, doi:[10.1016/j.applthermaleng.2015.11.116](https://doi.org/10.1016/j.applthermaleng.2015.11.116).
  164. Chang, C., Clasen, E., Song, K., Campbell, S., Rhee, K.T., and Jiang, H., "Quantitative Imaging of In-Cylinder Processes by Multispectral Methods", SAE Technical Paper 970872, 1997, doi:[10.4271/970872](https://doi.org/10.4271/970872).
  165. Nakashima, T., Saito, K., Basaki, M., and Furuno, S., "A Study of Stratified Charge Combustion Characteristics in New Concept Direct Injection SI Gasoline Engine", SAE Technical Paper 2001-01-0734, 2001, doi:[10.4271/2001-01-0734](https://doi.org/10.4271/2001-01-0734).
  166. Jansons, M., Lin, S., Fang, T., and Rhee, K.T., "Visualization of Pre-flame and Combustion Reactions in Engine Cylinders", SAE Technical Paper 2000-01-1800, 2000, doi:[10.4271/2000-01-1800](https://doi.org/10.4271/2000-01-1800).
  167. Takeuchi, S., Ohno, Y., Mitsui, K., and Arai, M., "High-speed and high-resolution color imaging system combined with multispectral optics: optical layout and feasibility study for combustion analysis", *Proc. of SPIE* 5580:261-269, 2005, doi:[10.1117/12.567324](https://doi.org/10.1117/12.567324).
  168. Meléndez, J., Aranda, J.M., de Castro, A.J., and López, F., "Measurement of forest fire parameters with multi-spectral imaging in the medium infrared", *Quantitative InfraRed Thermography Journal* 3(2):183-199, 2006, doi:[10.3166/qirt.3.183-200](https://doi.org/10.3166/qirt.3.183-200).
  169. Pastor, J.V., García, J.M., Pastor, J.M., and Buitrago, J.E., "Analysis Methodology of Diesel Combustion by Using Flame Luminosity, Two-Colour Method and Laser-Induced Incandescence", SAE Technical Paper 2005-24-012, 2005, doi:[10.4271/2005-24-012](https://doi.org/10.4271/2005-24-012).
  170. Akhloufi, M.A., Toulouse, T., Rossi, L., and Maldague, X., "Multimodal three-dimensional vision for wildland fires detection and analysis", *2017 Seventh International Conference on Image Processing Theory, Tools and Applications (IPTA)*:1-6, 2017, doi:[10.1109/IPTA.2017.8310085](https://doi.org/10.1109/IPTA.2017.8310085).
  171. Zeng, W., Sjöberg, M., Reuss, D.L., and Hu, Z., "The role of spray-enhanced swirl flow for combustion stabilization in a stratified-charge DISI engine", *Combustion and Flame* 168:166-185, 2016, doi:[10.1016/j.combustflame.2016.03.015](https://doi.org/10.1016/j.combustflame.2016.03.015).
  172. Vattulainen, J., Nummela, V., Hernberg, R., and Kytölä, J., "A system for quantitative imaging diagnostics and its application to pyrometric in-cylinder flame-temperature measurements in large diesel engines", *Measurement Science and Technology* 11(2):103-119, 2000, doi:[10.1088/0957-0233/11/2/303](https://doi.org/10.1088/0957-0233/11/2/303).
-

- 
173. Gleis, S., Frankl, S., Waligorski, D., Prager, D.I.M., and Wachtmeister, P.D.I.G., "Investigation of the High-Pressure-Dual-Fuel (HPDF) combustion process of natural gas on a fully optically accessible research engine", SAE Technical Paper 2019-01-2172, 2019.
  174. Zhao, H., and Ladommatos, N., "Optical diagnostics for soot and temperature measurement in diesel engines", *Progress in Energy and Combustion Science* 24(3):221-255, 1998, doi:[10.1016/s0360-1285\(97\)00033-6](https://doi.org/10.1016/s0360-1285(97)00033-6).
  175. Park, S., Shin, J., and Bae, C., "Spark ignited flame propagation of lean stratified air-gasoline mix-ture in a Constant Volume Combustion Chamber", in *THIESEL 2018 Conference on Thermo- and Fluid Dynamic Processes in Direct Injection Engines*. 2018: Valencia, Spain.
  176. Trindade, T.P., Sanches, J.M., and Fernandes, E.C., "Digital Color Image Processing Technique Applied to Gas Combustion Diagnostics", in *8th World Conference on Experimental Heat Transfer, Fluid Mechanics, and Thermodynamics*. 2013: Lisbon, Portugal.
  177. Kuhn, P.B., Ma, B., Connelly, B.C., Smooke, M.D., and Long, M.B., "Soot and thin-filament pyrometry using a color digital camera", *Proceedings of the Combustion Institute* 33(1):743-750, 2011, doi:[10.1016/j.proci.2010.05.006](https://doi.org/10.1016/j.proci.2010.05.006).
  178. Zha, K., Florea, R.-C., and Jansons, M. "Comparison of Soot Evolution Using High-Speed CMOS Color Camera and Two-Color Thermometry in an Optical Diesel Engine Fueled With B20 Biodiesel Blend and Ultra-Low Sulfur Diesel". in *Proceedings of the ASME 2011 Internal Combustion Engine Division Fall Technical Conference*. 2011. Morgantown, West Virginia, USA: ICEF2011.
  179. Jin, Y., Song, Y., Qu, X., Li, Z., Ji, Y., and He, A., "Three-dimensional dynamic measurements of CH\* and C2\* concentrations in flame using simultaneous chemiluminescence tomography", *Opt Express* 25(5):4640-4654, 2017, doi:[10.1364/OE.25.004640](https://doi.org/10.1364/OE.25.004640).
  180. Huang, H.-W., and Zhang, Y., "Flame colour characterization in the visible and infrared spectrum using a digital camera and image processing", *Measurement Science and Technology* 19(8):085406, 2008, doi:[10.1088/0957-0233/19/8/085406](https://doi.org/10.1088/0957-0233/19/8/085406).
  181. Huang, H.W., and Zhang, Y., "Analysis of the ignition process using a digital image and colour processing technique", *Measurement Science and Technology* 22(7):075401, 2011, doi:[10.1088/0957-0233/22/7/075401](https://doi.org/10.1088/0957-0233/22/7/075401).
  182. Huang, H.W., and Zhang, Y., "Digital colour image processing based measurement of premixed CH<sub>4</sub>+air and C<sub>2</sub>H<sub>4</sub>+air flame chemiluminescence", *Fuel* 90(1):48-53, 2011, doi:[10.1016/j.fuel.2010.07.050](https://doi.org/10.1016/j.fuel.2010.07.050).
  183. Sun, Z., Ma, Z., Li, X., and Xu, M., "Study of Flash Boiling Spray Combustion in a Spark Ignition Direct Injection Optical Engine Using Digital Image Processing Diagnostics", 2019-01-0252, 2019, doi:[10.4271/2019-01-0252](https://doi.org/10.4271/2019-01-0252).
  184. Veraverbeke, S., Dennison, P., Gitas, I., et al., "Hyperspectral remote sensing of fire: State-of-the-art and future perspectives", *Remote Sensing of Environment* 216:105-121, 2018, doi:[10.1016/j.rse.2018.06.020](https://doi.org/10.1016/j.rse.2018.06.020).
  185. Bradley, K.C., Gross, K.C., and Perram, G.P., "Imaging Fourier Transform Spectrometry of Combustion Events", *IEEE Sensors Journal* 10(3):779-785, 2010, doi:[10.1109/jsen.2009.2039546](https://doi.org/10.1109/jsen.2009.2039546).
-

186. Rhoby, M.R., Blunck, D.L., and Gross, K.C., "Mid-IR hyperspectral imaging of laminar flames for 2-D scalar values", *Opt Express* 22(18):21600-17, 2014, doi:[10.1364/OE.22.021600](https://doi.org/10.1364/OE.22.021600).
  187. Harley, J.L., Rankin, B.A., Blunck, D.L., Gore, J.P., and Gross, K.C., "Imaging Fourier-transform spectrometer measurements of a turbulent nonpremixed jet flame", *Opt Lett* 39(8):2350-3, 2014, doi:[10.1364/OL.39.002350](https://doi.org/10.1364/OL.39.002350).
  188. Liu, H., Zheng, S., Zhou, H., and Qi, C., "Measurement of distributions of temperature and wavelength-dependent emissivity of a laminar diffusion flame using hyper-spectral imaging technique", *Measurement Science and Technology* 27(2):025201, 2016, doi:[10.1088/0957-0233/27/2/025201](https://doi.org/10.1088/0957-0233/27/2/025201).
  189. Liu, H., Zheng, S., and Zhou, H., "Measurement of Soot Temperature and Volume Fraction of Axisymmetric Ethylene Laminar Flames Using Hyperspectral Tomography", *IEEE Transactions on Instrumentation and Measurement* 66(2):315-324, 2017, doi:[10.1109/tim.2016.2631798](https://doi.org/10.1109/tim.2016.2631798).
  190. Hsu, P.S., Lauriola, D., Jiang, N., Miller, J.D., Gord, J.R., and Roy, S., "Fiber-coupled, UV-SWIR hyperspectral imaging sensor for combustion diagnostics", *Appl Opt* 56(21):6029-6034, 2017, doi:[10.1364/AO.56.006029](https://doi.org/10.1364/AO.56.006029).
  191. Horn, B.K.P., and Schunck, B.G., "Determining optical flow", *Artificial Intelligence* 17(1-3):185-203, 1981, doi:[10.1016/0004-3702\(81\)90024-2](https://doi.org/10.1016/0004-3702(81)90024-2).
  192. Baker, S., Scharstein, D., Lewis, J.P., Roth, S., Black, M.J., and Szeliski, R., "A Database and Evaluation Methodology for Optical Flow", *International Journal of Computer Vision* 92(1):1-31, 2010, doi:[10.1007/s11263-010-0390-2](https://doi.org/10.1007/s11263-010-0390-2).
  193. Hovmöller, E., "The Trough-and-Ridge diagram", *Tellus* 1(2):62-66, 1949, doi:[10.1111/j.2153-3490.1949.tb01260.x](https://doi.org/10.1111/j.2153-3490.1949.tb01260.x).
  194. Crone, T.J., McDuff, R.E., and Wilcock, W.S.D., "Optical plume velocimetry: a new flow measurement technique for use in seafloor hydrothermal systems", *Experiments in Fluids* 45(5):899-915, 2008, doi:[10.1007/s00348-008-0508-2](https://doi.org/10.1007/s00348-008-0508-2).
  195. Kamimoto, T., Miyairi, Y., Nagakura, K., and Matsuoka, S., "Measurement of Flow Velocity in Diesel Flames by a Cross-Correlation Method", SAE Technical Paper 820357, 1982, doi:[10.4271/820357](https://doi.org/10.4271/820357).
  196. Shioji, M., Kimoto, T., Okamoto, M., and Ikegami, M., "An Analysis of Diesel Flame by Picture Processing", *JSME international journal. Ser. 2, Fluids engineering, heat transfer, power, combustion, thermophysical properties* 32(3):434-442, 1989, doi:[10.1299/jsmeb1988.32.3\\_434](https://doi.org/10.1299/jsmeb1988.32.3_434).
  197. Yamaguchi, I., Nakahira, T., Komori, M., and Kobayashi, S., "An Image Analysis of High Speed Combustion Photographs for D.I. Diesel Engine with High Pressure Fuel Injection", SAE Technical Paper 901577, 1990, doi:[10.4271/901577](https://doi.org/10.4271/901577).
  198. Winterbone, D.E., Yates, D.A., Clough, E., Rao, K.K., Gomes, P., and Sun, J.H., "Combustion in High-Speed Direct Injection Diesel Engines—A Comprehensive Study", *Proceedings of the Institution of Mechanical Engineers, Part C: Journal of Mechanical Engineering Science* 208(4):223-240, 2016, doi:[10.1243/pime\\_proc\\_1994\\_208\\_123\\_02](https://doi.org/10.1243/pime_proc_1994_208_123_02).
-

- 
199. Zha, K., Busch, S., Warey, A., Peterson, R.C., and Kurtz, E., "A Study of Piston Geometry Effects on Late-Stage Combustion in a Light-Duty Optical Diesel Engine Using Combustion Image Velocimetry", *SAE International Journal of Engines* 11(6):783-804, 2018, doi:[10.4271/2018-01-0230](https://doi.org/10.4271/2018-01-0230).
  200. Bergin, M.J., Reitz, R.D., Oh, S., Miles, P.C., Hildingsson, L., and Hultqvist, A., "Fuel Injection and Mean Swirl Effects on Combustion and Soot Formation in Heavy Duty Diesel Engines", SAE Technical Paper 2007-01-0912, 2007, doi:[10.4271/2007-01-0912](https://doi.org/10.4271/2007-01-0912).
  201. Dembinski, H.W., "The effects of injection pressure and swirl on in-cylinder flow pattern and combustion in a compression-ignition engine", *International Journal of Engine Research* 15(4):444-459, 2014, doi:[10.1177/1468087413491262](https://doi.org/10.1177/1468087413491262).
  202. Rao, L., and Kook, S., "Optimisation of Image Processing Parameters for Flame Image Velocimetry (FIV) Measurement in a Single-Cylinder, Small-Bore Optical Diesel Engine", SAE Technical Paper 2019-01-0719, 2019, doi:[10.4271/2019-01-0719](https://doi.org/10.4271/2019-01-0719).
  203. Dembinski, H.W.R., and Angstrom, H.-E., "Optical Study of Swirl during Combustion in a CI Engine with Different Injection Pressures and Swirl Ratios Compared with Calculations", SAE Technical Paper 2012-01-0682, 2012, doi:[10.4271/2012-01-0682](https://doi.org/10.4271/2012-01-0682).
  204. Zama, Y., Ochiai, W., Furuhashi, T., and Arai, M. "Velocity measurement inside a diesel spray by using time-resolved PIV under high ambient density condition". in *Proceedings of 12th Triennial International Conference on Liquid Atomization and Spray Systems*. 2012. Heidelberg, Germany.
  205. Gragston, M., Smith, C., Wu, Y., et al., "Simultaneous Species Concentration and Flow Velocity Imaging Using 2D Raman Scattering at Elevated Pressure", in *AIAA Scitech 2019 Forum*. 2019: San Diego, California.
  206. Catapano, F., Iorio, S.D., Sementa, P., and Vaglieco, B.M., "Optimization of the compressed natural gas direct injection in a small research spark ignition engine", *International Journal of Engine Research* 18(1-2):118-130, 2017, doi:[10.1177/1468087417692505](https://doi.org/10.1177/1468087417692505).
  207. Barone, M., Lombardi, S., Continillo, G., Sementa, P., and Vaglieco, B.M., "Application of the optical flow method for the experimental analysis of turbulent flame propagation in a transparent engine", *AIP Conference Proceedings* 1790(1):110002, 2016, doi:[10.1063/1.4968709](https://doi.org/10.1063/1.4968709).
  208. Westlye, F.R., "Experimental Study of Liquid Fuel Spray Combustion". 2016, Dissertation, Kongens Lyngby, Technical University of Denmark.
  209. Bjørgen, K.O.P., Emberson, D.R., and Lovas, T., "Diffuse Back-Illuminated Extinction Imaging of Soot: Effects of Beam Steering and Flame Luminosity", SAE Technical Paper 2019-01-0011, 2019, doi:[10.4271/2019-01-0011](https://doi.org/10.4271/2019-01-0011).
  210. Adam, T.F., "Optical Analysis of High Pressure Diesel Sprays using Image Segmentation Methods". 2016, Master's Thesis, Saarbrücken, Saarland University.
  211. Catapano, F., Sementa, P., and Vaglieco, B.M., "Air-fuel mixing and combustion behavior of gasoline-ethanol blends in a GDI wall-guided turbocharged multi-cylinder optical engine", *Renewable Energy* 96:319-332, 2016, doi:[10.1016/j.renene.2016.04.087](https://doi.org/10.1016/j.renene.2016.04.087).
-

- 
212. Zhao, H., "Laser Diagnostics and Optical Measurement Techniques in Internal Combustion Engines ", Warrendale, PA, U.S.A., SAE International, 2012, p. 16-21, ISBN: 978-0-7680-5782-9.
213. "File: Stimulated Emission.svg", [https://commons.wikimedia.org/wiki/File:Stimulated\\_Emission.svg](https://commons.wikimedia.org/wiki/File:Stimulated_Emission.svg), accessed Mar. 02, 2020.
214. Peterson, B., Baum, E., Böhm, B., Sick, V., and Dreizler, A., "High-speed PIV and LIF imaging of temperature stratification in an internal combustion engine", *Proceedings of the Combustion Institute* 34(2):3653-3660, 2013, doi:[10.1016/j.proci.2012.05.051](https://doi.org/10.1016/j.proci.2012.05.051).
215. Kneissl, M., Kolbe, T., Chua, C., et al., "Advances in Group III-Nitride-Based Deep UV Light-Emitting Diode Technology", *Semiconductor Science and Technology* 26(1):014036, 2011, doi:[10.1088/0268-1242/26/1/014036](https://doi.org/10.1088/0268-1242/26/1/014036).
216. Matveev, B.A., Zotova, N.V., Il'Inskaya, N.D., Karandashev, S.A., Remennyi, M.A., Stus, N.M., and Talalakin, G.N., "Towards efficient mid-IR LED operation: optical pumping, extraction or injection of carriers?", *Journal of Modern Optics* 49(5-6):743-756, 2002, doi:[10.1080/09500340110108576](https://doi.org/10.1080/09500340110108576).
217. Willert, C., Stasicki, B., Klinner, J., and Moessner, S., "Pulsed operation of high-power light emitting diodes for imaging flow velocimetry", *Measurement Science and Technology* 21(7):075402, 2010, doi:[10.1088/0957-0233/21/7/075402](https://doi.org/10.1088/0957-0233/21/7/075402).
218. Willert, C.E., Mitchell, D.M., and Soria, J., "An assessment of high-power light-emitting diodes for high frame rate schlieren imaging", *Experiments in Fluids* 53(2):413-421, 2012, doi:[10.1007/s00348-012-1297-1](https://doi.org/10.1007/s00348-012-1297-1).
219. Wilson, S., Gustafson, G., Lincoln, D., Murari, K., and Johansen, C., "Performance evaluation of an overdriven LED for high-speed schlieren imaging", *Journal of Visualization* 18(1):35-45, 2014, doi:[10.1007/s12650-014-0220-7](https://doi.org/10.1007/s12650-014-0220-7).
220. Bröder, D., and Sommerfeld, M., "Planar shadow image velocimetry for the analysis of the hydrodynamics in bubbly flows", *Measurement Science and Technology* 18(8):2513-2528, 2007, doi:[10.1088/0957-0233/18/8/028](https://doi.org/10.1088/0957-0233/18/8/028).
221. Menser, J., Schneider, F., Dreier, T., and Kaiser, S.A., "Multi-pulse shadowgraphic RGB illumination and detection for flow tracking", *Experiments in Fluids* 59(6), 2018, doi:[10.1007/s00348-018-2541-0](https://doi.org/10.1007/s00348-018-2541-0).
222. Zhao, H., "Laser Diagnostics and Optical Measurement Techniques in Internal Combustion Engines ", Warrendale, PA, U.S.A., SAE International, 2012, p. 36-37, ISBN: 978-0-7680-5782-9.
223. Wang, D., Zhang, T., and Kuang, H., "Relationship between the charge-coupled device signal-to-noise ratio and dynamic range with respect to the analog gain", *Appl Opt* 51(29):7103-14, 2012, doi:[10.1364/AO.51.007103](https://doi.org/10.1364/AO.51.007103).
224. "File: Bayer pattern on sensor.svg", [https://commons.wikimedia.org/wiki/File:Bayer\\_pattern\\_on\\_sensor.svg](https://commons.wikimedia.org/wiki/File:Bayer_pattern_on_sensor.svg), accessed Mar. 02, 2020.
225. "FASTCAM SA - Z Technical Datasheet". 2015, PHOTRON LIMITED: Tokyo, Japan.
-

- 
226. "Hyper Vision HPV-X2", <https://www.shimadzu.com/an/test/hpv/hpv-x2/index.html>, accessed Oct. 30, 2019.
227. Ding, H., Wang, Z., Li, Y., Xu, H., and Zuo, C., "Initial dynamic development of fuel spray analyzed by ultra high speed imaging", *Fuel* 169:99-110, 2016, doi:[10.1016/j.fuel.2015.11.083](https://doi.org/10.1016/j.fuel.2015.11.083).
228. Wu, S., Xu, M., Hung, D.L.S., and Pan, H., "In-nozzle flow investigation of flash boiling fuel sprays", *Applied Thermal Engineering* 117:644-651, 2017, doi:[10.1016/j.applthermaleng.2016.12.105](https://doi.org/10.1016/j.applthermaleng.2016.12.105).
229. Kastengren, A.L., Powell, C.F., Liu, Z., Fezzaa, K., and Wang, J. "High-Speed X-Ray Imaging of Diesel Injector Needle Motion". in *ASME 2009 Internal Combustion Engine Division Spring Technical Conference*. 2009. Milwaukee, Wisconsin, USA.
230. Rusly, A., Kook, S., Hawkes, E., and Zhang, R., "High-Speed Imaging of Soot Luminosity and Spectral Analysis of In-Cylinder Pressure Trace during Diesel Knock", SAE Technical Paper 2014-01-1259, 2014, doi:[10.4271/2014-01-1259](https://doi.org/10.4271/2014-01-1259).
231. "Product-Manual for DaVis 8.3 - High-Speed IRO (ext. Controller)". 2015, LaVision GmbH: Göttingen, Germany.
232. "International workshop on measurement and computation of turbulent non-premixed flames", <https://www.sandia.gov/TNF/abstract.html>, accessed Dec. 17, 2018.
233. Meijer, M., Somers, B., Johnson, J., et al., "Engine Combustion Network (Ecn): Characterization and Comparison of Boundary Conditions for Different Combustion Vessels", *Atomization and Sprays* 22(9):777-806, 2012, doi:[10.1615/AtomizSpr.2012006083](https://doi.org/10.1615/AtomizSpr.2012006083).
234. Payri, R., Gimeno, J., Cuisano, J., and Arco, J., "Hydraulic characterization of diesel engine single-hole injectors", *Fuel* 180:357-366, 2016, doi:[10.1016/j.fuel.2016.03.083](https://doi.org/10.1016/j.fuel.2016.03.083).
235. Stetsyuk, V., Crua, C., Pearson, R., and Gold, M., "Direct imaging of primary atomisation in the near-nozzle region of diesel sprays", in *ILASS – Europe 2014*. 2014.
236. Nilaphai, O., Hespel, C., Moreau, B., et al., "New high pressure and high temperature chamber for Diesel spray characterization", in *ILASS – Europe 2016*. 2016. p. 1-10.
237. Pickett, L.M., Manin, J., Kastengren, A., and Powell, C., "Comparison of Near-Field Structure and Growth of a Diesel Spray Using Light-Based Optical Microscopy and X-Ray Radiography", *SAE International Journal of Engines* 7(2):1044-1053, 2014, doi:[10.4271/2014-01-1412](https://doi.org/10.4271/2014-01-1412).
238. Kastengren, A., Ilavsky, J., Viera, J.P., et al., "Measurements of droplet size in shear-driven atomization using ultra-small angle x-ray scattering", *International Journal of Multiphase Flow* 92:131-139, 2017, doi:[10.1016/j.ijmultiphaseflow.2017.03.005](https://doi.org/10.1016/j.ijmultiphaseflow.2017.03.005).
239. Matusik, K.E., Duke, D.J., Kastengren, A.L., Sovis, N., Swantek, A.B., and Powell, C.F., "High-resolution X-ray tomography of Engine Combustion Network diesel injectors", *International Journal of Engine Research* 19(9):963-976, 2018, doi:[10.1177/1468087417736985](https://doi.org/10.1177/1468087417736985).
240. Kastengren, A.L., Tilocco, F.Z., Powell, C.F., Manin, J., Pickett, L.M., Payri, R., and Bazyn, T., "Engine Combustion Network (Ecn): Measurements of Nozzle Geometry and Hydraulic Behavior", *Atomization and Sprays* 22(12):1011-1052, 2012, doi:[DOI 10.1615/AtomizSpr.2013006309](https://doi.org/10.1615/AtomizSpr.2013006309).
-

- 
241. Duke, D.J., Finney, C.E.A., Kastengren, A., et al., "High-Resolution X-Ray and Neutron Computed Tomography of an Engine Combustion Network Spray G Gasoline Injector", *SAE Int. J. Fuels Lubr.* 10(2):328-343, 2017, doi:[10.4271/2017-01-0824](https://doi.org/10.4271/2017-01-0824).
  242. Bloomfield, P., "Fourier Analysis of Time Series: An Introduction", 2nd Edition, New York, Wiley-Interscience, 2000, doi: [10.1002/0471722235](https://doi.org/10.1002/0471722235), ISBN: 978-0-471-88948-9.
  243. Reuss, D.L., Kuo, T.-W., Khalighi, B., Haworth, D., and Rosalik, M., "Particle Image Velocimetry Measurements in a High-Swirl Engine Used for Evaluation of Computational Fluid Dynamics Calculations", SAE Technical Paper 952381, 1995, doi:[10.4271/952381](https://doi.org/10.4271/952381).
  244. Perini, F., Miles, P.C., and Reitz, R.D., "A comprehensive modeling study of in-cylinder fluid flows in a high-swirl, light-duty optical diesel engine", *Computers & Fluids* 105:113-124, 2014, doi:[10.1016/j.compfluid.2014.09.011](https://doi.org/10.1016/j.compfluid.2014.09.011).
  245. Deslandes, W., Dumont, P., Dupont, A., Baby, X., Charnay, G., and Boree, J., "Airflow Cyclic Variations Analysis in Diesel Combustion Chamber by PIV Measurements", SAE Technical Paper 2004-01-1410, 2004, doi:[10.4271/2004-01-1410](https://doi.org/10.4271/2004-01-1410).
  246. Schmitt, M., Frouzakis, C.E., Wright, Y.M., Tomboulides, A.G., and Boulouchos, K., "Direct numerical simulation of the compression stroke under engine-relevant conditions: Evolution of the velocity and thermal boundary layers", *International Journal of Heat and Mass Transfer* 91:948-960, 2015, doi:[10.1016/j.ijheatmasstransfer.2015.08.031](https://doi.org/10.1016/j.ijheatmasstransfer.2015.08.031).
  247. Kaiser, S.A., Schild, M., and Schulz, C., "Thermal stratification in an internal combustion engine due to wall heat transfer measured by laser-induced fluorescence", *Proceedings of the Combustion Institute* 34(2):2911-2919, 2013, doi:[10.1016/j.proci.2012.05.059](https://doi.org/10.1016/j.proci.2012.05.059).
  248. Musculus, M.P.B., "Effects of the In-Cylinder Environment on Diffusion Flame Lift-Off in a DI Diesel Engine", SAE Technical Paper 2003-01-0074, 2003, doi:[10.4271/2003-01-0074](https://doi.org/10.4271/2003-01-0074).
  249. Luong, M., Zhang, R., Schulz, C., and Sick, V., "Toluene laser-induced fluorescence for in-cylinder temperature imaging in internal combustion engines", *Applied Physics B* 91(3-4):669-675, 2008, doi:[10.1007/s00340-008-2995-5](https://doi.org/10.1007/s00340-008-2995-5).
  250. Schmitt, M., Frouzakis, C.E., Tomboulides, A.G., Wright, Y.M., and Boulouchos, K., "Direct numerical simulation of the effect of compression on the flow, temperature and composition under engine-like conditions", *Proceedings of the Combustion Institute* 35(3):3069-3077, 2015, doi:[10.1016/j.proci.2014.06.097](https://doi.org/10.1016/j.proci.2014.06.097).
  251. Mandanis, C., Schmitt, M., Koch, J., Wright, Y.M., and Boulouchos, K., "Wall Heat Flux and Thermal Stratification Investigations during the Compression Stroke of an engine-like Geometry: A comparison between LES and DNS", *Flow, Turbulence and Combustion* 100(3):769-795, 2017, doi:[10.1007/s10494-017-9879-x](https://doi.org/10.1007/s10494-017-9879-x).
  252. Schmitt, M., Frouzakis, C.E., Wright, Y.M., Tomboulides, A.G., and Boulouchos, K., "Investigation of wall heat transfer and thermal stratification under engine-relevant conditions using DNS", *International Journal of Engine Research* 17(1):63-75, 2015, doi:[10.1177/1468087415588710](https://doi.org/10.1177/1468087415588710).
  253. Schmitt, M., Frouzakis, C.E., Wright, Y.M., Tomboulides, A., and Boulouchos, K., "Direct numerical simulation of the compression stroke under engine relevant conditions: Local wall heat flux distribution", *International Journal of Heat and Mass Transfer* 92:718-731, 2016, doi:[10.1016/j.ijheatmasstransfer.2015.08.074](https://doi.org/10.1016/j.ijheatmasstransfer.2015.08.074).
-

- 
254. Zhao, H., "Laser Diagnostics and Optical Measurement Techniques in Internal Combustion Engines ", Warrendale, PA, U.S.A., SAE International, 2012, p. 270-271, ISBN: 978-0-7680-5782-9.
255. Tee, K.T., "Design and testing of an intake-air heater for an optically accessible Diesel engine". 2018, Bachelor's Thesis, Duisburg, University of Duisburg-Essen.
256. "Aerosol Generator – Datasheet". 2018, LaVision GmbH: Göttingen, Germany.
257. "Product-Manual for DaVis 8.2". 2014, LaVision GmbH: Göttingen, Germany.
258. Wickman, D.D., Senecal, P.K., and Reitz, R.D., "Diesel Engine Combustion Chamber Geometry Optimization Using Genetic Algorithms and Multi-Dimensional Spray and Combustion Modeling", SAE Technical Paper 2001-01-0547, 2001, doi:[10.4271/2001-01-0547](https://doi.org/10.4271/2001-01-0547).
259. Zhu, Y., Zhao, H., and Ladommatos, N., "Computational Study of the Effects of Injection Timing, EGR and Swirl Ratio on a HSDI Multi-Injection Diesel Engine Emission and Performance", SAE Technical Paper 2003-01-0346, 2003, doi:[10.4271/2003-01-0346](https://doi.org/10.4271/2003-01-0346).
260. Li, Y., Jia, M., Chang, Y., Liu, Y., Xie, M., Wang, T., and Zhou, L., "Parametric study and optimization of a RCCI (reactivity controlled compression ignition) engine fueled with methanol and diesel", *Energy* 65:319-332, 2014, doi:[10.1016/j.energy.2013.11.059](https://doi.org/10.1016/j.energy.2013.11.059).
261. Bensing, D., "Aufbau eines optisch zugänglichen Einzylinder-Viertaktmotors und charakterisierende Messungen". 2013, Dissertation, Duisburg, Essen, Universität Duisburg-Essen.
262. Schulz, C., and Sick, V., "Tracer-LIF diagnostics: quantitative measurement of fuel concentration, temperature and fuel/air ratio in practical combustion systems", *Progress in Energy and Combustion Science* 31(1):75-121, 2005, doi:[10.1016/j.peccs.2004.08.002](https://doi.org/10.1016/j.peccs.2004.08.002).
263. Arcoumanis, C., and Kamimoto, T., "Flow and Combustion in Reciprocating Engines", 1st Edition, Springer-Verlag Berlin Heidelberg, 2009, p. 187-189, doi: [10.1007/978-3-540-68901-0](https://doi.org/10.1007/978-3-540-68901-0), ISBN: 978-3-540-68901-0.
264. Fansler, T.D., and French, D.T., "Swirl, Squish and Turbulence in Stratified-Charge Engines: Laser-Velocimetry Measurements and Implications for Combustion", SAE Technical Paper 870371, 1987, doi:[10.4271/870371](https://doi.org/10.4271/870371).
265. Arcoumanis, C., Bicen, A.F., and Whitelaw, J.H., "Squish and Swirl-Squish Interaction in Motored Model Engines", *Journal of Fluids Engineering* 105(1):105-112, 1983, doi:[10.1115/1.3240925](https://doi.org/10.1115/1.3240925).
266. Annand, W.J.D., "Heat Transfer in the Cylinders of Reciprocating Internal Combustion Engines", *Proceedings of the Institution of Mechanical Engineers* 177(36):973-996, 1963, doi:[10.1243/pime\\_proc\\_1963\\_177\\_069\\_02](https://doi.org/10.1243/pime_proc_1963_177_069_02).
267. Jung, Y., Manin, J., Skeen, S., and Pickett, L.M., "Measurement of Liquid and Vapor Penetration of Diesel Sprays with a Variation in Spreading Angle", SAE Technical Paper 2015-01-0946, 2015, doi:[10.4271/2015-01-0946](https://doi.org/10.4271/2015-01-0946).
268. Sotillo, A.V. "Spray B Results of Evaporative Experiments". in *ECN Workshop 3.10*. 2015: Engine Combustion Network.
-

- 
269. Pastor, J.V., Payri, R., Garcia-Oliver, J.M., and Briceno, F.J., "Analysis of Transient Liquid and Vapor Phase Penetration for Diesel Sprays under Variable Injection Conditions", *Atomization and Sprays* 21(6):503-520, 2011, doi:[10.1615/AtomizSpr.2011003721](https://doi.org/10.1615/AtomizSpr.2011003721).
270. Neal, N., and Rothamer, D., "Measurement and characterization of fully transient diesel fuel jet processes in an optical engine with production injectors", *Experiments in Fluids* 57(10), 2016, doi:[10.1007/s00348-016-2239-0](https://doi.org/10.1007/s00348-016-2239-0).
271. Grochowina, M., Hertel, D., Tartsch, S., and Sattelmayer, T., "Ignition of Diesel Pilot Fuel in Dual-Fuel Engines", *Journal of Engineering for Gas Turbines and Power* 141(8), 2019, doi:[10.1115/1.4043485](https://doi.org/10.1115/1.4043485).
272. CMT. "Diesel rate of injection", <https://www.cmt.upv.es/ECN03.aspx>, accessed Oct. 1, 2018.
273. Woschni, G., "A Universally Applicable Equation for the Instantaneous Heat Transfer Coefficient in the Internal Combustion Engine", SAE Technical Paper 670931, 1967, doi:[10.4271/670931](https://doi.org/10.4271/670931).
274. NIST. "Nitrogen", <https://webbook.nist.gov/cgi/cbook.cgi?ID=C7727379&Type=JANAFG&Plot=on>, accessed Oct 1, 2018.
275. Lapuerta, M., Armas, O., and Hernández, J.J., "Diagnosis of DI Diesel combustion from in-cylinder pressure signal by estimation of mean thermodynamic properties of the gas", *Applied Thermal Engineering* 19(5):513-529, 1999, doi:[10.1016/s1359-4311\(98\)00075-1](https://doi.org/10.1016/s1359-4311(98)00075-1).
276. Pawlowski, A., Kneer, R., Lippert, A.M., and Parrish, S.E., "Investigation of the Interaction of Sprays from Clustered Orifices under Ambient Conditions Relevant for Diesel Engines", *SAE International Journal of Engines* 1(1):514-527, 2008, doi:[10.4271/2008-01-0928](https://doi.org/10.4271/2008-01-0928).
277. Wang, G., "Development of a 1D simulation model for an optically accessible Diesel engine in GT-Power". 2018, Bachelor's Thesis, Duisburg, University of Duisburg-Essen.
278. Pickett, L.M. "Liquid extinction analysis compared to CFD". in *ECN Workshop 5.9. 2018: Engine Combustion Network*.
279. Otsu, N., "A Threshold Selection Method from Gray-Level Histograms", *IEEE Transactions on Systems, Man, and Cybernetics* 9(1):62-66, 1979, doi:[10.1109/tsmc.1979.4310076](https://doi.org/10.1109/tsmc.1979.4310076).
280. MathWorks. "Morphologically close image", <https://www.mathworks.com/help/images/ref/imclose.html>, accessed Oct. 1, 2018.
281. Arai, M., Amagai, K., and Ebara, T., "Attitude Control of a Diesel Spray Under the Coanda Effect", SAE Technical Paper 941923, 1994, doi:[10.4271/941923](https://doi.org/10.4271/941923).
282. Shawal, S., Goschutz, M., Schild, M., Kaiser, S., Neurohr, M., Pfeil, J., and Koch, T., "High-Speed Imaging of Early Flame Growth in Spark-Ignited Engines Using Different Imaging Systems via Endoscopic and Full Optical Access", *SAE International Journal of Engines* 9(2), 2016, doi:[10.4271/2016-01-0644](https://doi.org/10.4271/2016-01-0644).
283. Chartier, C., Aronsson, U., Andersson, Ö., Egnell, R., and Johansson, B., "Influence of jet-jet interactions on the lift-off length in an optical heavy-duty DI diesel engine", *Fuel* 112:311-318, 2013, doi:[10.1016/j.fuel.2013.05.021](https://doi.org/10.1016/j.fuel.2013.05.021).
-

- 
284. Mueller, C.J., and Martin, G.C., "Effects of Oxygenated Compounds on Combustion and Soot Evolution in a DI Diesel Engine: Broadband Natural Luminosity Imaging", SAE Technical Paper 2002-01-1631, 2002, doi:[10.4271/2002-01-1631](https://doi.org/10.4271/2002-01-1631).
285. Dembinski, H.W.R., "The effects of injection pressure and swirl on in-cylinder flow pattern and combustion in a compression-ignition engine", *International Journal of Engine Research* 15(4):444-459, 2013, doi:[10.1177/1468087413491262](https://doi.org/10.1177/1468087413491262).
286. Schmidt, D.P., Rutland, C.J., and Corradini, M.L., "A Fully Compressible, Two-Dimensional Model of Small, High-Speed, Cavitating Nozzles", *Atomization and Sprays* 9(3):255-276, 1999, doi:[10.1615/AtomizSpr.v9.i3.20](https://doi.org/10.1615/AtomizSpr.v9.i3.20).
287. Chaves, H., and Ludwig, C., "Characterization of cavitation in transparent nozzles depending on the nozzle geometry", in *Proceedings of the 20th ILASS - Europe Meeting 2005*. 2005.
288. Pickett, L.M., Manin, J., Payri, R., Bardi, M., and Gimeno, J., "Transient Rate of Injection Effects on Spray Development", SAE Technical Paper 2013-24-0001, 2013, doi:[10.4271/2013-24-0001](https://doi.org/10.4271/2013-24-0001).
289. Pickett, L.M., and Siebers, D.L., "Fuel Effects on Soot Processes of Fuel Jets at DI Diesel Conditions", SAE Technical Paper 2003-01-3080, 2003, doi:[10.4271/2003-01-3080](https://doi.org/10.4271/2003-01-3080).
290. Payri, R., García-Oliver, J.M., Bardi, M., and Manin, J., "Fuel temperature influence on diesel sprays in inert and reacting conditions", *Applied Thermal Engineering* 35:185-195, 2012, doi:[10.1016/j.applthermaleng.2011.10.027](https://doi.org/10.1016/j.applthermaleng.2011.10.027).
291. Merola, S.S., Vaglieco, B.M., Corcione, F.E., and Mancaruso, E., "In-Cylinder Combustion Analysis by Flame Emission Spectroscopy of Transparent CR Diesel Engine", SAE Technical Paper 2003-01-1112, 2003, doi:[10.4271/2003-01-1112](https://doi.org/10.4271/2003-01-1112).
292. Macian, V., Payri, R., Ruiz, S., Bardi, M., and Plazas, A.H., "Experimental study of the relationship between injection rate shape and Diesel ignition using a novel piezo-actuated direct-acting injector", *Applied Energy* 118:100-113, 2014, doi:[10.1016/j.apenergy.2013.12.025](https://doi.org/10.1016/j.apenergy.2013.12.025).
293. Klein-Douwel, R.J.H., Donkerbroek, A.J., van Vliet, A.P., et al., "Soot and chemiluminescence in diesel combustion of bio-derived, oxygenated and reference fuels", *Proceedings of the Combustion Institute* 32(2):2817-2825, 2009, doi:[10.1016/j.proci.2008.06.140](https://doi.org/10.1016/j.proci.2008.06.140).
294. Augusta, R., Foster, D.E., Ghandhi, J.B., Eng, J., and Najt, P.M., "Chemiluminescence Measurements of Homogeneous Charge Compression Ignition (HCCI) Combustion", SAE Technical Paper 2006-01-1520, 2006, doi:[10.4271/2006-01-1520](https://doi.org/10.4271/2006-01-1520).
295. Srna, A., Bruneaux, G., von Rotz, B., Bombach, R., Herrmann, K., and Boulouchos, K., "Optical Investigation of Sooting Propensity of n-Dodecane Pilot/Lean-Premixed Methane Dual-Fuel Combustion in a Rapid Compression-Expansion Machine", *SAE International Journal of Engines* 11(6):1049-1068, 2018, doi:[10.4271/2018-01-0258](https://doi.org/10.4271/2018-01-0258).
296. "SQ Fused Silica". 2011, j-plasma GmbH: Jena, Germany.
297. "UV Enhanced Aluminum Typical Coating Performance". 2009, Edmund Optics Inc.
298. Zhao, M., and Kaiser, S., "A study of ECN 'Spray B' in a light-duty optically accessible Diesel engine based on high-speed imaging with LED retro-reflection", SAE Technical Paper 2019-01-0550, 2019, doi:[10.4271/2019-01-0550](https://doi.org/10.4271/2019-01-0550).
-

- 
299. ECN. "Modeling Standards and Recommendations", <https://ecn.sandia.gov/diesel-spray-combustion/computational-method/modeling-standards/>, accessed Aug. 27, 2019.
  300. Ryan, T.W., and Callahan, T.J., "Homogeneous Charge Compression Ignition of Diesel Fuel", SAE Technical Paper 961160, 1996, doi:[10.4271/961160](https://doi.org/10.4271/961160).
  301. Zhen, X., Wang, Y., Xu, S., Zhu, Y., Tao, C., Xu, T., and Song, M., "The engine knock analysis—An overview", *Applied Energy* 92:628-636, 2012, doi:[10.1016/j.apenergy.2011.11.079](https://doi.org/10.1016/j.apenergy.2011.11.079).
  302. Withrow, L., and Rassweiler, G.M., "Slow Motion Shows Knocking and Non-Knocking Explosions", SAE Technical Paper 360126, 1936, doi:[10.4271/360126](https://doi.org/10.4271/360126).
  303. Miller, C.D., "Roles of Detonation Waves and Autoignition in Spark - Ignition Engine Knock as Shown by Photographs Taken at 40,000 and 200,000 Frames Per Sec", SAE Technical Paper 470207, 1947, doi:[10.4271/470207](https://doi.org/10.4271/470207).
  304. Nakagawa, Y., Takagi, Y., Itoh, T., and Iijima, T., "Laser Shadowgraphic Analysis Of Knocking In S.I. Engine", SAE Technical Paper 845001, 1984, doi:[10.4271/845001](https://doi.org/10.4271/845001).
  305. Spicher, U., and Kollmeier, H.P., "Detection of Flame Propagation During Knocking Combustion by Optical Fiber Diagnostics", SAE Technical Paper 861532, 1986, doi:[10.4271/861532](https://doi.org/10.4271/861532).
  306. Tanoue, K., Jimoto, T., Kimura, T., Yamamoto, M., and Hashimoto, J., "Effect of initial temperature and fuel properties on knock characteristics in a rapid compression and expansion machine", *Proceedings of the Combustion Institute* 36(3):3523-3531, 2017, doi:[10.1016/j.proci.2016.08.036](https://doi.org/10.1016/j.proci.2016.08.036).
  307. Kawahara, N., and Tomita, E., "Visualization of auto-ignition and pressure wave during knocking in a hydrogen spark-ignition engine", *international journal of hydrogen energy* 34(7):3156-3163, 2009, doi:[doi.org/10.1016/j.ijhydene.2009.01.091](https://doi.org/10.1016/j.ijhydene.2009.01.091).
  308. Hayashi, T., Taki, M., Kojima, S., and Kondo, T., "Photographic Observation of Knock with a Rapid Compression and Expansion Machine", SAE Technical Paper 841336, 1984, doi:[10.4271/841336](https://doi.org/10.4271/841336).
  309. Qi, Y., Wang, Z., Wang, J., and He, X., "Effects of thermodynamic conditions on the end gas combustion mode associated with engine knock", *Combustion and Flame* 162(11):4119-4128, 2015, doi:[10.1016/j.combustflame.2015.08.016](https://doi.org/10.1016/j.combustflame.2015.08.016).
  310. Pan, J., and Sheppard, C.G.W., "A Theoretical and Experimental Study of the Modes of End Gas Autoignition Leading to Knock in S. I. Engines", SAE Technical Paper 942060, 1994, doi:[10.4271/942060](https://doi.org/10.4271/942060).
  311. Wang, Z., Liu, H., and Reitz, R.D., "Knocking combustion in spark-ignition engines", *Progress in Energy and Combustion Science* 61:78-112, 2017, doi:[10.1016/j.peccs.2017.03.004](https://doi.org/10.1016/j.peccs.2017.03.004).
  312. Park, S.S., Jung, Y., and Bae, C., "Diesel Knock Visualization and Frequency Analysis of Premixed Charge Compression Ignition Combustion with a Narrow Injection Angle", SAE Technical Paper 2013-01-0906, 2013, doi:[10.4271/2013-01-0906](https://doi.org/10.4271/2013-01-0906).
  313. Andreae, M.M., Cheng, W.K., Kenney, T., and Yang, J., "On HCCI Engine Knock", SAE Technical Paper 2007-01-1858, 2007, doi:[10.4271/2007-01-1858](https://doi.org/10.4271/2007-01-1858).
-

- 
314. Thirouard, B., Cherel, J., and Knop, V., "Investigation of Mixture Quality Effect on CAI Combustion", SAE Technical Paper 2005-01-0141, 2005, doi:[10.4271/2005-01-0141](https://doi.org/10.4271/2005-01-0141).
315. König, G., and Sheppard, C.G.W., "End Gas Autoignition and Knock in a Spark Ignition Engine", SAE Technical Paper 902135, 1990, doi:[10.4271/902135](https://doi.org/10.4271/902135).
316. Ma, X., Xu, H., Jiang, C., and Shuai, S., "Ultra-high speed imaging and OH-LIF study of DMF and MF combustion in a DISI optical engine", *Applied Energy* 122:247-260, 2014, doi:[10.1016/j.apenergy.2014.01.071](https://doi.org/10.1016/j.apenergy.2014.01.071).
317. Aoyama, T., Hattori, Y., Mizuta, J.i., and Sato, Y., "An Experimental Study on Premixed-Charge Compression Ignition Gasoline Engine", SAE Technical Paper 960081, 1996, doi:[10.4271/960081](https://doi.org/10.4271/960081).
318. Hultqvist, A., Christensen, M., Johansson, B., Richter, M., Nygren, J., Hult, J., and Aldjn, M., "The HCCI Combustion Process in a Single Cycle - Speed Fuel Tracer LIF and Chemiluminescence Imaging", SAE Technical Paper 2002-01-0424, 2002, doi:[10.4271/2002-01-0424](https://doi.org/10.4271/2002-01-0424).
319. Noguchi, M., Tanaka, Y., Tanaka, T., and Takeuchi, Y., "A Study on Gasoline Engine Combustion by Observation of Intermediate Reactive Products during Combustion", SAE Technical Paper 790840, 1979, doi:[10.4271/790840](https://doi.org/10.4271/790840).
320. Onishi, S., Jo, S.H., Shoda, K., Jo, P.D., and Kato, S., "Active Thermo-Atmosphere Combustion (ATAC) - A New Combustion Process for Internal Combustion Engines", SAE Technical Paper 790501, 1979, doi:[10.4271/790501](https://doi.org/10.4271/790501).
321. Beretta, G., Rashidi, M., and Keck, J., "Turbulent flame propagation and combustion in spark ignition engines", *Combustion and flame* 52:217-245, 1983, doi:[10.1016/0010-2180\(83\)90135-9](https://doi.org/10.1016/0010-2180(83)90135-9).
322. Zeldovich, Y., "Regime classification of an exothermic reaction with nonuniform initial conditions", *Combustion and Flame* 39(2):211-214, 1980, doi:[10.1016/0010-2180\(80\)90017-6](https://doi.org/10.1016/0010-2180(80)90017-6).
323. Martz, J.B., Kwak, H., Im, H.G., Lavoie, G.A., and Assanis, D.N., "Combustion regime of a reacting front propagating into an auto-igniting mixture", *Proceedings of the Combustion Institute* 33(2):3001-3006, 2011, doi:[10.1016/j.proci.2010.07.040](https://doi.org/10.1016/j.proci.2010.07.040).
324. Musculus, M.P.B., Lachaux, T., Pickett, L.M., and Idicheria, C.A., "End-of-Injection Over-Mixing and Unburned Hydrocarbon Emissions in Low-Temperature-Combustion Diesel Engines", SAE Technical Paper 2007-01-0907, 2007, doi:[10.4271/2007-01-0907](https://doi.org/10.4271/2007-01-0907).
325. König, G., Maly, R.R., Bradley, D., Lau, A.K.C., and Sheppard, C.G.W., "Role of Exothermic Centres on Knock Initiation and Knock Damage", SAE Technical Paper 902136, 1990, doi:[10.4271/902136](https://doi.org/10.4271/902136).
326. Sun, Z., Blackshear, P.L., and Kittelson, D.B., "Spark Ignition Engine Knock Detection Using In-Cylinder Optical Probes", SAE Technical Paper 962103, 1996, doi:[10.4271/962103](https://doi.org/10.4271/962103).
327. Kawahara, N., Tomita, E., and Sakata, Y., "Auto-ignited kernels during knocking combustion in a spark-ignition engine", *Proceedings of the Combustion Institute* 31(2):2999-3006, 2007, doi:[10.1016/j.proci.2006.07.210](https://doi.org/10.1016/j.proci.2006.07.210).
-

- 
328. Hettinger, A., and Kulzer, A., "A new method to detect knocking zones", *SAE International Journal of Engines* 2(1):645-665, 2009, doi:[10.4271/2009-01-0698](https://doi.org/10.4271/2009-01-0698).
329. Kaiser, J.F., "Nonrecursive Digital Filter Design Using the I0-sinh Window Function", in *Proceedings of the 1974 IEEE International Symposium on Circuits and Systems*. 1974. p. 20–23.
330. Digital Signal Processing Committee of the IEEE Acoustics, S., and Signal Processing Society, eds., "Programs for Digital Signal Processing", New York, IEEE Press, 1979, ISBN: 0879421274.
331. Percival, D.B., and Walden, A.T., "Spectral Analysis for Physical Applications: Multitaper and Conventional Univariate Techniques", Cambridge, Cambridge University Press, 1993, doi: [10.1017/CBO9780511622762](https://doi.org/10.1017/CBO9780511622762), ISBN: 9780511622762.
332. Draper, C., "Pressure waves accompanying detonation in the internal combustion engine", *Journal of the Aeronautical Sciences* 5(6):219-226, 1938.
333. Hickling, R., Feldmaier, D.A., Chen, F.H., and Morel, J.S., "Cavity resonances in engine combustion chambers and some applications", *The Journal of the Acoustical Society of America* 73(4):1170-1178, 1983, doi:[10.1121/1.389261](https://doi.org/10.1121/1.389261).
334. Draper, and Stark, C., "The physical effects of detonation in a closed cylindrical chamber". 1935, NACA Technical Report 493. p. 361-379.
335. Draper, C.S., "Pressure Waves Accompanying Detonation in the Internal Combustion Engine", *Journal of the Aeronautical Sciences* 5(6):219-226, 1938, doi:[10.2514/8.590](https://doi.org/10.2514/8.590).
336. Flowers, D., Aceves, S., Smith, R., Torres, J., Girard, J., and Dibble, R., "HCCI in a CFR Engine: Experiments and Detailed Kinetic Modeling", SAE Technical Paper 2000-01-0328, 2000, doi:[10.4271/2000-01-0328](https://doi.org/10.4271/2000-01-0328).
337. Morse, P.M., and Ingard, K.U., "Theoretical acoustics", Princeton, Princeton university press, 1968, ISBN: 0691024014.
338. Heywood, J., "Internal combustion engine fundamentals", New York, McGraw-Hill Education, 1988, p. 454-461, ISBN: 007028637X.
339. "AVL INDICOM 2013 - User's Guide, CALCGRAF - GRAPHICAL FORMULA EDITOR". 2012, AVL List GmbH: Graz, Austria.
340. Brecq, G., Bellettre, J., and Tazerout, M., "A new indicator for knock detection in gas SI engines", *International Journal of Thermal Sciences* 42(5):523-532, 2003, doi:[10.1016/s1290-0729\(02\)00052-2](https://doi.org/10.1016/s1290-0729(02)00052-2).
341. Samimy, B., and Rizzoni, G., "Engine Knock Analysis and Detection Using Time-Frequency Analysis", SAE Technical Paper 960618, 1996, doi:[10.4271/960618](https://doi.org/10.4271/960618).
342. Tahir, M.I., "Optical studies of spray characteristics in an optical diesel engine via schlieren imaging with corrective lenses ". 2017, Master's Thesis, Duisburg, University of Duisburg-Essen.
-

---

## Chapter 9 Appendices

---

### 9.1 Comparison of retro-reflection with Mie scattering and schlieren

#### 9.1.1 Introduction

Mie scattering and schlieren are commonly-used optical methods for liquid spray and fuel vapor imaging, respectively. Mie scattering is a possible method for obtaining data to compare the liquid length in the IVG optical Diesel engine with those in other optical engines or combustion vessels. Schlieren is an ECN-standard method for spray penetration measurements. In this section, Mie scattering and schlieren (with collimated light) are demonstrated and the results are compared with the fire-deck retro-reflection method (with uncollimated light). As a first step, in this work only the signals are compared and no further quantification is made to compare with the data from the ECN.

#### 9.1.2 Liquid spray measurement by Mie scattering

##### *Experimental apparatus and conditions*

The Mie scattering experiment was performed only under non-reacting conditions at low swirl. The fuel was injected at every 6th cycle at 1500 bar pressure. The in-cylinder core temperature targeted 900 K and the density targeted  $22.8 \text{ kg/m}^3$  by fixing the peak cylinder pressure at 61.5 bar and varying intake temperature from 25 to 70 °C. The rest of the engine operating conditions is the same as in Table 4.3.

Figure 9.1 shows the optical arrangement for Mie scattering imaging with the main parameters (also for fire-deck retro-reflection) listed in Table 9.1. A diode laser provided a continuous-wave 405 nm beam with a power of 50 mW vertically into one of the spacer windows. The beam was just below the fire deck, so that it could go through the short squish region (1.2 – 1.5 mm of height) during fuel injection. Although the beam did not go through all of the fuel droplets, the scattered light from the laser light by the top droplets could be “passed” to the rest of the liquid spray. However, the signal was still very low so that the exposure time was increased by more than 10 times and the frame rate was correspondingly decreased compared to the retro-reflection imaging set-up in Table 9.1. For a reasonable comparison, the blue LEDs in the fire-deck retro-reflection imaging were also run continuously. The incident-light intensity was decreased (compared to that with Table 9.1) by tuning the incident angle of the LEDs and their condensers. In different datasets, the camera was focused at the fire deck, which was close to the near-nozzle spray, or at 4 mm below around the spray tip (by moving the camera backward). The Mie scattering and fire-deck retro-reflection were performed during the same engine run to guarantee the same boundary conditions (neglecting the temperature rise due to hotter walls). Totally 100 engine cycles were recorded for each dataset (one engine run), including BG images for retro-reflection (without spray), spray images by retro-reflection, BG images for Mie scattering, spray images by Mie scattering. Each image subset contains 24 to 26 cycles. In the datasets shown here, the retro-reflection measurement was always performed first.

---

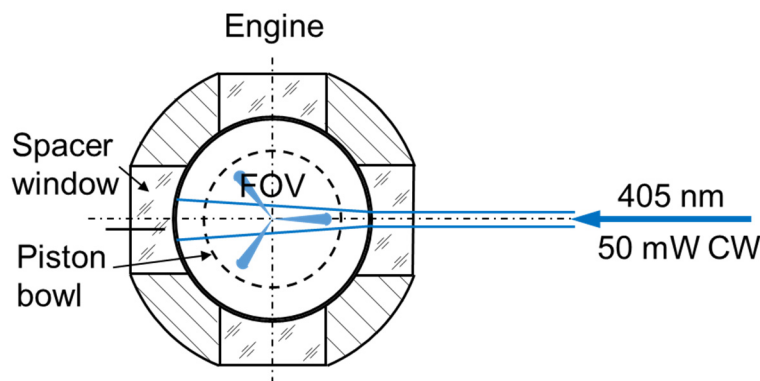


Figure 9.1 Arrangement of optics and engine cylinder for Mie scattering imaging. FOV: field-of-view.

Table 9.1 Imaging parameters for Mie scattering and fire-deck retro-reflection imaging.

Frame rate	10 kHz
Resolution	1024 × 1024
Projected pixel size	0.066 mm/pixel
Exposure time	98.4 μs
Camera lens	Nikon 105 mm <i>f</i> /2.8
Filter	None
Recorded cycles	100 (total)

**Image processing**

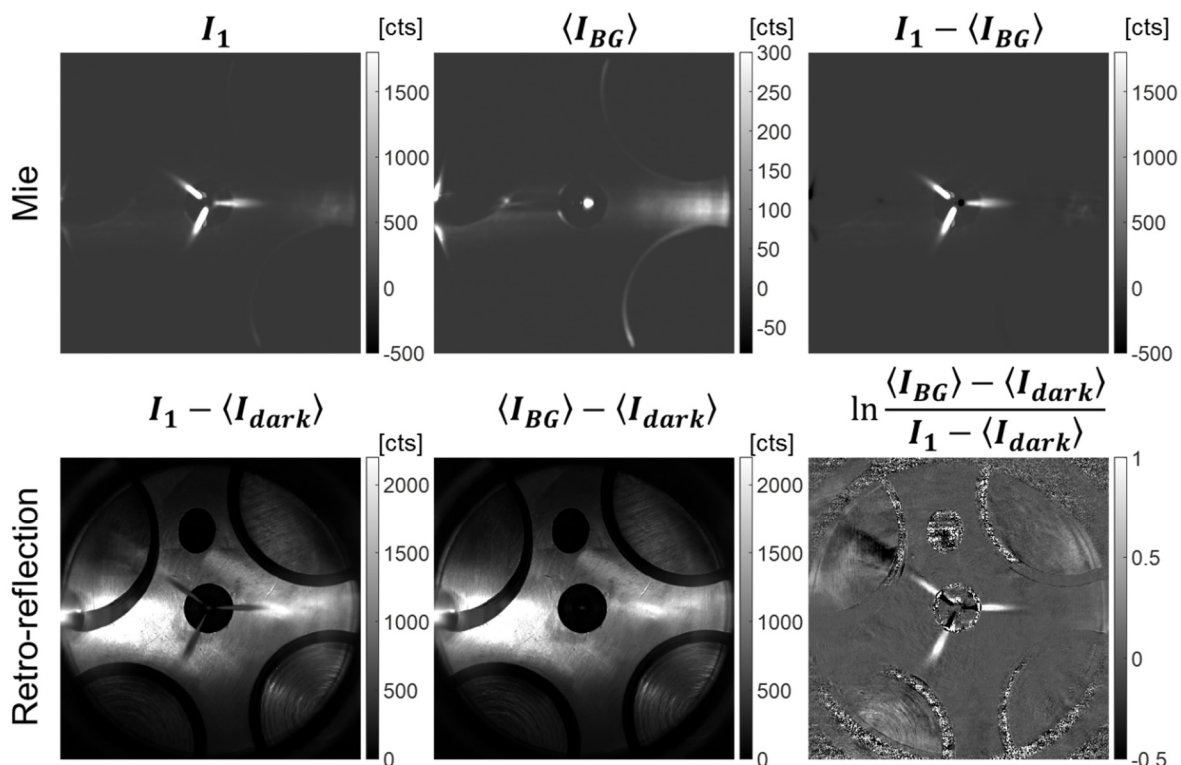


Figure 9.2 Processing procedures of BG subtraction for Mie scattering and optical-thickness calculation for fire-deck retro-reflection.

In order to find the difference between the Mie-scattered signal and the optical-thickness signal by retro-reflection, the signal profiles along the spray axis was obtained and compared with each other. As shown in Figure 9.2, for both methods, the BG images were averaged at a certain frame number

across different cycles. Here the 17th frame was chosen, recording the spray from 1.33 to 1.43 ms ASOI. For fire-deck retro-reflection, the single-frame optical thickness was calculated following the same procedures as in Figure 4.5. For Mie scattering, the single-frame signal was obtained by BG subtraction. Thereafter, the single-frame signal was averaged also across the engine cycles and the signal along the spray axis was plotted. As discussed in Section 4.3.2, the apparent axial distance from the nozzle hole exit was divided by  $\tan(17.5^\circ)$  to account for the angle between the orifice axis and the fire deck. Here only jet 3 is investigated.

### Results and discussion

The profiles along the spray axis of the Mie-scattered signal and the optical-thickness signal by retro-reflection focused at the fire deck at three different in-cylinder temperatures are compared in Figure 9.3. First, it is noticed that the optical-thickness signal shows more noise than the Mie-scattered signal. As discussed in Section 4.3.2, the negative region of the optical-thickness signal is due to the non-reflective area at the nozzle. Here the initial negative region in the Mie-scattered signal is because of the reflected light spot on the nozzle as seen in the mean BG image in Figure 9.2. The Mie-scattered signal peaks and falls at a shorter distance from the nozzle than the optical-thickness signal. This indicates that if using the same non-zero percentage of the peak value as a threshold, like previously commonly applied for Mie scattering [39], or using forward-extrapolation, like previously applied for DBI [150], the fire-deck retro-reflection method will result in a higher liquid length than the Mie scattering. Beyond the spray tip, the Mie-scattered signal stays around at zero, while there is a negative region in the optical-thickness curve because of beam-steering, as discussed in Section 4.3.2. The gaps between the optical-thickness curves as well as their zero-crossing points are larger compared to those of the Mie scattering, indicating a higher sensitivity to temperature and a steeper slope of liquid length with temperature, if the slight temperature increase during an engine run is neglected.

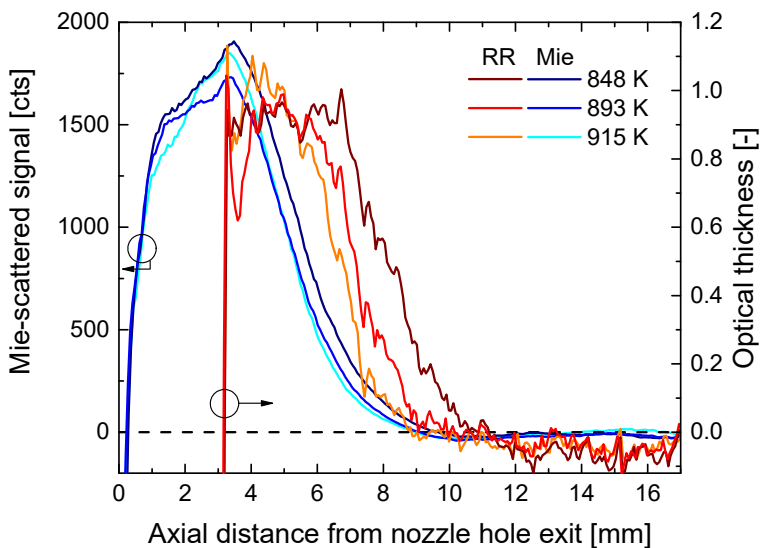


Figure 9.3 Profiles along the hole-3 spray axis of the Mie-scattered signal and the optical-thickness signal by retro-reflection at different in-cylinder core temperatures. Images were focused at the fire deck. “RR” – retro-reflection.

To investigate the influence of the focus plane, signal profiles at similar in-cylinder temperatures focused at the fire deck and at 4 mm below were compared in Figure 9.4. For the Mie scattering signal, it is seen that the peak moves closer to the nozzle and becomes higher at the lower object plane. The decreasing slope is steeper. For the optical-thickness signal, not much difference is seen. For both

methods, the zero-crossing points stay nearly unchanged. Thus, the effect of the object plane on both signals is little.

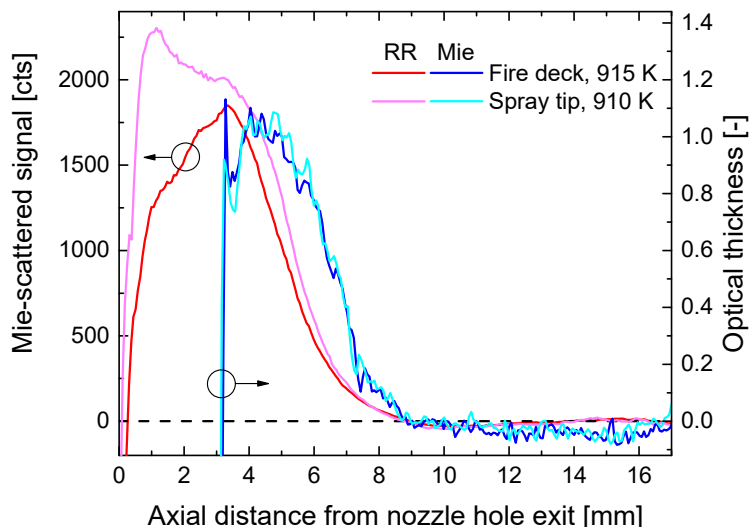


Figure 9.4 Profiles along the hole-3 spray axis of the Mie-scattered signal and the optical-thickness signal by retro-reflection at similar in-cylinder core temperatures and focused at different planes. “RR” – retro-reflection.

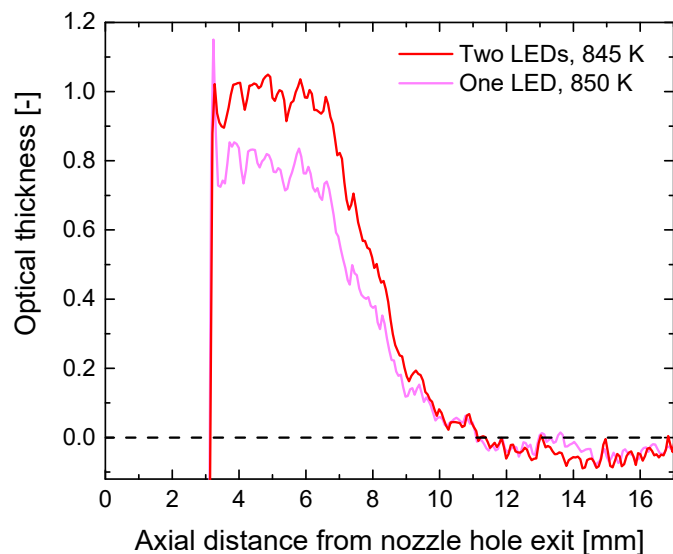


Figure 9.5 Profiles along the hole-3 spray axis of the optical-thickness signal by retro-reflection at similar in-cylinder core temperatures with one LED and two LEDs.

Only to understand the optical-thickness signal by fire-deck retro-reflection more, the signal profile along the spray axis of jet 3 with one LED (at the side of jet 3) is compared with that with both LEDs and at a similar in-cylinder temperature in Figure 9.5. It is seen that with one LED the optical-thickness profile is approximately proportionally lower compared to that with two LEDs. This means that if using the same threshold for liquid length quantification, a lower value will be obtained with the one-LED set-up. Thus, unlike in the case of the DBI method, the optical thickness obtained by the fire-deck retro-reflection method is influenced by the incident-light angle or intensity, leading to its difficulty for standardization. However, the zero-crossing point is not changed here, also close to the point in a previous dataset with a similar in-cylinder temperature with the imaging parameters in Chapter 4. This

indicates that the zero-crossing point may be an eligible metric, which is not influenced by the illumination set-up, for the fire-deck retro-reflection method.

### 9.1.3 Gaseous spray measurement by schlieren imaging

#### Experimental apparatus and conditions

The schlieren experiment was performed under both non-reacting and reacting conditions and at both swirl levels. The fuel was injected at 1500 bar pressure. The in-cylinder core temperature targeted 900 K and the density targeted  $22.8 \text{ kg/m}^3$  by fixing the peak cylinder pressure at 61.5 bar (non-reacting) / 59.9 bar (reacting) and varying intake temperature from 25 to 110 °C. The rest of the engine operating conditions is the same as in Table 4.3.

Figure 9.6 shows the optical arrangement for schlieren imaging in comparison with fire-deck retro-reflection. The main parameters listed in Table 9.2. The light from a green LED (LED Engin LZ1-10G100) with emission centered at 523 nm was collected by a condenser lens ( $f = 16 \text{ mm}$ ), filtered by an aperture (iris diaphragm) near the focus, and converged again to a collimated beam by a convex lens ( $f = 40 \text{ mm}$ ). A coated neutral-density (ND) filter with an optical density of 0.5 was used as a beam splitter, reflecting approximately 68% of the light onto the fire deck via the  $45^\circ$  mirror. The retro-reflected light went back through the beam splitter with a total transmitted light of 22% approximately. Then it was converged by another convex lens ( $f = 500 \text{ mm}$ ) and captured by a high-speed camera (Photron SA-Z). A cut-off disc with a diameter of 5 mm was placed at the focus, resulting in a dark-field schlieren, because otherwise the reflected light from the surfaces of the piston window would obscure the signal reflected from the fire deck. The deflected light by the fire deck or the spray will bypass the cut-off disc, as indicated by the dashed line in Figure 9.6. The deflected light by the fire deck or the spray will bypass the cut-off disc, as indicated by the dashed line in Figure 9.6. The focus ring of the camera lens was fixed at infinity, and the image was focused at the fire deck by moving the second collimating lens ( $f = 500 \text{ mm}$ ), so that the beam steering could be also focused well [342]. The LED was run in a skip-illumination mode (1 on / 1 off) under reacting conditions so that the ignition could be captured as well.

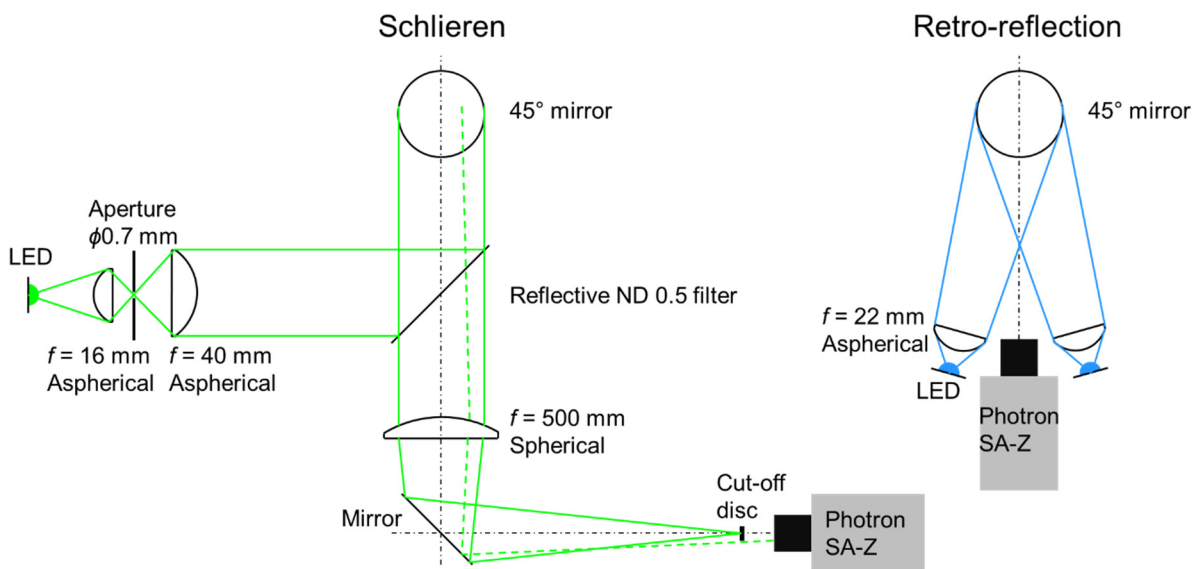


Figure 9.6 Schematic of optics for (left) schlieren imaging and (right) fire-deck retro-reflection. The dashed line indicates a ray deflected by the fire-deck surface or the fuel spray in schlieren imaging.

Table 9.2 Imaging parameters for schlieren imaging.

	Non-reacting	Reacting
Frame rate	50 kHz	100 kHz
Resolution	640 × 660	384 × 360
Projected pixel size	0.094 mm/pixel	
LED pulse duration	3 μs	
Exposure time	18.4 μs	8.4 μs
Camera lens	Nikon 105 mm <i>f</i> /2.8	
Filter	None	
Illumination	All images	Skip (1 on / 1 off)
Recorded cycles	50	25

**Image processing**

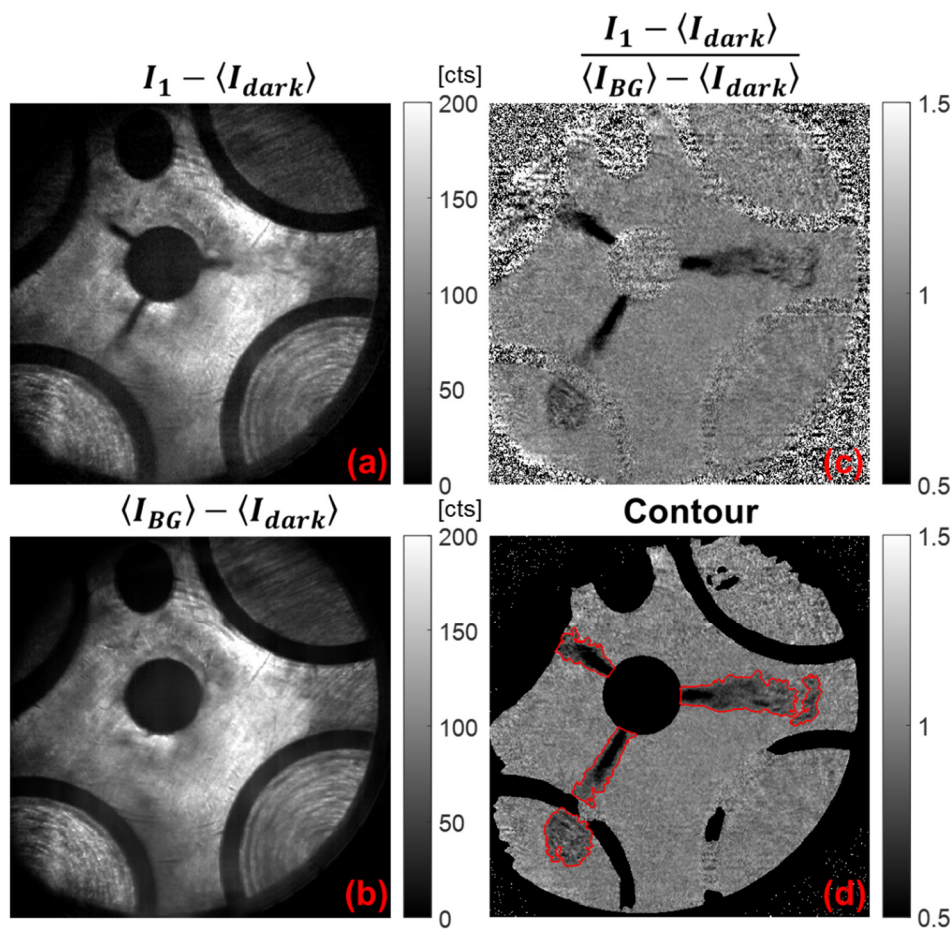


Figure 9.7 Processing procedures for schlieren images.

The single-shot spray images and the mean BG images (across 50 images before SOI) were first subtracted by the mean dark image, resulting in Figure 9.7a and Figure 9.7b, respectively. The FOV here is smaller than the full piton bowl, limited by the size of the beam splitter. From both Figure 9.7a and Figure 9.7b, it is seen that the background is essentially the retro-reflected light from the fire deck. This is different from a normal dark-field schlieren image [146, 147], where the background is totally dark because of the cut-off disc. Thus, it can be deduced that the fire-deck surface is far from specular, giving diffuse reflection. An exemplary deflected ray trace is shown by the dashed line in Figure 9.6. However, in Figure 9.7a, the beam steering from the spray is still seen, indicating the fire-deck surface is not as “rough” as a diffuser [153]. This also explains why both liquid- and gas-phase fuel is seen with the fire-deck retro-reflection method (see Figure 4.5). Since the background signal is not uniform across

the fire deck, the single-shot spray image (corrected by the mean dark image, Figure 9.7a) was divided by the mean BG image (corrected by the mean dark image, Figure 9.7b), resulting in the normalized-intensity image (Figure 9.7c). Thereby, the fuel spray is identified by the extinction (liquid fuel) and gradients (fuel vapor). A 5×5-pixel median filter as well as a mask from image intensity and geometry were applied to image c. Then a threshold of 0.87 was selected to obtain the spray contour, overlaid on a masked version of image, shown in Figure 9.7d. The time derivative method applied in Figure 4.5 was not used here, because the derivative signal was too weak. Under reacting conditions, the “off” frames were processed with the same method as shown in Figure 4.11.

### ***Results and discussion***

The processed single-cycle spray images from schlieren and fire-deck retro-reflection at similar in-cylinder temperatures are compared in Figure 9.8. For both cases, the spray contours are overlaid on the normalized-intensity images. Since more difficulty was found for fuel vapor detection near the wall region at high swirl compared to that at low swirl (see Figure 4.19 and Figure 4.20), here the images at high swirl are compared. It is seen that before spray impingement (ca. 0.35 ms ASOI), similar results are obtained by those two methods. As seen near 0.39 ms ASOI, after the impingement, the convected fuel vapor by the swirl flow located at the lower edge of the intake valve is better detected with the schlieren method. In the uncolimated retro-reflection method, the illumination is not spatially uniform so that the intake valve region contributes noisy or no signal. However, the fuel vapor flowing against the wall, which has probably already been well mixed with the air, cannot be captured by both methods, as seen near 0.57 ms ASOI. The author thinks that a true schlieren method without deflection by the fire deck probably would detect that. At 1.65 ms ASOI, after EOI, the fuel vapor distribution is much better detected by the schlieren method, since the processing for schlieren here is based on the beam steering (contrast), while that for fire-deck retro-reflection based on the movement of the fuel vapor. For both methods, the part of the jet head at the intake valve seat cannot be detected because of poor reflectivity. Therefore, as already discussed in Section 4.4.2, the effect of swirl on spray penetration and spray dispersion angle cannot be fully addressed with the current diagnostics in this work, unfortunately.

Following the results shown in Figure 4.16, to see the effect of ignition on the spray penetration measurement, single-cycle images obtained with schlieren at a non-reacting condition and a reacting condition with similar in-cylinder temperatures are compared in Figure 9.9. Low swirl datasets are used here. Under reacting conditions, the flame contour from the preceding “off” frame is overlaid on the current image. Before ignition, at both 0.28 and 0.34 ms ASOI, it is seen that the sprays at the reacting condition are shorter and narrower than those at the non-reacting condition. This phenomenon is consistent with that found in combustion vessels [146, 149], where the beam-steering effect is diminished because of LTR, as discussed in Section 0.

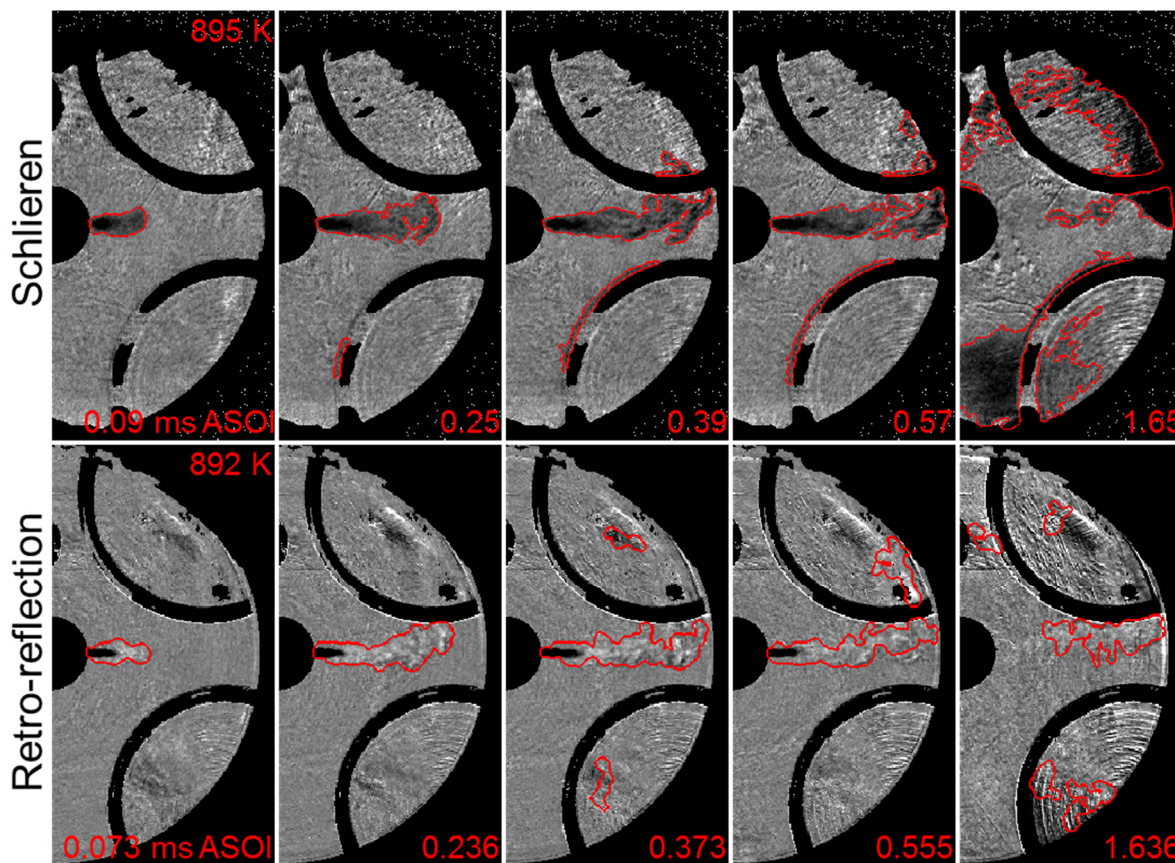


Figure 9.8 Comparison of single-cycle processed spray images centered at jet 3 from schlieren and fire-deck retro-reflection at high swirl and similar in-cylinder core temperatures. The background is the normalized-intensity image. The time ASOI in the schlieren experiment might have a slight offset, since the SOI is taken from the mean at that operating condition.

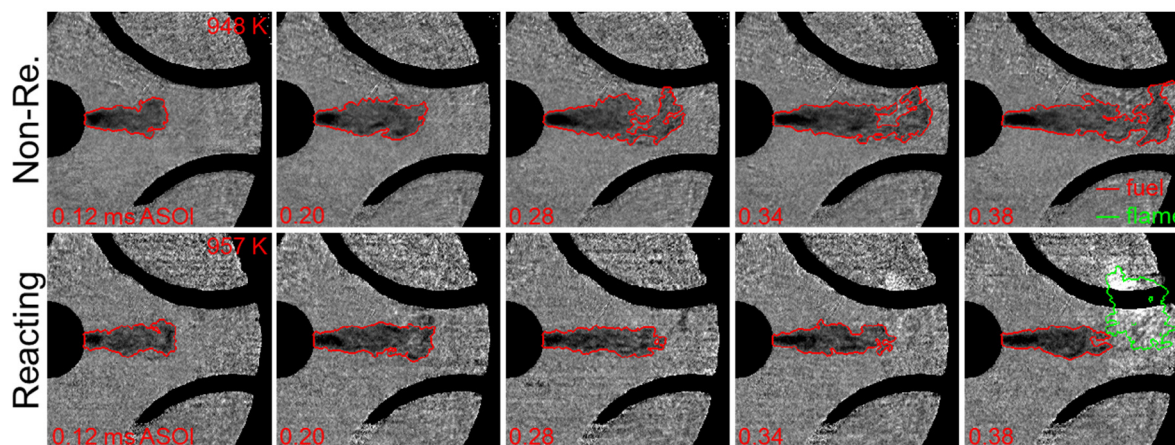


Figure 9.9 Comparison of single-cycle images centered at jet 3 obtained with schlieren between a non-reacting condition and a reacting condition at low swirl and similar in-cylinder core temperatures.

### 9.1.4 Conclusions

Compared to the axial signal profile from Mie scattering of a liquid spray, that of optical thickness by fire-deck retro-reflection peaks and decreases at a longer distance from the nozzle, leading to a longer liquid length if using the same non-zero percentage of the peak value as a threshold or using forward-

extrapolation. A steeper slope of liquid length against temperature can be also deduced. Even though the spray axis is not parallel to the object plane (see Figure 4.6), both signals show little change when focusing at different planes throughout the liquid spray. Unlike DBI, the optical-thickness signal by fire-deck retro-reflection is influenced by the incident-light angle or intensity. However, the zero-crossing point does not seem to be influenced.

True schlieren imaging cannot be achieved with the current engine set-up. Using a collimated beam and the fire-deck as a reflector, the fuel-vapor detection is slightly improved over less collimated illumination. A more uniform illumination can be achieved, but after spray impingement the fuel vapor flowing against the wall still cannot be detected.

---

# DuEPublico

Duisburg-Essen Publications online

UNIVERSITÄT  
DUISBURG  
ESSEN

*Offen im Denken*

ub | universitäts  
bibliothek

Diese Dissertation wird über DuEPublico, dem Dokumenten- und Publikationsserver der Universität Duisburg-Essen, zur Verfügung gestellt und liegt auch als Print-Version vor.

**DOI:** 10.17185/duepublico/71836

**URN:** urn:nbn:de:hbz:464-20200622-151137-2

Alle Rechte vorbehalten.